METHODS FOR DERIVING TEMPERATURE PROFILES OF MARS FROM OH MEINEL AIRGLOW OBSERVATIONS

STEPHANIE CONWAY

A DISSERTATION SUBMITTED TO
THE FACULTY OF GRADUATE STUDIES
IN PARTIAL FULFILMENT OF THE REQUIREMENTS
FOR THE DEGREE OF
DOCTOR OF PHILOSOPHY

GRADUATE PROGRAM IN EARTH AND SPACE SCIENCE
YORK UNIVERSITY
TORONTO, ONTARIO

MARCH, 2012

Abstract

Observations of the OH Meinel Band airglow emission from vibrationally excited ground electronic state OH radicals have long been used to gain valuable information about the dynamics and state of the upper atmosphere of Earth. In this work, we attempt to develop methods for use in the Martian atmosphere. The middle Martian atmosphere is a layer of rich dynamics, such as planetary and gravity waves, however it is not well understood. It is important to develop methodologies to aid in achieving a better understanding of this part of the Martian atmosphere.

In this work, methods for the retrieval of temperatures and OH Meinel Band volume emission rates from possible future limb observations of the Martian atmosphere are developed and compared with the goal of determining general instrument requirements for the observation and analysis of yet to be detected emissions of the Martian nighttime OH Meinel Band airglow.

To this end, a non-linear fitting algorithm is developed to fit modelled wavelength bin radiance spectra to observations to recover temperatures and total vibrational level volume emission rates. Three different approaches for retrieval are developed: an Onion Peeling approach, a Global Optimization approach and an approach using Derived Absolute Wavelength Bin Radiance Spectra. The Global Optimization method is found to be the most robust and is used to estimate the

order of magnitude of instrument optical properties necessary for the detection of the emission and the retrieval of temperatures and emission rates.

The results of this investigation will advance the application of remote sensing techniques to planetary atmospheres. The developed retrieval methods are flexible and, as such, are not limited in application to the Martian OH Meinel Band airglow. They can be used on any planet where emissions of OH Meinel Band airglow have been observed, such as Venus.

Acknowledgements

It is a pleasure to thank the many people who made this thesis possible.

I am greatly indebted in the preparation of this thesis to my supervisor, Dr. Ian McDade, whose enthusiasm and guidance have been invaluable to me. I am also indebted to Dr. John McConnell who gave me direction when I was floundering and held me accountable for my progress. Without his help I would still be agonizing over the first few chapters of this thesis.

I am grateful to my colleagues and friends at York University for providing a warm and fun environment in which to learn and grow.

I would like to thank my sisters, my extended family and my friends for all their love and encouragement, and my patient husband Vyacheslav whose support during the final stages of this Ph.D. is so appreciated.

Lastly, and most importantly, I wish to thank my parents, Fred and Madeleine Conway. They fostered in me a love for learning which has never wavered. To them I dedicate this thesis.

Table of Contents

List of Tables

List of Figures

List of Symbols

a	Chapman function parameter	179
A	magnetic coupling energy in cm^{-1}	26
A	aperture size in cm^2	150
$A_T(\upsilon')$	total radiative transition probability for OH(υ')	13
$A(\upsilon', \upsilon'')$	transition probability for a $\nu' - \nu''$ band	11
$\tilde{A}$	averaging kernel	64
$\alpha(\lambda)$	vector of $\frac{A(J',\upsilon' \rightarrow J'',\upsilon'')}{A_T(T_{ROT})} \frac{2(2J'+1)}{Q_{\upsilon'}(T_{ROT})} exp(\frac{-E_{\upsilon',i'}(J')}{kT_{ROT}})$ values	78
b	Chapman function parameter	179
B	molecule rotational constant in cm^{-1}	26
$\mathbf{B}(\lambda)$	synthetic limb emission spectrum in ph s^{-1} cm^{-2}	36
d_{avg}	average hard shell diameter of OH and CO_2	42
D	centrifugal distortion constant for a non rigid molecule in cm^{-1}	27
$E_{\upsilon',i'}(J)$	difference between the rotational energy of J state and ZPE	32
ϵ	vector of systematic and random errors in observations	59
η_D	dark current shot noise in electrons	151
η_R	read out noise in electrons	151
$f(\lambda)$	instrument response function in fractional units	36

$F(\upsilon, J)$	rotational energy of the OH molecule of rotational level J	26
g	number of tangent heights	81
G_υ	vibrational energy of the OH molecule of vibrational level υ	28
$\tilde{G}_y$	gain matrix	63
$\mathbf{\Gamma}$	synthetic AD local VER spectrum	36
$\mathbf{\Gamma}^{full}$	synthetic AD local VER spectrum for all tangent heights	81
h	Planck's constant = 6.626E-34 in m kg s^{-1}	20
h_{max}	Chapman function parameter, height of the peak emission rate	179
H_j	tangent height, where j is the layer index	68
$\tilde{H}$	Hessian matrix	53
$\tilde{I}$	the identity matrix	54
I_A	effective moment of inertia about the internuclear axis in kg m^2	26
I_B	moment of inertia about the center of mass in kg m^2	26
J	total angular momentum quantum number (integer)	21
J'	upper level total angular momentum quantum number	21
J''	lower level total angular momentum quantum number	21
$\overrightarrow{J}$	total molecular angular momentum vector	23
J	merit function	51
k_1	rate coefficient in cm^3 s^{-1}	9
k_2	rate coefficient in cm^3 s^{-1}	10
k^M	total collisional removal rate coefficient by species M	11
$k_T^{CO_2}(\upsilon')$	total collisional removal rate coefficient with CO_2 for OH(υ')	12
$\tilde{K}$	Jacobian matrix relating observations to parameters	49
L_i	atmospheric layer	72

λ	wavelength of emission	30
Λ	total electron orbital angular momentum quantum number	20
m	number of observations	50
m_ℓ	magnetic quantum number	20
m_s	secondary spin quantum number	20
n	number of state parameters	50
$n_{col}(\upsilon')$	number of collisions per total lifetime	42
N	axial component of $\overrightarrow{N}$	24
$N_A\mu$	reduced molar mass of OH and CO_2 in kg mole^{-1}	42
N_{CO2}	number density of CO_2 in molecules cm^{-3}	41
N_υ	number density of vibrational level υ in particles cm^{-3}	32
$\overrightarrow{N}$	total rotation angular momentum vector including electron spin	23
Ω	axial component of the total electron angular momentum	22
Ω	field of view intrinsic to the instrument in steradians	150
p	atomic orbital with angular quantum momentum number = 1	20
P	probability density function	56
$\tilde{P}$	matrix of geometric pathlengths	69
π	p-type molecular orbital	20
Π	electronic ground state for molecules with $\Lambda = 1$	20
$\mathbf{q_i}$	vector of local OH Meinel Band volume emission rates	73
q_e	quantum efficiency	150
$\mathbf{Q_i}$	observed instrument degraded local VER spectrum	73
Q_υ	rotation partition function for a given rotational temperature	32
R	universal gas constant, 8.314472 J K^{-1} mole^{-1}	42

R	Transfer function	63
$\mathbf{R_i}$	observed local VER spectrum for ith tangent height	73
$\mathbf{R}^{full}$	observed local VER spectrum for all tangent heights	81
R_p	radius of planet in km	69
s	atomic electron orbital with angular quantum number = 0	20
$\overrightarrow{S}$	total electron spin angular momentum vector	20
$\tilde{S}$	total error	66
$\tilde{S}_a$	*a priori* covariance matrix	59
$\tilde{S_m}$	covariance matrix of retrieval noise	65
$\tilde{S}_s$	covariance matrix of smoothing error	65
$\tilde{S}_y$	estimated measurement covariance matrix	59
σ	s-type molecular orbital	20
σ	standard deviation	56
Σ	axial component for $\overrightarrow{S}$	20
T_{atm}	atmospheric temperature in K	39
T_{ROT}	rotational temperature in K	32
$\tau(\upsilon')$	total lifetime of OH(υ') in s	41
$\tau_{rad}(\upsilon')$	radiative lifetime of vibrational level υ' in s	41
$\tau_{chem}(\upsilon')$	chemical lifetime of vibrational level υ' in s	41
$\tau_{col}(\upsilon')$	mean time between collisions in s	41
t_s	integration time in seconds	150
υ	vibrational quantum number	9
υ'	upper vibrational level quantum number for a R-V band	21
υ''	lower vibrational level quantum number for a R-V band	21

$\overline{\nu}$	frequency of radiation in cm^{-1}	30
$\overline{\nu}_v$	energy of vibrational transition in cm^{-1}	29
$\overline{\nu}_r$	energy of rotational transition in cm^{-1}	29
V_{max}	Chapman function parameter, peak emission rate	179
$V(J', v' \rightarrow J'', v'')$	volume emission rates of $(J', v', i \rightarrow J'', v'', i)$ transition	32
$V(v', v'')$	volume emission rate for a given $(v' - v'')$ band	13
$V(z)$	Chapman Function	179
$V_T(v')$	volume emission rate for all bands for a given v' level	34
$\mathbf{x}$	vector of parameters describing the state of the atmosphere	48
$\overline{\mathbf{x}}$	maximum probability state of state parameters	60
$\mathbf{x_a}$	*a priori* state vector	51
x_k	vector of trial parameters at the k^{th} iteration	51
$\widehat{\mathbf{x}}$	retrieved state vector	51
$\mathbf{y}$	vector of observed limb radiances in photons s^{-1} cm^{-2} $\mathring{A}^{-1}$	48
$\widehat{\mathbf{y}}$	vector of reconstructed observations	51
Y	tightness of molecular coupling, $Y = \frac{A}{B}$	26
z	Chapman function parameter, height	179
Z_{rot}	number of collisions necessary to effect rotational relaxation	40
ZPE	zero point energy	32
ζ	adjustable parameter for the gradient descent method	52

List of Acronyms

AD	Absolute instrument Degraded
BD	Boltzmann Distribution
IR	InfraRed
LTE	Local Thermodynamic Equilibrium
NLTE	Non-local Thermodynamic Equilibrium
PDF	Probability Density Function
R-V	Rotational-Vibrational
RMS	Root Mean Square
SCIAMACHY	SCanning Imaging Absorption spectroMeter for Atmospheric CartograpHY
SPICAV/SOIR	Spectroscopy for Investigation of Characteristics of the Atmosphere of Venus / Solar Occultation at InfraRed
TES	Thermal Emission Spectrometer

THEMIS-VIS	Thermal Emission Imaging System Visible Imaging Subsystem
VER	Volume Emission Rate
VIRTIS	Visible and Infra-Red Thermal Imaging Spectrometer
VIS	Visible
WBR	Wavelength Bin Radiance

1 Introduction

Optical methods have long been used to provide information about the state of the upper atmosphere and in some cases gain information regarding chemical reactions (*Hunten and McElroy*, 1966) that cannot be determined in a laboratory setting. The main advantage of these methods is that, in most cases, much data can be recovered without locally sampling the air.

The daytime ionization and photodissociation of upper atmospheric constituents by solar radiation gives rise to numerous photochemical reactions whose effects can persist into the night. Many of these reactions subsequently cause molecular and atomic emission in the ultraviolet, visible and infrared regions of the spectrum. These emissions are collectively known as 'airglow emissions'. Since the 1950s, the observation of airglow has been an important tool for obtaining information about the state and structure of the upper atmosphere. Spectroscopic and radiometric measurements of the various emissions can be used to monitor winds, planetary waves, atmospheric temperatures and for the recovery of local and column abundances of atmospheric species (e.g., *Garcia-Muñoz*, 2006).

The Earth's airglow consists of emissions from at least 25 identified excited species: 11 atomic and 14 molecular that give rise to more than 1000 different molecular features and approximately 130 excited atomic features (*Khomich et al.*,

2008). Many of the same emissions have been observed in the Martian atmosphere; a list of observed airglow emissions in the Martian atmosphere is presented in Table 1.1.

In this work we will focus on one particular airglow feature, the OH Meinel Band airglow, which consists of the emissions of rotationally and vibrationally excited OH molecules. The excited OH radical emits on both the day side and the night side of the planet, and is formed by at least two different processes. The night side emission, known as nightglow, differs from that of the day side, known as dayglow. The nightglow emission is dominated by neutral chemiluminescent reactions of reactive transient species produced during the day.

The nighttime OH Meinel airglow had been measured for more than 20 years in the Earth's atmosphere before it was positively identified in 1950 by *Herzberg* (1950) and confirmed by *Meinel* (1950) later that year. The possibility had been previously discussed by *Déjardin, G. and Bernard, R.* (1938) and *Nicolet* (1948), but ultimately discounted as the presence of OH in the atmosphere was then considered unlikely. *Shklovsky* (1950a,b; 1951) then identified additional OH Meinel bands and was the first to calculate the transition probabilities for the rotational-vibrational bands. Shklovsky was also the first to estimate the intensity of bands that, at that time, had yet to be detected based on his derived transition probabilities. Later, *Heaps and Herzberg* (1952) improved upon these empirical transition probabilities and calculated a mathematically-based spectral intensity distribution of the OH Meinel spectrum. The peak altitude of the OH emission was subsequently determined using rocket measurements to be near 87 km with a full width half maximum of about 8 km (*Heppner and Meredith*, 1958; *Baker and Stair*, 1988). As early as

Species		Wavelength (Å)	Species		Wavelength (Å)
Ar		867	N		1134
		1048			1200
		1066	N_2	V-K Band	2762
H	Lyman γ	973	CO	H-B Band	1088 - 1152
	Lyman β	1026		Cam. Band	1900 - 2700
	Lyman α	1216		4+ Band	1280 - 2800
O		989	C		1561
		1040			1657
	triplet	1304	O^+		834
	doublet	1356	CO_2^+	doublet	2883 - 2896
		2972		Band	2800 - 5000
O_2	IR Atmos Band	12700	NO	$\gamma + \delta$ Band	1900 - 2700

Table 1.1: Observed airglow emissions in the Martian atmosphere. All the above listed emissions are dayglow emissions save for the NO $\gamma + \delta$ Bands. The H Lyman α emission and the O_2 infrared (IR) Atmospheric Band have been observed in both day and night. The H-B band refers to the Hopfield-Birge Bands, Cam. Band to the Cameron Band and the 4+ Band to the Fourth Positive Band of CO. The V-K band refers to the Vegard-Kaplan band of NO. Refs: *Witasse* (2000) reviews observations made by the Mars and Mariner missions and past ground based observations, *Bertaux et al.* (2005) and *Bertaux et al.* (2011) present observations made by the SPICAM instrument on board Mars Express.

1950, explanations were advanced by *Bates and Nicolet* (1950) and *Herzberg* (1950) regarding the nature of the emission which have been further developed over the last half century. However, many questions regarding the excitation and deactivation processes have yet to be resolved.

Observations of OH Meinel airglow have long been used to recover information about the Earth's atmosphere, in particular mesospheric temperatures (e.g., *Meriwether Jr.*, 1989) and mesospheric oxygen atom densities (e.g., *McDade and Llewellyn*, 1988). Also observations of the emissions have been used to detect and study gravity waves (e.g., *Taylor et al.*, 2009). In cometary science the presence of OH Meinel airglow emissions in the tails of comets has been used as a possible tracer for water bound to minerals (*Jenniskens and Laux*, 2004).

The goal of this work is to build on this heritage and develop techniques for extracting Martian atmospheric properties from potential limb airglow observations made by a future orbital instrument. Although the OH Meinel airglow has not yet been detected on Mars, it is expected to exist on both the day and night side of the planet due to the presence of ozone and hydrogen (e.g., *Migliorini et al.*, 2011), the species thought to produce the OH Meinel airglow. The only attempt to observe OH Meinel airglow was made by the Mars 5 automatic station. Based on this attempt an upper limit of 50 R [1] was set in the limb (*Krasnopolsky and Krysko*, 1976).

[1] 1R = 10^{10} photons per square metre per column per second

1.1 Mars

Mars exploration has been an important part of the space programs of the former Soviet Union, the United States, Europe, and Japan since the 1960s. Many space missions have been conducted to gather information about the current conditions and history of the Martian atmosphere. Yet many outstanding questions still remain concerning our neighbour and the most Earth-like planet in our solar system.

The original Martian atmosphere was thought to be very dense, with model predictions of atmospheric pressures varying between 0.6 - 5 bar (e.g., *Ehresmann et al*, 2011). This original atmosphere would have consisted of three main consistuents: carbon dioxide, water vapour and molecular nitrogen. This contrasts with the thin atmosphere of present day Mars, with an average surface pressure of 6 mbar, although the relative composition is thought to be unchanged (*Krasnopolsky*, 2010). The same three main constituents are thought to have been present on the Earth and Venus just after their formation, however the three atmospheres developed quite differently (*Krasnopolsky*, 2011). By understanding the present Martian upper atmosphere, we will gain insight into the history of the planet and the changes in climate that have occurred over the past billion years.

The study of Mars also helps us gain a better understanding of atmospheric chemical processes. In physics, to explain the nature of a phenomenon one attempts to predict key properties of the phenomenon under different controlled conditions. However, it is almost impossible to reproduce atmospheric processes in the laboratory as such processes depend on many factors. Yet, if the same processes

occur in the atmosphere of another planet, say in the Martian atmosphere where the atmospheric conditions are different from those on Earth, it may be possible to gain insight into the nature of the phenomena. As such, the Martian atmosphere can be thought of as a laboratory for atmospheric research with settings different from those of Earth's atmospheric laboratory. This approach can be applied to gain insight into one particular puzzle at least - the processes responsible for the deactivation of OH Meinel airglow as will be discussed further in the following section.

The final reason may be the most important for the general public. Mars is our neighbour and is the most similar to Earth in terms of surface environment. Human exploration of Mars is the next major milestone in the great space endeavour and in preparation for future exploration, it is imperative that we gain as much insight into our neighbour, the Red planet, as possible.

1.2 The OH Meinel Airglow on Mars

The atmospheric dynamics and thermal structure of the Martian atmosphere between 50 and 100 km have been mostly neglected by Mars missions (*Forget et al.*, 2009). The Mariner 6, 7 and 9 missions focused on the lower atmosphere and the upper atmosphere above 100 km. Subsequent missions concentrated on the lower atmosphere, instruments on board the Mars Global Surveyor (MGS) and Mars Express have been monitoring the Martian atmosphere below 50 km for the last several years. Until recently only a limited number of density measurements above 50 km existed. These include density profiles from the entry of the Viking,

Pathfinder and Mars Exploration rovers and from the aerobraking of MGS, Mars Odyssey and Mars Reconnaissance Orbiter missions. These measurements revealed an upper atmosphere of rich dynamics containing various types of planetary waves likely interacting with the mean circulation (*Magalhães et al.*, 1999; *Angelats i Coll et al.*, 2004; *Forbes et al.*, 2002). In 2006 the Mars Climate Sounder on board the Mars Reconnaissance Orbiter began making thermal limb emission measurements of the Martian atmosphere between 5 km and 90 km (*Kleinböhl et al.*, 2009), however there is much remaining to learn. Based on modelling, the emission layer of the OH Meinel nightglow is expected to lie between 45 and 80 km (*García Muñoz et al.*, 2005) and observations of this emission would compliment the observations made by the Mars Climate Sounder in this altitude region. It is essential that we gain more information about the properties of the atmosphere at these altitudes for future mission planning. Aerobraking, a technique used to adjust the orbit of the spacecraft, and the descent phase of surface missions occur through this region.

The relationship between the spectral characteristics of the emission and the rotational temperature of the emitting OH molecules is fairly well understood and the method by which temperature may be recovered from OH observation is the focus of the present work. There is a general assumption that OH molecules excited to lower rotational and vibrational levels are rotationally thermalized and thus the recovered rotational temperatures are indicative of the kinetic temperature of the surrounding atmosphere. The reasoning behind this assumption is discussed in Section 2.5.1. In addition information regarding the existence of planetary waves in this atmospheric region can be deduced from the variations in the rotational temperature. This method has been used extensively to monitor gravity waves in

Earth's atmosphere (*Marsh et al.*, 2006; *Sentman at al.*, 2003; *Viereck and Deehr*, 1989). The OH volume emission rates, and consequently the number densities of the emitting vibrational states from 45 to 80 km, can also be recovered from optical observations of the OH Meinel Band airglow emissions.

OH is involved in the catalytic destruction of ozone in the terrestrial mesosphere and is also coupled to the water cycle. The same processes are expected to occur on Mars (*Migliorini et al.*, 2011). Martian photochemistry is regulated by the water cycle, particularly the photolysis of water vapour which forms odd hydrogen[2] species such as OH. Using measurements of Lyman-α airglow by Mariner 6, 7 and 9, the amount and distribution of hydrogen above 80 km was determined by *Anderson* (1974). However, to-date there are no measurements of odd hydrogen compounds save for a speculative constraint that $[H][O_3] < 10^{15}$ cm^{-6} at 60 km (*Krasnopolsky and Krysko*, 1976). This constraint is based on the above mentioned observations of the Mars 5 automatic station.

The main sink process for odd oxygen[3] at night on Mars is thought to be the Bates-Nicolet mechanism, which is also thought to be the primary potential source of vibrationally excited OH in the Martian atmosphere. The Bates-Nicolet mechanism is involved in the catalytic cycle that destroys ozone. The ozone molecule is destroyed when it reacts with a hydrogen atom and produces the excited OH molecule (*Bates and Nicolet*, 1950). The hydroxyl molecule eventually combines

[2]Odd hydrogen is a chemical family which participates in ozone destruction and is comprised of hydrogen atoms (H), hydroxyl radicals (OH), and hydroperoxyl radicals (HO_2).

[3]Odd oxygen is a chemical family comprising both atomic oxygen (O) and ozone (O_3).

with atomic oxygen to re-produce hydrogen, which recommences the cycle.

$$H + O_3 \rightarrow OH(v') + O_2 \tag{1.1}$$

$$OH(v') + O \rightarrow H + O_2 \tag{1.2}$$

The net effect is

$$O + O_3 \rightarrow 2O_2 \tag{1.3}$$

where $OH(v')$ is vibrationally excited or ground state OH and v' indicates the vibrational state quantum number. Thus both an atomic oxygen (O) and ozone molecule (O_3) are destroyed to create two molecular oxygen molecules (O_2). Measurements of excited OH number densities will help us gain a better understanding of both the HOx [4] catalytic destruction cycle and the odd oxygen cycle on Mars.

1.3 Origins of vibrationally excited OH molecules responsible for the OH Meinel Band emission

There are two postulated excitation processes for creation of the vibrationally excited ground state $^2\Pi$ OH radical. The first, mentioned above, is the Bates-Nicolet mechanism.

$$H + O_3 \xrightarrow{k_1} OH(v') + O_2 \tag{1.4}$$

where $OH(v')$ represents vibrationally excited OH in its $^2\Pi$ ground electronic state and k_1 is the rate coefficient in $cm^3\ s^{-1}$.

[4]The HOx chemical family referes to the ensemble of hydroxyl (OH) and hydroperoxyl (HO_2)

The exothermicity of this reaction is 3.34 eV, which limits the nascent vibrational excitation level of the product OH molecule to $v' \leq 9$. This is consistent with terrestrial observations (*Herzberg*, 1971).

The other vibrational excitation process, also suggested by *Bates and Nicolet* (1950) involves a reaction between atomic oxygen (O) and a hydroperoxyl radical (HO_2),

$$O + HO_2 \xrightarrow{k_2} OH(v') + O_2 \tag{1.5}$$

k_2 is the rate coefficient in $cm^3\ s^{-1}$. The exothermicity of this reaction limits the vibrational excitation of the OH product to $v' \leq 6$ so this can not be the exclusive excitation mechanism on Earth.

The Bates-Nicolet mechanism is thought to be the primary source of OH in terrestrial planets (*Migliorini et al.*, 2011), and on Earth it is generally accepted that the mechanism involving HO_2 does not contribute significantly (*Meriwether Jr.*, 1989). There is some evidence that it may play a role in the Venusian atmosphere (*Piccioni et al.*, 2008). However, in this work it is assumed that the Bates-Nicolet mechanism is the only significant source of vibrationally excited OH in the Martian atmosphere between 45 - 80 km.

1.4 Processes controlling OH Meinel emission rates from particular v' levels

The vibrational excitation process gives rise to OH radicals whose vibrational energy states differ very significantly from their equilibrium state when thermalized with the surrounding atmosphere. Accordingly, processes occur that move towards re-

establishing thermal equilibrium. Vibrationally excited molecules can relax via spontaneous emission

$$OH(\upsilon') \xrightarrow{A(\upsilon',\upsilon'')} OH(\upsilon'') + h\nu \tag{1.6}$$

which is the source of individual $\mathrm{OH}(\upsilon') \rightarrow \mathrm{OH}(\upsilon'')$ emission bands of the OH Meinel Band airglow. $A(\upsilon', \upsilon'')$ (s^{-1}), is the transition probability for spontaneous emission in the $J'\upsilon' \rightarrow J''\upsilon''$ transition, this will be discussed in greater detail in the next chapter. $\mathrm{OH}(\upsilon')$ can also relax via collisional deactivation,

$$OH(\upsilon') + M \xrightarrow{k^M(\upsilon',\upsilon'')} OH(\upsilon'') + M \tag{1.7}$$

where M is a molecule in the surrounding atmosphere and $k^M(\upsilon', \upsilon'')$ is the total collisional removal rate coefficient for molecule M.

Two limiting cases have been proposed for deactivation models (*McDade and Llewellyn*, 1987). The first is the Sudden Death model, where the excited OH molecule is assumed to be completely deactivated to the ground state of OH or to some other chemical product.

$$OH(\upsilon') + M \rightarrow OH(0) + M + \Delta E \tag{1.8}$$

The second proposed limiting case is the Collisional Cascade model where the vibrational excited OH molecule is deactivated by single quantum steps at each collision with the quenching molecule,

$$OH(\upsilon') + M \rightarrow OH(\upsilon' - 1) + M + \Delta E \tag{1.9}$$

These are limiting extreme cases and do not preclude intermediate models such as multi-quantum collisional cascade.

For the Earth's OH Meinel nightglow both deactivation models can explain the observations leading to an ambiguity regarding the relative importance of the two relaxation pathways. As opposed to the terrestrial case, *García Muñoz et al.* (2005) indicated that on Mars the vibrational distribution would differ substantially between the two mechanisms. In their work, a time dependant photochemical model of the Martian atmosphere was developed to determine the diurnal changes in composition of the minor species in a neutral atmosphere driven by the variations of solar radiation throughout the day. The COSPAR mean Mars temperature profile (*Seiff*, 1982), shown in Fig. 1.1, was adopted with no temporal variations in the model. This temperature profile has also been adopted throughout this work. Since the main component of the Martian atmosphere is CO_2, the model considers CO_2 as the sole quenching species (M in Eqs 1.6-1.8).

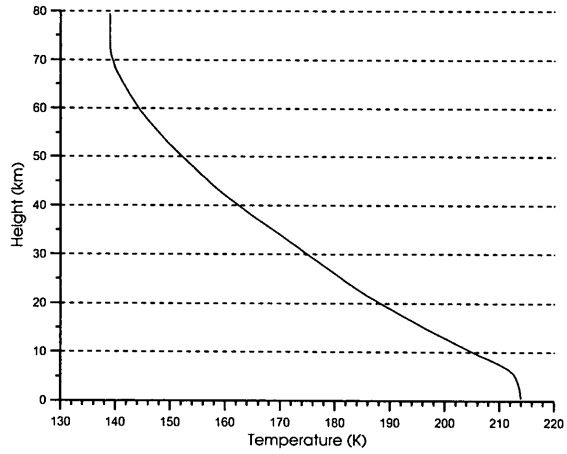

Figure 1.1: COSPAR mean Mars temperature profile (*Seiff*, 1982).

In the Sudden Death model the total collisional removal rate coefficient, $k_T^{CO_2}(v')$,

is equal to $k^{CO_2}(\upsilon', 0)$ and the probability of all other collision induced transitions is zero as only the direct deactivation to the ground state is considered possible. In the Collisional Cascade model $k_T^{CO_2}(\upsilon') = k^{CO_2}(\upsilon', \upsilon' - 1)$ as only relaxation via of a single quantum step is assumed to occur.

The total volume emission rates $V_T(\upsilon')$ from each vibrational level υ' are then given by,

$$V_T(\upsilon') = A_T(\upsilon')[OH(\upsilon')] \tag{1.10}$$

where $A_T(\upsilon')$ is the total radiative transition probability of OH(υ') and $[OH(\upsilon')]$ is the instantaneous number density of OH(υ') determined by the model. The calculated volume emission rates of the OH Meinel airglow on Mars at midnight for both the Sudden Death and Collisional Cascade deactivation models from *García Muñoz et al.* (2005) are illustrated in Fig. 1.2.

In this work the term volume emission rate (VER) will refer to the total volume emission rate of a given υ' level ($V_T(\upsilon')$) and not a band or individual transition, and the term wavelength bin radiance (WBR) refers to the measured or simulated emission rate at a specific wavelength bin. The wavelength bin size is determined by the spectral sampling interval. The VERs calculated for the Sudden Death and Collisional Cascade models at midnight in the Martian atmosphere differ very significantly save for the $\upsilon' = 9$ VER profile where both emission rate curves are identical. The excited OH molecules produced by the Bates-Nicolet mechanism are limited to $\upsilon' \leq 9$ and thus there is no enhancement to the Collision Cascade VERs due to contributions from higher vibrational levels, the profile consists solely of emissions of OH molecules excited to the $\upsilon' = 9$ vibrational level. Therefore

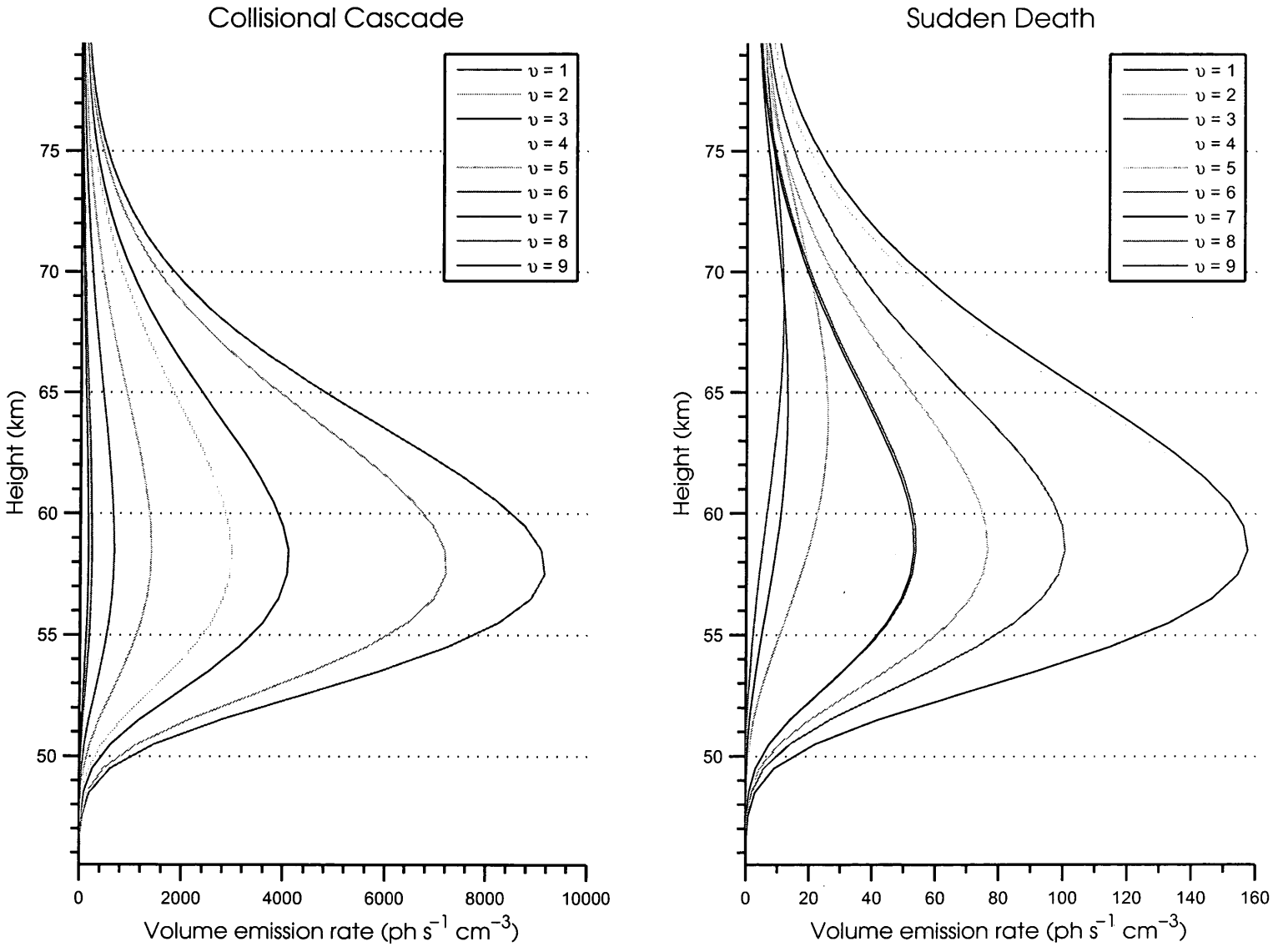

Figure 1.2: Volume emission rate profiles for a given v' level in the Martian atmosphere at midnight for the Collisional Cascade and Sudden Death deactivation models from *García Muñoz et al.* (2005). Note the different volume emission rate scales.

in the Collision Cascade model the $v' = 9$ profile is the weakest. In contrast, the $v' = 9$ level in the Sudden Death model has the highest VERs due in part to the high $A_T(9)$. The emission rate profiles for all v' for the Collisional Cascade model are similar in shape and peak at a similar altitude. The volume emission rate profiles in the Sudden Death model are similar in shape for $v' = 4 - 9$, however, the shape of the lower levels are dissimilar as the peaks of the VER profiles, and accordingly the peaks of the concentration profiles, shift upwards as the vibrational level decreases. The upward shift is related to the increase in relative importance of radiative deactivation as the source of OH(v') for lower vibrational levels.

The two sets of modelled volume emission rates result in two notably different spectra both in terms of relative intensity and in terms of spectral distribution, save for the transitions of $v' = 9$. The emission lines for the Collisional Cascade model are considerably more intense than those of the Sudden Death model and the relative intensities of the emission lines of the different vibrational levels also differ. Modelled line wavelength bin radiance spectra, integrated over the finite line widths arising from pressure and Doppler broadening which are not addressed in this work, for the two deactivation models at a rotational temperature of 200 K calculated at 79.5 km are shown in Fig. 1.3. The spectra are calculated as described in the Chapter 2. The spectral range shown is 2.95 - 3.2 μm which includes $\Delta v = 1$ transitions, specifically the OH(1-0), OH(2-1) and OH(3-2) bands.

Recently in studies of the Earth-based measurements of the Venusian OH Meinel airglow, *Krasnopolsky* (2010) introduced an intermediate relaxation pathway theory for atmospheres composed primarily of CO_2, such as those of Mars and Venus. To reconcile the deactivation process to the Venusian observations Krasnopolsky

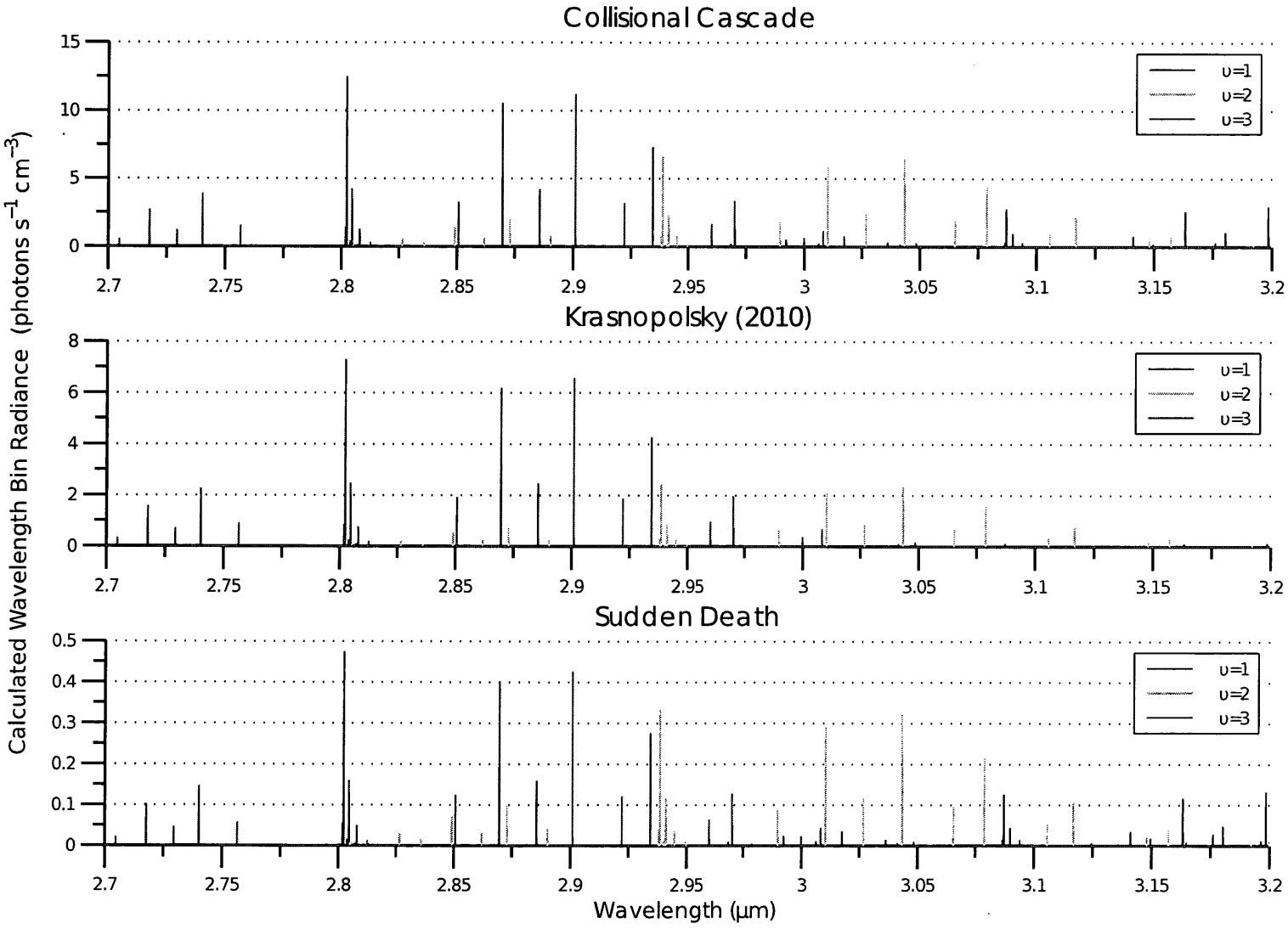

Figure 1.3: Model line wavelength bin radiance spectra for three deactivation models: Collisional Cascade, Sudden Death and the model suggested by *Krasnopolsky* (2010) in the Martian atmosphere at 79.5 km and at 200 K for the 2.95 - 3.2 μm spectral region. The calculated emissions are integrated over the line shape spectra and located on the line centres. Transition probabilities from *Turnbull and Lowe* (1989). This spectral region includes emission lines from the OH(1-0) in red, OH(2-1) in green and OH(3-2) in black.

suggested that quenching of all OH vibrational states $v' > 2$ by CO_2 to $v'' \leq 2$ have yields of 0.4, 0.35, 0.25 for $v'' = 0$, 1, 2 and equal yields for the quenching of $v' = 2$ to $v'' = 0, 1$. The Garcia-Muñoz photochemical model (*García Muñoz et al.*, 2005) was adapted for this deactivation model and the resulting volume emission rate profiles at midnight are shown in Fig. 1.4.

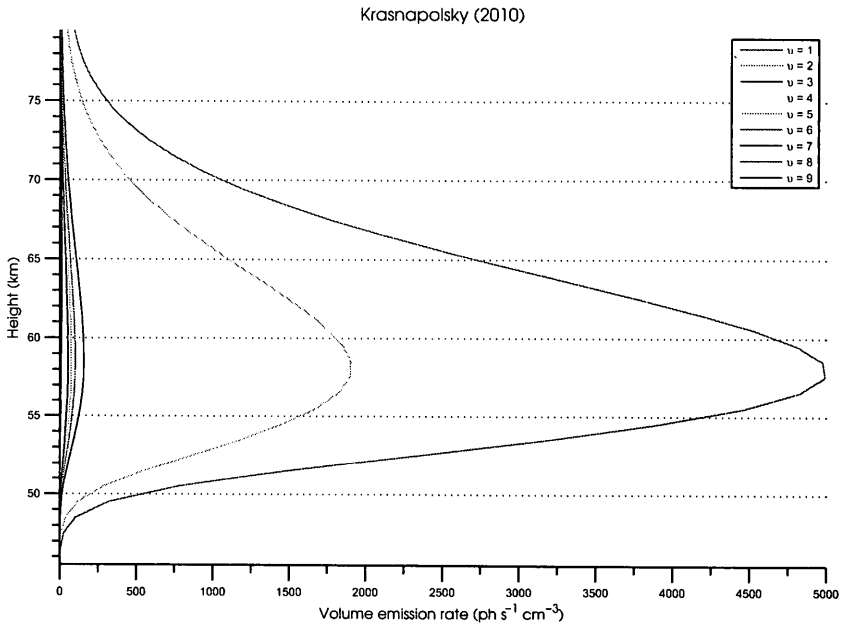

Figure 1.4: VER profiles for a given v' level in the Martian atmosphere at midnight for deactivation model suggested in *Krasnopolsky* (2010).

The volume emission rates calculated for this third deactivation model resemble the profiles for the Sudden Death case for $v' = 3 - 9$. However, the emission rates calculated for $v' = 1 - 2$ are considerably stronger. Consequently the spectrum associated with this deactivation model, shown in Fig. 1.3, only differs from the Sudden Death model for transitions from $v' = 1 - 2$. Only through observation of transitions of these two vibrational levels would the Sudden Death, Collisional Cascade and *Krasnopolsky* (2010) deactivation models be distinguishable. However,

additional emission lines from other vibrational levels would be beneficial.

Observations of Martian OH Meinel nightglow could resolve the ambiguity regarding the chemical process responsible for the deactivation process of OH airglow, a process that also occurs in Earth's atmosphere. Thus observations of the Martian atmosphere will help clarify our understanding of our atmosphere.

2 Synthetic OH Meinel Band Emission Spectra

2.1 The OH Radical electronic structure

In 1950, A.B. Meinel reported the first relatively high resolution infrared (IR) and visible (VIS) observations of Earth's night sky spectrum that he made from the Yerkes Observatory (*Meinel*, 1950). In the spectrum, Meinel discovered a new group of emission features subsequently identified as being the rotation-vibration (R-V) transitions within the ground electronic state of the OH radical, the first transitions of this type ever observed in the atmosphere. The series of emission bands were given the name the OH Meinel Band airglow after their discoverer.

To simulate the OH radical R-V emission spectrum, it is essential to understand the vibrational and rotational characteristics of the OH molecule. The hydroxyl molecule is a free radical and is highly reactive (*Herzberg*, 1971). The molecule is short-lived at all altitudes in the atmosphere, with a chemical lifetime of less than one second (*Isaksen and Dalsøren*, 2011). Vibrationally excited and ground state OH molecules react rapidly with a variety of atmospheric constituents.

The OH radical is a diatomic molecule consisting of covalently bonded hydrogen and oxygen atoms. The electronic configuration of the OH radical's electronic

ground state is designated (*Herzberg*, 1971),

$$(1s\sigma)^2(2s\sigma)^2(2p\sigma)^2(2p\pi)^3 \tag{2.1}$$

where $1s$, $2s$ and $2p$, indicate the atomic subshells from which the molecular subshells arise. The symbols σ and π indicate the molecular subshells and the superscript indicates the number of electrons in the molecular subshell.

The projection of the total electron orbital angular momentum along the internuclear axis, Λ, is used to characterize molecules. In the case of OH $\Lambda = 1$, in $\frac{h}{2\pi}$ units where h is Planck's constant, making the ground electronic state a Π state. This can also be determined from the electronic configuration, since the valence molecular orbital is in the π subshell.

By Pauli's exclusion principle there can be only four electrons in the two orbitals of the π subshell. There are two possible magnetic quantum numbers, $m_\ell = \pm 1$ and two possible secondary spin quantum numbers, $m_s = \pm\frac{1}{2}$ for each electron in the two π orbitals making a total of four possible substates arising from the electron configuration. Since there are three electrons in the highest lying molecular subshell, as shown in the configuration given in 2.1, the total spin angular momentum vector, $\vec{S}$,[5] is $|\frac{1}{2}|$ with the total possible axial components designated Σ, are $\Sigma = \frac{1}{2} + -\frac{1}{2} + -\frac{1}{2} = -\frac{1}{2}$ or $\Sigma = \frac{1}{2} + -\frac{1}{2} + \frac{1}{2} = \frac{1}{2}$. This results in two spin-orbit substates for the ground electronic configuration.

The multiplicity, indicated by the superscript in the term symbol $^2\Pi$ describes the electronic degeneracy, or near degeneracy, of the radical and is given by $2|\vec{S}|+1$.

[5]The over arrow, *i.e.*, $\vec{a}$ indicates a Cartesian vector

Hence the OH radical is called a doublet because it has a multiplicity of 2. The multiplicity is related to the Ω degeneracy discussed in Section 2.3.1.

2.2 The Rotational-Vibrational Spectrum of the OH Radical

The OH Meinel Band airglow is produced by the rotational-vibrational emission of vibrationally excited radical in the electronic ground state of OH (OH(v')) in the atmosphere. Emission from vibrationally excited OH radicals with $v' \leq 9$ is observed in Earth's upper atmosphere (*Herzberg*, 1971). The R-V emission spectrum is generated by transitions from an upper vibrational level v' to a lower vibrational level v'' while simultaneously changing rotational levels from J' in the upper v' state to J'' is the lower vibrational state v''

$$v', J' \rightarrow v'', J'' \tag{2.2}$$

where J is the total angular momentum quantum number. For most molecules exhibiting R-V emission or absorption spectra, $v' = v'' + 1$ is the norm, *i.e.*, $\Delta v = -1$ for spontaneous emission and $\Delta v = +1$ for stimulated absorption. But in the case of OH, first overtone and high overtone transitions with $\Delta v > \pm 1$ occur. The collection of possible rotational transitions accompanying a single vibrational transition create a 'band' of lines distributed about the band origin.

2.3 The OH Meinel Airglow Emission Lines

2.3.1 Degeneracy of the OH radical

There are two types of near degeneracy associated with the OH radical: Ω degeneracy and Λ-type doubling.

Λ-type doubling is a splitting of individual rotation levels caused by the two possible orientations of the orbital angular momentum vector associated with the rotation of the electrons around the internuclear axis. The magnitude of this Λ splitting is small compared to the spin multiplet (spin-orbit) structure (*Hill and van Vleck*, 1928). The effect of the Λ doubling can be ignored, as its detection would require an instrument of much greater resolution than is considered in this work.

Ω, the axial component of the total electron orbital angular momentum of the molecule, is given by $\Omega = \Sigma + \Lambda$ where Σ is the axial component of the electron spin angular momentum and Λ the orbital angular momentum along the internuclear axis as before. For the OH radical $\Lambda = 1$ and there are two possible values for Σ, $\Sigma = \pm\frac{1}{2}$ and hence the two subbands indicated by the multiplicity. Thus there are two possible values for Ω: $\Omega = \frac{1}{2}$ and $\Omega = \frac{3}{2}$. The two Ω sub-states correspond to two near degenerate ground states, designated $^2\Pi_{\frac{3}{2}}$ and $^2\Pi_{\frac{1}{2}}$ where the superscript indicates a multiplicity of 2 and thus a total spin of $\frac{1}{2}$ and the subscript indicates the resulting two Ω states; $\Omega = \frac{1}{2}$ and $\Omega = \frac{3}{2}$, each with its own set of transitions. It is important to model the transitions arising from both Ω states in developing a representative synthetic spectrum of the OH molecule's R-V emission spectrum.

The details of the Ω splitting are related to the coupling of molecular rotation

and electron spin, which was first discussed by Friedrich Hund (*Herzberg*, 1971). Hund distinguished several scenarios that are commonly referred to as Hund's Coupling Cases. In the case of the OH radical, the doublet splitting is fairly small, so it behaves similarly to what is known as Hund's Case B (*Herzberg*, 1971). In Hund's Case B, the electron spin momentum vector $\vec{S}$ is coupled first to the total non-spin angular momentum vector $\vec{N}$ to provide the total angular momentum vector of the molecule $\vec{J}$. Fig. 2.1 illustrates the relationship between the different angular momenta.

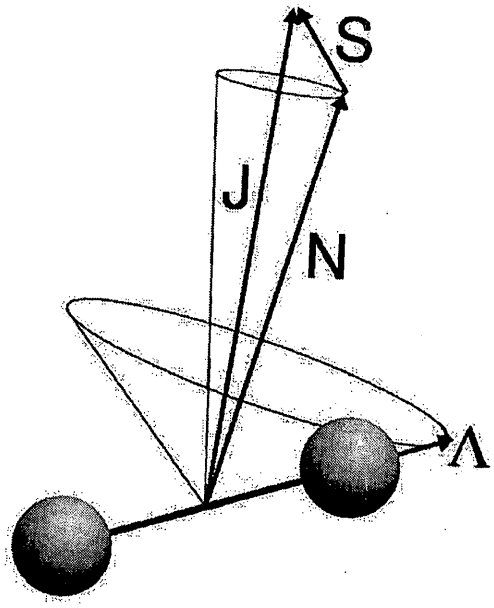

Figure 2.1: Vector diagram of Hund's Case B (*Bernath*, 2005).

The total angular momentum vector $\vec{J}$, the vector sum of $\vec{N}$ and $\vec{S}$, is fixed in place relative to the molecule. $\vec{N}$ is the total angular momentum due to the mechanical rotation of the nuclei and orbital angular momentum (*i.e.*, the total angular momentum apart from spin). As mentioned above, Λ is the projection of

this vector onto the internuclear axis. The quantum number N, sometimes referred to as the rotation quantum number, can take on integer values $\geq \Lambda$ and for the lowest rotational state $N = \Lambda$. $\overrightarrow{S}$ is the spin angular momentum vector, with axial component Σ as described earlier. These two vectors precess slowly about $\overrightarrow{J}$, while the internuclear axis nutates about $\overrightarrow{N}$ more rapidly (*Herzberg*, 1971).

The quantum number J, related to $\overrightarrow{J}$, is the previously mentioned total angular momentum quantum number. It can take on the following values:

$$J = N + \Sigma, (N-1) + \Sigma, \ldots, |\Sigma| \tag{2.3}$$

Thus for the lowest level of the ground electronic state of the OH molecule where $N = \Lambda$,

$$J = \Lambda + \Sigma, (\Lambda - 1) + \Sigma, \ldots, |\Sigma| \tag{2.4}$$

Therefore,

$$J = \begin{cases} 1 + \frac{1}{2} = \frac{3}{2} & \text{or} \\ 1 - \frac{1}{2} = \frac{1}{2} \end{cases}$$

resulting in the two Ω subbands associated with the $^2\Pi_{\frac{3}{2}}$ and $^2\Pi_{\frac{1}{2}}$ states, for any particular $\upsilon' - \upsilon''$ transition band.

For any change in υ, J may change by 0 or ± 1. The lines associated with $\Delta J = J' - J'' = 0$ are known as the Q branch lines, those with $\Delta J = +1$ are known as the R branch lines and those with $\Delta J = -1$ known as P branch lines. The three branches are shown schematically for a singlet Σ molecule in Fig. 2.2. Note that for the $^1\Sigma$ case $J = N$, so ΔJ is synonymous with ΔN.

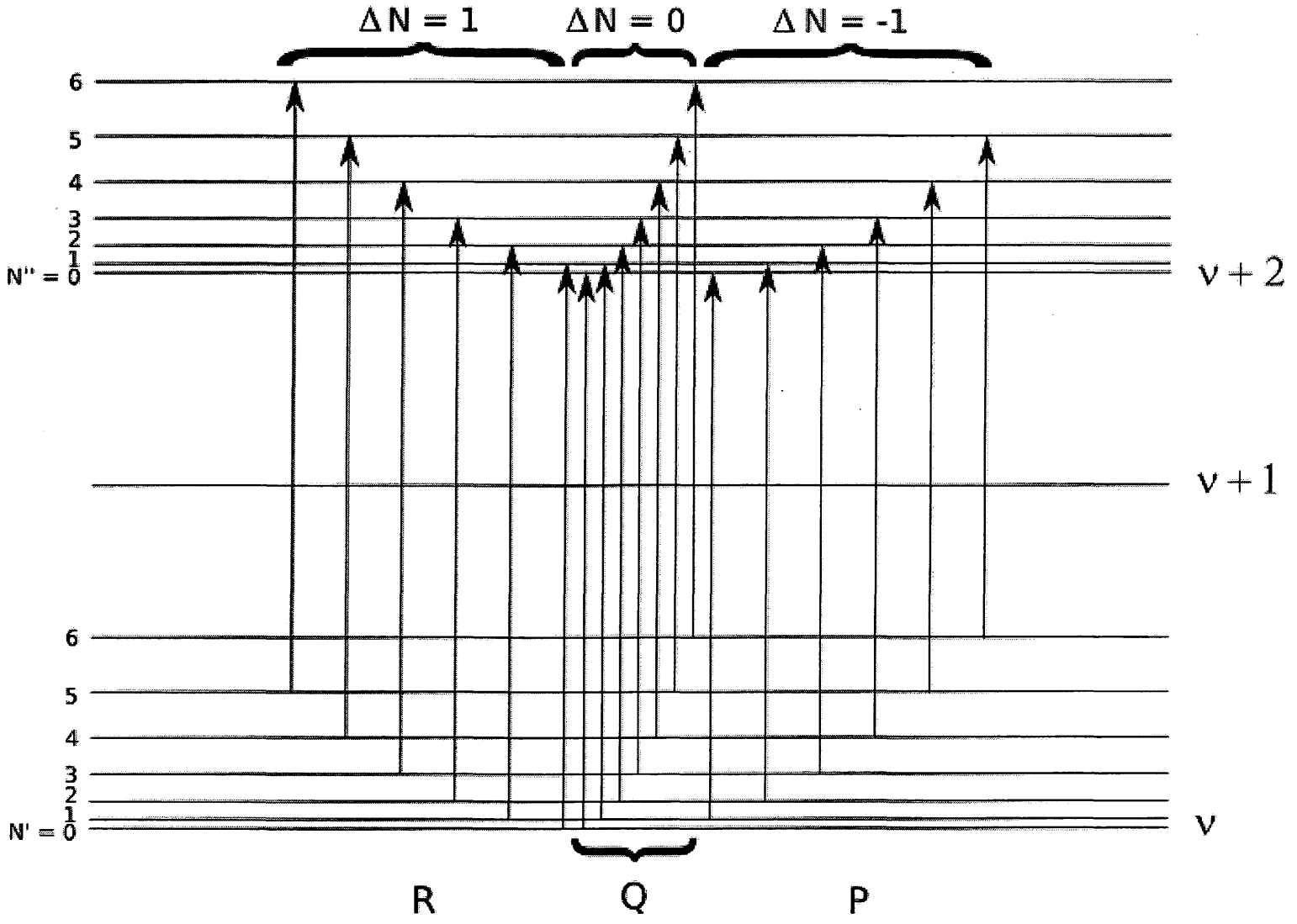

Figure 2.2: Schematic diagram of the rotational vibrational transitions for an absorbtion band for $\Delta\upsilon = 2$ and a singlet Σ molecule.

2.3.2 Rotational Energies of the OH molecule

The equation for the rotational energy of a doublet type molecule with molecular rotation and electron spin coupled as in Hund's Case B was first derived by *Hill and van Vleck* (1928).

For the $^2\Pi_{\frac{3}{2}}$ sublevels of OH the rotational energy, F(v,J), is given by

$$F_1 = B[(J+\frac{1}{2})^2 - \Lambda^2 - \frac{1}{2}\sqrt{(4(J+\frac{1}{2})^2 + Y(Y-4)\Lambda^2)}] \tag{2.5}$$

and for the the $^2\Pi_{\frac{1}{2}}$ sublevels by

$$F_2 = B[(J+\frac{1}{2})^2 - \Lambda^2 + \frac{1}{2}\sqrt{(4(J+\frac{1}{2})^2 + Y(Y-4)\Lambda^2)}] \tag{2.6}$$

B is the rotational constant given by $\frac{h}{8\pi^2 c I_B}$ and Y is a measure of the tightness of the coupling, $Y = \frac{A}{B}$ where A is the magnetic coupling energy proportionality factor, $A = \frac{h}{8\pi^2 c I_A}$. I_B is the moment of inertia about the centre of mass and is perpendicular to I_A, the effective inertia about the internuclear axis. The values A, Y and B depend on the vibrational level and are listed in Table 2.1.

For the $^2\Pi_{\frac{3}{2}}$ sublevels $J = N + \frac{1}{2}$ and for the $^2\Pi_{\frac{1}{2}}$ sublevels $J = N - \frac{1}{2}$. Substituting these values into the previous for rotational energy equations yields,

$$F_1 = B[(N+1)^2 - \Lambda^2 - \frac{1}{2}\sqrt{(N+1)^2 + Y(Y-4)\Lambda^2)}] \tag{2.7}$$

and

$$F_2 = B[N^2 - \Lambda^2 + \frac{1}{2}\sqrt{(4N^2 + Y(Y-4)\Lambda^2)}] \tag{2.8}$$

	B	A	Y	D
υ	cm^{-1}	cm^{-1}		cm^{-1}
0	18.531	-139.05	-07.504	0.00191
1	17.820	-139.32	-07.818	0.00187
2	17.119	-139.59	-08.154	0.00183
3	16.424	-139.85	-08.515	0.00180
4	15.733	-140.09	-08.904	0.00178
5	15.042	-140.30	-09.327	0.00176
6	14.345	-140.44	-09.790	0.00176
7	13.636	-140.49	-10.303	0.00178
8	12.905	-140.40	-10.890	0.00180
9	12.141	-140.28	-11.556	0.00186

Table 2.1: Molecular Constants from *Coxon and Foster* (1982). The molecular constants are given in wavenumbers (cm^{-1}), an energy unit based on $\frac{E(Joules)}{hc}$ with c in cm s^{-1} and h in mks units.

where $N = \Lambda, \Lambda + 1, \Lambda + 2 \ldots$

Since the molecule is not completely rigid, the centrifugal force exerted by the rotation causes the internuclear radius to increase slightly as it rotates at higher rates (*Herzberg*, 1971). This results in a modification of the rotational energy by an amount $DN^2(N+1)^2$ where D, known as the rotational distortion constant, is a small correction term. The values of D depend on the vibrational level and are shown in Table 2.1.

Including this correction and the known value for the axial component of the total orbital angular momentum for the OH radical ($\Lambda = 1$) gives our final expression for th rotational energy of the $^2\Pi_{\frac{3}{2}}$ and $^2\Pi_{\frac{1}{2}}$ sublevels,

$$F_1 = B[(N+1)^2 - 1 - \frac{1}{2}\sqrt{(N+1)^2 + Y(Y-4))}] - DN^2(N+1)^2 \qquad (2.9)$$

and

$$F_2 = B[N^2 - 1 + \frac{1}{2}\sqrt{(4N^2 + Y(Y-4))}] - DN^2(N+1)^2 \qquad (2.10)$$

2.3.3 Vibrational Energies of the OH molecule

The vibrational energies of the lowest substate levels of the OH molecule, G_v, are listed in Table 2.2. The Bates-Nicolet mechanism, the sole excitation process considered in this work, associates the formation of vibrationally excited OH in the atmosphere to the following exothermic reaction (*Bates and Nicolet*, 1950),

$$H + O_3 \longrightarrow OH(v') + O_2 \qquad (2.11)$$

The reaction has an excitation limit of 3.3eV, which limits the OH vibrational excitation to $v' = 9$. This is consistent with terrestrial observations (*Herzberg*, 1971). Accordingly, only the first nine vibrational levels are considered in the present work.

v	0	1	2	3	4	5
G_v	0.0	3569.6	6073.7	10214	13291.8	16207.1
v	6	7	8	9	10	
G_v	18958.8	21544.3	23959	26196.1	28245.358	

Table 2.2: G_v the vibrational energy for the non-rotating v vibrational level in cm^{-1} *Coxon* (1980), *Coxon and Foster* (1982)

2.3.4 The OH Rotation-Vibration Transitions

The OH R-V emission spectra is made up of the emission lines from transitions between rotational levels of an upper vibrational level, v', to a lower vibrational

level, v'', with $\Delta v = v' - v'' \geq 1$. The wavelength of these lines depends on the difference in energy between the upper and lower vibrational and rotational states of the transition.

The individual transition energies, $\overline{\nu}_r$ and $\overline{\nu}_\nu$ in wavenumber units, cm^{-1}, are defined as:

$$\overline{\nu}_v = G(v') - G(v'') \tag{2.12}$$

and

$$\overline{\nu}_r = F_{v'}(N') - F_{v''}(N'') \tag{2.13}$$

Since the energy associated with the change in vibrational level is much greater than that associated with the change in rotational level (*i.e.*, $\overline{\nu}_v > \overline{\nu}_r$), the resulting rotation-vibration spectrum for a given $v' \rightarrow v''$ transition, as illustrated in Fig. 2.2, is made up of many closely spaced emission lines centred about frequency $\overline{\nu}_v$ which is known as the band origin (*Modest*, 2003).

The wavelengths of the band origins for the Meinel bands in air as reported in *Chamberlain* (1961) are given in Table 2.3.

v'	$v''=0$	1	2	3	4	5	6	7	8
1	28007								
2	14336	29369							
3	9788	15047	30854						
4	7522	10273	15824	32483					
5	6169	7911	10828	16682	34294				
6	5273	6497	8342	11433	17642	36334			
7	4641	5562	6862	8824	12115	18734	38674		
8	4173	4904	5886	7275	9373	12898	19997	41409	
9	3817	4419	5201	8256	7748	10010	13817	21496	44702

Table 2.3: Wavelengths of the band origins of the Meinel bands in air in $\mathring{A}$ (*Chamberlain*, 1961)

The expression for the energies in cm^{-1}, $\overline{\nu}$, of the two OH subbands are: for $^2\Pi_{\frac{3}{2}}$

$$\begin{aligned}\overline{\nu} &= (G(\upsilon') - G(\upsilon'')) + (B'(N'+1)^2 - B''(N''+1)^2) \\ &\quad - (\frac{1}{2}B'\sqrt{(N'+1)^2 + Y(Y-4))}] - \frac{1}{2}B''\sqrt{(N''+1)^2 + Y(Y-4))}]) \\ &\quad - (D'N'^2(N'+1)^2 - D''N''^2(N''+1)^2) \end{aligned} \tag{2.14}$$

or for $^2\Pi_{\frac{1}{2}}$

$$\begin{aligned}\overline{\nu} &= (G(\upsilon') - G(\upsilon'')) + (B'N'^2 - B''N''^2) \\ &\quad - (\frac{1}{2}B'\sqrt{N'^2 + Y(Y-4))}] - \frac{1}{2}B''\sqrt{N''^2 + Y(Y-4))}]) \\ &\quad - (D'N'^2(N'^2+1)^2 - D''N''^2(N''^2+1)^2) \end{aligned} \tag{2.15}$$

The calculation of the associated line strengths are detailed in Section 2.4.1.

Line positions are converted from wavenumbers, $\overline{\nu}$, to wavelengths in $\mathring{A}$,

$$\lambda = \frac{10^8}{\overline{\nu}} \tag{2.16}$$

where λ is the wavelength in $\mathring{A}$ and $\overline{\nu}$ is the wavenumber in cm^{-1}.

The selection rule for vibrational transitions is

$$\Delta\upsilon = \pm 1, \pm 2, \pm 3, \ldots \tag{2.17}$$

where $\Delta\upsilon = \upsilon' - \upsilon''$. $\Delta\upsilon$ positive corresponds to absorption and $\Delta\upsilon$ negative to emission as already stated. In the case of OH $\Delta\upsilon = \pm 2$ transitions dominate unlike

other molecules where $\Delta v = \pm 1$ transitions usually dominate. This is because the electronic potential energy of the OH molecule versus the internuclear separation (approximately a Morse function) differs very significantly from that of a simple harmonic oscillator, *i.e.*, the anharmonicity of the OH molecule. Transitions up to $\Delta v = 6$ have been observed in the terrestrial night sky (*Herzberg*, 1971). In Venus' atmosphere only transitions up to $\Delta v = 2$, the first overtone bands, have been confirmed (*Piccioni et al.*, 2008), although many lines have yet to be identified. Thus in the absence of contradictory evidence, only transitions with Δv up to 6 are considered in this work.

For a molecule similar to Hund's case B with a Π ground electronic state the rotational selection rule is

$$\Delta N = 0, \pm 1 \tag{2.18}$$

corresponding to three series of transition lines known as branches as previously mentioned and illustrated is Fig. 2.2. $\Delta N = -1$ lines are known as lines of the P branch, $\Delta N = 0$ known as the Q branch and $\Delta N = 1$ lines of the R branch.

2.4 Intensity of OH airglow emission lines

To determine the intensities of the individual spectral lines in a R-V band in the atmosphere it is important to understand how the vibrationally excited OH interacts with the surrounding atmosphere.

2.4.1 Populations of rotational states

Under the assumption of thermalization of the rotational levels (which we will address later in Section 2.5.1), the wavelength bin radiance (WBR) of individual emission lines in photons cm^{-3} s^{-1} are described by the following equation (*Mies*, 1974),

$$V(J', v' \rightarrow J'', v'') = N_{v'} A(J', v' \rightarrow J'', v'') \frac{2(2J'+1)}{Q_{v'}(T_{ROT})} exp(\frac{-E_{v'}(J')}{kT_{ROT}}) \qquad (2.19)$$

Here N_v, (particles cm^{-3}), is the number density of the excited rotational levels in the v' vibrational level, $A(J', v' \rightarrow J'', v'')$ is as before, $E_{v'}(J')$ is the total energy of the upper v', J' level, $Q_v(T_{ROT})$ is the rotation partition function which essentially normalizes the absolute populations and T_{ROT} is the rotational temperature.

The transition probabilities $A(J', v' \rightarrow J'', v'')$, which relate the absolute volume emission rates of a particular line, in photons cm^{-3} s^{-1}, to the number density of the emitting level in molecules cm^{-3} for all the levels considered in this work, are based on an empirical expression for the dipole moment function given by *Turnbull and Lowe* (1989).

The lowest possible vibrational energy of the molecule is the energy of the lowest vibration-rotation state and is called the zero point energy (ZPE). $E_v(J')$ is defined as the difference between the rotational level (F_1, F_2) and the zero point energy (ZPE). For the OH molecule the $^2\Pi$ state is inverted thus the vibrational state with the lowest energy is the $N = 1$ state of the $^2\Pi_{\frac{3}{2}}$ subband.

$$ZPE = F_1(1, v') \qquad (2.20)$$

For the $^2\Pi_{\frac{3}{2}}$ state,

$$E_{v'}(J') = E_{v'}(N' + \frac{1}{2}) = F_1(N', v') - F_1(1, v') \tag{2.21}$$

and for the $^2\Pi_{\frac{1}{2}}$ state,

$$E_{v'}(J') = E_{v'}(N' - \frac{1}{2}) = F_2(N', v') - F_1(1, v') \tag{2.22}$$

in cm^{-1} units.

The rotational partition function, $Q_{v'}(T_{ROT})$, which is sometimes referred as the sum of all states, is given by,

$$Q_{v'}(T_{ROT}) = \sum_J 2(2J' + 1)exp(\frac{-E_{v'}(J')}{kT_{ROT}}) \tag{2.23}$$

If the rotational levels are assumed to be thermalized the populations can be expressed by using a single rotational partition function, e.g.:

$$\begin{aligned} Q_{v'}(T_{ROT}) &= \sum_J 2(2J' + 1)exp(\frac{-(F_1(v', N') - ZPE)}{kT_{ROT}}) \\ &+ \sum_J 2(2J' + 1)exp(\frac{-(F_2(v', N') - ZPE)}{kT_{ROT}}) \end{aligned} \tag{2.24}$$

The volume emission rate of each $(v' \rightarrow v'')$ band is proportional to the number density $(N_{v'})$ of both Ω components and the thermally averaged transition probability for the $v' \rightarrow v''$ band, $A^{TOT}_{v' \rightarrow v''}$, also referred to as the Einstein coefficient.

$$V(v', v'') = A^{TOT}_{v' \rightarrow v''}(T_{ROT})N_{v'} \tag{2.25}$$

The Einstein coefficients, or transition probabilities for each $v' \rightarrow v''$ band, are given by *Turnbull and Lowe* (1989) as,

$$A^{TOT}_{v' \rightarrow v''}(T_{ROT}) = \sum_{J' \rightarrow J''} A(J', v' \rightarrow J'', v'') \frac{2(2J'+1)}{Q_{v'}(T_{ROT})} exp(\frac{-hcE_{v'}(J')}{kT_{ROT}}) \qquad (2.26)$$

$A(J', v' \rightarrow J'', v'')$ and $Q_{v'}$, are as above, k is Boltzmann's constant in mks units, c is the speed of light in cm s^{-1} and h is Planck's constant in mks units.

A sample of thermally averaged Einstein coefficients, $A^{TOT}_{v' \rightarrow v''}$, assuming Boltzmann distribution of the rotational states, calculated at 200K can be found in Table 2.4. $A_T(v') = \sum_{v''} A^{TOT}_{v' \rightarrow v''}$ is the total transition probability, or inverse radiative lifetime, for vibrational level v'

The transition probabilities for the $\Delta v = 2$ sequence are greater than those for any other sequence due to the anharmonicity of the OH molecule as mentioned in the previous section.

The total volume emission rate for each vibrational level, as defined in Chapter 1, is simply the sum of the emission rates for all of the bands or from the given v', *i.e.*:

$$V_T(v') = \sum_{v''} V(v', v'') = A_T(v') N_{v'} \qquad (2.27)$$

The value $V_T(v')$ is referred to as the volume emission rate (VER) throughout this work.

Substituting this into expression (2.19) gives an equation for the wavelength bin radiance. The WBR depends on the temperature and $N_{v'}$,

$$V(J', v' \rightarrow J'', v'') = V_T(v') \frac{A(J', v' \rightarrow J'', v'')}{A_T(v')} \frac{2(2J'+1)}{Q_{v'}(T_{ROT})} exp(\frac{-E_{v',i}(J')}{kT_{ROT}}) \qquad (2.28)$$

v'	$v'' = v'$ - 1	$v'' = v'$ - 2	$v'' = v'$ - 3	$v'' = v'$ - 4	$v'' = v'$ - 5	$v'' = v'$ - 6	A_T
1	22.71						22.71
2	30.43	15.42					45.85
3	28.12	40.33	2.032				70.48
4	20.30	69.77	7.191	0.299			97.56
5	11.05	99.42	15.88	1.315	0.051		127.7
6	4.00	125.6	27.94	3.479	0.273	0.010	181.3
7	2.34	145.1	42.91	7.165	0.847	0.063	198.4
8	8.60	154.3	12.68	12.68	1.007	0.230	237.8
9	23.72	148.9	19.94	19.94	4.053	0.620	275.9

Table 2.4: Thermally averaged Einstein coefficients for the $v' \rightarrow v''$ vibrational band, $A^{TOT}_{v' \rightarrow v''}$, at 200K from *Turnbull and Lowe* (1989) in units of s^{-1}

2.5 Synthetic OH Meinel airglow spectrum

Using our expression for the wavelength bin radiance, Eqs. 2.14, 2.15 and 2.16 to determine the emission intensity and the associated wavelength we assemble a temperature dependant synthetic line emission spectrum of the OH Meinel Band airglow, $\mathbf{B}(\lambda)$[6], for a given wavelength range. An example of such a synthetic spectrum is shown in Fig. 2.3 using a terrestrial OH vibrational distribution as reported by *Takahashi and Batista* (1981) and *McDade and Llewellyn* (1987).

To simulate measurements of the OH emission the synthetic emission line spectrum must be convolved with the response function of the observing instrument, $f(\lambda)$. The convolution of the synthetic line spectrum with the instrument function is represented by:

$$\mathbf{\Gamma}(T, \lambda) = f(\lambda) * \mathbf{B}(\lambda) \tag{2.29}$$

where $\mathbf{\Gamma}(T, \lambda)$ is the instrument convolved spectrum for a given rotational temperature. An example of such a spectrum for an instrument whose response function is a Gaussian with a half width of 20 $\mathring{A}$ can be seen in the lower panel of Fig. 2.3.

To illustrate the relationship between the rotational temperature and a hypothetical observed spectrum, the spectrum of the 1-0 band is generated at three temperatures, 200 K, 500 K and 1000 K as shown in Fig. 2.4

The different emission lines of the P, Q and R branches do not all behave alike when temperature is increased. For the 1-0 band the P1(1), P1(2), Q1(1), Q1(2), R1(1) relative emission rates decrease as the temperature is increased for the range of temperatures expected in the Martian atmosphere. In this line notation the letter

[6]Bold face, *i.e.*, **a** indicates a data vector

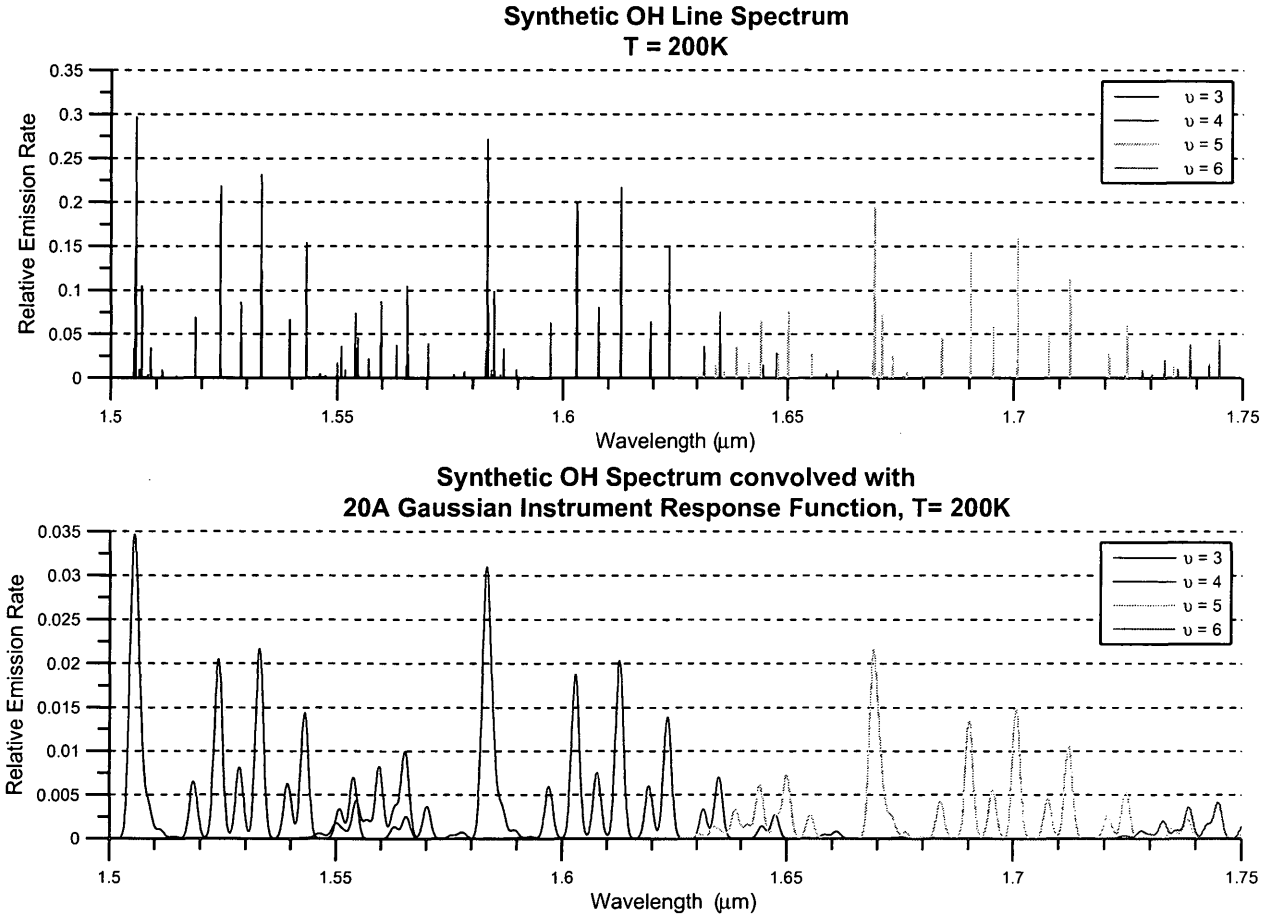

Figure 2.3: Normalized relative intensity synthetic OH Meinel spectra using relative populations for *Takahashi and Batista* (1981) and *McDade and Llewellyn* (1987) for the 1.5 - 1.75 μm spectral region. The unconvolved emission line spectrum is in the upper panel and the instrument convolved spectrum with a 20$\mathring{A}$ Gaussian instrument function is in the lower panel. To distinguish the emissions of the different vibrational levels their associated components are not co-added in overlapping regions.

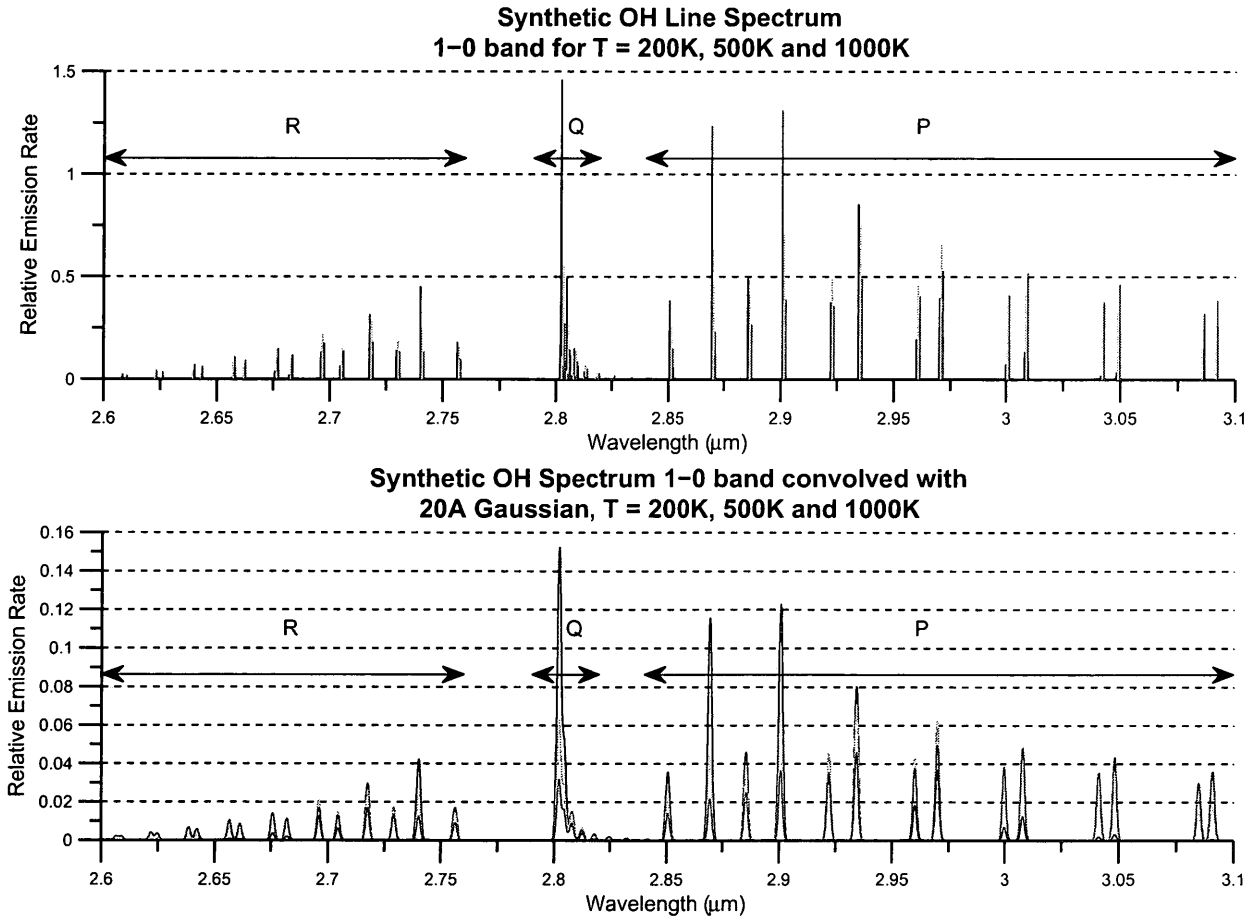

Figure 2.4: Synthetic OH Meinel spectra for the OH(1-0) Band at 200 K in blue, 500 K in green and 1000 K in red. The spectra are normalized to the same total band intensity at each temperature. The unconvolved line emission spectra are in the upper panel. A small wavelength shift between the line emission spectrum for different temperatures is introduced for clarity. The instrument convolved spectra with a 20$\mathring{A}$ Gaussian are in the lower panel.

indicates the branch, the first number indicates the subband, (1 for the $^2\Pi_{\frac{3}{2}}$ and 2 for the $^2\Pi_{\frac{1}{2}}$ subband), and the number between parenthesis indicates the upper rotational level N. Conversely the P1(3) - P1(14), P2(1) - P2(14), Q1(3) - Q1(14), Q2(1) - Q2(14), R1(2) - R1(14), R2(1) - R2(14) lines increase in intensity with temperature. These lines are weaker at the expected temperatures of the Martian OH Meinel airglow layer than the previous set of lines.

The actual line positions vary with the vibrational level but in general the intensity of the lines closest to the band origin, *i.e.*, low N', decrease with temperature, while the lines further away, *i.e.* high N', increase with temperature.

2.5.1 Local Thermodynamic Equilibrium

This study assumes that the rotational state distribution for each v' is thermalized with the surrounding gas kinetic temperature, this implies that the rotational temperature of OH(v') corresponds to the temperature of the background atmosphere (*i.e.*, $T_{ROT} = T_{atm}$). It is also assumed that the level populations are well described by an Boltzmann distribution (BD), basically the $(2J' + 1)exp(\frac{-E_{v',i}(J')}{kT_{ROT}})$ term in equation 2.28. CO_2 exhibits non-local thermodynamic emissions in the terrestrial atmosphere and is likely to do so in the Martian atmosphere. Thus this assumption bears investigation.

Observations suggesting the possibility that the assumption of isothermal BD in rotation may not be valid for N' > 6 were first published in the early 1970s (e.g., *Harrison et al*, 1970; *Harrison et al*, 1973). Laboratory measurements also exist of emitting OH molecules with short radiative lifetimes exhibiting non-thermalized rotational distributions (*Charters et al.*, 1971). *Pendleton et al.* (1993) have shown

for terrestrial observations of the Meinel bands that low rotational levels ($N' = 1$, 2, 3) are well described (within 1%) by a BD and the breakdown in local thermodynamic equilibrium (LTE) only occurs for higher N' levels due to the significantly larger energy spacing between adjacent N' levels which renders collisional rotational relaxation slower relative to spontaneous emission.

To avoid this problem, it is common practice (*Takahashi et al.*, 1999; *Innis et al.*, 2001; *von Savigny et al.*, 2004; *Perminov*, 2009) to only use lines arising from the lowest-lying rotational states for temperature determination. However, this may not resolve possible errors in retrieved VER associated with non-local thermodynamic equilibrium (NLTE) effects. Under these conditions the emission lines from high N' levels are greatly amplified relative to their thermal values. The VER retrieval methods described later assume LTE and thus may not capture the amplification of these high N' lines and consequently could lead to a under estimation of the VER. The magnitude of the possible error in recovered v' level VER associated with this breakdown will be discussed below.

To determine the impact on the Martian OH Meinel airglow, we must consider the number of collisions an excited OH molecule typically experiences within its radiative lifetime. For the lower rotational levels of OH the number of collisions required to effect rotational relaxation, *i.e.*, collisional deactivation to some lower N level, Z_{rot}, is of the order of 10 (*Kistiakowsky and Tabbutt*, 1959), however, this number is much larger for high rotational levels (*Pendleton et al.*, 1993) because the probability of rotational deactivation per collision decreases with the increasing rotational energy gap between adjacent levels as noted above - this gap increases with N. Although this larger number is not precisely known, *Pendleton et al.* (1989)

suggests that $Z_{rot} = 400$ for high N' levels and $Z_{rot} = 10$ for low N' levels. *Innis et al.* (2001), suggests 200 to 300 collisions are required to assure thermalization. We will conservatively assume that 400 collisions are necessary to thermalize the high N' levels of OH(υ') and 10 for low N' levels of OH(υ').

The total number of collisions an OH(υ') molecule will suffer within its total lifetime can be calculated based on the total lifetime, $\tau(\upsilon')$, and the mean collision time, $\tau_{col}(\upsilon')$, of OH(υ'). To estimate the total lifetime of OH(υ') it is necessary to calculate the mean radiative lifetime $\tau_{rad}(\upsilon')$ and the mean chemical lifetime, $\tau_{chem}(\upsilon')$, predominantly controlled by quenching. The mean radiative lifetime for a given υ' level is estimated using the following expression:

$$\tau_{rad}(\upsilon') = \frac{1}{\sum_{\upsilon''} A^{TOT}_{\upsilon' \rightarrow \upsilon''}(T_{ROT})} \tag{2.30}$$

As $A^{TOT}_{\upsilon' \rightarrow \upsilon''}(T_{ROT})$ is only weakly dependant on temperature, T_{ROT} is assumed to be the same as the kinetic temperature.

The mean chemical lifetime for a given υ' level is estimated using the following expression:

$$\tau_{chem}(\upsilon') = \frac{1}{k^T_{CO2}(\upsilon') N_{CO2}} \tag{2.31}$$

where $k^T_{CO2}(\upsilon')$ is the total collisional removal rate coefficient with a CO_2 collider for a given υ' in cm^3 s^{-1} from *García Muñoz et al.* (2005) and N_{CO2} is the number density of CO_2 in molecules cm^{-3}. The CO_2 number density profile is from the photochemical model presented in *García Muñoz et al.* (2005).

The actual lifetime for OH(υ') is the reciprocal of the sum of the reciprocals of

the radiative lifetime and chemical lifetime:

$$\tau(\upsilon')^{-1} = \tau_{rad}(\upsilon')^{-1} + \tau_{chem}(\upsilon')^{-1} \tag{2.32}$$

The lifetimes for $\upsilon' = 1 - 9$ and $T_{ROT} = T_{atm}$ have been calculated for the COSPAR mean temperature profile (shown in Fig. 1.1) and are presented in Fig. 2.5.

Assuming a CO_2 background atmosphere, the mean collision time of $OH(\upsilon')$ under gas kinetic theory is given by:

$$\tau_{col}(\upsilon') = \sqrt{\frac{\pi N_A \mu}{8RT_{atm}}} \frac{1}{\pi d_{avg}(\upsilon')^2 10^6 N_{CO2}} \tag{2.33}$$

where $N_A\mu$ is the reduced molar mass of OH and CO_2 in kg mole^{-1}, R is the molar gas constant in J K^{-1} mol^{-1}, T_{atm} is the temperature. d_{avg} is the average hard sphere diameter of the two molecules in meters and $10^6 N_{CO2}$ is the number density of CO_2 converted to molecules m^{-3}. The hard sphere diameter of CO_2 is 4.53 $\mathring{A}$ (*Lide*, Internet version 2012). The hard sphere diameter of OH varies with vibrational level because the averaged bond distance increases with vibrational level (*Burtt and Sharma*, 2008). We account for the variation in hard sphere diameter as suggested by *Burtt and Sharma* (2008): Starting with a hard shell diameter of 3.45 $\mathring{A}$ for the ground vibrational state of OH and the diameter is increased by 0.05 $\mathring{A}$ per unit increase in vibrational level. This leads to a slight variation in calculated mean collision time with υ' level as shown in Fig. 2.5.

The number of collisions within the $OH(\upsilon')$ lifetime, n_{col}, is defined as the ratio

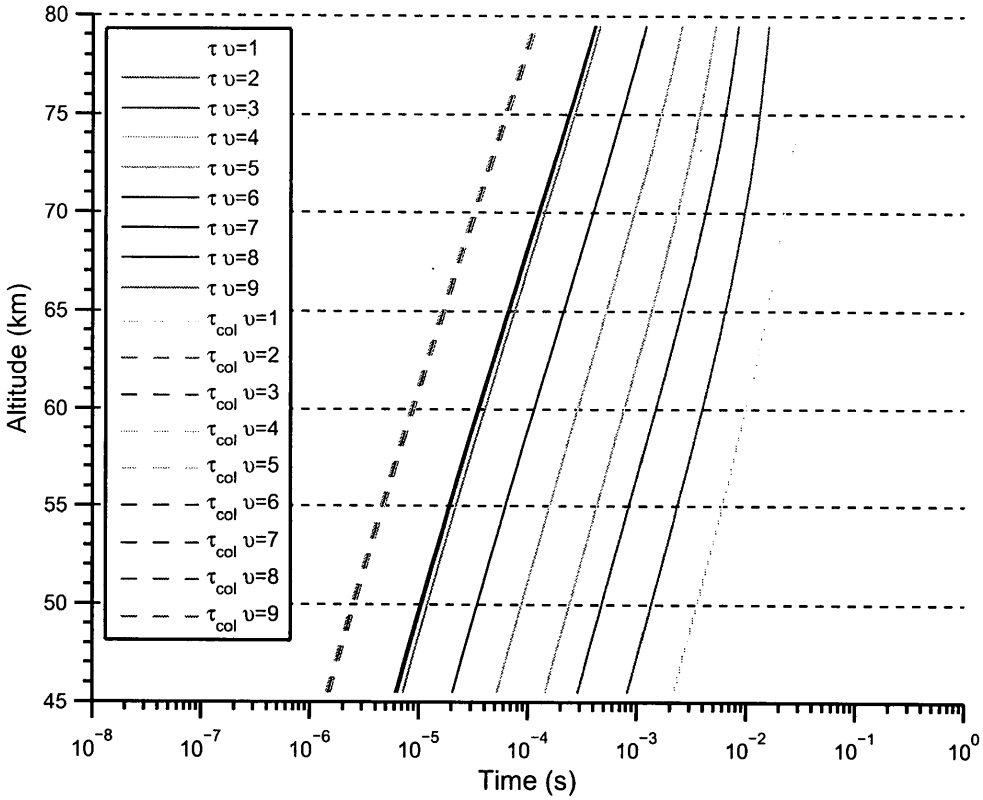

Figure 2.5: Temperature dependant total lifetime, $\tau(\upsilon)$ and mean collision time, $\tau_{col}(\upsilon')$, for OH($\upsilon' = 1 - 9$) in the nighttime Martian atmosphere. Due to scale and weak dependance of $\tau_{col}(\upsilon')$ on the vibrational level, $\tau_{col}(\upsilon')$ is seen as the same for all υ'.

of the actual lifetime, $\tau(v')$, to the estimated mean collision time, $\tau_{col}(v')$:

$$n_{col}(v') = \frac{\tau(v')}{\tau_{col}(v')} \tag{2.34}$$

The number of collisions for $v' = 1 - 9$ are plotted in Fig. 2.6

According to these estimates, under the assumption that 10 collisions are required assure thermalization of low N' states, the low N' states for $v' = 1 - 6$ will be thermalized. Due to their short lifetimes complete thermalization of the nascent rotational populations of $v' = 7 - 9$ will likely not occur even for low rotational levels. The high N' states will be thermalized, using our conservative assumption that requires 400 collisions, for most of the OH Meinel Band airglow layer for $v' = 1$ and the bottom half of the layer for $v' = 2$. It is unlikely that the remaining high N' states of vibrational levels 3 - 6 will be completely thermalized.

The percent increase in VER with the addition of the NLTE rotation and thus the percent error when assuming LTE is plotted in Fig. 2.7

To estimate the error in inferred VER caused by NLTE effects, the ratios between observed and BD populations detailed by *Pendleton et al.* (1993) and *Pendleton et al.* (1989), listed in Table 2.5 are used. Ratios for $N' = 8$, 9, 11, 14 and 15 were not available. Linear interpolation and extrapolation were used to approximate the missing values. The ratios were calculated for the P1 branch emissions only however we employ these same ratios for the Q1, R1, P2, Q2 and R2 branches.

The coarse estimate of the percent error in VER caused by assuming a Boltzmann distribution in the height region where a NLTE component may contribute to the observed spectrum is 0.3% for the 1-0 band and 0.6% for the 2-0 and 2-1 bands.

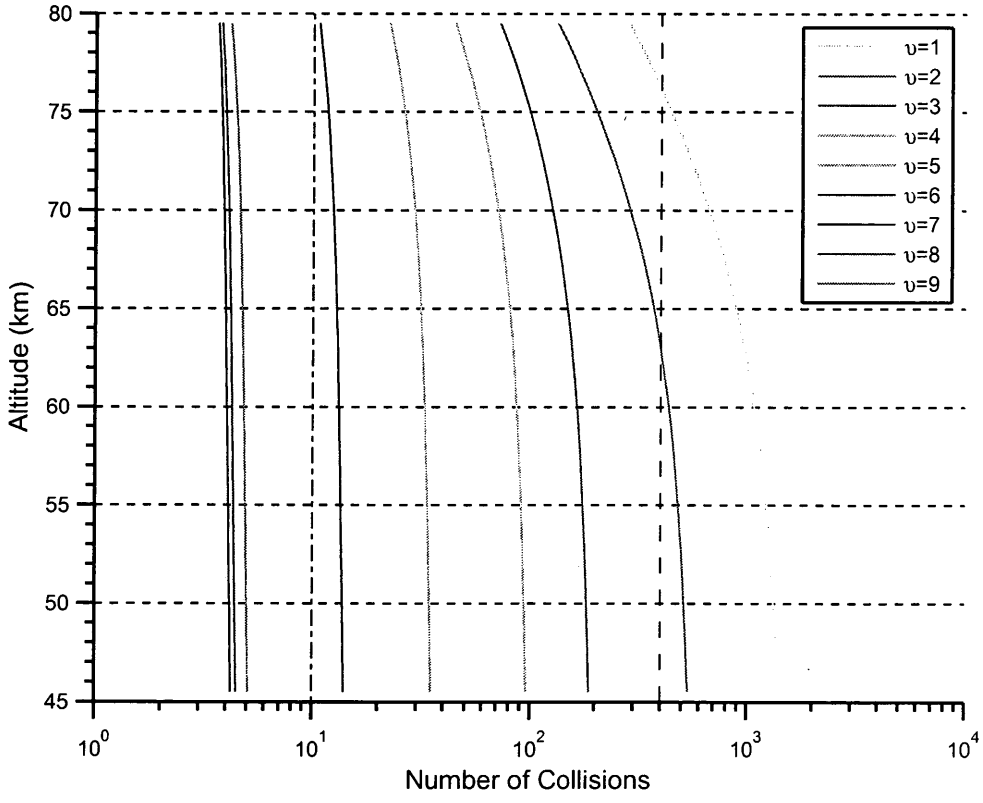

Figure 2.6: Number of collisions during the total lifetime of OH(υ') for $\upsilon' = 1 - 9$ and mean collision time for OH(υ) in the nighttime Martian atmosphere, the dot-dashed and dashed lines indicate 10 collisions and 400 collisions respectively.

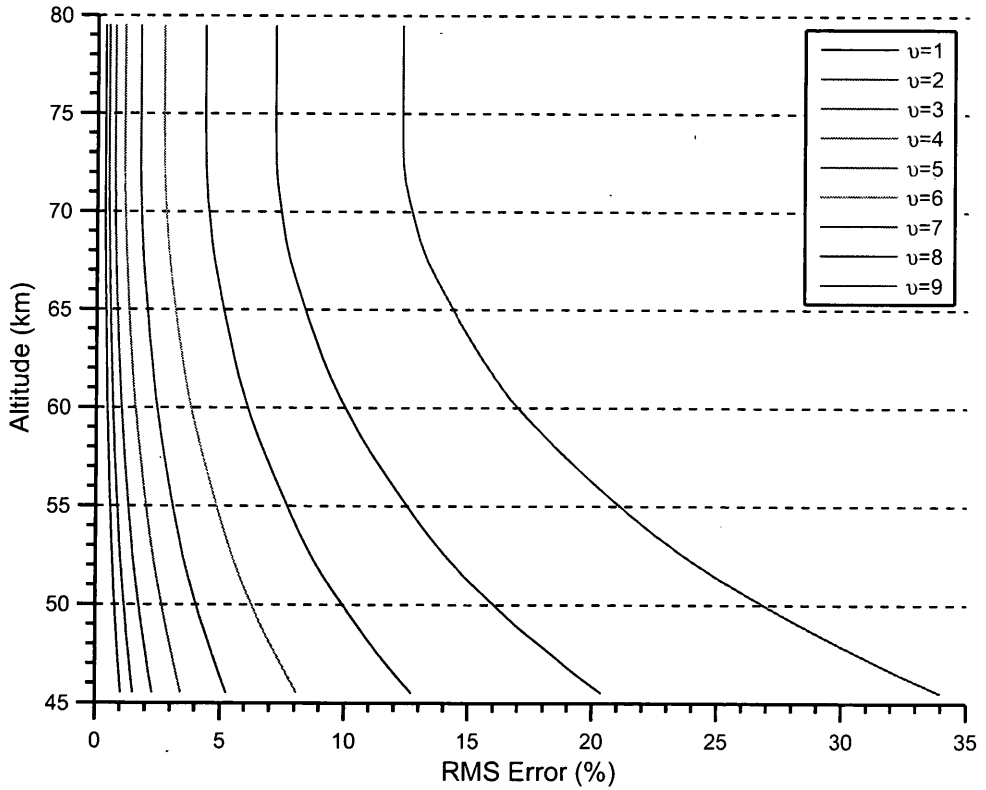

Figure 2.7: Percent error in VER due to neglect of the NLTE component.

N'	Ratio of observed to BD	Source
1	1	*Pendleton et al.* (1993)
2	1	*Pendleton et al.* (1993)
3	1	*Pendleton et al.* (1993)
4	1	*Pendleton et al.* (1993)
5	1.11	*Pendleton et al.* (1993)
6	1.31	*Pendleton et al.* (1993)
7	1.97	*Pendleton et al.* (1993)
8	335	Linear interpolation
9	668	Linear interpolation
10	10^3	*Pendleton et al.* (1993)
11	25 500	Linear interpolation
12	5 x 10^4	10^4-10^5 given in *Pendleton et al.* (1993)
13	10^5	*Pendleton et al.* (1993)
14	1.5 x 10^5	Linear extrapolation
15	2 x 10^5	Linear extrapolation

Table 2.5: Ratios of observed N' line populations to BD predicted values. Linear interpolation and extrapolation were used to estimate ratios for $N' = 8$, 9, 11, 14 and 15.

These low values are due to the predominance of the low N' lines in the spectrum. The error increases for higher vibrational levels exceeding 5% at the bottom of the OH Meinel airglow emission layer for $v' = 5$. The increase in error is due to the decrease in weight of the unenhanced low N' lines. The error also increases with an increase in temperature.

To minimize the effect of NLTE rotation on the recovered temperatures and volume emission rates the emission line selected for optimization should be from rotational levels low v' levels and $N' \leq 3$. In Chapter 6, when assessing performance requirements of potential observational instrumentation, we will endeavour to identify a spectral window which is composed primarily of $N' = 1-3$ transitions of $v' = 1 - 2$.

3 Numerical Methodology

As stated in the introduction, the goal of this work is to develop a method for retrieving temperatures and volume emission rates from limb observations of the OH Meinel Band airglow emission in the atmosphere of Mars and to assess the performance requirements of potential observational instrumentation. In this chapter we discuss the general problem of retrieval that will then be applied to the recovery of temperatures and volume emission rates from limb OH Meinel airglow observations.

3.1 The Retrieval Problem

In general, the retrieval problem can be expressed in the following manner: given a dependant variable, how can we determine its corresponding, usually multiple, independent variables? For the atmosphere, the retrieval problem is, given some specific set of observations, $\mathbf{y}$, such as a series of airglow radiances observed at different heights and wavelengths, what is the state of the atmosphere, $\mathbf{x}$, associated with the particular set of observations? For any one observation y_i the observed quantity will depend in some way on an atmospheric state parameter x_j, *i.e.*, $y_i = f_i(x_j)$. The question is given observation y_i how do we determine the value x_j? In this case it seems relatively simple, we use the inverse of the function of f_i to solve

for the set of independent parameters,

$$x_j = f_i^{-1}(y_i) \tag{3.1}$$

If each observation, y_i, is some linear function of more than one parameter, $y_i = f(\mathbf{x})$, the state parameters $\mathbf{x}$, a column vector of all the atmospheric parameters which describe the state of the atmosphere, can be recovered by solving a set of linear equations (one equation per observation) as long as the problem is not underdetermined (*i.e.*, the number of observations is greater than or equal to the number of state parameters). However, when the relationship is nonlinear, *i.e.*, y_i is not a linear function of $\mathbf{x}$, this method is not directly applicable, but one often linearizes the problem.

In cases where the observations depend non-linearly on the state parameters, a matrix known as the Jacobian is employed as part of the linearization process. It is important to note that the number of observations, m, must be equal to or exceed the number of parameters needed to capture the state of the atmosphere, which although infinite we discretize to n parameters, for the problem to have a unique solution.

The Jacobian, $\tilde{K}$, is a matrix of the partial derivatives of the function with

respect to every state parameter, that is

$$\tilde{K} = \begin{bmatrix} \frac{\partial f_1}{\partial x_1} & \frac{\partial f_1}{\partial x_2} & \frac{\partial f_1}{\partial x_3} & \cdots & \frac{\partial f_1}{\partial x_n} \\ \frac{\partial f_2}{\partial x_1} & \frac{\partial f_2}{\partial x_2} & \frac{\partial f_2}{\partial x_3} & \cdots & \frac{\partial f_2}{\partial x_n} \\ \frac{\partial f_3}{\partial x_1} & \frac{\partial f_3}{\partial x_2} & \frac{\partial f_3}{\partial x_3} & \cdots & \frac{\partial f_3}{\partial x_n} \\ \cdots & \cdots & \cdots & \cdots & \cdots \\ \frac{\partial f_m}{\partial x_1} & \frac{\partial f_m}{\partial x_2} & \frac{\partial f_m}{\partial x_3} & \cdots & \frac{\partial f_m}{\partial x_n} \end{bmatrix} \tag{3.2}$$

where m is the number of observations and n is the number of state parameters. The Jacobian is a transformation matrix mapping the state ($\mathbf{x}$) from parameter space to observation space. If $\mathbf{y}(\mathbf{x} = 0) = 0$, the retrieval problem can be expressed as,

$$\mathbf{y} = \tilde{K}\mathbf{x} \tag{3.3}$$

where $\mathbf{y}$ is a m x 1 column matrix of observations, $\mathbf{x}$ is a n x 1 column matrix of state parameters and $\tilde{K}$ is the m x n Jacobian matrix, ideally evaluated at the exact, but unknown, state $\mathbf{x}$ where the problem has been linearized.

Therefore, the key to solving for the state is a matter of determining the appropriate inverse of the Jacobian matrix

$$\mathbf{x} = \tilde{K}^{-1}\mathbf{y} \tag{3.4}$$

This method is also effective for linear functions because the Jacobian will be the same for all possible state parameters. Also note Eq. 3.4 is only meaningful when $m = n$ and the Jacobian is square and thus has a defined inverse. Strategies do exist to overcome this restriction. If the relationship between the y_i and x_j is non-linear,

as is the case in the present problem, the Jacobian will only reflect the immediate behaviour of the function and this method will not necessarily retrieve the correct state solution. Therefore, an iterative approach is required. In an iterative method a set of trial parameters, $\mathbf{x}_k$, initialized with some assumed *a priori* state $\mathbf{x}_a$, are repeatedly improved upon until the results converge on a stable solution, $\widehat{\mathbf{x}}$. The function used to quantify how well the reconstructed results $\widehat{\mathbf{y}}$, based on a set of evolving parameters, reproduces the actual observations is called the merit function. The iterative method tested in this work is the Levenberg-Marquardt optimization method.

3.2 Levenberg-Marquardt Optimization

The Levenberg-Marquardt (*Marquardt*, 1963) optimization algorithm is a blend of gradient descent and Gauss-Newton iteration. The goal of the algorithm is to minimize the probability state merit function, J, the previously mentioned function which describes the relationship between the reconstructed and the actual observations. The merit function J above should not be confused with the angular momentum quantum number J used in the previous chapter. The details of the merit function will be discussed further in Section 3.3.2. The method is often initialized with a climatological state of the atmosphere based on an *a priori* starting assumption, $\mathbf{x}_a$, then the algorithm iterates and updates $\mathbf{x}_k$, where in this case k indicates the iteration, until the parameters converge on a reconstructed observation vector, $\widehat{\mathbf{y}}$ that agrees within an error threshold set by the estimated uncertainties in the observation vector.

The Levenberg-Marquardt algorithm combines the local quadratic convergence of the Gauss-Newton algorithm with the stability of the gradient descent method. Thus the Levenberg-Marquardt algorithm is more robust than the Gauss-Newton algorithm, although slightly slower, and is much faster than the gradient descent method. Its use is appropriate when some heuristic knowledge of the parameter to be fit exists and a reasonable *a priori* can be provided to the algorithm. The Levenberg-Marquard optimization algorithm should be suitable for spectral fitting of the OH airglow on Mars as observations of the Martian atmosphere's temperature profile from past and present missions and model predictions of OH volume emissions rates, which can be used as the *a priori*, exist. Similar constraints exist for applications to Earth observations.

The merit function, J, is minimized when ∇J, a n x 1 vector of all the first derivatives with respect to the n state parameters, approaches 0. The gradient descent optimization method uses ∇J, weighted by an adjustable parameter ζ to update the trial parameters

$$\mathbf{x}_{k+1} = \mathbf{x}_k - \zeta \nabla J \tag{3.5}$$

where k is the iteration index number, $\mathbf{x}_k$ is the n x 1 vector of recovered state parameters from the previous iteration and $\mathbf{x}_{k+1}$ is the vector of recovered state parameters from the present iteration. When the merit function calculated for the new trial parameters ($\mathbf{x}_{k+1}$) is smaller than the merit function for $\mathbf{x}_k$, ζ is increased. When $\mathbf{x}_{k+1}$ fails to decrease the value of the merit function, ζ is decreased and a backward step is taken. The calculated variation in the parameter, $\zeta \nabla J$, can be significant, potentially causing large oscillations in the intermediate $\mathbf{x}_k$ parameters.

Thus it is more efficient to employ this method when there is a large difference between the solution reconstructed data, $\widehat{\mathbf{y}}$ and the actual observations, $\mathbf{y}$.

The Gauss-Newton method linearizes the gradient of the merit function at its minimum, $\nabla J(\widehat{\mathbf{x}}) = 0$, about the current estimate of the state vector, $\mathbf{x}_k$, using Taylor expansion (*Ranganathan*, 2004).

$$\nabla J(\widehat{\mathbf{x}}) = \nabla J(\mathbf{x}_k) + (\widehat{\mathbf{x}} - \mathbf{x}_k)^T \nabla^2 J(\mathbf{x}_k) + \text{ higher order terms of } (\widehat{\mathbf{x}} - \mathbf{x}_k) \quad (3.6)$$

It is assumed that the merit function is quadratic in the vicinity $\mathbf{x}_k$ and thus the higher order terms can be neglected. The Gauss-Newton update rule for the linear case can then be obtained by solving for the state of the atmosphere which minimizes the merit function,

$$\widehat{\mathbf{x}} = \mathbf{x}_k - \nabla^2 J(\mathbf{x}_k)^{-1} \nabla J(\mathbf{x}_k) = \mathbf{x}_k - \tilde{H}^{-1} \nabla J(\mathbf{x}_k) \quad (3.7)$$

and the update rule for the non-linear case can be obtained by replacing $\widehat{\mathbf{x}}$ by $\mathbf{x}_{k+1}$

$$\mathbf{x}_{k+1} = \mathbf{x}_k - (\nabla^2 J(\mathbf{x}_k))^{-1} \nabla J(\mathbf{x}_k) = \mathbf{x}_k - \tilde{H}^{-1} \nabla J(\mathbf{x}_k) \quad (3.8)$$

$\nabla^2 J$ is a n x n matrix called the Hessian ($\tilde{H}$), which consists of all the second order partial derivatives of, in this case, the merit function J.

$$\tilde{H} = \begin{bmatrix} \frac{\partial^2 J}{\partial^2 x_1} & \frac{\partial^2 J}{\partial x_1 \partial x_2} & \frac{\partial^2 J}{\partial x_1 \partial x_3} & \cdots & \frac{\partial^2 J}{\partial x_1 \partial x_n} \\ \frac{\partial^2 J}{\partial x_2 \partial x_1} & \frac{\partial^2 J}{\partial^2 x_2} & \frac{\partial^2 J}{\partial x_2 \partial x_3} & \cdots & \frac{\partial^2 J}{\partial x_2 \partial x_n} \\ \frac{\partial^2 J}{\partial x_3 \partial x_1} & \frac{\partial^2 J}{\partial x_3 \partial x_2} & \frac{\partial^2 J}{\partial^2 x_3} & \cdots & \frac{\partial^2 J}{\partial x_3 \partial x_n} \\ \cdots & \cdots & \cdots & \cdots & \cdots \\ \frac{\partial^2 J}{\partial x_n \partial x_1} & \frac{\partial^2 J}{\partial x_n \partial x_2} & \frac{\partial^2 J}{\partial x_n \partial x_3} & \cdots & \frac{\partial^2 J}{\partial^2 x_n} \end{bmatrix} \tag{3.9}$$

Because the Gauss-Newton method assumes that $J(\mathbf{x})$ is locally quadratic in nature, it is most suitable when the merit function is small as it causes only small, modifications to the evolving parameters in contrast to the gradient descent method, which is more efficient when the merit function is large.

Levenberg proposed using a blend of the two update rules to benefit from the advantages of both methods. He proposed the following modified update rule:

$$\mathbf{x}_{k+1} = \mathbf{x}_k - (\tilde{H} + \zeta \tilde{I})^{-1} \nabla J(\mathbf{x}_k) \tag{3.10}$$

where $\tilde{I}$ is the identity matrix. The update rule is used as follows: if $J(\mathbf{x})$ is decreasing, this implies that the quadratic assumption is reasonable and the trial parameters are close to the solution region. ζ is reduced by a factor of 10 to decrease the weight of gradient descent. If $J(\mathbf{x})$ is found to increase the opposite is true and therefore ζ is increased by a factor of 2 to slowly increase the influence of gradient descent.

A disadvantage of the method that Levenberg proposed is that when ζ is large the computationally expensive Hessian plays little role. Marquardt provided the following insight: the second derivative can be used to scale the gradient descent

component resulting in a larger adjustment when far from the solution region. The update rule for the Levenberg-Marquardt algorithm is then modified to:

$$\mathbf{x}_{k+1} = \mathbf{x}_k - (\tilde{H} + \zeta diag[\tilde{H}])^{-1} \nabla J(\mathbf{x}_k) \tag{3.11}$$

where $diag[\tilde{H}]$ is a diagonal square matrix of the diagonal elements of the Hessian. The same method for varying ζ is used.

The drawback with this approach, and in the Levenberg method, is the use of the computationally expensive inverse of $\tilde{H}$ every time the parameters are updated. This can become prohibitively slow computationally when fitting for a large number of parameters. However, it is still much faster than gradient descent alone, and returns a significantly more refined solution than Gauss-Newton iteration. Another problem with the Levenberg-Marquard method is that it is very difficult to construct or extract the covariance matrix of the estimated errors in the recovered parameters. However, when the method is coupled with Optimal Estimation theory this difficulty is resolved.

3.3 Optimal Estimation Theory

The development of the Optimal Estimation theory (*Rodgers*, 1976) is the result of a desire to create a treatment to express the measurement error, which exists in all observations and the corresponding retrieval error.

Following the Bayesian approach (*Rodgers*, 1976), the experimental error can be described as a probability density function (PDF) that quantifies uncertainties in the observation y_i in the following manner: the probability that the true value

lies between y_i and $y_i + dy_i$ is $P(y_i)dy_i$ where $P(y_i)$ is the observation PDF. It is assumed that all errors in the observation system are random and, by the central-limit theory, result in an approximately normal (*i.e.*, Gaussian) distribution for the PDFs shown in Fig. 3.1. The normal distribution is assumed to be a normalized Gaussian function with its peak at the mean expectation value $\overline{y}$ and a width defined by the estimated standard deviation σ (*N.B.* unrelated to molecular orbital σ).

$$P(y_i) = \frac{1}{(2\pi)^{\frac{1}{2}}\sigma} exp[-\frac{(y_i - \overline{y_i})^2}{2\sigma^2}] \tag{3.12}$$

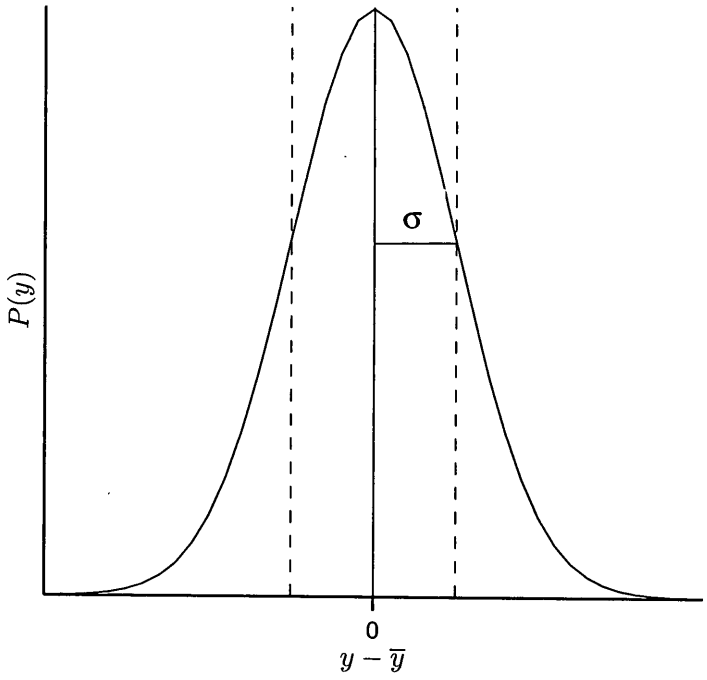

Figure 3.1: Gaussian probability function with standard deviation σ.The mean is centred at 0 as the x-axis is in $y - \overline{y}$ units.

Instead of single data points, sets of data, $\mathbf{y}$, are used for retrievals. Consequently a PDF for an entire probability space $P(\mathbf{y})$, be it measurement space or

solution space, must be defined. The different elements of the observational dataset may be correlated thus a covariance matrix ($\tilde{S}_y$) is introduced to characterize the relationships between estimated errors of the measurements. The diagonal elements of the covariance matrix are the error variances (σ^2) and all other entries express cross-correlation between elements.

The vector form of the Gaussian PDF is:

$$P(\mathbf{z}) = ((2\pi)^{\frac{n}{2}} \tilde{S}_z^{\frac{1}{2}})^{-1} exp[-\frac{1}{2}(\mathbf{y} - \overline{\mathbf{y}})^T \tilde{S}_y^{-1}(\mathbf{y} - \overline{\mathbf{y}})] \tag{3.13}$$

3.3.1 Bayes' Theorem

The goal of Bayes' theorem is to predict reliably the effects of measurement errors on the retrieved state vector, that is, how measurement errors propagate into recovered state space. To quantify this effect five PDF's must be defined.

The state PDF $P(\mathbf{x})$ expresses confidence in the knowledge of the state itself. Its value is normalized so that $\int_{-\infty}^{\infty} P(\mathbf{x})\, d\mathbf{x} = 1$. The measurement PDF $P(\mathbf{y})$ describes the degree of knowledge or confidence in the estimated measurement errors and $P(\mathbf{y})d\mathbf{y}$ is the probability that the measured value should actually lie between the observed $\mathbf{y}$ and $\mathbf{y} \pm d\mathbf{y}$. The joint probability $P(\mathbf{x}, \mathbf{y})$ represents the relationship between the state and the measurements. $P(\mathbf{x}, \mathbf{y})d\mathbf{x}d\mathbf{y}$ is the probability that $\mathbf{x}$ lies between $\mathbf{x}$ and $\mathbf{x} \pm d\mathbf{x}$ and $\mathbf{y}$ lies between $\mathbf{y}$ and $\mathbf{y} \pm d\mathbf{y}$. The PDF of the state can be found by integrating over all $\mathbf{y}$, i.e.:

$$P(\mathbf{x}) = \int_{-\infty}^{\infty} P(\mathbf{x}, \mathbf{y})\, d\mathbf{y} \tag{3.14}$$

and the measurement PDF can be derived in a similar manner,

$$P(\mathbf{y}) = \int_{-\infty}^{\infty} P(\mathbf{x}, \mathbf{y})\, d\mathbf{x} \tag{3.15}$$

There are also two conditional PDFs: $P(\mathbf{y}|\mathbf{x})d\mathbf{y}$ is the probability that $\mathbf{y}$ lies between $\mathbf{y}$ and $\mathbf{y} + d\mathbf{y}$ given $\mathbf{x}$ and $P(\mathbf{x}|\mathbf{y})d\mathbf{x}$ is the same probability for $\mathbf{x}$ given $\mathbf{y}$. In the context of this work, $P(\mathbf{y}|\mathbf{x})$ is the probability of actual measurements $\mathbf{y}$ being correct given the state of the atmosphere $\mathbf{x}$. Inversely $P(\mathbf{x}|\mathbf{y})$ is the probability of a state ($\mathbf{x}$) given a set of observations ($\mathbf{y}$) and is the quantity that is sought.

$P(\mathbf{y}|\mathbf{x})$ is thus defined as the joint PDF weighted by the state PDF and $P(\mathbf{x}|\mathbf{y})$ is defined as the joint PDF weighted by the measurement PDF

$$P(\mathbf{y}|\mathbf{x}) = \frac{P(\mathbf{x}, \mathbf{y})}{P(\mathbf{x})} \tag{3.16}$$

$$P(\mathbf{x}|\mathbf{y}) = \frac{P(\mathbf{x}, \mathbf{y})}{P(\mathbf{y})} \tag{3.17}$$

Combining the two previous expressions we obtain Bayes' theorem which describes $P(\mathbf{x}|\mathbf{y})$ in terms of PDF's,

$$P(\mathbf{x}|\mathbf{y}) = \frac{P(\mathbf{y}|\mathbf{x})P(\mathbf{x})}{P(\mathbf{y})} \tag{3.18}$$

$P(\mathbf{y})$ is simply a normalization factor and can be neglected.

3.3.2 The Maximum Probability State Merit Function

For a problem of the form

$$\mathbf{y} = F(\mathbf{x}) + \boldsymbol{\epsilon} \tag{3.19}$$

where $F(\mathbf{x})$ is the m x 1 vector of the results of the forward model which is not strictly a analytical function, $\boldsymbol{\epsilon}$ is a m x 1 vector of systematic and random errors assuming no covariance between the observations and $\mathbf{y}$ is a m x 1 vector of the actual observations. The probability density functions $P(\mathbf{y}|\mathbf{x})$, the probability of a measurement being accurate given an atmosphere state, and $P(\mathbf{x})$, the probability of a state, can be defined using the vector form of the Gaussian PDF (3.13) with F($\mathbf{x}$) and $\mathbf{x_a}$, the vector of forward modelled observations and the vector of the *a priori* state, as the mean value for the their respective PDFs.

$$P(\mathbf{y}|\mathbf{x}) = \frac{1}{c_1} exp[-\frac{1}{2}(\mathbf{y} - F(\mathbf{x}))^T \tilde{S}_y{}^{-1}(\mathbf{y} - F(\mathbf{x}))] \tag{3.20}$$

$$P(\mathbf{x}) = \frac{1}{c_2} exp[-\frac{1}{2}(\mathbf{x} - \mathbf{x}_a)^T \tilde{S}_a{}^{-1}(\mathbf{x} - \mathbf{x}_a)] \tag{3.21}$$

c_1 and c_2 are parameters given by $c_1 = 2\pi^{\frac{n_1}{2}} \tilde{S}_y$ and $c_2 = 2\pi^{\frac{n_2}{2}} \tilde{S}_a$. $\tilde{S}_a$ is the n x n *a priori* covariance matrix which ascribes the uncertainty, or measure of confidence, assigned to the *a priori* information and $\tilde{S}_y$ is the m x m estimated measurement covariance matrix. Substituting these values into (3.18) gives the following expression:

$$
\begin{aligned}
P(\mathbf{x}|\mathbf{y}) &= P(\mathbf{y}|\mathbf{x})P(\mathbf{x}) \\
&= \frac{1}{c_1 c_2} exp[-\frac{1}{2}[(\mathbf{y}-F(\mathbf{x}))^T \tilde{S_y}^{-1}(\mathbf{y}-F(\mathbf{x})) + \\
&\quad (\mathbf{x}-\mathbf{x}_a)^T \tilde{S_a}^{-1}(\mathbf{x}-\mathbf{x_a})] \qquad (3.22)
\end{aligned}
$$

or

$$
2lnP(\mathbf{x}|\mathbf{y}) = -[(\mathbf{y}-F(\mathbf{x}))^T \tilde{S_y}^{-1}(\mathbf{y}-F(\mathbf{x})) + (\mathbf{x}-\mathbf{x}_a)^T \tilde{S_a}(\mathbf{x}-\mathbf{x}_a)] + c_3 \qquad (3.23)
$$

from which we can derive the maximal probability merit function,

$$
J = (\mathbf{y}-F(\mathbf{x}))^T \tilde{S_y}^{-1}(\mathbf{y}-F(\mathbf{x})) + (\mathbf{x}-\mathbf{x}_a)^T \tilde{S_a}(\mathbf{x}-\mathbf{x}_a) \qquad (3.24)
$$

The maximal probability state, $\overline{\mathbf{x}}$, which is the state with the maximal probability of representing the true state of the atmosphere given the observations is found by maximizing equation 3.23 or by minimizing the maximal probability merit function J equation 3.24. The following section discusses how the Levenberg-Marquard method may be combined with Optimal Estimation to minimize this merit function for a non-linear retrieval problem.

3.3.3 Coupling the Levenberg-Marquard method with Optimal Estimation

The maximum probability merit function (3.24), derived in the previous section, is given by,

$$J = (\mathbf{y} - F(\mathbf{x}))^T \tilde{S}_y^{-1} (\mathbf{y} - F(\mathbf{x})) + (\mathbf{x} - \mathbf{x_a})^T \tilde{S}_a^{-1} (\mathbf{x} - \mathbf{x}_a) \tag{3.25}$$

This function is used as the merit function of the Levenberg-Marquardt iterative fitting method.

The gradient of this function is

$$\nabla_x J = [-\nabla_x F(\mathbf{x})]^T \tilde{S}_y^{-1} (\mathbf{y} - F(\mathbf{x})) + \tilde{S}_a^{-1} (\mathbf{x} - \mathbf{x}_a) \tag{3.26}$$

Since $\tilde{K} = \nabla_x F(\mathbf{x})$,

$$\nabla_x J = -\tilde{K}^T \tilde{S}_y^{-1} (\mathbf{y} - F(\mathbf{x})) + \tilde{S}_a^{-1} (\mathbf{x} - \mathbf{x}_a) \tag{3.27}$$

The Hessian of the function is

$$\begin{aligned} \tilde{H} &= \nabla_x^2 J = \tilde{S}_a^{-1} + \tilde{K}^T \tilde{S}_y^{-1} [\nabla_x F(\mathbf{x})] - \nabla_x \tilde{K}^T \tilde{S}_y^{-1} (\mathbf{y} - F(\mathbf{x})) \\ &= \nabla_x^2 J = \tilde{S}_a^{-1} + \tilde{K}^T \tilde{S}_y^{-1} K - \nabla_x \tilde{K}^T \tilde{S}_y^{-1} (\mathbf{y} - F(\mathbf{x})) \end{aligned} \tag{3.28}$$

The second derivative of the forward model $\nabla_x \tilde{K}$ is small for moderately linear cases such as observations of OH Meinel Band emissions considered here and thus

can be neglected.

$$\tilde{H} = \tilde{S_a}^{-1} + \tilde{K}^T \tilde{S_y}^{-1} \tilde{K} \tag{3.29}$$

After substituting (3.27) and (3.29) into the Levenberg-Marquard update rule (3.11) we obtain,

$$\mathbf{x}_{k+1} = \mathbf{x}_k - \frac{\nabla J(\mathbf{x}_k)}{\tilde{H} + \zeta diag[\tilde{H}]} \tag{3.30}$$

$$\mathbf{x}_{k+1} = \mathbf{x}_k - \frac{-\tilde{K}^T \tilde{S_y}^{-1}(\mathbf{y} - F(\mathbf{x}_k)) + \tilde{S_a}^{-1}(\mathbf{x}_k - \mathbf{x}_a)}{\tilde{S_a}^{-1} + \tilde{K}^T \tilde{S_y}^{-1} \tilde{K} + \zeta diag[\tilde{S_a}^{-1} + \tilde{K}^T \tilde{S_y}^{-1} \tilde{K}]} \tag{3.31}$$

where the quotients indicate vector multiplication by the inverse matrices.

This provides the update rule for the Levenberg-Marquard optimization method coupled with Optimal Estimation, where here again k identifies the iteration index number.

3.3.4 Error Estimation

To quantify how the retrieved state, $\widehat{\mathbf{x}}$, reflects the true state of the atmosphere it is necessary to determine how the observational errors propagate to the final retrieved solution. To fully characterize the solution errors it is essential to quantify the sensitivity of the retrieval to potential sources of error in the observations. As previously discussed the observed quantities are assumed to be a function of the true state of the atmosphere, $\mathbf{x}$, reflected by the appropriate forward model, $F(\mathbf{x})$, and some error component, $\boldsymbol{\epsilon}$

$$\mathbf{y} = F(\mathbf{x}) + \boldsymbol{\epsilon} \tag{3.32}$$

The retrieved state vector $\widehat{\mathbf{x}}$, is a function R, known as the Transfer function, of the observations, $\mathbf{y}$, and the *a priori* estimate of the state of the atmosphere, $\mathbf{x}_a$, *i.e.*:

$$\widehat{\mathbf{x}} = R(\mathbf{y}, \mathbf{x}_a) \tag{3.33}$$

R relates the retrieved state to the true state of the atmosphere by combining the two previous expressions

$$\widehat{\mathbf{x}} = R(F(\mathbf{x}) + \epsilon, \mathbf{x}_a) \tag{3.34}$$

If we linearize the Transfer function about $\mathbf{x} = \mathbf{x}_a$ we obtain the following expression

$$\widehat{\mathbf{x}} = R(F(\mathbf{x}_a) + \tilde{K}(\mathbf{x} - \mathbf{x}_a) + \boldsymbol{\epsilon}, \mathbf{x}_a) \tag{3.35}$$

where $\tilde{K}$ is analogous to the aforementioned Jacobian $\frac{\partial F}{\partial \mathbf{x}}$ evaluated at $\mathbf{x}_a$ but is instead estimated by a perturbation method. In this context the Jacobian describes the sensitivity of the reconstruction to the true state.

Linearizing again, this time with respect to $\mathbf{y}$ yields

$$\widehat{\mathbf{x}} = R(F(\mathbf{x}_a), \mathbf{x}_a) + \tilde{G}_y(\tilde{K}(\mathbf{x} - \mathbf{x}_a) + \boldsymbol{\epsilon}) \tag{3.36}$$

$\tilde{G}_y$ is the n x n gain matrix which describes the sensitivity of the retrieved state to the observations, $\frac{\partial \widehat{\mathbf{x}}}{\partial \mathbf{y}}$.

Rearranging Eq. 3.36 we obtain an expression for the estimated error of the retrieval, *i.e.*, the difference between the retrieved state and the true state

$$\widehat{\mathbf{x}} - \mathbf{x} = (\tilde{A} - \tilde{I})(\mathbf{x} - \mathbf{x}_a) + \tilde{G}_y\boldsymbol{\epsilon} \tag{3.37}$$

where $\tilde{I}$ is the identity matrix.

The first term, $(\tilde{A}-\tilde{I})(\mathbf{x}-\mathbf{x}_a)$, is related to the smoothing error and the second term, $\tilde{G}_y\boldsymbol{\epsilon}$, is known as the retrieval noise that arises from random and systematic measurement errors.

$\tilde{A}$ is the averaging kernel that characterizes the sensitivity of the retrieved state to the true state, $\tilde{A}=\tilde{G}_y\tilde{K}=\frac{\partial\hat{\mathbf{x}}}{\partial\mathbf{x}}$ and $(\tilde{A}-\tilde{I})$ is the sensitivity of the retrieved state to the chosen *a priori*, $\frac{\partial\hat{\mathbf{x}}}{\partial\mathbf{x}_a}$. The averaging kernel by itself can be used to quantify how the retrieval may inherently smooth the recovery parameters and how much the retrieval depends on the *a priori* choice. It is a valuable diagnostic tool as it can be used to identify erroneous retrievals. For an ideal observing system, one with no smoothing, $\tilde{A}$ will be the unit matrix. For a retrieval that fails to improve upon the *a priori* for all parameters the averaging kernel will be a null matrix.

For the Levenberg-Marquard optimization the relationship between the retrieved state and the *a priori* can be found by using the update rule (3.31)

$$\hat{\mathbf{x}}=\mathbf{x}_a-\frac{-\tilde{K}^T\tilde{S}_y{}^{-1}(\mathbf{y}-F(\hat{\mathbf{x}}))+\tilde{S}_a{}^{-1}(\hat{\mathbf{x}}-\mathbf{x}_a)}{\tilde{S}_a{}^{-1}+\tilde{K}^T\tilde{S}_y{}^{-1}\tilde{K}+\zeta diag[\tilde{S}_a{}^{-1}+\tilde{K}^T\tilde{S}_y{}^{-1}\tilde{K}]} \tag{3.38}$$

For the ideal Jacobian (the Jacobian that accurately maps the measurements to state space) $\zeta=0$, so the Levenberg-Marquard term is neglected, which reduces the equation to the Gauss-Newton iterative update rule as before,

$$\hat{\mathbf{x}}=\mathbf{x}_a-\frac{-\tilde{K}^T\tilde{S}_y{}^{-1}(\mathbf{y}-F(\mathbf{x}))+\tilde{S}_a{}^{-1}(\hat{\mathbf{x}}-\mathbf{x}_a)}{\tilde{S}_a{}^{-1}+\tilde{K}^T\tilde{S}_y{}^{-1}\tilde{K}} \tag{3.39}$$

The gain matrix is then

$$\tilde{G}_y = \frac{\partial \hat{\mathbf{x}}}{\partial \mathbf{y}} = \frac{\tilde{K}^T \tilde{S}_y^{-1}}{\tilde{S}_a^{-1} + \tilde{K}^T \tilde{S}_y^{-1} \tilde{K}} \tag{3.40}$$

and the averaging kernel becomes

$$\tilde{A} = \tilde{G}_y \tilde{K} = \frac{\tilde{K}^T \tilde{S}_y^{-1} \tilde{K}}{\tilde{S}_a^{-1} + \tilde{K}^T \tilde{S}_y^{-1} \tilde{K}} \tag{3.41}$$

The smoothing error, $\tilde{S}_s$, sometimes called the nullspace error, is the error resulting from the smoothing that occurs between observation points as mentioned above.

$$\begin{aligned} \tilde{S}_s &= \varepsilon[(\tilde{A} - \tilde{I})(\mathbf{x} - \mathbf{x}_a)(\mathbf{x} - \mathbf{x}_a)^T(\tilde{A} - \tilde{I})^T] \\ &= (\tilde{A} - \tilde{I})[\varepsilon(\mathbf{x} - \mathbf{x}_a)(\mathbf{x} - \mathbf{x}_a)^T](\tilde{A} - \tilde{I})^T \\ &= (\tilde{A} - \tilde{I})\tilde{S}_a(\tilde{A} - \tilde{I})^T \end{aligned} \tag{3.42}$$

Substituting into the expression for $\tilde{A}$, the smoothing error becomes

$$\tilde{S}_s = \frac{1}{\tilde{S}_a^{-1} + \tilde{K}^T \tilde{S}_y^{-1}} \tilde{S}_a^{-1} \frac{1}{\tilde{S}_a^{-1} + \tilde{K}^T \tilde{S}_y^{-1}} \tag{3.43}$$

The covariance matrix for the retrieval noise $\tilde{S_m}$ is given by:

$$\tilde{S_m} = \tilde{G}_y \tilde{S}_y \tilde{G}_y^T \tag{3.44}$$

Substituting this into the expression for $\tilde{G}_y$ gives an expression for the retrieval

error in terms of $\tilde{S_a}$, $\tilde{K}$ and $\tilde{S_y}$, *i.e.*,

$$S_m = \frac{1}{\tilde{S_a}^{-1} + \tilde{K}^T \tilde{S_y}^{-1}} \tilde{K}^T \tilde{S_y}^{-1} K \frac{1}{\tilde{S_a}^{-1} + \tilde{K}^T \tilde{S_y}^{-1}} \tag{3.45}$$

The sum of these two errors gives the total estimated error $\tilde{S}$ of the retrieval

$$\tilde{S} = \tilde{S_s} + \tilde{S_m} = \frac{1}{S_a^{-1} + \tilde{K}^T S_y^{-1}} \tag{3.46}$$

The diagonal of the $\tilde{S}$ covariance matrix contains the total estimated variances of the individual components of the retrieved state vector, $\widehat{\mathbf{x}}$. The off diagonal elements are the correlations between the error variances. For non-correlated errors these elements should be 0.

This error analysis approach has been incorporated in the present work; however the estimated error will not be referenced in the simulations that follow as the *a priori* error, $\tilde{S_a}$, is greatly exaggerated to decrease the weight of the *a priori* which is a mere starting point. Instead direct comparison with our assumed true profiles will be used to assess the accuracy of the retrievals.

4 Atmospheric State Retrievals from Limb Observations

Limb measurements of atmospheric properties, such as airglow radiances, are widely used to recover information on the vertical profile of a variety of atmospheric constituents, (see *Carlotti et al.*, 2001). These measurements are made by an instrument that views the atmosphere tangentially from high altitudes, while orbiting the planet on a space platform as shown in Fig. 4.1. By making observations, for example limb enhanced airglow radiances or attenuation of sunlight, through the atmospheric limb at various tangent heights, information regarding the vertical distribution of atmospheric constituents and atmospheric properties can be derived. Due to the orbital motion of the spacecraft, horizontal averaging during the observation period due to the inherent geometric horizontal integration along the path, the measurements do not correspond to a single location on the planet. For what are known as 1-D retrieval methods presented in this chapter, horizontal homogeneity of state parameters is assumed, that is to say that atmospheric parameters are assumed to vary only in the vertical along the line of sight, hence the term '1-D'. 2-D tomographic techniques that relax this homogeneity assumption have been developed for certain conditions but are beyond the scope of this work (*McDade*

and Llewellyn, 1993; *Degenstein et al.*, 2003; *Degenstein et al.*, 2004; *Steck et al.*, 2005).

Any limb observation of electromagnetic radiation (EMR) is primarily characterized by its tangent height (H), which is the altitude of the tangent point, or minimum ray height, of the line of sight of the instrument as depicted in Fig. 4.1. Refraction effects, *i.e.*, bending of the path of EMR, are not important at the height of the Martian OH Meinel airglow layer. For daytime observations of atmospheric airglow, stray light scattering from the atmosphere below the tangent height may contribute to and thus interfere with the observation. However, for nighttime observations, such as the measurement of OH Meinel Band nightglow, out-of-field contribution effects are not a significant concern.

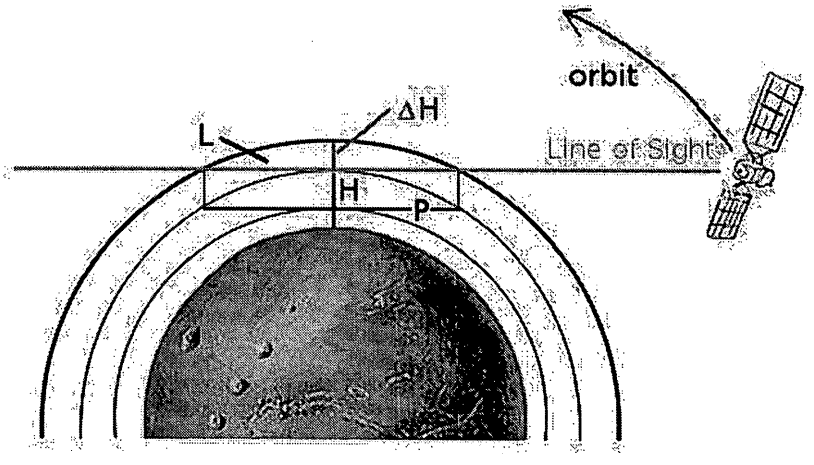

Figure 4.1: Limb viewing geometry. The instrument observes through some layer with index L, bounded by a lower tangent height of H. ΔH corresponds to the thickness of the layer and P is the pathlength through the layer used for any subsequent inversions.

At the simplest level, the atmosphere may be divided into a series of shells, defined by the tangent heights, tangent height boundaries, and altitude shell bound-

aries as shown in Fig. 4.2. These shells, of chosen thickness ΔH, are assumed to have constant horizontal properties (the assumption of horizontal homogeneity) and averaged vertical properties. The geometric pathlengths, $P_{i,j}$, as shown are the total geometric length that the light follows through each layer of the atmosphere, where i indicates the tangent height index and j indicates the altitude index of each layer probed along the line of sight.

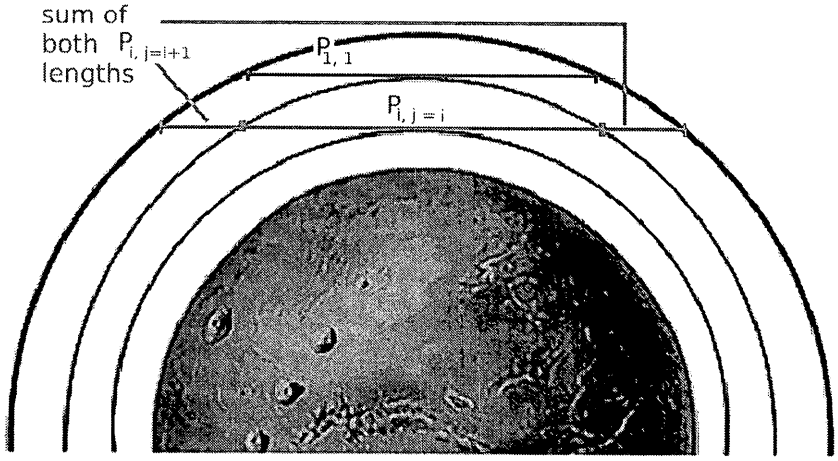

Figure 4.2: Pathlengths for layers L_1 and L_i. Tangent height i and shell index j increase downwards.

In general for a spherical atmosphere,

$$P_{i,j} = 2\sqrt{(H_j + R_p)^2 - (H_i + R_p)^2} - \sum_{k=j+1}^{i} P_{i,k} \qquad 0 \leq \mathrm{j} \leq \mathrm{i} \qquad (4.1)$$

where H_i represents the height of the tangent point above the surface, H_j is the height of the preceding layer and R_p is the surface radius of the planet. All the geometric pathlengths for all the tangent heights together form the pathlength matrix, $\tilde{P}$. Mean pathlengths calculated for the Martian atmosphere for tangent heights between 70.5 km and 79.5 km are shown in Table 4.1.

Tangent Height(km)	L_1	L_2	L_3	L_4	L_5	L_6	L_7	L_8	L_9	L_{10}
79.5	166.1									
78.5	68.8	166.0								
77.5	52.8	68.8	166.0							
76.5	44.5	52.8	68.8	166.0						
75.5	39.2	44.5	52.8	68.8	166.0					
74.5	35.5	39.2	44.5	52.8	68.8	165.9				
73.5	32.6	35.5	39.2	44.5	52.8	68.7	165.9			
72.5	30.4	32.6	35.4	39.2	44.5	52.8	68.7	165.9		
71.5	28.5	30.3	32.6	35.4	39.2	44.5	52.7	68.7	165.9	
70.5	27.0	28.5	30.3	32.6	35.4	39.2	44.5	52.7	68.7	165.8

Table 4.1: Calculated geometric pathlengths in km for Martian atmosphere for tangent heights 70.5 - 79.5 km and shell thickness of 1 km.

In the absence of absorption and refraction, these geometric pathlengths can be used as a metric for the enhancement of, for example, airglow emissions when observed in the limb viewing direction. The observed emissions are enhanced because the line of sight passes through more of the atmosphere than would be sampled by a nadir instrument looking straight down or a ground instrument looking up.

Under optically thin conditions, *i.e.*, no absorption along the path, this enhancement makes the observation of weaker emissions, such as the emission of OH Meinel nightglow, more accessible. The retrieval methods in the present work are designed to recover parameters from airglow observations made under such limb observing conditions. However, an optically thick situation with absorption, the limb enhancement may produce 'saturated' intensities which only convey information down to the point from where the emission may be fully transmitted to the instrument (*Livesey and Read*, 2000) unless this absorption can be modelled.

Although dust is usually confined to the lower atmosphere of Mars, Mars Global Surveyor's Thermal Emission Spectrometer (TES) observed lofting of low atmosphere dust reaching heights of 80 km during the 2001 dust storm (*Clancy et al.*, 2010). During such dust events, the retrieval of vertical profiles of constituents and their emission from limb observations may be compromised.

As for clouds, which may attenuate some of the limb emissions, the analysis of observations from the Thermal Emission Imaging System visible imaging subsystem (THEMIS-VIS) has resulted in the identification of two types of clouds, likely mainly composed of CO_2 ice, in the mesosphere of Mars: equatorial clouds and northern mid-latitude winter clouds. The equatorial mesospheric clouds are thought to be rare as they were detected in only 5 imaging sequences out of 2048

(*McConnochie et al.*, 2010) and thus we do not anticipate that they will compromise limb observations of the Meinel airglow of Mars. The northern mid-latitude winter mesospheric clouds of Mars are more common with a detection rate of 17% in Acidalia, but have only been detected under twilight conditions (*McConnochie et al.*, 2010) and thus should not interfere with the nighttime measurements of Meinel Band airglow emissions on Mars.

As stated in the Introduction, the primary goal of this work is to develop a method for simultaneously recovering atmospheric temperatures and volume emission rates from limb observations of the Meinel nightglow spectrum in the Martian atmosphere. To recover vertical profiles of these parameters a mechanism for decomposing the limb observations must be employed. In the following sections different approaches to the problem are discussed.

4.1 The Onion Peeling Approach

The 'Onion Peeling' approach is a common method for the retrieval of constituent vertical profiles from limb observations. Based on the Abel transform inversion technique using two point interpolation (*Dasch*, 1992), the retrieval is carried out sequentially, stepping down through the atmosphere from a null upper boundary to retrieve products, such as VERs and temperatures as a function of altitude, from observations made at different tangent heights.

In the case of limb observations of OH Meinel Band airglow spectra, it can be seen from Figs 4.1 and 4.2 that the method would start at the uppermost layer (L_1). If it is assumed that there is no emission above the top boundary layer (null upper

boundary layer assumption) the observed spectrum $\mathbf{R}_1(\lambda)$ depends on $\mathbf{q}_1(\lambda)$, the vector of absolute wavelength bin radiances (WBRs) of the top layer weighted by the geometric pathlength in cm, $P_{1,1}$, convolved in wavelength with the instrument function, $f(\lambda)$ as before, sampled in Å. In the present work, the term absolute WBR refers to the WBR of a specific layer without any pathlength enhancement or contributions from other layers derived for specific wavelengths.

$$\mathbf{R}_1(\lambda) = f(\lambda) * P_{1,1}\mathbf{q}_1(\lambda) \tag{4.2}$$

$\mathbf{R}_1(\lambda)$ and $\mathbf{q}_1(\lambda)$ are spectrophotometric limb spectra composed of all transitions within the spectral region sampled at m discrete wavelength intervals.

Due to the associative nature of convolution this is equivalent to:

$$\mathbf{R_1}(\lambda) = f(\lambda) * P_{1,1}\mathbf{q_1}(\lambda) = P_{1,1}(f(\lambda) * \mathbf{q_1}(\lambda)) \tag{4.3}$$

The pathlength is then used to solve for $\mathbf{Q}_1(\lambda)$, the absolute WBR spectrum convolved with the instrument function discretely sampled at m wavelengths for layer 1, $\mathbf{Q}_1(\lambda) = f(\lambda) * \mathbf{q}_1(\lambda)$.

$$\mathbf{Q_1}(\lambda) = \frac{\mathbf{R}_1(\lambda)}{P_{1,1}} \tag{4.4}$$

$\mathbf{Q_1}(\lambda)$ is the vector of observations that the non-linear iterative fitting method described in Chapter 2 will fit, *i.e.* $\mathbf{y}$. The forward spectral model used for this optimization is:

$$F(\mathbf{x}) = \mathbf{\Gamma}_1(T_1, \lambda) = f(\lambda) * \mathbf{B}(\lambda) \tag{4.5}$$

$\mathbf{\Gamma_1}$ is calculated using equation 2.29 from Chapter 2 and is used in conjunction with the non-linear fitting method described in Chapter 3 to recover for temperature (T_1) and the volume emission rate (V_{T1}) for the top layer. Note that all transitions within the spectral region are fit concurrently, thus the volume emission rate for multiple vibrational levels can be recovered simultaneously.

Once the parameters are recovered for this uppermost layer the algorithm proceeds to the next layer below. The observed limb radiances for the line of sight, $\mathbf{R}_2(\lambda)$, depend on the absolute WBRs from the second layer ($\mathbf{Q}_2$) and the top layer ($\mathbf{Q}_1$) weighed by their respective pathlengths.

$$\mathbf{R}_2(\lambda) = P_{2,1}\mathbf{Q}_1(\lambda) + P_{2,2}\mathbf{Q}_2(\lambda) \tag{4.6}$$

The calculated pathlengths and the simulated emission spectrum ($\mathbf{\Gamma}_1(T_1, \lambda)$) of the uppermost layer generated using the previously recovered temperatures and/or VER are used to isolate the convolved absolute WBRs for the second layer.

$$\mathbf{Q_2}(\lambda) = \frac{\mathbf{R}_2(\lambda) - P_{2,1}\mathbf{\Gamma}_1(T_1, \lambda)}{P_{2,2}} \tag{4.7}$$

In our application the simulated best fit wavelength bin radiance spectrum convolved with the instrument function, $\mathbf{\Gamma}_1(T_1, \lambda)$, is used instead of the derived rates, $\mathbf{Q}_1(\lambda)$, thus using the recovered temperature, to avoid the propagation of observational errors. Using the derived convolved WBR spectrum for the second layer, $\mathbf{Q}_2(\lambda)$, the fitting algorithm will recover the temperatures and VER associated with the second layer (T_2 and V_{T2}) using the same forward spectral model and non-linear fitting algorithm as above.

The algorithm continues downward in the same manner, recovering temperatures and VERs at each layer, for all the assumed spherical shells in the OH airglow emission layer, using the following generalized recursive expression to determine the contributions from each layer

$$\mathbf{Q}_i(\lambda) = \frac{1}{P_{i,i}}(\mathbf{R}_i(\lambda) - \sum_{j=i}^{i-1} P_{i,j}\mathbf{\Gamma_j}(T_j, \lambda_j)) \tag{4.8}$$

where i indicates the layer index.

A known limitation of the onion peeling approach is its susceptibility to downward noise propagation. Retrieval errors in one tangent height propagate down to lower layers (*Carlotti*, 1988). That is, the error in the reconstructed observations of one layer will propagate down to the subsequent layers as the algorithm attempts to compensate the error above. The onion peeling approach also recovers on a localized scale (*Dasch*, 1992), *i.e.*, one layer at a time, and thus retrievals are subject to instabilities due to the lack of constraint between layers. Modified approaches, such as constrained linear inversion, can impose smoothing constraints and can take into account any covariance between layers.

4.2 Temperature Recovered from Derived Absolute Wavelength Bin Radiance Spectra

An alternate method was developed specifically for the recovery of temperature profiles from OH nightglow limb observations using the spectrum model detailed in Chapter 2. This approach decouples the recovery of temperatures from the recovery of OH Meinel VER by exploiting their different effects on the emission spectrum:

the temperature controls the relative rotational intensities within a given band from a given height, *i.e.*, the shape of the band envelope, while the VER of a given v' determines the absolute intensity of the observed emission.

First the absolute instrument degraded (AD) wavelength bin radiance profiles at all selected wavelengths are recovered from the limb observed data set. The profiles are derived as described below.

In lieu of decomposing the profile layer by layer, the absolute wavelength bin radiance profile a single wavelength bin, λ_1, is determined at the same number of recovery shells as the observed tangent heights, n, by using the pathlength matrix $\tilde{P}$ discussed in Section 4.1. In other words the pathlength matrix is used as the weighting function to recover the AD WBR for λ_1 at each shell

$$\mathbf{R}(\lambda_1) = \tilde{P}\mathbf{Q}(\lambda_1) \tag{4.9}$$

where $\mathbf{R}(\lambda_1)$ is now a column vector of the observed limb emission intensities from each tangent height for wavelength λ_1 and $\mathbf{Q}(\lambda_1)$ is a column vector of the instrument function convolved absolute wavelength bin radiance profile for λ_1. Therefore the absolute instrument degraded wavelength bin radiance profile can be determined for wavelength λ_1 by

$$\mathbf{Q}(\lambda_1) = \tilde{P}^{-1}\mathbf{R}(\lambda_1) \tag{4.10}$$

Noting that the number of layers and number of chosen shells is the same, *i.e.*, $\tilde{P}$ is a square matrix with a defined inverse $\tilde{P}^{-1}$. Rather than calculating the inverse of $\tilde{P}$ which can be time consuming, the system of equations is instead solved using

Gaussian elimination.

The AD WBR profiles for a range of different wavelengths for a single vibrational level v' are then reassembled to obtain a spectrum of convolved absolute WBR for the vibrational level for each recovery shell height, $\mathbf{Q}_j(v')$ where j is the layer index as before.

These spectra are normalized to unity which, as will be shown below, removes the dependance on the vibrational level volume emission rate. This normalization is a computational shortcut and has no physical significance.

$$\mathbf{Q}_j^N(v') = \frac{\mathbf{Q}_j(v')}{\sum \mathbf{Q}_j(v')} \tag{4.11}$$

where

$$\sum_{\lambda} \mathbf{Q}_j^N(v') = 1 \tag{4.12}$$

The superscript ^{N} indicates that the spectrum has been normalized.

The iterative fitting method is then used to best fit the temperature for this instrument convolved spectrum using the simulated normalized instrument convolved emission spectra $\mathbf{\Gamma}_j^N(T, \lambda)$ which only includes transitions from vibrational level v' as the forward model,

$$F(\mathbf{x}) = \mathbf{\Gamma}_j^N(T, \lambda) = \frac{\mathbf{\Gamma}_j(T, \lambda)}{\sum \mathbf{\Gamma}_i(T, \lambda)} \tag{4.13}$$

where

$$\sum_{\lambda} \mathbf{\Gamma}_i^N(T, \lambda) = 1 \tag{4.14}$$

Recall that $\mathbf{\Gamma}_i^N(T, \lambda)$ is a column vector of all the calculated absolute line VER of a

given υ' level, $\mathbf{B}(\lambda)$, convolved with the instrument function $f(\lambda)$ and normalized at their calculated wavelengths.

$$\mathbf{\Gamma}_j^N(T,\lambda) = \frac{f(\lambda) * \mathbf{B}_j(\lambda)}{\sum f(\lambda) * \mathbf{B}_j(\lambda)} \tag{4.15}$$

For a spectral region containing only emission from a single vibrational level $\mathbf{B}_j(\lambda)$ can be expressed as

$$\mathbf{B}_j(\lambda) = V_T(\upsilon')\boldsymbol{\alpha}(\lambda) \tag{4.16}$$

where $\boldsymbol{\alpha}(\lambda)$ is a vector of all $\frac{A(J',\upsilon' \rightarrow J'',\upsilon'')}{A_T(T_{ROT})} \frac{2(2J'+1)}{Q_{\upsilon'}(T_{ROT})} exp(\frac{-E_{\upsilon',i'}(J')}{kT_{ROT}})$ from the υ' vibrational level at the calculated λ within the spectral range. The wavelength of emission is calculated as described in section 2.3.4.

Thus,

$$\begin{aligned} \mathbf{\Gamma}_j^N(T,\lambda) &= \frac{f(\lambda) * V_T(\upsilon')\boldsymbol{\alpha}(\lambda)}{\sum f(\lambda) * V_T(\upsilon')\boldsymbol{\alpha}(\lambda)} \\ &= \frac{V_T(\upsilon')}{V_T(\upsilon')} \frac{f(\lambda) * \boldsymbol{\alpha}(\lambda)}{\sum f(\lambda) * \boldsymbol{\alpha}(\lambda)} \end{aligned} \tag{4.17}$$

The $V_T(\upsilon')$s cancel out and it is now clear that the normalized spectrum is completely independent of the emission rate.

$$\mathbf{\Gamma}_j^N(\lambda,T) = \frac{f(\lambda) * \boldsymbol{\alpha}}{\sum f(\lambda * \boldsymbol{\alpha}} \tag{4.18}$$

where as before,

$$\sum_{\lambda} \mathbf{\Gamma}_j^N(\lambda,T) = 1 \tag{4.19}$$

Thus no knowledge of the emission rate is necessary to recover the temperature of

the layer.

By fitting the normalized absolute instrument degraded WBR spectra of each layer the temperature can be recovered without having to evaluate the VER of the bands involved.

This approach, however, is limited in that it can only recover from emission lines of bands from a single v' vibrational level. When normalizing the emission over a wavelength interval that contains lines from more than one vibrational level, it is not possible to completely remove the dependance on the VER as residual information about the emission rates are contained in the relative intensity of the scaled absolute WBR of the transitions from different vibrational levels. For example, to recover the temperatures from a spectral region consisting of transitions from v_1' and v_2' the emission lines from both vibrational levels must be accounted for when generating a synthetic spectrum

$$\begin{aligned} \mathbf{\Gamma_j^N}(T,\lambda) &= \frac{f(\lambda) * (B_j(v_1',\lambda) + B_j(v_2',\lambda))}{\sum f(\lambda) * (B_j(v_1',\lambda) + B_j(v_2',\lambda))} \\ &= \frac{f(\lambda) * (V_T(v_1')\boldsymbol{\alpha}(v_1',\lambda) + V_T(v_2')\boldsymbol{\alpha}(v_2',\lambda))}{\sum f(\lambda) * (V_T(v_1')\boldsymbol{\alpha}(v_1',\lambda) + V_T(v_2')\boldsymbol{\alpha}(v_2',\lambda))} \end{aligned} \tag{4.20}$$

In the previous equation (4.20) the dependance of $\mathbf{B}(\lambda)$ and $\boldsymbol{\alpha}(\lambda)$ on the vibrational level is expressly stated for clarity.

$V_T(v_1)$ and $V_T(v_2)$ do not cancel out, thus it is not possible to remove the dependance on the VER by normalization.

The main benefit of this approach is that by isolating the recovery of temperatures, the algorithm simplifies the optimization and increases the speed of the temperature profile retrieval. Unlike the onion peeling method which seeks to remove

contributions from the other tangent heights, in this method these contributions are used to determine the AD wavelength bin radiance profile for the selected wavelengths, thus making use of the entire dataset. The main disadvantage in the use of this technique as the retrieval algorithm is that it is essentially performing two types of fitting on the dataset. This disassociates the recovered products from the original data and so amplifies the effect of noise on the recovered temperatures. Also, the Gaussian elimination matrix solver is not able to account for the noise in the spectrum. Instead the method recovers a temperature profile which best fits all the measurements including their noise components. This makes it difficult to quantify the estimated level of error in the recovered temperatures. A more complex method for deriving the profiles that would account for noise in the spectrum may minimize this uncertainty, but would significantly slow down the algorithm and would not resolve the issue of repeated retrieval.

4.3 The Global Optimization Approach

Another approach to the problem at hand is Global Optimization. The primary idea of this method is to fit the entire set of observations over all tangent heights and wavelengths in a single step using the entire sequence of limb observed spectra. Thus the set of observations to be fitted ($\mathbf{y}$) and the forward model ($F(\mathbf{x})$) are

$$\mathbf{y} = \mathbf{R}^{full} \tag{4.21}$$

$$F(\mathbf{x}) = \tilde{P}\mathbf{\Gamma}^{full} \tag{4.22}$$

where $\mathbf{R}^{full}$ is a square matrix of all the observed emissions at all sampled tangent heights and wavelengths (consisting of all g rows of m data points) and $\mathbf{\Gamma}^{full}$ is a square matrix of all the forward modelled instrument degraded WBR for all wavelengths in the range and for all tangent heights (also consisting of g rows of m elements), which depend on the state parameters to be recovered, *i.e.*, the temperatures of each height and the volume emission rate for each vibrational level at each recovery height. As mentioned previously if the temperature profile is known, the fitting method can recover the VER profile and vice versa or both profiles can be recovered, the merits of each method will be evaluated in Chapter 5. g is the number of input tangent heights and m is the number of observed wavelength emission rate samples. The square matrices are concatenated into column vectors for the purpose of fitting,

The main advantage of this method is that it minimizes the error propagation associated with the onion peeling method. The method is also more robust when dealing with noise in the observations as it makes use of all the observational data. The recovered profile is the best fit for all layers since it fits all layers simultaneously. Also the retrieval error can be well characterized using Optimal Estimation as the optimization is performed directly on the observations. The Global Optimization approach is flexible in that it can be used on any part of the observed OH Meinel airglow emission spectrum irrespective of the number of bands contributing within a chosen spectral window. There is a cost, however, since this method performs one fitting, the data set is considerably larger (g x m elements), whereas the two other methods perform sequential fittings on a much smaller scale (m x 1). Also, the Jacobian calculated at each iteration of the Levenberg-Marquardt optimization

method is a n x m matrix, where n is the number of state parameters for all the layers of the atmosphere, *i.e.*, $n = 2$ x g for the retrieval of temperatures and the VER of one vibrational level. In contrast, for the onion peeling approach and the approach using derived absolute volume emission rate profiles, n consists of only the parameters for a single level, *i.e.* $n = 2$ for the example mentioned above. Thus the non-linear fitting associated with Global Optimization is more computer intensive than the other methods.

The relative merits of the three approaches will be evaluated in the following chapter.

5 Simulations and test of algorithms

5.1 Modes of retrieval for temperatures and volume emission rates

The three retrieval methods discussed in Chapter 4 are tested in this chapter to determine the approach best suited to the retrieval of temperatures and volume emission rates for limb observations of OH Meinel Band airglow. Recall that the term volume emission rate (VER) refers to the total volume emission rate of a given v' level ($V_T(v')$) and the term wavelength bin radiance (WBR) refers to the observed or synthetic emission rate for a specific wavelength bin, defined by the sampling interval. Additionally, the term absolute WBR refers to the radiance being emitted at a given wavelength in a specific layer without pathlength enhancement or contributions from any other layer. The Onion Peeling method and the Global Optimization approach will be tested for three cases. The first case is the retrieval of temperatures with knowledge of volume emission rate profiles. This retrieval method could be used in conjunction with a photochemical model, that would accurately predict the volume emission rates of the specific v' levels. The second case is the recovery of the VERs using the known temperature profile, that would be possible in the situation where another instrument simultaneously measured

atmospheric temperatures. The final case is the simultaneous recovery of both the temperature and vibrational level volume emission rate profiles. In this case the recovery method is completely independent of information from other instruments or photochemical models; however, it is less flexible due to additional requirements regarding the emission lines used for retrieval, discussed below. The approach using derived absolute WBR is tested for temperature retrieval with no knowledge of the VER. This approach was designed for this case alone.

The accurate recovery of both VER and temperatures requires that the manner in which the spectrum varies with changes in each of the parameters differ. Therefore, the associated Jacobians, being a measure of this change, must be dissimilar. As mentioned in Chapter 2, the intensity of the P1(1), P1(2), Q1(1), Q1(2) and R1(1) lines decrease with increasing rotational temperature for a fixed total band intensity. These lines, hereafter referred to as the negative set, are stronger than the higher N' lines which increase with temperature, which we will refer to as the positive set. The higher N' lines considered in this work are as follows: P1(3) - P1(14), P2(1) - P2(14), Q1(3) - Q1(14), Q2(1) - Q2(14), R1(2) - R1(14) and R2(1) - R2(14).

For a spectral region containing emissions of the positive set the Jacobian relating limb intensities to WBRs and the Jacobian relating calculated limb intensities to temperature are similar in form. An increase in either VER or temperature results in an increase in limb intensity of the emission lines, although the increase differs significantly in magnitude, as shown in Fig. 5.1 (b) and (d). Attempting to recover both VER and temperature quantities from a given spectral region results in a non-unique solution. An increase in one quantity can be offset by a decrease

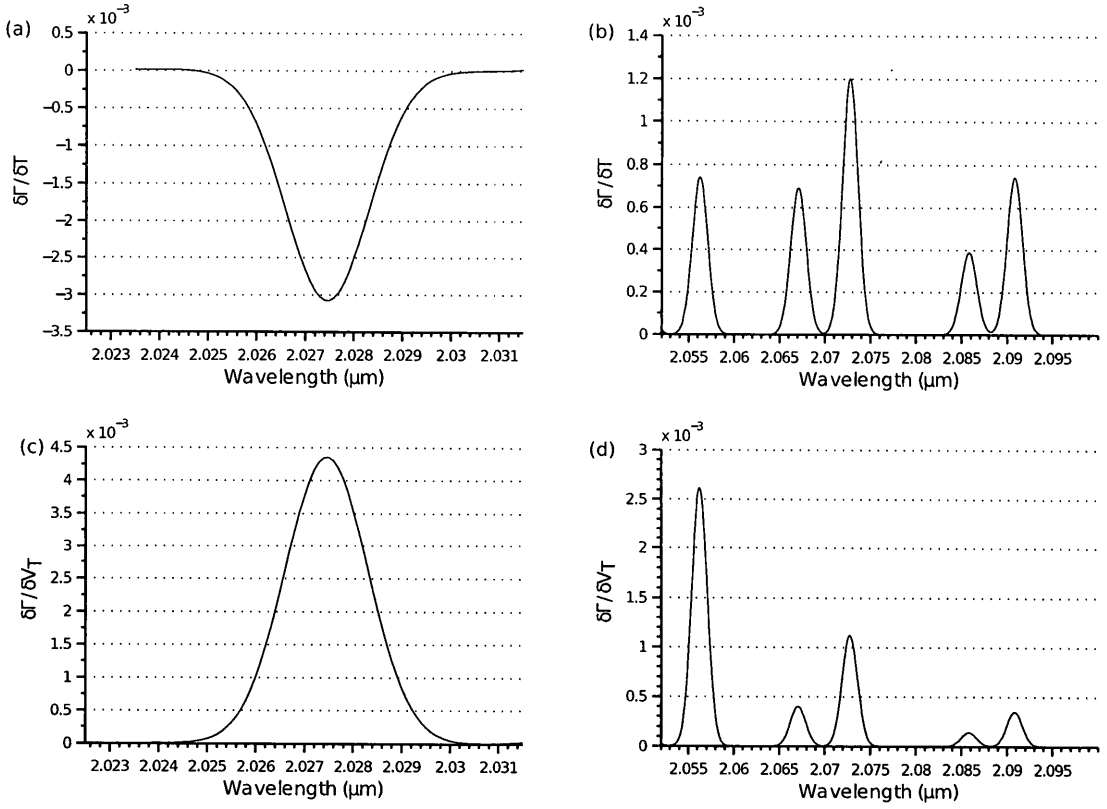

Figure 5.1: Example of Jacobians, $\frac{\delta\Gamma}{\delta T}$ and $\frac{\delta\Gamma}{\delta V_T}$ for the spectrum of a single atmospheric layer containing emissions exclusively from the positive set and exclusively from the negative set at 140 K and for VERs of 100 photons s^{-1} cm^{-3}. The Jacobian describes how the synthetic instrument convolved spectrum ($\mathbf{\Gamma}(\lambda)$) varies with changes in either parameter. $\frac{\delta\Gamma}{\delta T}$ for the negative set is shown in (a) and the positive set in (b). $\frac{\delta\Gamma}{\delta V_T}$ for the negative set is shown in (c) and the positive set in (d). Note that the spectral region chosen with for the negative set contains only one line while the region selected for the positive set contains multiple lines.

in the other, thus many combinations of the quantities can minimize the merit function.

The retrieval of both temperatures and VERs from a given spectral region containing only emission lines from the negative set also results in a non-unique solution. Although the temperature and VER Jacobians differ in amplitude and are opposite in sign, as the VER Jacobian is positive and the temperature Jacobian is negative as shown in Fig. 5.1 (a) and (c), a similar problem arises: any increase in one sought-after parameter can be reflected as an increase in the other and vice versa. The shape of the Jacobian curve and not the magnitude which determines if the parameters can be recovered independently.

However, when lines from both groups are included in a given target spectral window, the emission spectrum varies between increasing and decreasing with temperature while continuing to simply increase with VER resulting in two dissimilar Jacobian curves. This makes the recovery of both quantities possible. To assure that the retrieval technique is not preferentially fitting the lines of one set over the other, which could result in a bias in the recovered temperatures, it is desirable to choose spectral windows where the intensities of emission lines from the positive set and the negative set are comparable. Two such preferred spectral windows have been identified and are described in the following section.

5.2 Spectral Regions

The retrieval methods are tested on simulated data sets to gauge their strengths and weaknesses. Two regions of the OH Meinel Band nightglow spectrum are identified

for detailed testing: The first is the 1.96-2.10 μm spectral window which contains lines of the OH(8-6) band, hereafter referred as region A. The second region lies between 2.79 and 2.95 μm and is referred to as region B. This region is slightly wider than the first region and contains lines of both the OH(1-0) and the OH(2-1) bands. The synthetic line and convolved absolute WBR spectra of the target observations for both of these regions are illustrated in Fig. 5.2. Since region B contains lines from two different v' levels it will also be possible to gain a sense of the capacity of each retrieval method to recover more than one v' level. In both cases the emission of lines from the negative set are balanced by emission of lines of the positive set. The ratio at 200 K of positive set line intensities to negative set line intensities is 1:1.14 in region A and 1:0.89 in region B. Consequently the Jacobians relating limb intensities to temperature and to volume emission rates, shown in Fig. 5.3 are uncoupled, making the simultaneous recovery of temperature and volume emission rates possible. Complete listings of the OH Meinel transitions in both spectral windows given in Tables 5.1 and 5.2. It would also be possible to fit multiple micro windows simultaneously, however this approach was not explored in this work.

To reproduce a data set including the observed spectra from all tangent heights of the limb scan, simulated spectra for 1 km thick atmospheric layers from 45.5 km to 79.5 km are generated using the COSPAR Mars temperature profile shown in Fig. 1.1. The volume emission rate profiles for the Collisional Cascade case considered by *García Muñoz et al.* (2005) are used for these simulations (Fig. 1.2).

For these tests random instrument noise is added to the simulated spectra to assess the sensitivity of the retrieval methods to instrument error effects. The method

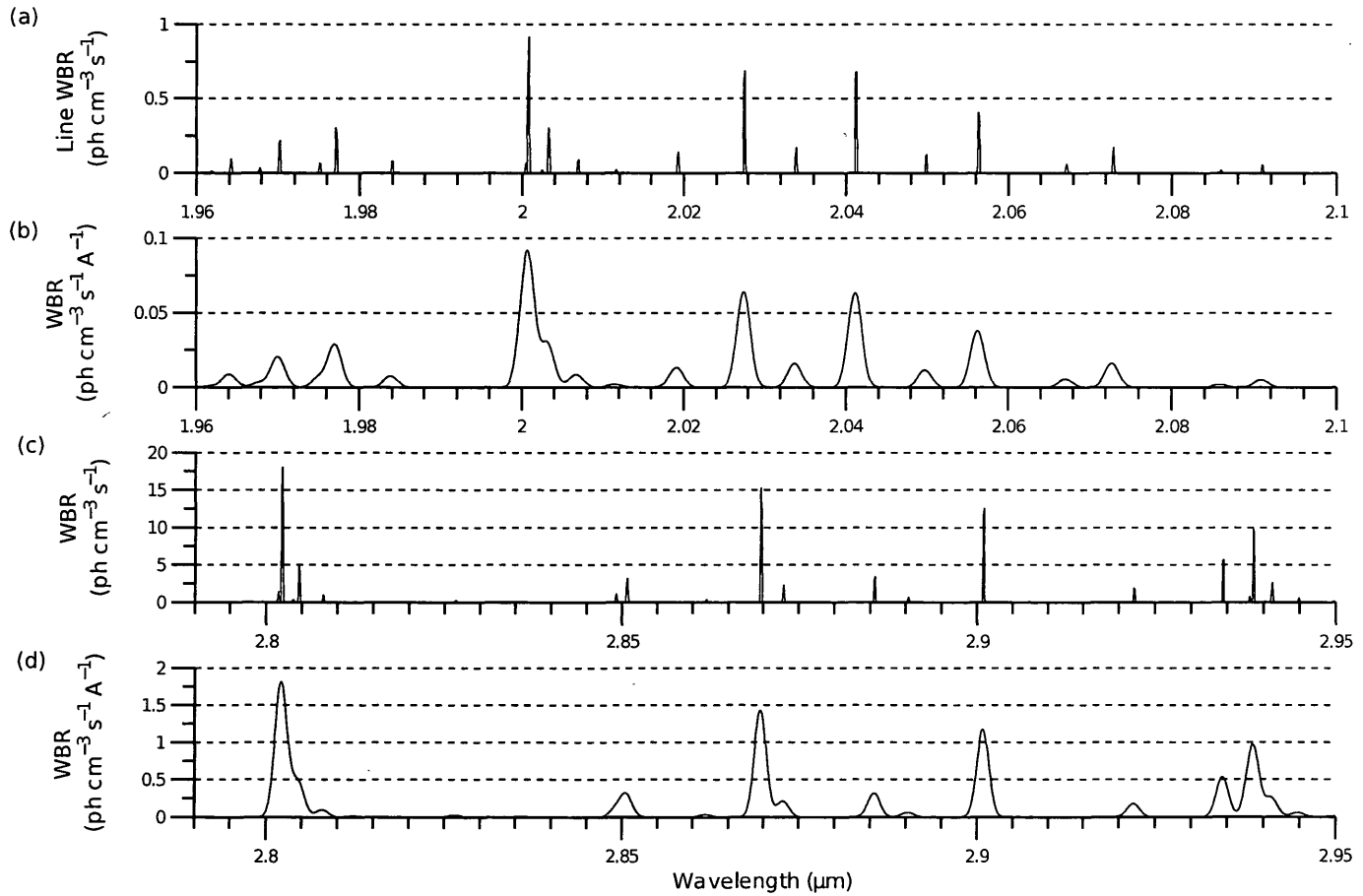

Figure 5.2: Synthetic wavelength bin line radiance spectra of region A and region B at 139 K are shown in (a) and (c). Instrument convolved wavelength bin radiance spectra at 139 K for regions A and B are in (b) and (d).

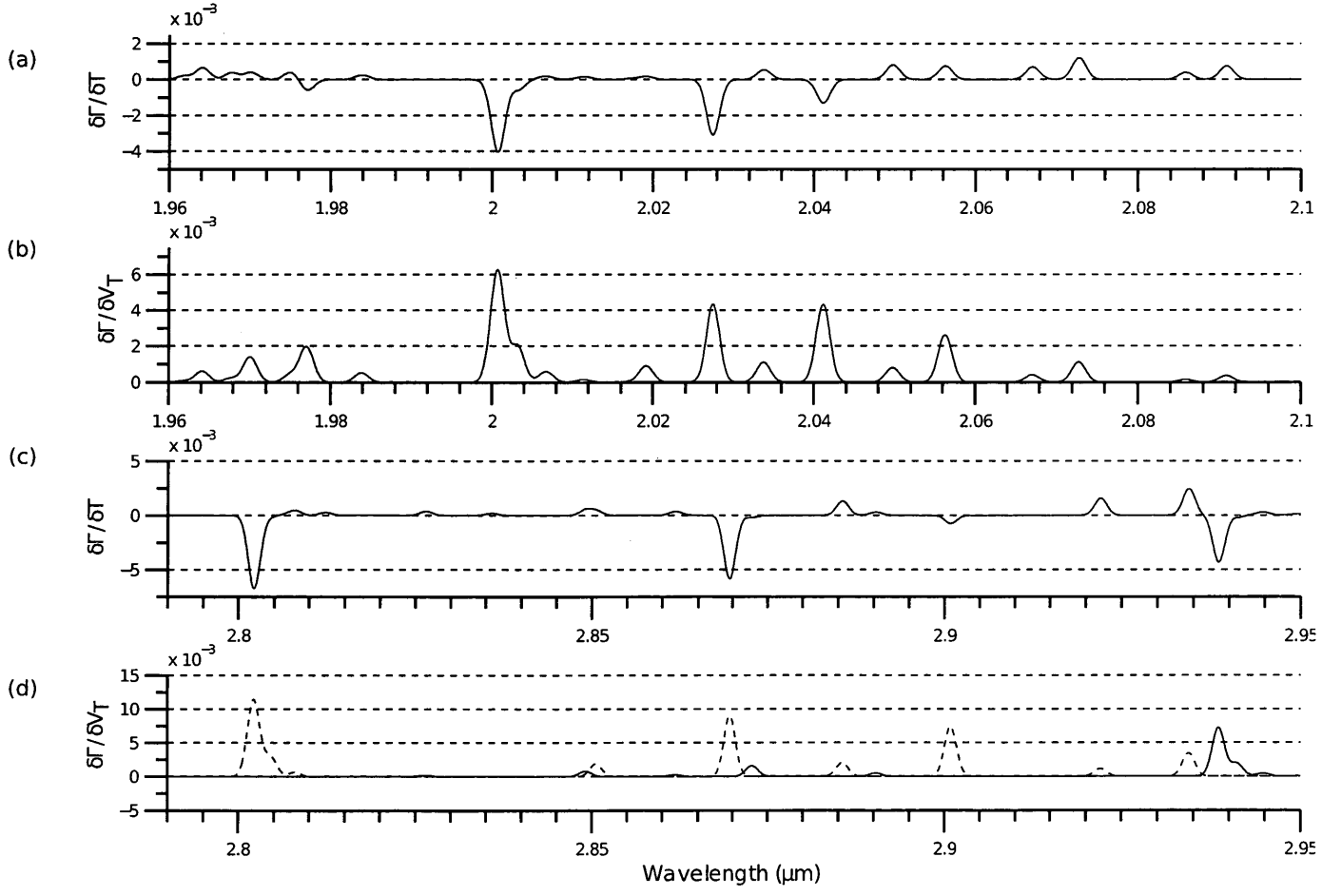

Figure 5.3: Calculated Jacobians for a single layer at 140 K and for VERs of 100 photons s^{-1} cm^{-3} relating convolved limb WBR to the temperature $(\frac{\delta\Gamma}{\delta T})$ for region A in (a) and region B in (c) and relating convolved limb WBR to the volume emission rate $(\frac{\delta\Gamma}{\delta V})$ of $v' = 8$ for region A in (b) and for $v' = 1$ as a dashed line and $v' = 2$ as a solid line for region B in (d).

OH(8-6) band						
N	P1	Q1	R1	P2	R2	Q2
(1)	20276	20008	19772	20193	20005	19840
(2)	20413	20033	19702	20339	20025	19759
(3)	20564	20069	19642	20499	20058	19678
(4)	20729	20116		20672	20103	19619
(5)	20910	20175		20860	20161	
(6)		20245			20232	
(7)		20328			20315	
(8)		20424			20411	
(9)		20533			20520	
(10)		20655			20643	
(11)		20792			20780	
(12)		20943	19624		20932	
(13)			19686			

Table 5.1: Wavelength ($\mathring{A}$) of emission lines within region A (1.96-2.10 μm) in the air.

to simulate instrument noise effects is as follows: two numbers are generated using an intrinsic random number generator (RNG) which returns uniformly distributed numbers between 0 and 1. The RNG is seeded to assure that the same noise profiles and characteristics may be applied to the data set for each of the retrieval methods under test to allow for a more meaningful comparison. The first number determines if the noise is positive or negative and the second, weighed by the desired percent noise, determines the amplitude of the simulated noise. Therefore constructive and destructive noise of random amplitudes between 0 and the desired percent noise is generated. Example of simulated WBR observations with noise at the 25% level for tangent heights 45.5 km, 52.5 km, 59.5 km, 66.5 km, 73.5 km and 79.5 km are shown in Fig. 5.4 and simulated WBR profile at 2 μm without noise and with 25% noise are plotted in Fig. 5.5. Since the noise is uniformly distributed the average

OH(1-0) band						
N	P1	Q1	R1	P2	Q2	R2
(1)	28698	28023		28507	28019	
(2)	29010	28047		28857	28038	
(3)	29345	28081		29222	28071	
(4)		28126			28115	
(5)		28182			28171	
(6)		28249			28239	
(7)		28328			28318	
(8)		28418			28410	
(9)		28521			28513	
(10)		28636			28628	
(11)		28762			28755	
(12)		28902			28895	
(13)		29054			29047	
(14)		29219			29213	
OH(2-1) Band						
N	P1	Q1	R1	P2	Q2	R2
(1)		29387	28729		29382	28904
(2)		29413	28492		29403	28620
(3)		29450	28266		29438	28359
(4)		29498	28052		29486	28121
(5)						27903

Table 5.2: Wavelength ($\AA$) of emission lines within region B (2.79 and 2.95 μm) in the air.

amount of noise will be approximately 12.5% of the signal when 25% noise is added to a spectrum.

In the following sections the performance of the retrieval methods in each mode for the selected spectral regions is assessed by analyzing 10 independent random noise realizations at each noise level. In Fig. 5.6 the total root mean square error of the recovered temperature profiles with respect to the truth is plotted against the number of realizations. Unless otherwise mentioned the root mean square (RMS) error refers to the RMS error with respect to the assumed truth. The recovered temperature profile from the first realization includes significant error, however successive more successful retrievals mitigate the initial RMS error causing the total RMS error to decrease and become more stable. At 10 realizations the total RMS error has plateaued at an RMS error value still affected by the initial poor retrieval. As the number of realizations increases further the effect of a bad retrieval diminishes. The cumulative standard deviation of the recovered temperature profiles, also shown in Fig. 5.6, does not vary significantly with the number of realizations. Therefore, a total of 10 realizations is deemed adequate for a comprehensive evaluation, as the effects of the initial bad retrieval are not yet completely mitigated nor is the total RMS falsely exaggerated by a single bad retrieval.

For the sake of comparison, a recovered temperature is deemed to be accurate if its RMS error is less than 5 K. During preliminary analysis it was found that a temperature retrieval with random noise error of less than 5 K usually coincided with the VER retrieval within 15% of the true VER, ergo an accuracy requirement of 15% is set for volume emission rates.

For the following simulations the *a priori* profile of the parameters to be recov-

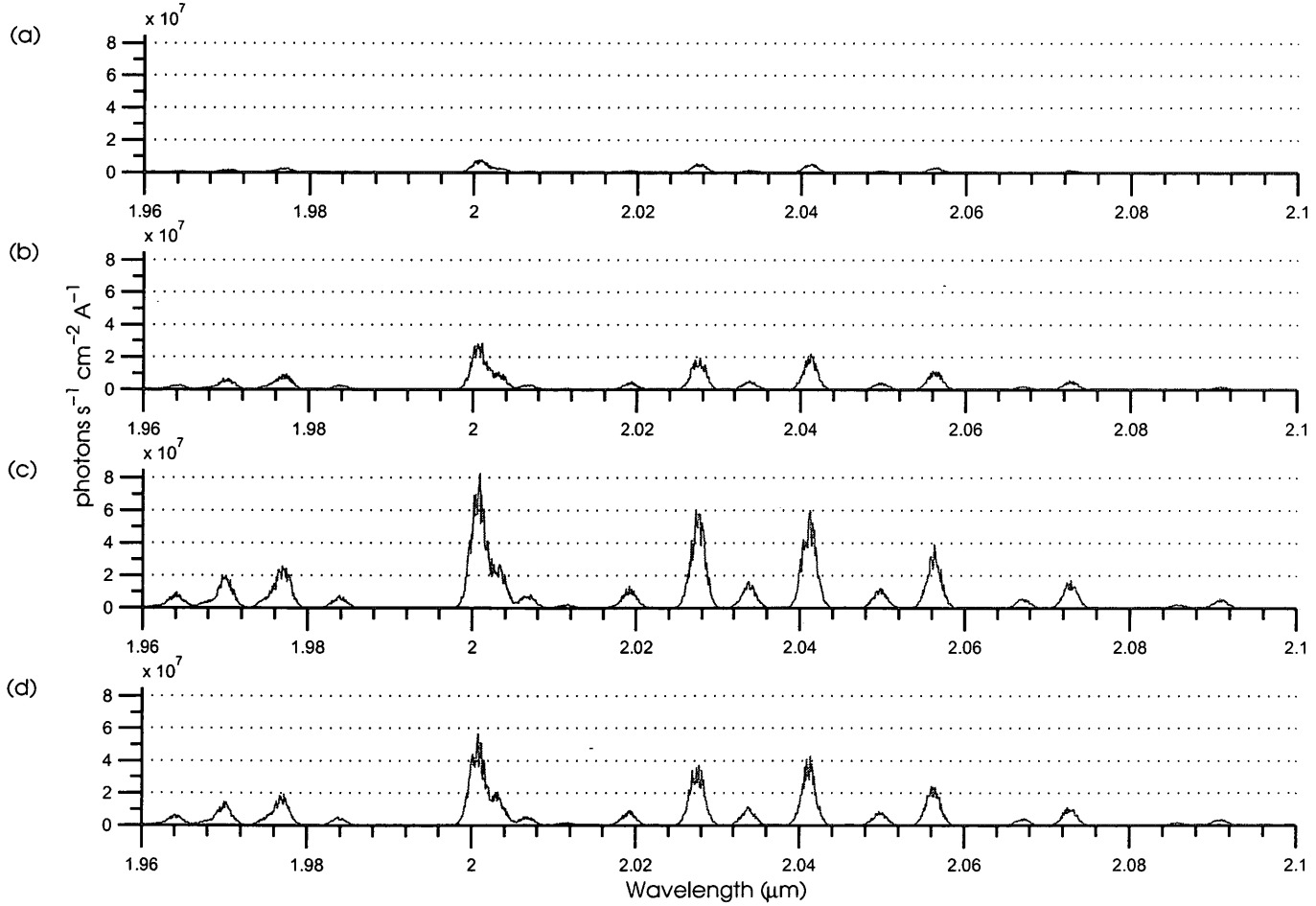

Figure 5.4: Example of simulated limb WBR spectra for region A with 25% noise for tangent heights (a) 74.5 km, (b) 67.5 km, (c) 57.5 km, (d) 47.5 km.

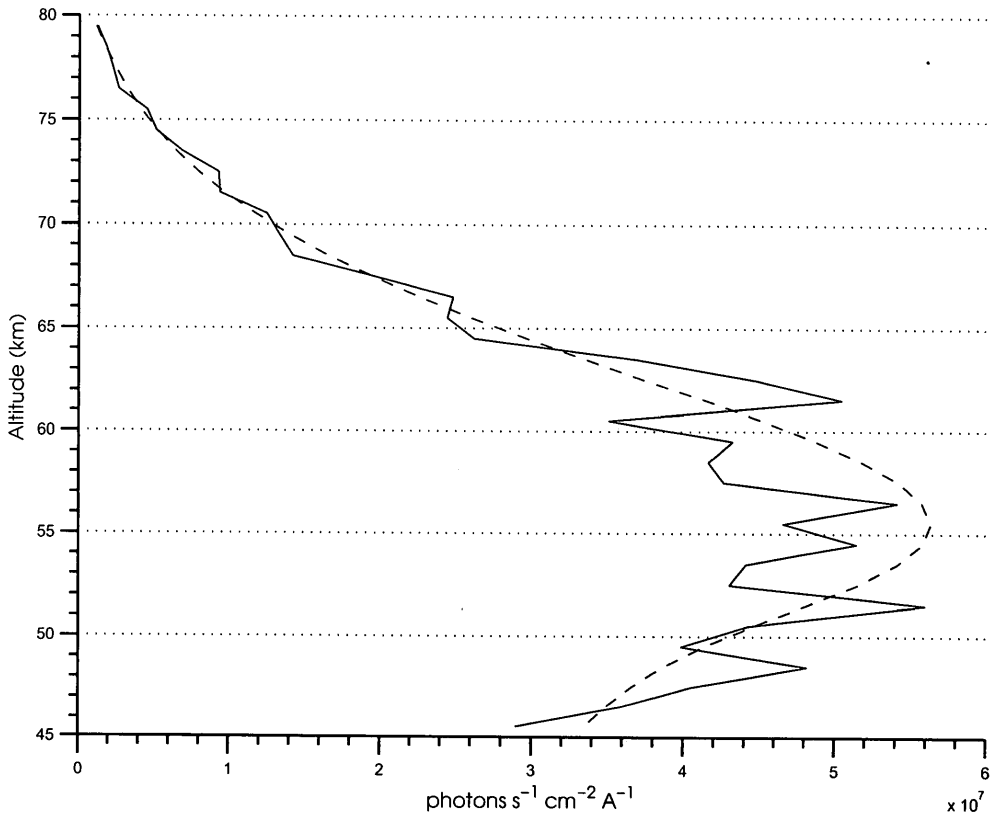

Figure 5.5: Example of simulated wavelength bin radiance profile at 2 μm without noise (black dashed line) and with 25% noise (solid black line).

ered is chosen to be 70% of the true profile and the confidence in this value is $\pm$100% to reduce the effect of the *a priori* on the recovered parameters. The measurement error is dependent on the error level assigned to the simulation, save for the noiseless case where the error variance is set to 1%. The error on a measurement of 0 is always 0.001 photons cm^{-3} s^{-1}. For these simulations both the *a priori* confidence and the measurement error are treated as uncorrelated. The instrument function is chosen to be a Gaussian with a half width of 20$\mathring{A}$ and the sampling interval is set at 1$\mathring{A}$. Ten synthetic full limb scan observations, *i.e.*, synthetic WBR spectra for all tangent heights, were generated for the noise levels ranging from 0 - 50% at

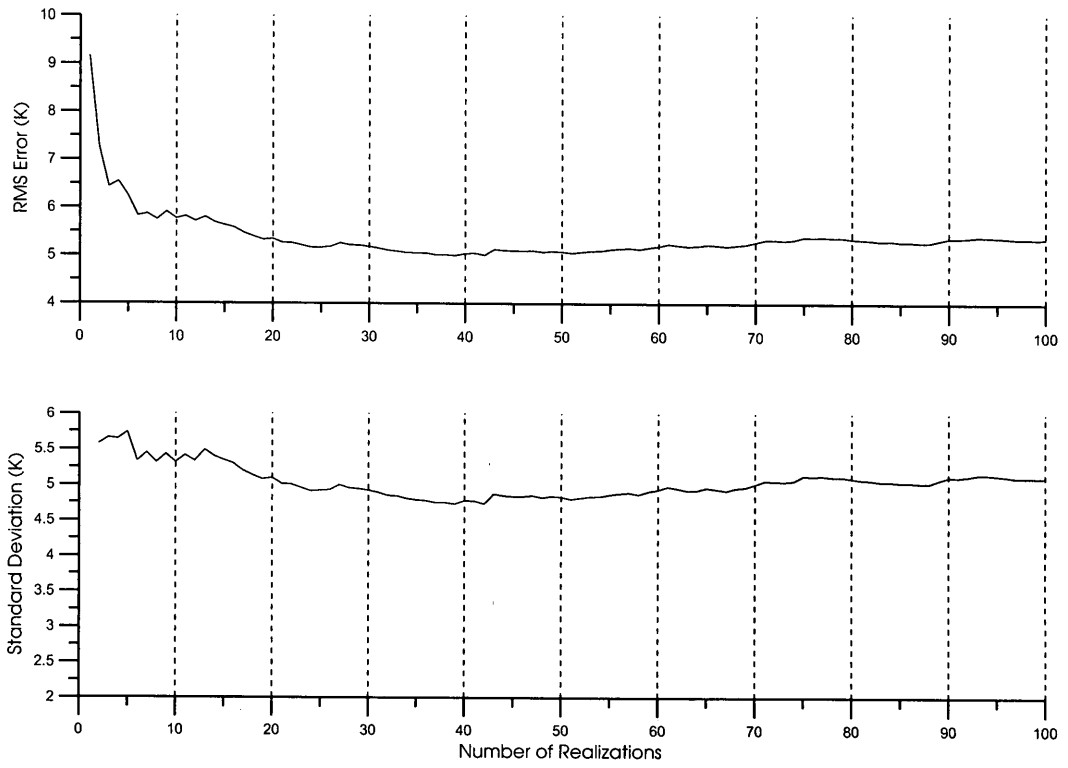

Figure 5.6: In the upper panel the cumulative root mean square error of recovered temperature profiles from synthetic observations with 25% noise using the Global Optimization plotted against number of realizations. In the lower panel the standard deviation of the recovered temperature profiles are plotted against the number of realizations.

5% intervals for each region to be used for the retrieval method testing.

5.3 Onion Peeling Simulations

The Onion Peeling method fits the generated spectrum to the synthetic observed spectrum within a given spectral window from each tangent height downward sequentially from the top of the emitting layer. As previously discussed. this retrieval method produces a downward propagation of error and therefore it is expected that

the most accurate retrievals will occur at the top of the OH Meinel airglow layer and that the recovered parameters will become increasingly prone to error in the subsequent heights below. Also, due to the sequential nature of the recovery algorithm, large oscillations in recovered quantities are expected between the more error prone heights, *i.e.*, below the peak, as the parameters at each height are recovered individually with no smoothing between the layers.

5.3.1 Case 1: Temperature Recovery with Knowledge of VERs using the Onion Peeling approach

The results of the temperature profile retrieval using the Onion Peeling method with knowledge of the volume emission rate profiles used to create the simulated data are summarized in the following figures.

The first figure, Fig. 5.7, shows the recovered temperature profiles for the 10 different input simulations generated with the same overall percent level of noise but different random distributions at noise levels from 0% to 25%. The recovered profiles from region A (1.96-2.10 μm) and region B (2.79 and 2.95 μm) follow a similar trend. The retrieval from the noiseless set of simulated observations results in recovered profiles almost identical to the true profile. When the Onion Peeling method is used to recover temperatures from simulated input with noise, the retrievals for the lowest heights, *i.e.*, the heights with weak VER below the peak, become scattered with some dependance on the *a priori* temperatures. As the amount of noise increases, this effect spreads to higher heights eventually throughout the entire profile. In the stable area of the recovered profiles, namely the region where the profiles converge which usually correlates to the most accurate retrievals, there

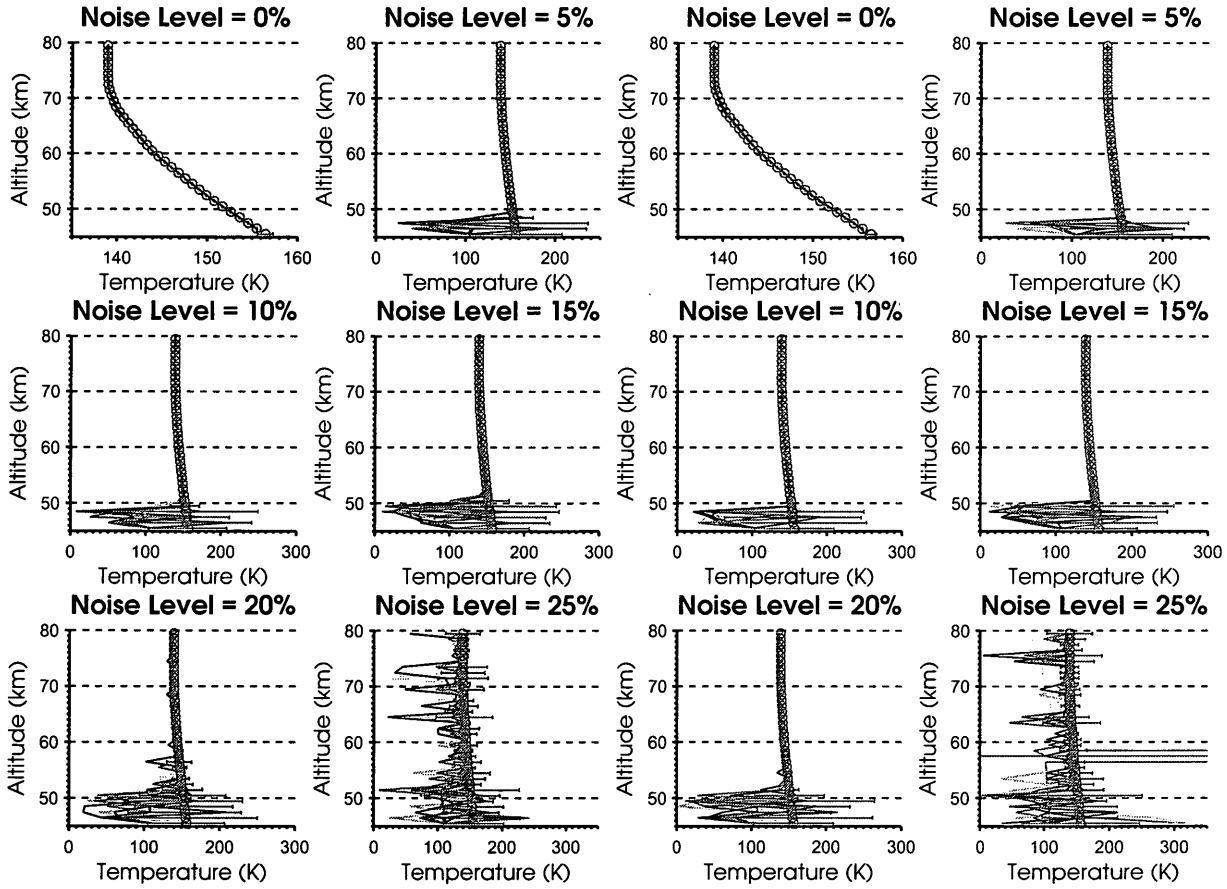

Figure 5.7: Case 1: Recovered temperature profiles from 10 simulated limb observed WBR spectra for noise levels ranging for 0-25% for region A in the two left columns and region B in the two right columns. The red circles represent the true temperatures and the red error bars indicate the root mean square error of the 10 recovered temperatures from the true temperature for the given height which are for convenience plotted on the true profile. In the plot of profiles recovered at the 25% noise level from spectral region B, one recovered temperature for the 57.5 km height level falls well beyond the scale of the plot and is consequently not shown. The associated RMS error also spans beyond the scale of the plot.

is an absence of significant oscillation. However in the unstable region, the range in temperatures broaden with increasing noise level indicating an increase in error in the recovered temperatures. At 25% the errors throughout the recovered profile exceed the 5 K target and the oscillations in the profile become more severe. Finally, for noise levels of 30% and beyond, not shown in Fig. 5.7, the retrieval method fails to recover temperatures with sufficient accuracy. The recovered temperatures oscillate with no apparent correlation with the true temperature profile.

Figure 5.8 is a pixel plot of the root mean square error in K of the recovered temperatures for the 10 random realizations for both spectral regions. The increase in the recovered error, the spread of the instabilities from the bottom of the airglow layer to higher heights with increasing noise, and the breakdown of the method above a noise level of 25% are evident. The height ranges of retrievals which meet the accuracy requirements (*i.e.*, with RMS error less than 5 K) are indicated by the white line and are also listed in Table 5.3 along with the total root mean square error of the temperatures recovered within the height ranges.

	Region A		Region B	
Noise Level	Height Range (km)	RMS (K)	Height Range (km)	RMS (K)
0 %	45.5 - 79.5	0.14	45.5 - 79.5	0.03
5 %	49.5 - 79.5	0.46	48.5 - 79.5	0.57
10%	50.5 - 79.5	0.78	49.5 - 79.5	0.80
15%	51.5 - 79.5	1.58	50.5 - 79.5	1.47
20%	57.5 - 79.5	2.58	52.5 - 79.5	2.67

Table 5.3: Case 1: Height range of recovered temperatures with RMS error less than 5 K and root mean square error for temperatures within height range.

Although the range of accurate temperatures of region B at 20% is greater than that of region A, this is due to a single temperature recovered for region A at a

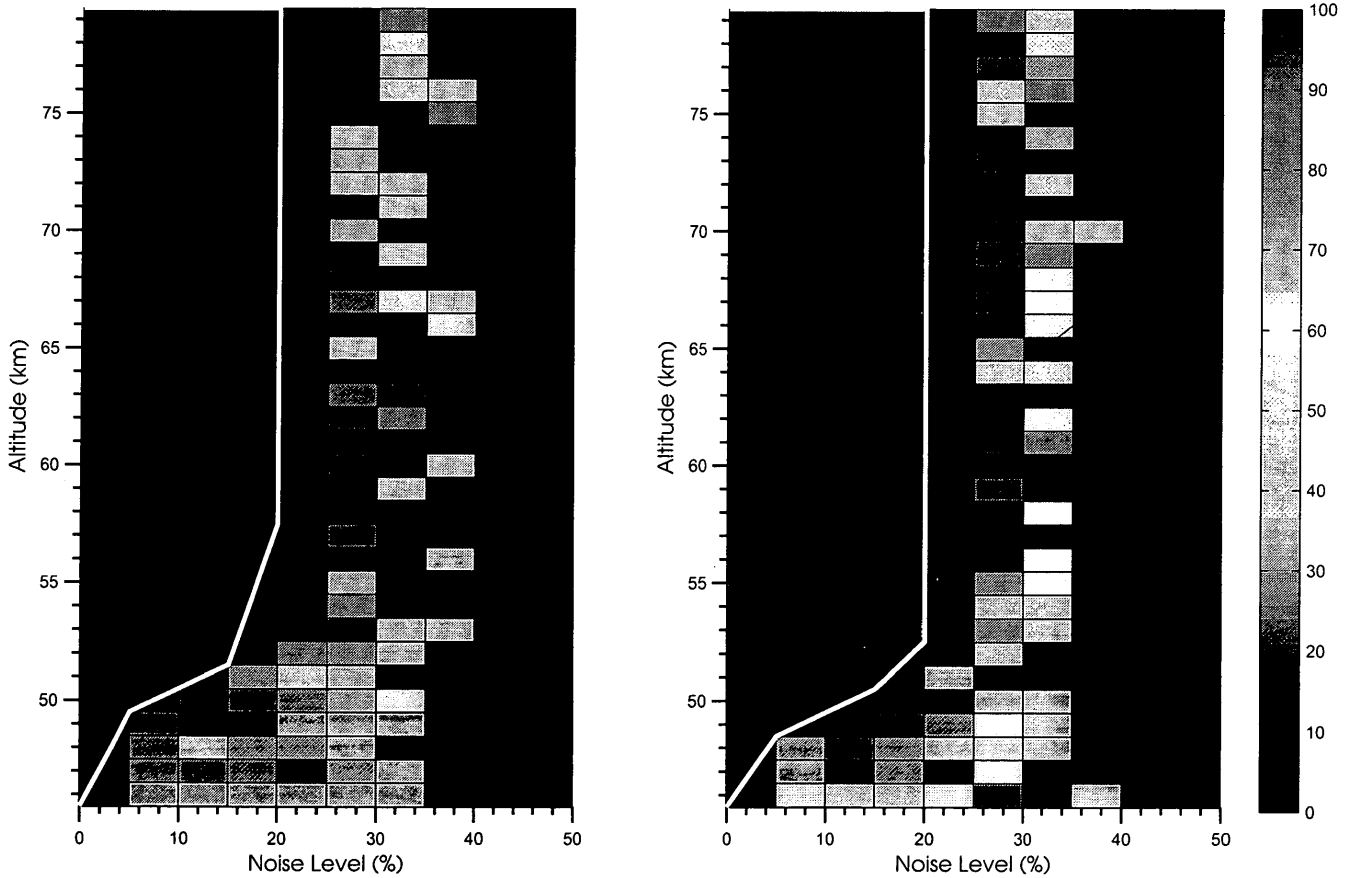

Figure 5.8: Case 1: Pixel plot of the root mean square error of the temperatures recovered from the 10 simulated limb observations with noise levels ranging from 0-50%. The plot of RMS error of the recovered profiles from spectral region A is shown in the left panel and from spectral region B is shown in the right panel. The white line delineates the height ranges where the RMS error is less than 5 K. The units of the colour scale are in Kelvin.

height of 56.5 km failing to improve upon the *a priori* temperature. All other retrieved temperatures errors at this height for region A are below 5 K. Thus the effectiveness of the retrieval method in both spectral regions are essentially comparable. This follows as even though region B contains lines from bands from two different vibrational levels, since the emission rates of both these levels are provided, the Levenberg-Marquardt optimization method is fitting a single parameter at each height for the retrieval in both of the spectral regions. Thus the number of bands should have no effect on the retrieval.

5.3.2 Case 2: Volume Emission Rate Recovery with Knowledge of Temperatures using the Onion Peeling approach

In this section the results of retrieval of volume emission rates from the data sets generated for the various noise levels using the Onion Peeling method will be discussed. The true temperature profile is provided making the VERs the only unknown parameters.

In Fig. 5.9 the recovered volume emissions rates profiles from the simulated data sets with 0%, 15% and 25% noise for the OH(8-6) band of region A and the OH(1-0) and OH(2-1) bands of region B are compared. Unlike the temperature retrieval the recovered profiles from region A and B differ, which is expected as in region A the method recovers a single parameter per height and in region B the method recovers two parameters at each height. In both regions the VER profiles recovered from noiseless data are nearly identical to the true profile. At the 15% noise level the RMS error increases as the recovered emission rates are slightly offset negatively from the true rates. The cause for this offset will be discussed in

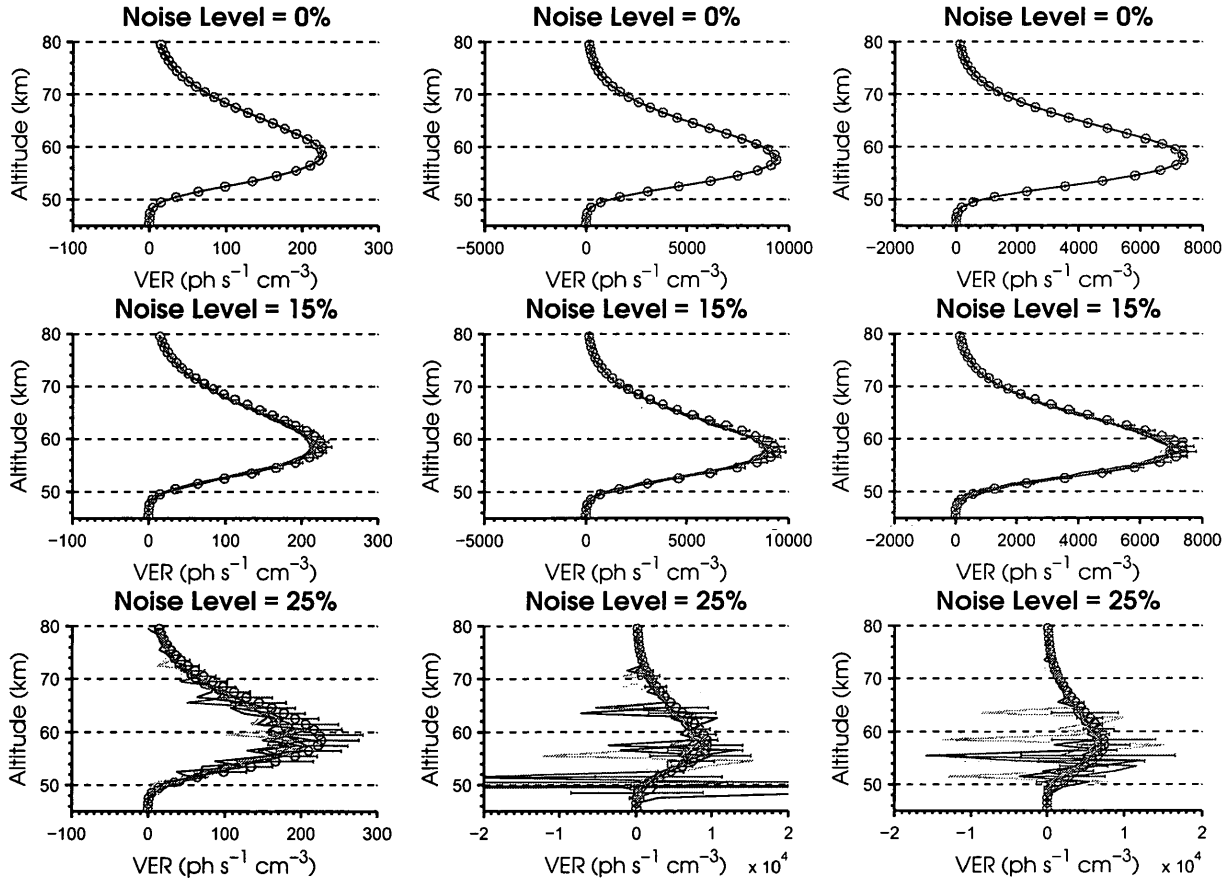

Figure 5.9: Case 2: Recovered volume emission rate profiles from 10 simulated limb observed spectra for noise levels of 0%, 15% and 25% for $v' = 8$ recovered from spectral region A in the left column and for $v' = 1$ and $v' = 2$ recovered from spectral region B in the middle and rightmost columns respectively. The red circles are the true volume emission rates and the red error bars indicate the root mean square error of the 10 volume emission rates recovered for the given height. VERs for $v' = 1$ recovered from two realizations in region B with noise level of 25% fall beyond the scope of the plot between 46.5-51.km.

Section 5.3.3. Finally, at the 25% level in VERs recovered from region A the offset and consequently the RMS percent error increases, beyond the 15% error threshold and medium scale oscillations are present throughout the profile. Large oscillations in the recovered VERs and a lack of stability occur in the recovered VER profiles from the simulated data with 25% noise from region B. These oscillations are more apparent in the peak of the emission layer, but are present throughout. The size of the oscillations are proportional to the VER, thus for smaller emission rates the oscillations are less obvious. In some cases the oscillations in the recovered emission rates for the (1-0) band correlate with oscillations in the recovered rates of the (2-0) band, but in many cases there is no relationship. This lack of correlation is to be expected as the only significant overlap between these two bands in the given spectral region occurs near 2.85 μm and these lines are relatively weak. The wings of a few other lines also overlap but again the intensity is very weak. Therefore the bands are essentially separate and thus no strong correlation in the retrieval errors is expected.

In the RMS percent error pixel graphs, shown in Fig. 5.10, the slight spread of error from the bottom of the layer upwards is evident. Also the breakdown of the method for error levels beyond 20% is also visible. In region A the root mean square error of the recovered VER beyond the 35% noise level is 30% which indicates that in many cases the retrieval method is unable to improve upon the initial guess, *i.e.*, the *a priori*. This is preferable to the large oscillating errors of region B as recovering the *a priori* clearly signifies that the retrieval was unsuccessful. In region B, however, the error at these noise levels far exceed 30% which further suggests the lack of stability noted at the 20% noise level. The ranges of accurate VER

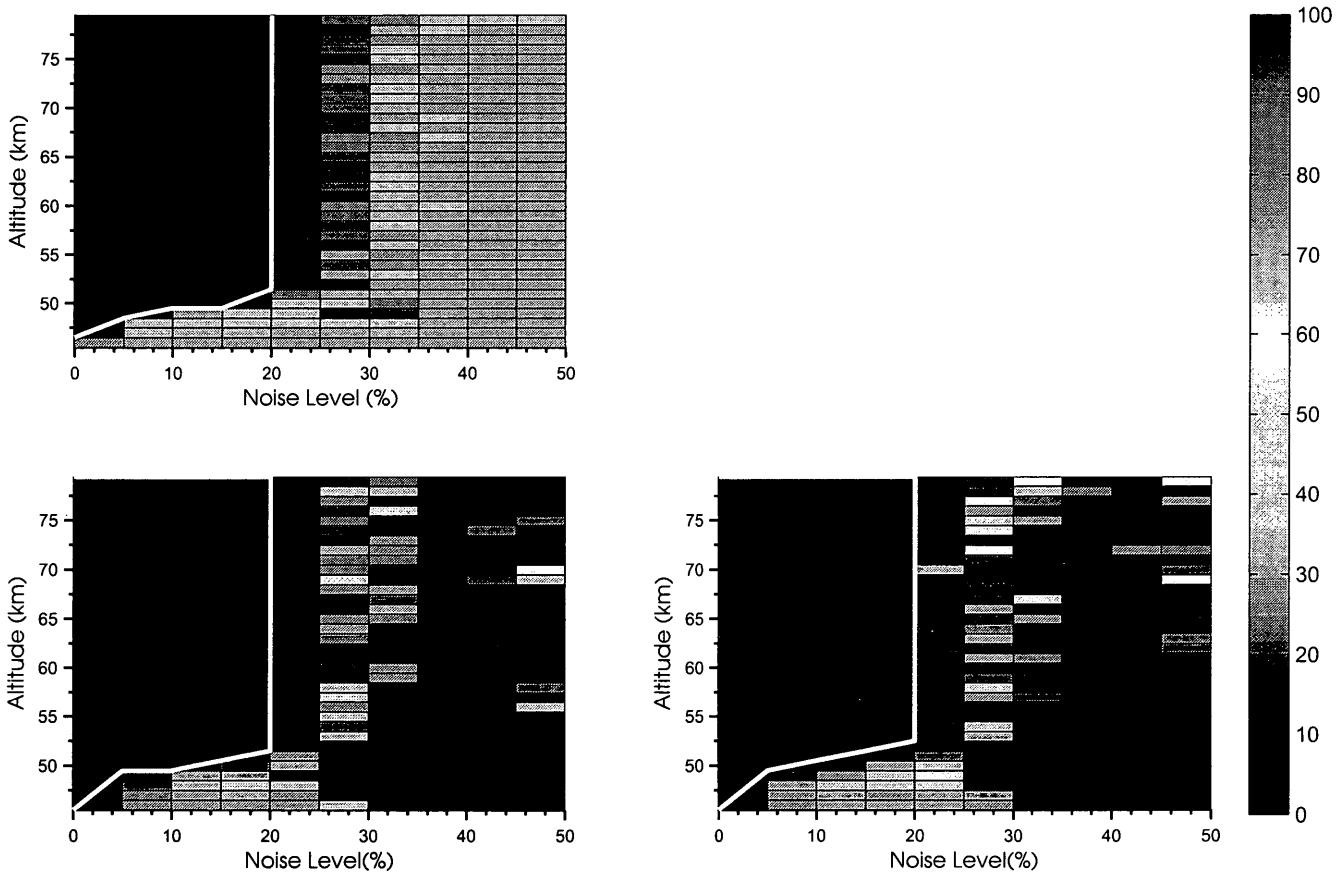

Figure 5.10: Case 2: Pixel plot of the percent root mean square error of the volume emission rates recovered from the 10 simulated limb observations with noise levels ranging from 0 - 50%. The percent RMS error of the $v' = 8$ volume emission rates retrieved from spectral region A are shown on in top panel and the percent RMS error of the $v' = 1$ and $v' = 2$ volume emission rates recovered from spectral region B are shown on the left and right of the bottom panel. The white line delineates the height ranges where the percent RMS error is less than 15%. The units of the colour scale are in percent.

retrievals, shown in Table 5.4, are nearly identical for the $v' = 8$ case in region A and the $v' = 1$ and $v' = 2$ cases in region B.

	Region A $v = 8$		Region B $v = 1$		$v = 2$	
Noise level	Height Range (km)	RMS (%)	Height Range (km)	RMS (%)	Height Range (km)	RMS (%)
0 %	46.5 - 79.5	0.02	45.5 - 79.5	0.51	45.5 - 79.5	0.69
5 %	48.5 - 79.5	1.95	49.5 - 79.5	1.38	49.5 - 79.5	1.15
10%	49.5 - 79.5	2.76	49.5 - 79.5	2.81	50.5 - 79.5	2.71
15%	49.5 - 79.5	5.91	50.5 - 79.5	5.35	51.5 - 79.5	4.91
20%	51.5 - 79.5	9.21	51.5 - 79.5	9.14	52.5 - 79.5	10.61

Table 5.4: Case 2: Height range of recovered volume emission rate retrievals with less than 15% error and root mean square percent error of VERs within the height ranges.

In the presence of significant amounts of noise the recovered VER profiles from emission lines from more than one v' level lack stability. However within the 0 - 20% range, where the Onion Peeling method recovers emission rates within the error tolerance, there seems to be no disadvantage to recovering the VERs from both v' simultaneously when compared to the recovered VER profiles from a single v' level, *i.e.*, the retrieved VER profiles from spectral region A.

5.3.3 Case 3: Simultaneous Temperature and Volume Emission Rate Recovery using the Onion Peeling approach

The results of the simultaneous retrieval of temperatures and volume emission rates realizations using the Onion Peeling retrieval method are discussed in this section.

In Fig. 5.11 the ten recovered temperature profiles are shown along with the root mean square error of the recovered temperatures from the true temperature

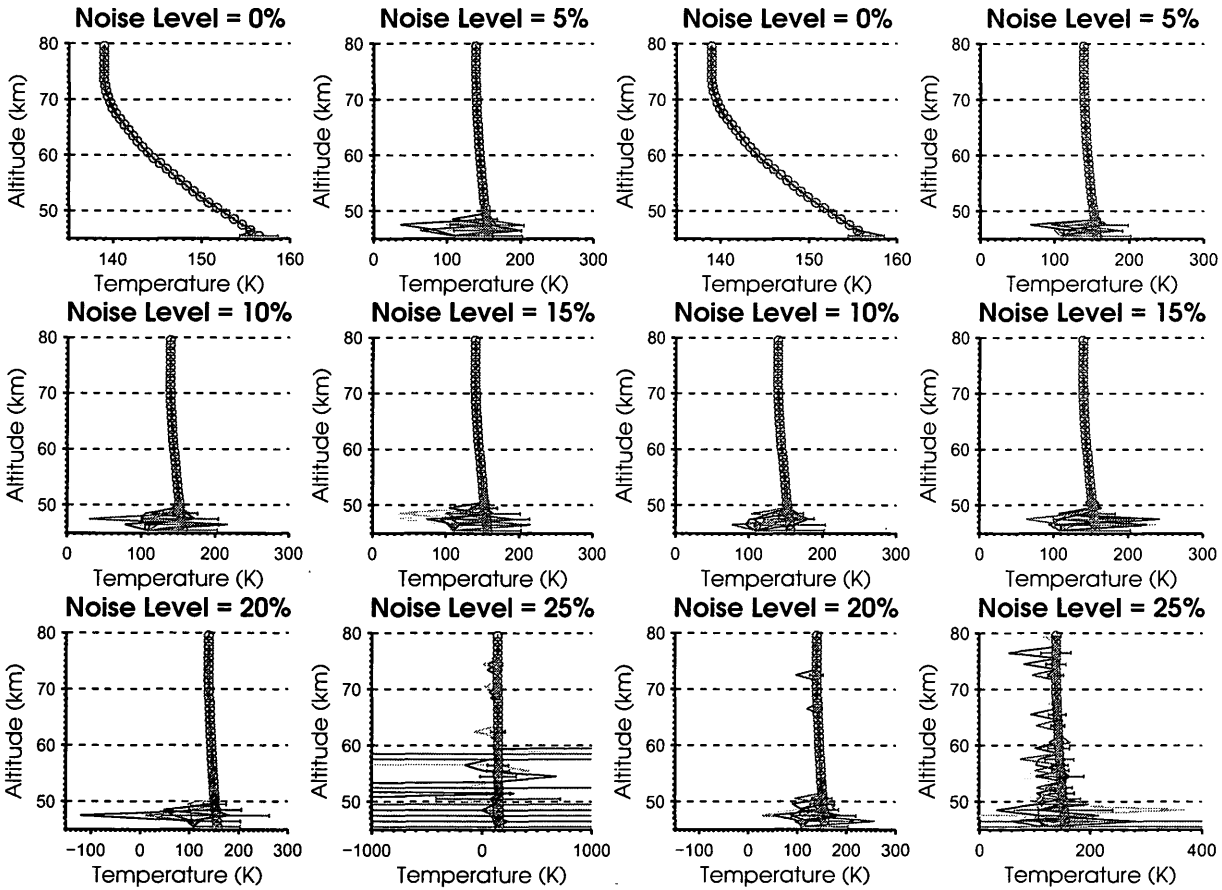

Figure 5.11: Case 3: Temperature profiles recovered while simultaneously retrieving volume emission rates from the 10 simulated limb observed spectra with noise levels ranging for 0 - 25%. The temperatures recovered from spectral region A are shown in leftmost two columns and from spectral region B in the rightmost two columns. The red circles indicate the true temperatures and the red error bars indicate the root mean square error of the 10 temperatures recovered at that height. In the plot of profiles recovered at the 25% noise level from both spectral regions A and B some data points were truncated and the associated RMS errors for these heights are also truncated.

at each height for noise levels between 0 and 25%. The recovered profiles for both regions are near identical to the true profile for the noiseless cases save for the bottom layer where the error in the recovered temperatures is approximately 2 K. This error is caused by the minor errors throughout the profile compounding, as the recovery at the bottom height uses the weighted sum of the spectra generated based on the recovered temperatures of the upper height levels to determine the spectral contribution of this final layer. Since the emission of this lowest height level is relatively weak these minor errors cause some inaccuracy in the calculated convolved WBR spectrum which in turn causes the recovered temperature to be in error.

For recovered temperature profiles from data sets with noise levels between 5 - 15% there is a similar spread in the retrieved temperatures at the bottom of the OH Meinel airglow layer as noted for Case 1. The range is wider for temperatures retrieved from spectral region A than from spectral region B. Minor oscillations throughout the profiles begin to appear at 20% in addition to a continued increase the range of recovered temperatures at the lower heights.

In the plot of temperatures recovered from synthetic observations of region B with 20% noise there are notable errors at 72.5 km and 66.5 km in one recovered profile (also shown in Fig. 5.15 (d)). At the 72.5 km height level the retrieval method is not able to improve upon the initial temperature or the initial VER. The VERs recovered from the subsequent height levels are more accurate but differ from stability by approximately the same amount as the initial error. As for the recovered temperatures, there is another unexpectedly large error at the 66.5 km height which is likely a consequence of the previous error. Additional simulations

were run for similar scenarios, *i.e.*, where a retrieval method fails to improve upon the initial guess, to gauge the effect on the retrievals of the subsequent heights. Although in some cases there was no discernible impact, in most cases there was at least one other aberrant retrieval. There was no obvious connection between the 'failed' retrieval and the erroneous retrieval. This suggests that the retrieved parameters following a 'failed' retrieval are unreliable and should be disregarded.

Finally at the 25% noise level in both regions, many recovered temperatures approach the true temperatures, however there is little consistency and thus the recovered profiles are not reliable. When recovering from a noisy data set the Onion Peeling method in this mode will often fail to improve upon the initial guess temperature, but again without any consistency.

In Fig. 5.12 the volume emission rate profiles from 10 realizations at the 0%, 15% and 25% noise levels along with the root mean square percent error at each height level are shown. Similarly to the temperature retrieval described above the recovered VERs for the noiseless case of region A and both bands of region B are near perfect, except for the 45.5 km height where the RMS error is between 10-15%. The cause of the error in the VER recovered from the lowest level are consistent with those previously mentioned. At the 15% noise levels, for all three bands, there is an increase in the range in the recovered VERs at each height which, although seeming more pronounced at the higher VERs, is approximately proportional to the VER. Again at 25% there is little difference in the recovered VERs of the three bands: the majority of the recovered VERs are offset from the true values and lie somewhere between the true VER and the *a priori*. However, a small fraction of the recovered VERs exceed the true emission rate value and others are below the

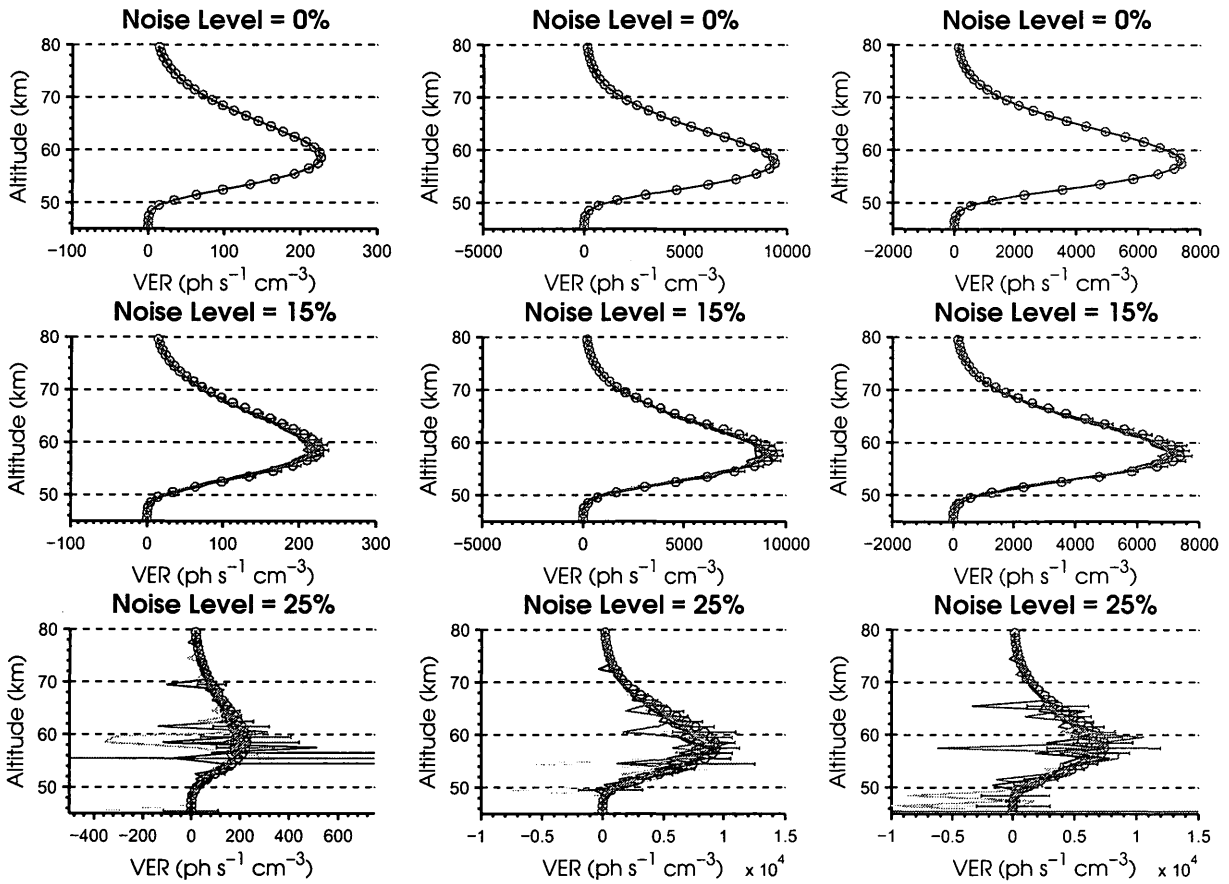

Figure 5.12: Case 3: Volume emission rate profiles recovered while simultaneously recovering temperatures from 10 simulated limb observed spectra for noise levels for 0%, 15% and 25% for $v' = 8$ recovered from spectral region A in the left column and for $v' = 1$ and $v' = 2$ recovered from spectral region B in the middle and right columns respectively. The red circles are the true VERs at each height and red error bars indicate the root mean square percent error of the 10 volume emission rates recovered for the given height. Note the change of scale at the 25% noise level. Some recovered VERs are truncated due to the plot scale.

a priori value, even negative.

Fig. 5.13 and Fig. 5.14 are the average temperature error and average VER percent error pixel plots for the 10 realizations of the Onion Peeling retrieval methods for noise levels between 0% and 50%. The pixel plots are very similar to those of temperature retrieval of Case 1 and the VER retrieval of Case 2: a gradual increase in error from the heights with weak emission below the peak spreading upwards as the noise level increases. At the 25% error level the errors exceed the set accuracy limit and the oscillations in the profile are more pronounced. For noise levels of 30% and beyond the recovered profiles are very unstable and are very inaccurate.

The height ranges of retrieved parameters that meet the accuracy requirements of 5 K for temperatures and 15% for volume emission rates for region A and B are given in Table 5.5 and Table 5.6. The tables also list the the root mean square error for all temperatures and volume emission rates recovered within their respective height ranges. The height ranges of accurate temperature retrievals for region A and B do not differ by more than 1 km, nor do they differ from height ranges of accurate volume emission rates by more than 1 km. The height ranges are also very similar to the height ranges determined for the VER retrieval of Case 2 and slightly larger than the temperatures height ranges determined for Case 1. This suggests that the simultaneous retrieval is just as, or even more, accurate than the individual retrieval of VERs and temperatures particularly since it would be unlikely that the modeled VER or the measured temperatures required for the retrievals of Cases 1 and 2 would be without error. In addition these results suggest that there is no disadvantage when using the Onion Peeling method, in retrieving volume emission rates and temperatures from a spectral region containing bands of more than one

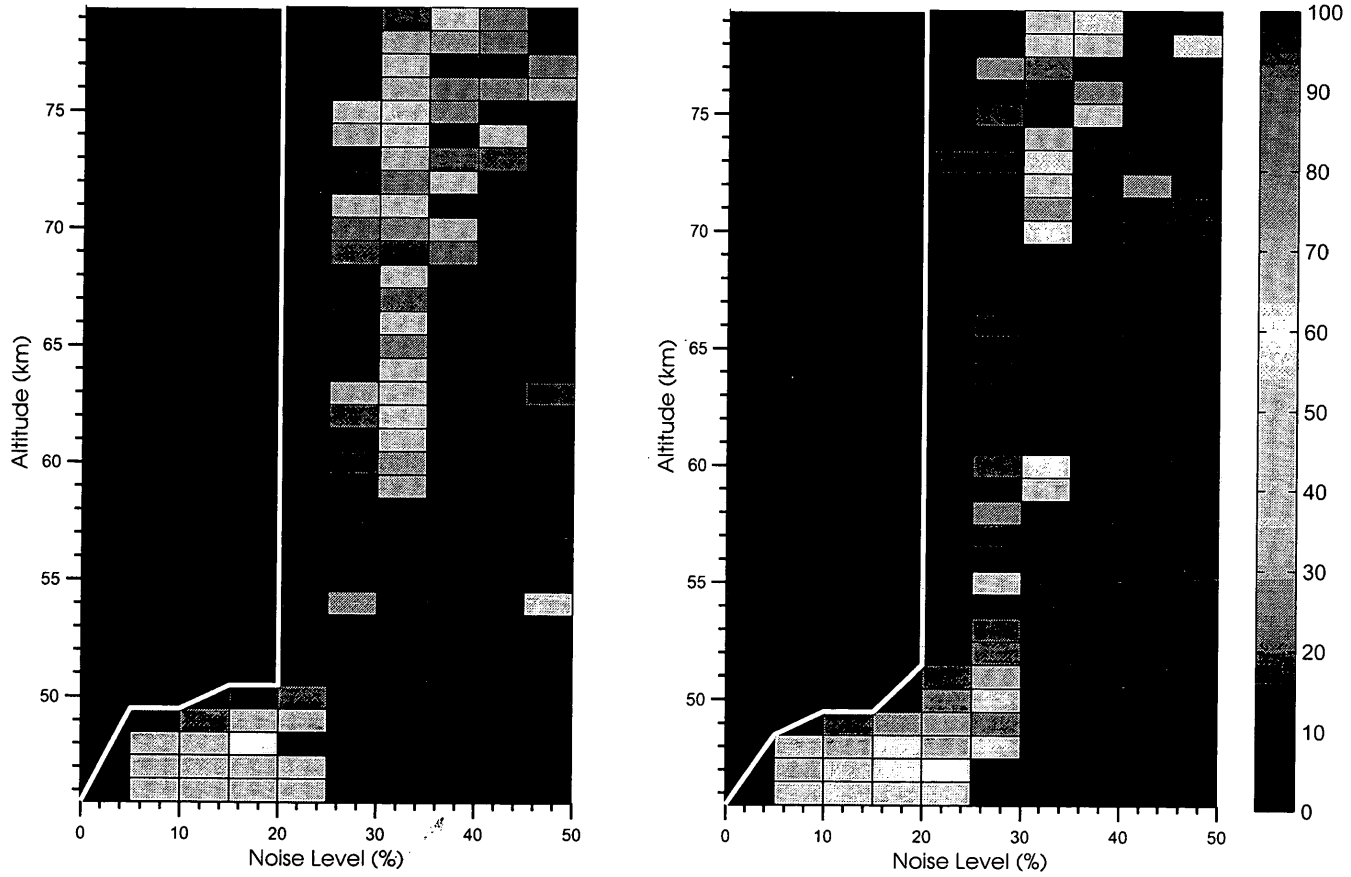

Figure 5.13: Case 3: Pixel plot of the root mean square error of the temperatures recovered simultaneously with volume emission rates from the 10 simulated limb instrument degraded WBR spectra with noise levels ranging from 0 - 50%. RMS error of profiles recovered from spectral region A is shown on the left and from spectral region B is shown on the right. The white line delineates the height ranges where the RMS error is less than 5 K. The units of the colour scale are in Kelvin.

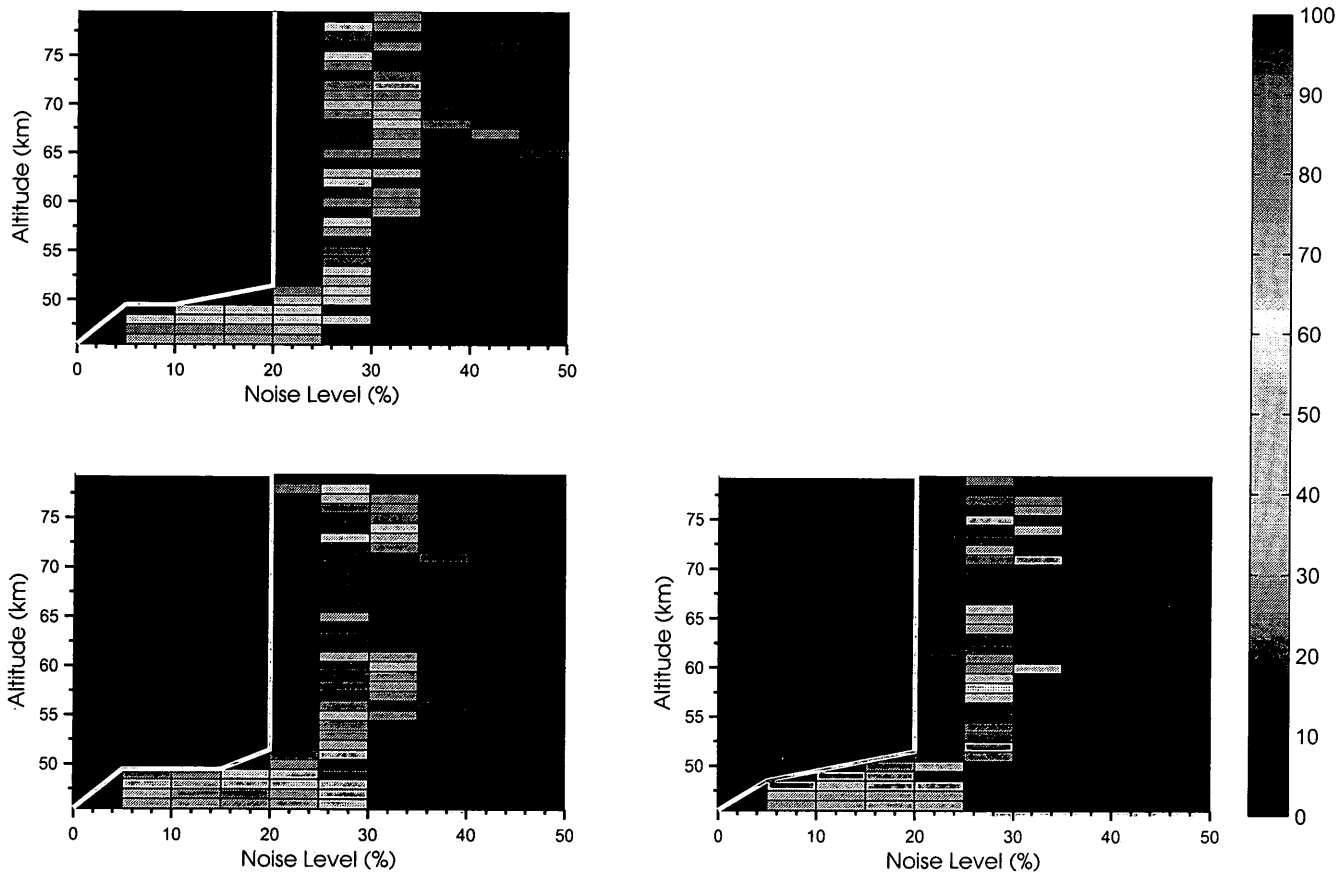

Figure 5.14: Case 3: Pixel plot of the percent root mean square error of the volume emission rates recovered simultaneously with temperatures from the 10 simulated limb observations with noise levels ranging from 0 - 50%. The percent RMS errors of the $v' = 8$ volume emission rates retrieved from spectral region A are shown on in top panel and the percent RMS error of the $v' = 1$ and $v' = 2$ volume emission rates recovered from spectral region B are shown on the bottom left and bottom right panels, respectively. The white line delineates the height ranges where the percent RMS error is less than 15%. The units of the colour scale are in percent.

v'.

	Region A		Region B	
Noise Level	Height Range (km)	RMS (K)	Height Range (km)	RMS (K)
0 %	45.5 - 79.5	0.37	45.5 - 79.5	0.11
5 %	49.5 - 79.5	0.59	48.5 - 79.5	0.76
10%	49.5 - 79.5	0.98	49.5 - 79.5	0.80
15%	50.5 - 79.5	1.04	50.5 - 79.5	1.51
20%	50.5 - 79.5	1.78	51.5 - 79.5	2.96

Table 5.5: Case 3: Height ranges of temperature retrievals accurate to within 5 K and total root mean square error for temperatures within these height ranges.

	Region A $v = 8$		Region B $v = 1$		Region B $v = 2$	
Noise Level	Height Range (km)	RMS (%)	Height Range (km)	RMS (%)	Height Range (km)	RMS (%)
0 %	45.5 - 79.5	0.02	45.5 - 79.5	0.65	45.5 - 79.5	0.75
5 %	49.5 - 79.5	1.54	49.5 - 79.5	1.26	48.5 - 79.5	2.82
10%	49.5 - 79.5	2.86	49.5 - 79.5	3.40	49.5 - 79.5	3.45
15%	50.5 - 79.5	5.31	49.5 - 79.5	6.00	50.5 - 79.5	5.21
20%	51.5 - 79.5	9.25	51.5 - 79.5	10.08	51.5 - 79.5	9.76

Table 5.6: Case 3: Height ranges of volume emission rate retrievals with error less than 15% and total root mean square percent error for VER within these height ranges.

The relationship between the errors in the parameters recovered is of interest. In Fig. 5.15 the percent RMS error of the recovered temperatures and volume emission rates for one run at the 20% noise level (a) and two runs at the 25% noise level (b) and (c) are shown, the percent error is used so the scales of temperature retrieval errors and VER retrieval errors are comparable. Although for some heights there seems to be similar structure in the temperature errors and VER errors, in general there is no clear correlation between the accuracy of the recovered parameters. In

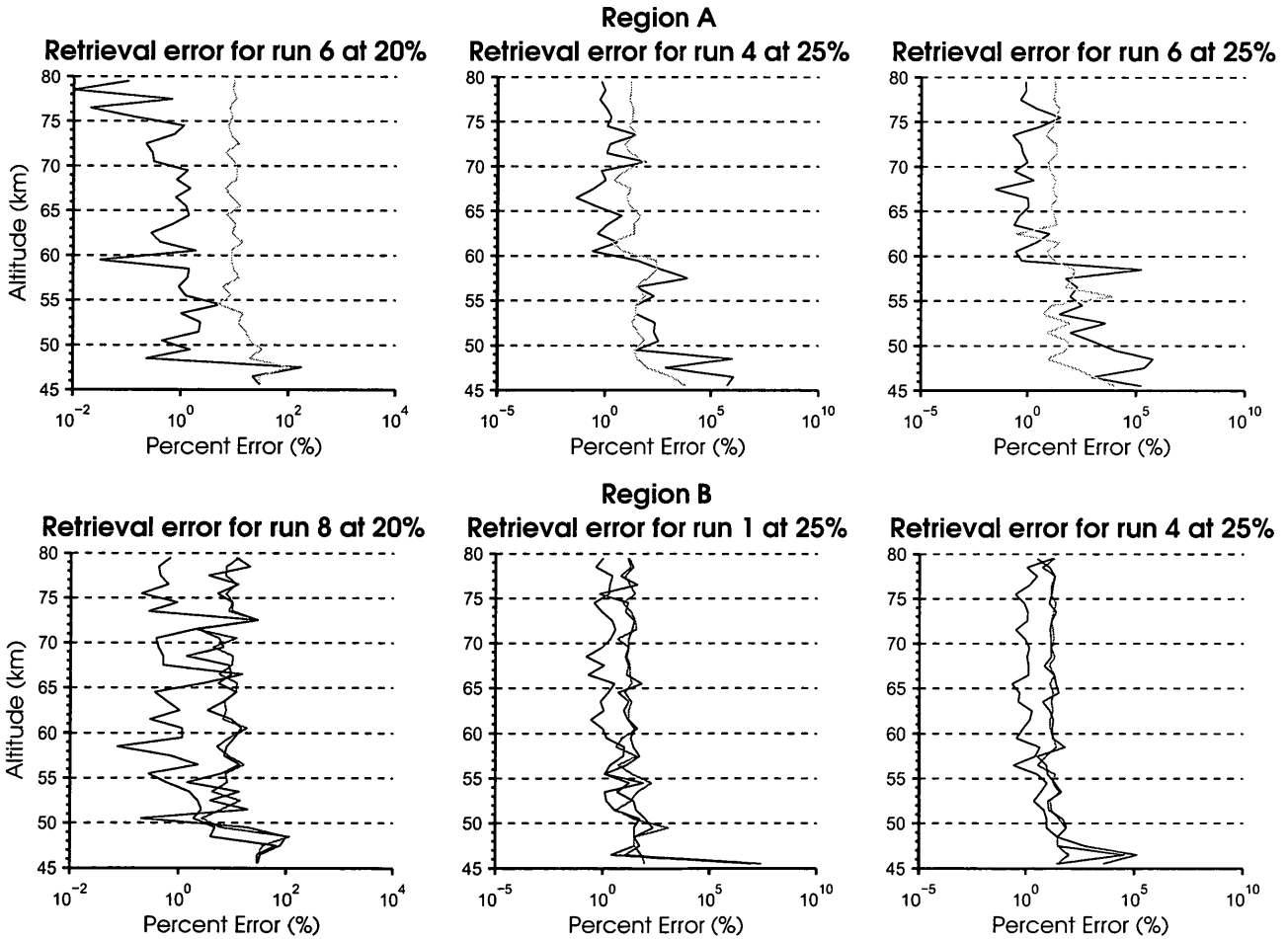

Figure 5.15: Case 3: Percent RMS error of the recovered temperatures (in black) and volume emission rates ($v' = 8$ in green, $v' = 1$ in blue and $v' = 2$ in red) for: realization 6 the 20% noise level, realizations 4 and 6 at the 25% noise level for region A in the top panel and realization 8 at the 20% noise level and realizations 1 and 4 at the 25% noise level of region B. The RMS percent error profiles selected correspond to the recovered profiles that were truncated in Fig. 5.11 and thus represent some of the more extreme errors.

the same way RMS percent retrieval error profiles are shown from region B: Fig. 5.15 one realization at the 20% noise level (d) and two realizations at the 25% noise level (e) and (f). Here the relationship between the errors in recovered volume emission rates for $v' = 1$ and $v' = 2$ is inconsistent. At some heights the two error curves are highly correlated, at others they are anti correlated and at others the relationship is unclear. As for temperature errors, again there is some similar structure but no clear indication of interconnection. This suggests that there is no consistent correlations in the oscillations of the temperature and VER profiles.

An offset in recovered VER from the true profile can also be seen in the stable region (region with little or no oscillation) of the recovered profile from both spectral regions. The profiles centre about 10 - 11% for the 20% noise level shown in (a) and (d) and 16%-17% for the 25% noise level shown in (b), (c), (e) and (f). The cause of the offset is identical to the cause of the offset in Case 2 but will be discussed in greater detail here.

The noise applied to the synthetic spectrum is directly proportional to the simulated observed wavelength bin radiances, thus it affects the recovered v' VER in a fairly consistent manner as the VER is also directly proportional to the wavelength bin radiances. A bias is created when the mean noise level is not 0. The bias is most apparent in peaks of the Gaussians formed by the convolution with the instrument function, it appears in Fig. 5.16 that the best fit modelled spectrum fails to capture these peaks, however in reality the entire spectrum is offset by a similar proportion.

This offset is also related to the improved temperature retrievals in Case 3 in comparison to those of Case 1. The temperature recovered with the offset VER is in many cases highly accurate. This suggests that for simultaneous retrieval, the

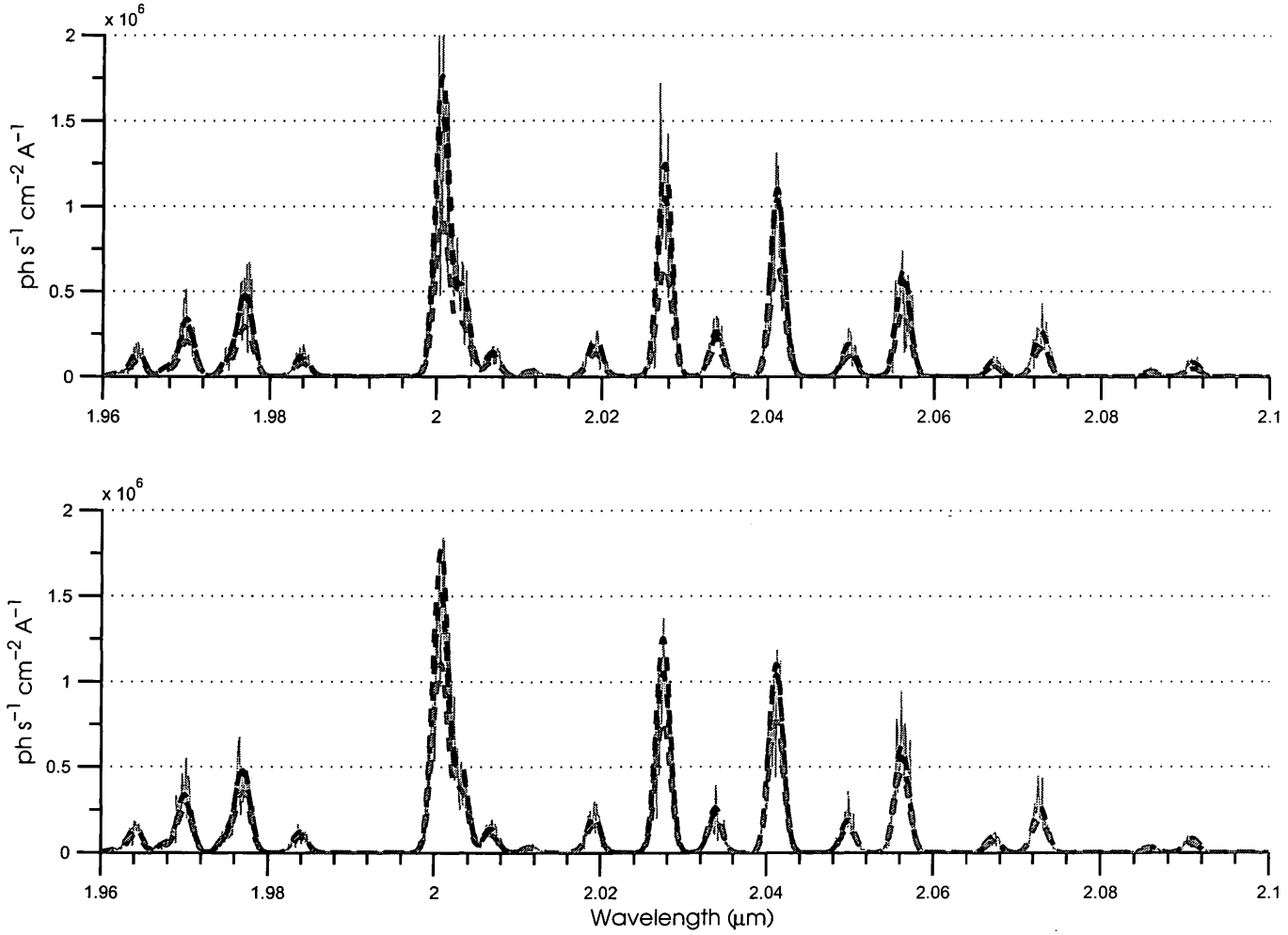

Figure 5.16: Two synthetic observations and related best fit spectra for Case 1 and Case 3 using the Onion Peeling fitting method. The two sample synthetic spectra, in grey, are from run 7 and run 10 with 30% noise for the 79.5 km height level. The true spectrum is the black dashed line, the Case 1 fit is the the blue dashed line and the Case 3 fit is the red dashed line.

volume emission rate retrieval is primarily affected by this type of noise making accurate temperature retrievals possible. Examples of this can be seen in Fig. 5.16, which contains the spectra of height level 79.5 km for two runs at the 30% noise level. In both plots the fitted spectra generated while fitting for temperature alone are more similar to the simulated observations yet the temperatures recovered have RMS errors of 21.5 K and 22.5 K respectively. The fitted spectra generated while fitting for temperature and VER appear to be somewhat dwarfed versions of the observations. The RMS errors in temperatures are approximately 1 K, yet the RMS percent errors in recovered VER are 38% and 26%, respectively.

The noise applied to the synthetic spectra in these simulations is illustrative and it is recognized that it does not directly reflect instrumental noise. Instrument noise, discussed in the next chapter, is not necessarily directly proportional to the observed wavelength bin radiance, so it is unlikely that the improvement in recovered temperatures due to the bias in recovered VER will occur.

If we ignore this unrealistic improvement to the recovered temperature profiles, the simultaneously recovered temperature and volume emission rate profiles are comparable in terms of accuracy to the retrievals of Case 1 and Case 2. This suggests that there is no significant penalty to the simultaneous retrieval. In addition there only are minor differences, in terms of range of accurate retrievals and in RMS errors, between the profiles recovered from region A and region B. This indicates that there is also no significant disadvantage to recovering the volume emission rates of two bands in addition to temperature.

5.4 Temperatures Recovered from Derived Absolute Wavelength Bin Radiance Spectra

The retrieval method using derived absolute WBR spectra recovers only temperatures, but differs from Case 1 as it does not require any knowledge of the volume emission rates. It is also unlike Case 3 as the method does not recover the VER simultaneously. Thus the results will be loosely compared to the results of the other methods as this approach is unconventional.

Initially the derived absolute instrument degraded (AD) WBR profiles are recovered at selected wavelengths, for simplicity in this work we select all sampled wavelengths within the given range, from the simulated limb observations data set using the pathlength matrix as the weighing function. Examples of recovered profiles from a simulated limb scan data set with 25% noise at 1.97 μm, 2 μm, 2.03 μm and 2.05 μm are shown in Fig. 5.17. The accuracy of the Gaussian elimination recovered AD WBR profiles clearly decreases as the noise level increases. At the 15% and 25% noise levels the recovered profiles oscillate about the true profile (perfectly recovered at the 0% noise level). In addition the relative error increases at the lower height levels. These inaccuracies are reflected in the recovered temperature profiles discussed in the following section.

The recovered AD WBRs for all selected wavelengths at each tangent height are then reassembled to form AD wavelength bin radiance spectra for each tangent height. The spectrum at each height is then normalized to some arbitrary value, in this work the spectra were normalized to 100 photons s^{-1} cm^{-3}. This normalized spectrum is then used to recover the temperature. Examples of normalized AD

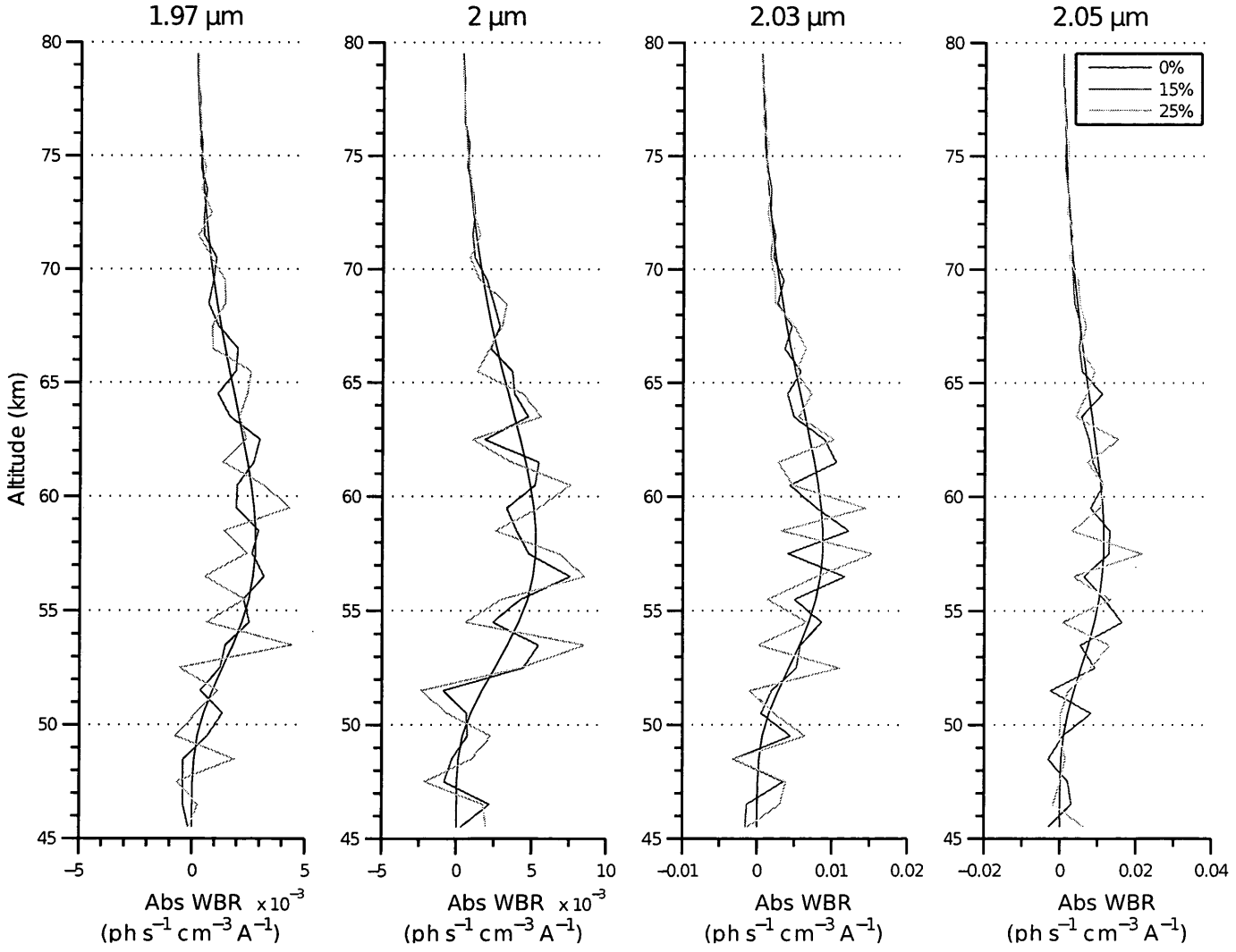

Figure 5.17: Sample recovered instrument-convolved absolute WBR profiles at 1.97 μm, 2 μm, 2.03 μm and 2.05 μm at the 0%, 15% and 25% noise levels.

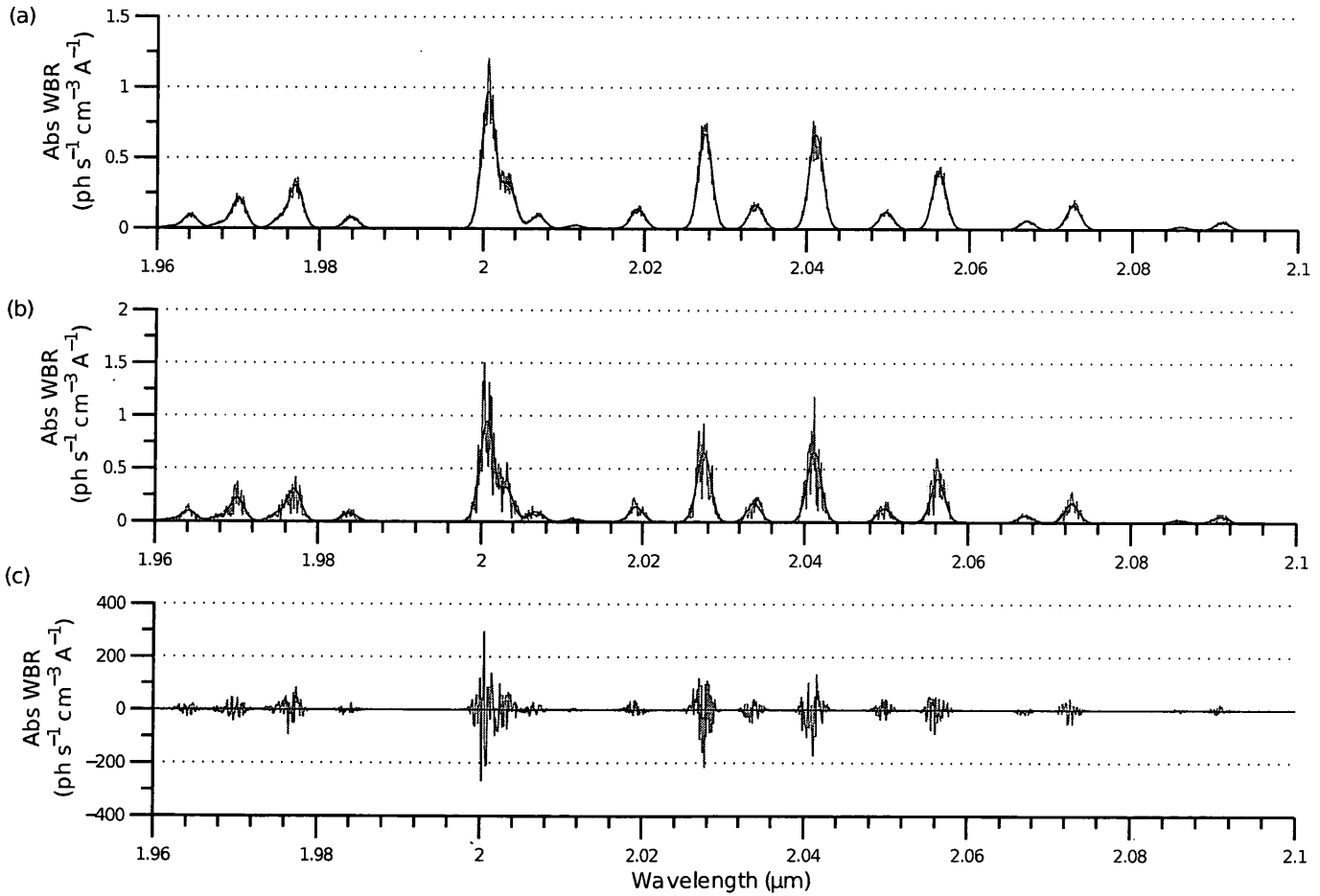

Figure 5.18: Sample normalized recovered instrument degraded absolute WBR spectra at (a) 79.5 km, (b) 68.5 km and (c) 45.5 km. The true noiseless spectra are in black and the reassembled spectra for the 25% noise case are in red. The spectra are normalized to 100 photons s^{-1} cm^{-3}.

WBR spectra are plotted in Fig. 5.18. At 79.5 km the reassembled normalized AD WBR spectrum for the 25% noise level (in red) is, as expected, a noisier version of the spectrum with no noise (in black). At 68.5 km the amount of noise in the derived spectrum from simulated observations with 25% noise exceed 25% of the true signal, in some cases reaching nearly 100%. At 45.5 km the derived normalized spectrum for the 25% noise levels fluctuates wildly from negative to positive and is greatly exaggerated by the normalization to a greater integral sum as the original spectrum is weak. Accurate temperature retrieval from such a spectrum is not possible as will be seen in the following section.

The Levenberg-Marquardt optimization method is then used to find the best fit temperature. The temperatures recovered at each height level are then assembled to form the recovered temperature profile. It should be noted that once temperatures are recovered VER retrieval would then be possible using the recovered AD WBRs and the recovered temperature profile.

The results of the realizations using this approach are discussed in the following section together with reasons for the fluctuations in the spectra and growth in noise.

5.4.1 Case 4: Temperature Recovery with no Knowledge of VER from Derived Absolute Wavlength Bin Radiance Spectra

The temperature profiles recovered from the synthetic limb data at noise levels between 0% to 25% are shown in Fig. 5.19, together with the RMS error of the 10 temperatures recovered at every height level. As with the Onion Peeling method, the retrieval at 0% noise is near perfect. Once noise is added, the range of temperatures recovered at the lowest heights (the unstable region) vary widely. The

range in temperatures is larger than Case 1 as is the number of heights within the unstable region. The cause of this error differs as the method does not rely on the recovered parameters from previous heights, thus errors do not propagate downward in that manner. Instead the amount of noise increases due to the Gaussian elimination method that was used to determine the AD WBRs at each height as discussed in the previous section. Since the method treats every sampling interval separately and has no mechanism for dealing with noise the Gaussian elimination method finds the absolute convolved WBR that best fits all the noisy measurements without any smoothing between intervals. This results in fluctuating spectra for each height. In Fig. 5.20 the retrieved contributions from 3 layers are shown for synthetic AD wavelength bin radiances with 25% error. The recovered spectrum for the topmost layer, shown in Fig. 5.20 (a), is most constrained as it contributes to the observations from every tangent height. The result of the constraint is that the recovered spectrum is relatively smooth as the Gaussian elimination method determines the intensities that best fits all the observations. This does not perforce guarantee accuracy as the method may incorporate a portion of the noise into the recovered spectrum which would in turn cause the recovered temperature to be inaccurate. Further down the profile, as shown in Fig. 5.20 (b), the recovered spectrum is less constrained as the number of layers it contributes to decreases. The resulting spectrum is more noisy as the best fit recovered AD WBRs offset the errors in more constrained height levels and consequently the recovered temperatures are more prone to error. This is the standard problem of recovery below the peak. The amount of noise increases until the bottommost level, Fig. 5.20 (c), which is determined simply by the difference between the weighed contributions

of the all upper height levels and the observation at the tangent height 45.5 km which causes the spectrum to be extremely noisy with little correlation with the true contribution at this height level.

At the 10% and 15% noise levels the unstable region extends further upward and the spread of temperatures recovered in the stable region begins to increase. This indicates an increase in error throughout the profile. Also a negative offset in the recovered temperatures begins to appear at the bottom of the stable region. This negative offset is caused by the Levenberg-Marquardt optimization method fitting into the exaggerated peaks of the more intense transitions of the negative set (which increase with decreasing temperature thus causing a negative offset) caused by the noise. No negative offset in temperatures is observed for either the Onion Peeling approach or the Global Optimization approach thus it is likely related to the normalization. The offset increases at the 20% noise level and at the 25% noise level the offset exceeds 5 K.

In the pixel plot of the root mean square error of temperatures from the 10 realizations at each of the noise levels, Fig. 5.21, no sharp breakdown in the method is apparent. Instead the height range of accurate temperatures simply decreases, almost linearly, until only the temperature of the top tangent height is recovered with adequate accuracy, which occurs at the 30% noise level. Even beyond this point the amount of error increases relatively smoothly, in sharp contrast to the abrupt increase in noise at 30% of the Onion Peeling method. The amount of noise in the spectra derived for each height depends on the actual configuration of noise in the observations and thus it would not be a simple task to improve the predicted noise levels to increase the accuracy of the recovered temperatures. This proves to

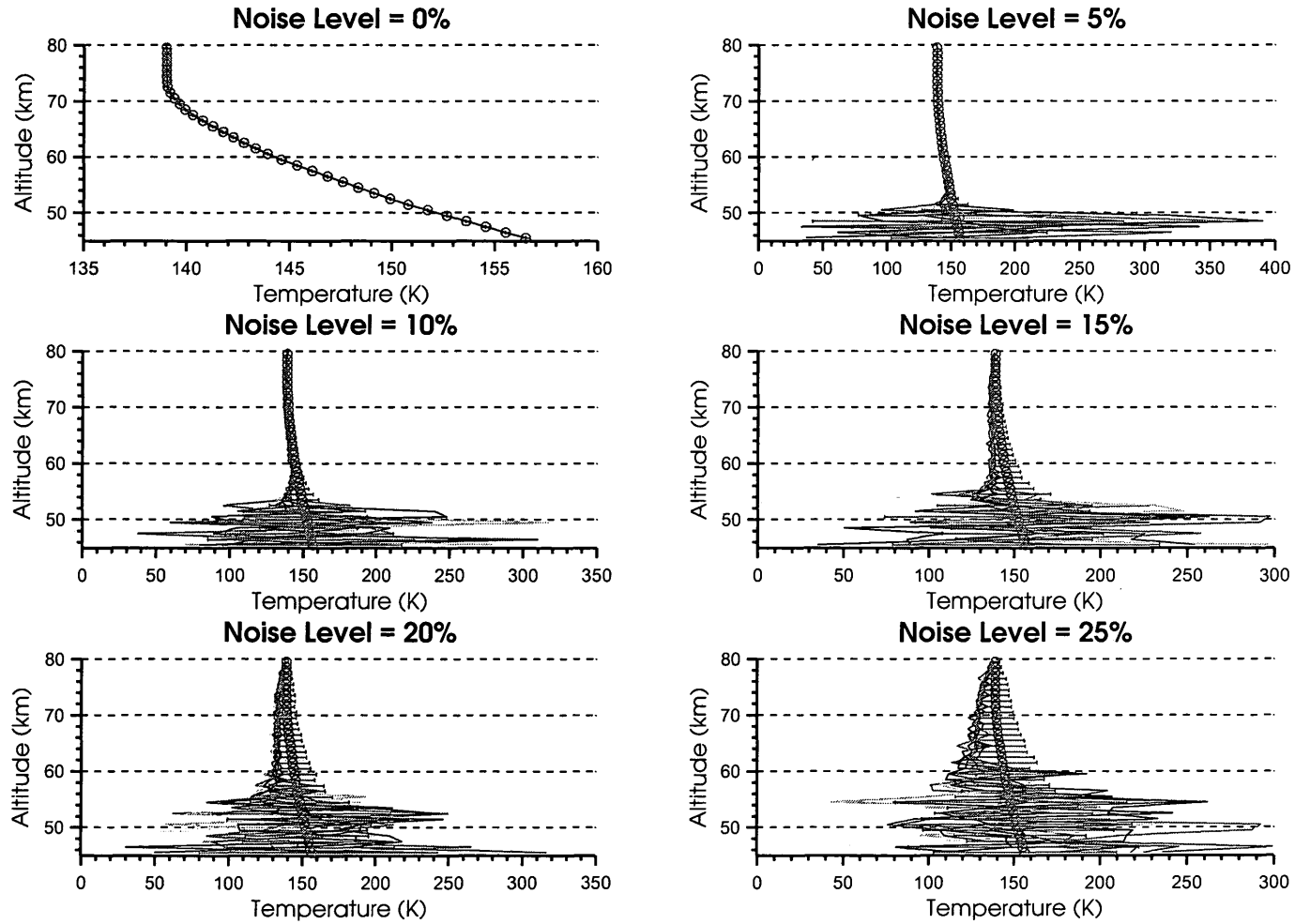

Figure 5.19: Case 4: Recovered temperature profiles from 10 simulated AD WBR spectra for noise levels ranging for 0-25% for region A. The red circles represent the true temperatures and the red error bars indicate the root mean square error of the 10 recovered temperatures from the true temperature for the given height.

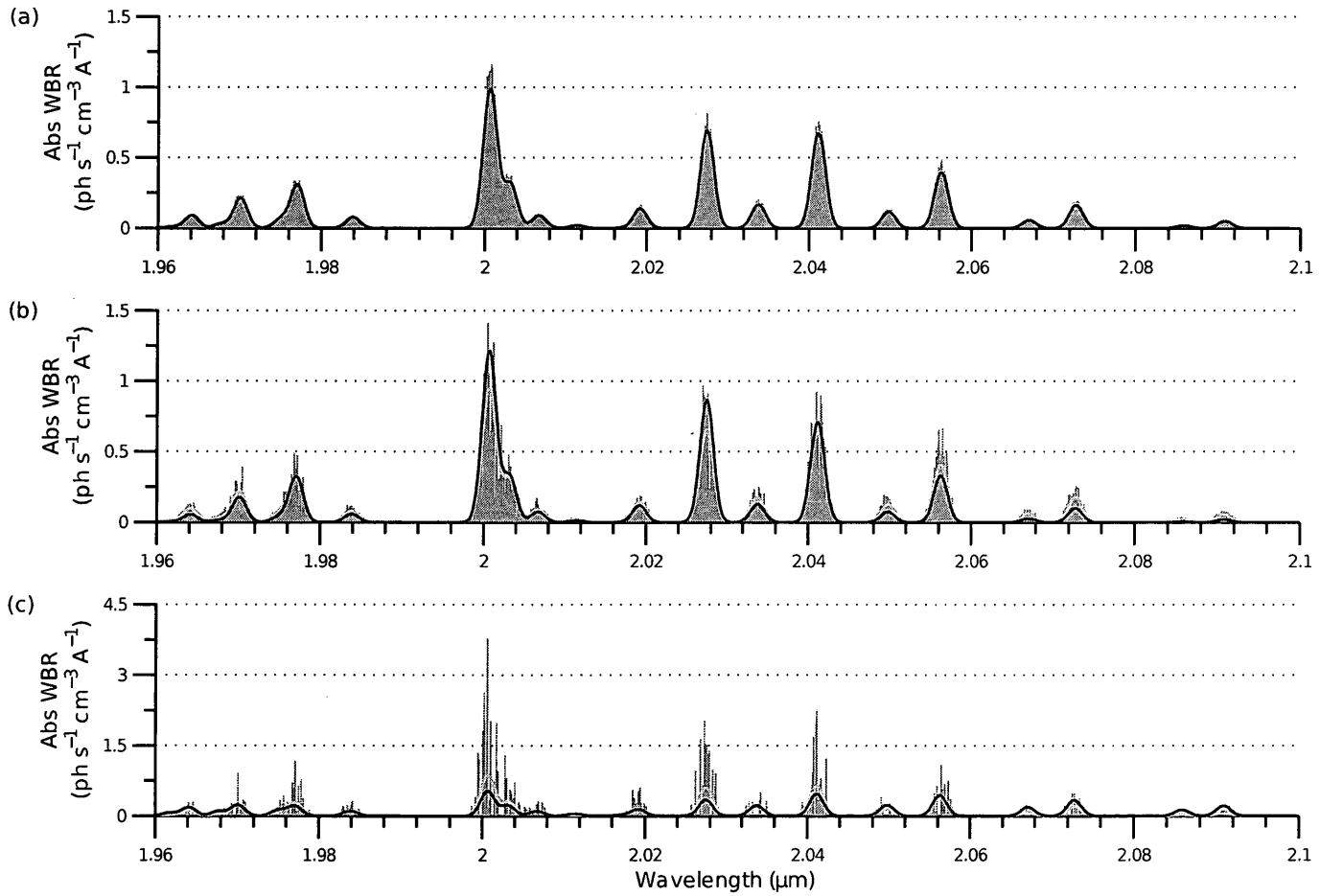

Figure 5.20: Case 4: Examples of derived convolved absolute WBR spectra for synthetic limb scan observations with 25% noise for height levels (a) 79.5 km, (b) 63.5 km and (c) 45.5 km. Included in each plot are the recovered spectra for each height in grey, the best fit spectra in green and the true spectra in blue all normalized to 100 photons s^{-1} cm^{-3}. The RMS error of the recovered temperatures are (a) 3.2 K, (b) 35.8 K and (c) 132.1 K.

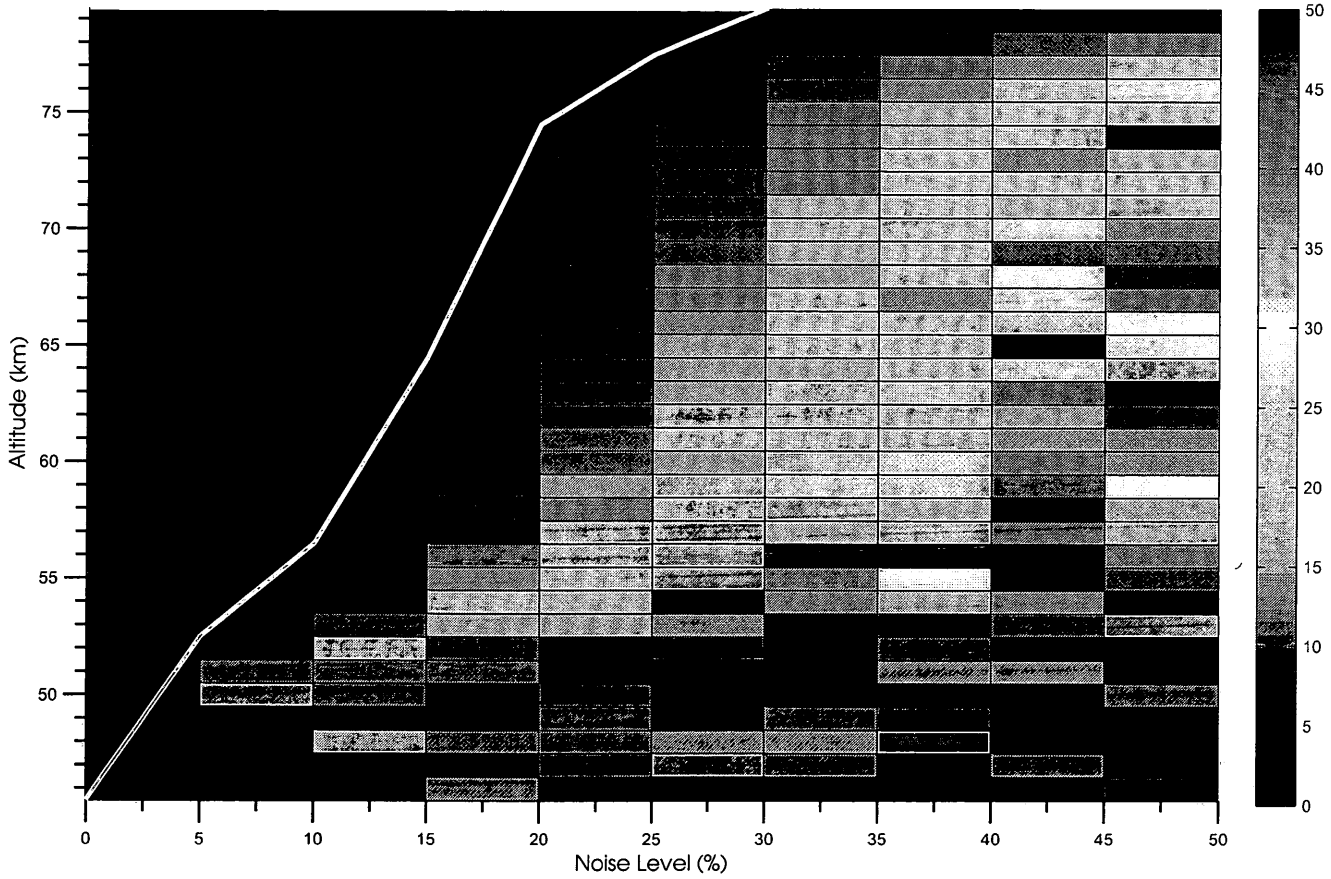

Figure 5.21: Case 4: Pixel plot of the root mean square error of the temperatures recovered from the 10 simulated limb observations with noise levels ranging from 0 - 50% from spectral Region A. The white line delineates the height ranges where the RMS error is less than 5 K. The units of the colour scale are in Kelvin.

be a major drawback of the temperature retrieval method using derived absolute WBR spectra in its present form. The height ranges of retrievals with less than 5 K error, listed in Table 5.7, are more limited than those of the Onion Peeling retrieval method. The only advantage, in comparison to the Onion Peeling method, is that this method is able to recover very limited temperatures for noise levels beyond 20%, as listed in Table 5.7.

	Region A	
Noise Level	Height Range (km)	RMS (K)
0 %	45.5 - 79.5	0.00
5 %	52.5 - 79.5	1.19
10%	56.5 - 79.5	1.89
15%	64.5 - 79.5	2.21
20%	74.5 - 79.5	1.52
25%	77.5 - 79.5	1.06
30%	79.5	0.48

Table 5.7: Case 4: Height ranges of recovered temperatures with less than 5 K RMS error and the associated root mean square error of the temperatures within the range. Only the temperature for the topmost layer is recovered with less than 5 K RMS error at the 30% noise level, below this layer the recovered temperatures oscillate beyond 5 K RMS error.

As discussed in the previous chapter it may be possible to improve the accuracy of recovered instrument convolved absolute WBR profiles, and thus improve the accuracy of recovered temperature profiles results, by using a fitting method which would account for the noise when isolating the contributions from each height. However, for this work the Gaussian elimination method proved to be sufficient.

5.5 Global Optimization Simulations

The Global Optimization method uses the iterative Levenberg-Marquardt optimization method to fit the observed spectra for all heights simultaneously recovering the entire temperature and/or volume emission rate profile in one step. Since all the observed spectra are fitted at the same time error propagation should not occur. However, similarly to the previous two methods the recovered parameters for the lowest tangent heights are prone to error, but the cause of the error is slightly different. The parameters for the tangent heights at the bottom of the OH Meinel Band airglow layer are less well constrained as they contribute to the least amount of limb observations. This lack of constraint makes the retrievals more prone to error as errors in these parameters would not contribute much to the cost function. In addition, the airglow is only emitting weakly at the lower part of the emission layer and for limb observations the emission of the tangent height layer is minor relative to the sum of the contributions from the layers above. The contribution of the tangent height layer may lie below the estimated variance of observation error covariance matrix and thus may not be considered by the fitting algorithm making accurate retrieval impossible.

5.5.1 Case 5: Temperature Recovery with Knowledge of VERs using the Global Optimization Approach

The temperatures recovered using Global Optimization from the synthetic limb observations for both region A, containing the (8-6) band, and region B, containing both the (1-0) and (2-1) bands, are analyzed in this section. The retrieval method

is provided the VER profiles of the aforementioned bands and thus only recovers the temperature at each height. These temperatures can be combined to form a temperature profile.

The ten recovered temperature profiles from both regions A and B and the RMS error at each height level are shown in Fig. 5.22. The recovered temperatures for the noiseless case are nearly identical to the true temperatures save for the lowest layer for region A and 2 lowest layers for region B where the method cannot improve upon the *a priori* temperatures. This is caused by the estimated error variance exceeding the contribution of these heights to the observation, meaning that the emission emanating from the height in question is smaller than the estimated noise level of the observed signal and is thus indistinguishable from the noise. Although there is no noise in the simulated data, the estimated error standard deviation is 1% as mentioned in Section 5.1 and 1% of the observed limb emission of the height level exceeds the actual contribution emanating for the height level. With the addition of noise the least constrained levels, located at the bottom of the airglow layer, become more prone to negative error and strong negative error spikes between 45 km and 50 km occur in the majority of the profiles recovered from region A, but are not prevalent in the retrieved profiles from region B. The errors are less severe for profiles recovered from region B possibly due to the ratio of emission of the positive and negative sets. Since there are more lines which increase in intensity with increasing temperature, *i.e.*, emission lines of transitions from the positive set, large negative errors are less probable. As the noise increases the number of heights affected also increases at approximately the same pace for both regions. At the 40% noise level, scattered small negative errors begin to appear in the central

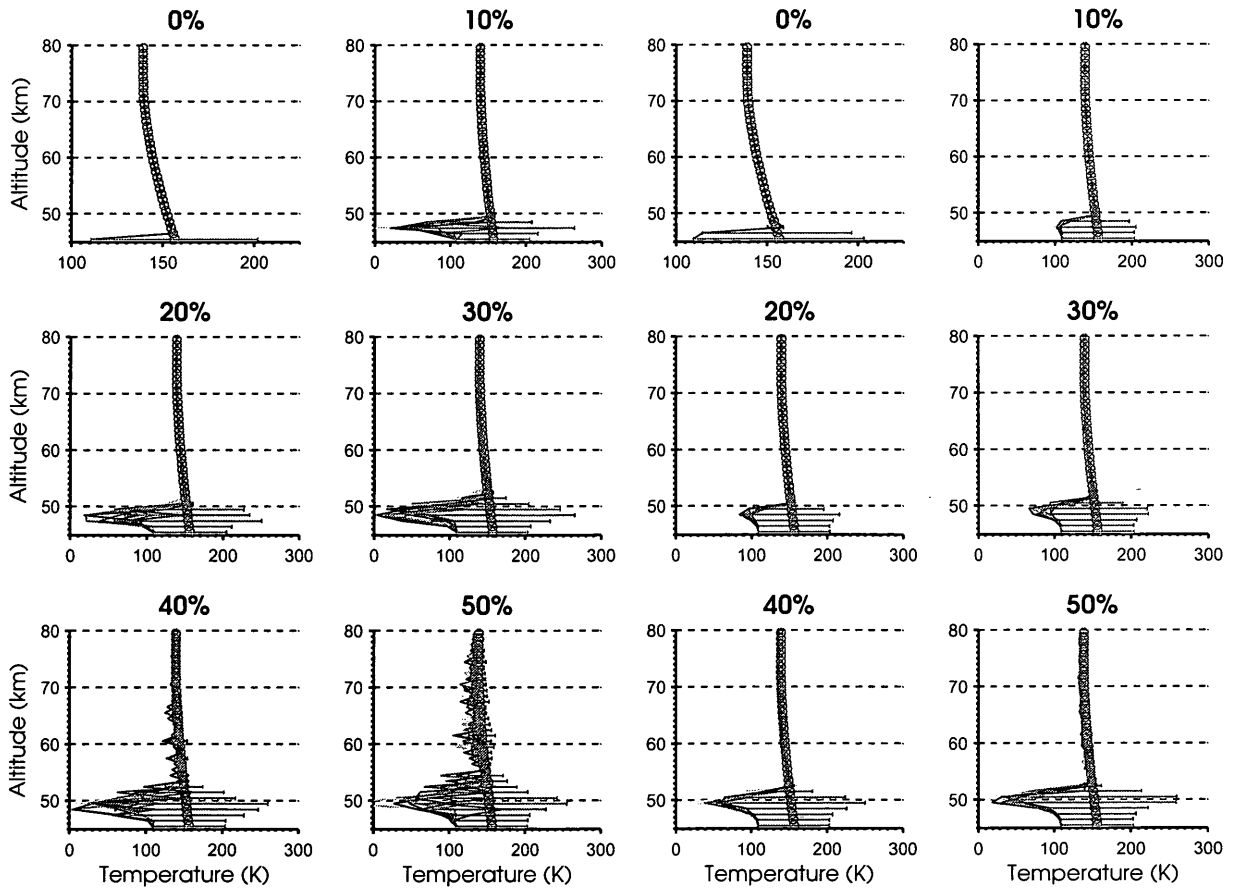

Figure 5.22: Case 5: Recovered temperature profiles from 10 simulated limb observed spectra for noise levels ranging for 0 - 50% for region A in the two columns on the left and region B in the two columns on the right. The red circles indicate the true temperatures and the red error bars indicate the root mean square error of the 10 temperatures recovered for the given height.

region of the profile recovered from region A which increase in number, size and extent at the 50% noise level. As is the case for the temperature recovered from derived absolute WBR spectra, see section 5.4, the erroneous retrievals are caused by the Levenberg-Marquardt iterative method fitting into the noisy peaks of the more intense transitions of the negative set. For the recovered profiles from region B only very minor scattered negative errors are present at the 50% noise level. The profiles recovered from region B are less prone to this error as mentioned above.

In Fig. 5.23 the pixel plot of root mean square errors of the temperatures recovered from the synthetic observations of spectral regions A and B are shown. The retrieval errors of the temperatures recovered from the lower height levels and the scattered errors beginning at 40% for region A and at 50% for region B are evident. In region B, temperatures are recovered with error less than 5 K for noise levels up to 45% for most heights in contrast to region A where the range of accurate temperatures begins to decline sharply beyond the 35% noise level.

The Global Optimization temperature recovery clearly surpasses the temperature retrieval by the Onion Peeling methods and the temperature recovery method using derived absolute WBR spectra as it recovers temperature with high fidelity with 40% or 45% noise and from larger ranges of heights. The list of height ranges of accurate temperature retrieval and the total root mean square error of the recovered temperatures within these ranges are shown in Table 5.8.

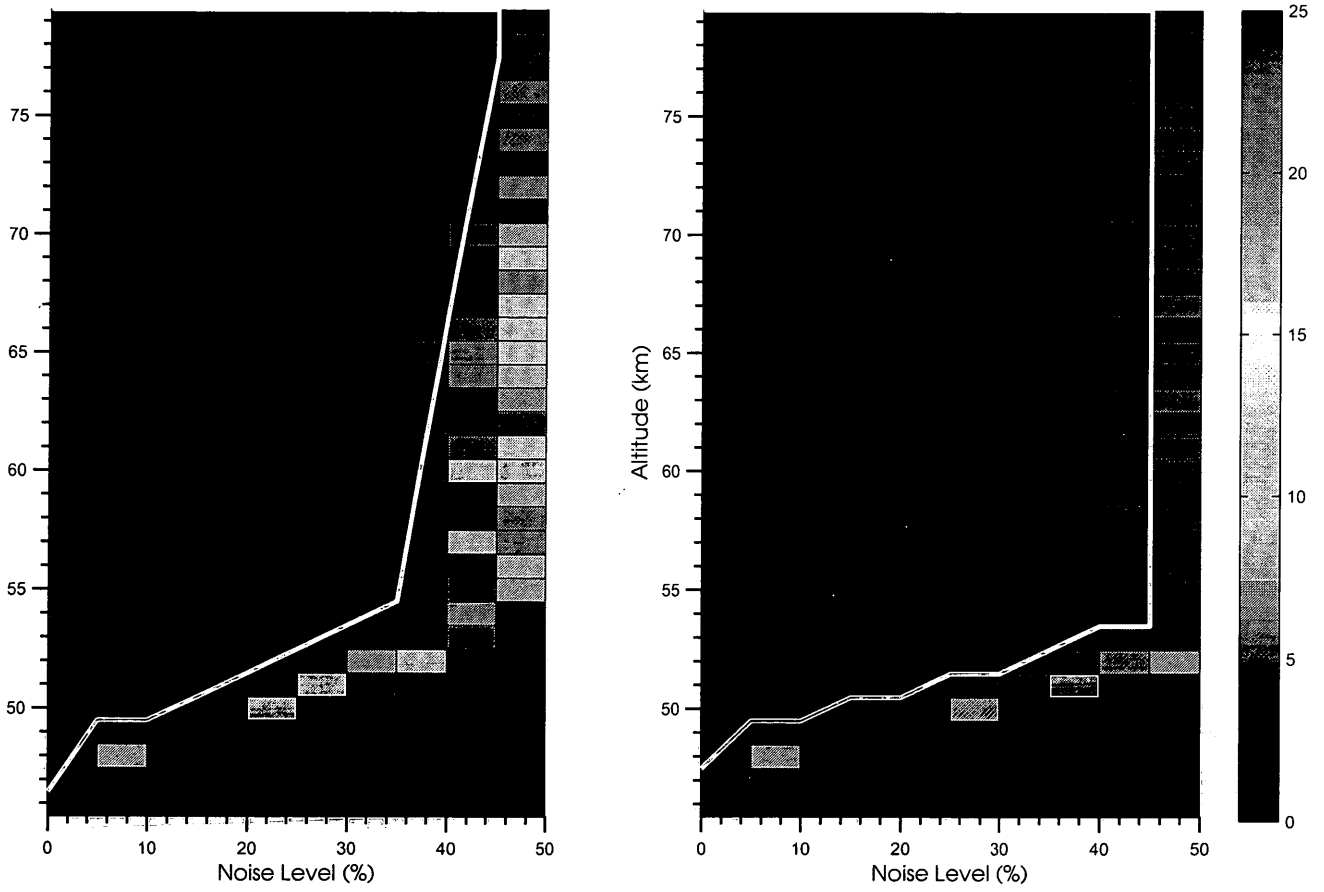

Figure 5.23: Case 5: Pixel plot of the root mean square error of the temperatures recovered from the 10 simulated limb instrument degraded WBR spectra with noise levels ranging from 0 - 50%. RMS errors of profiles recovered from spectral region A are shown in the left panel and from spectral region B in the right panel. The white line delineates the height ranges where the RMS error is less than 5 K. The units of the colour scale are in Kelvin.

	Region A		Region B	
Noise Level	Height Range (km)	RMS (K)	Height Range (km)	RMS(K)
0 %	46.5 - 79.5	0.23	47.5 - 79.5	0.25
5 %	49.5 - 79.5	0.23	49.5 - 79.5	0.31
10%	49.5 - 79.5	0.68	49.5 - 79.5	0.60
15%	50.5 - 79.5	0.83	50.5 - 79.5	0.86
20%	51.5 - 79.5	0.88	50.5 - 79.5	1.02
25%	52.5 - 79.5	1.29	51.5 - 79.5	1.29
30%	53.5 - 79.5	1.75	51.5 - 79.5	1.76
35%	54.5 - 79.5	2.70	52.5 - 79.5	2.19
40%	66.5 - 79.5	3.59	53.5 - 79.5	2.84
45%	77.5 - 79.5	4.10	53.5 - 79.5	3.80

Table 5.8: Case 5: Height ranges of temperature retrievals with less than 5 K RMS error and total RMS error for recovered temperatures within the height ranges.

5.5.2 Case 6: Volume Emission Rate Recovery with Knowledge of Temperatures using the Global Optimization Approach

The results of the volume emission rates retrievals using the Global Optimization approach with knowledge of the true temperature profile from the simulated limb data sets for noise levels from 0% to 50% are discussed in this section.

The recovered volume emission rate profiles for 0%, 15%, 35% and 50% noise levels, shown in Fig. 5.24, along with their root mean square percent errors, are very similar for all three bands. The VERs recovered from noiseless synthetic limb data and the synthetic data with 15% noise almost perfectly reproduce the true VER profiles, although the expected minor errors at the bottom of the profile would not be visible due to the scale. At the 35% noise level the VERs recovered from all three bands are negatively offset relative to the true VERs. The magnitude of the offsets are proportional to the emission rate and are thus more evident near the

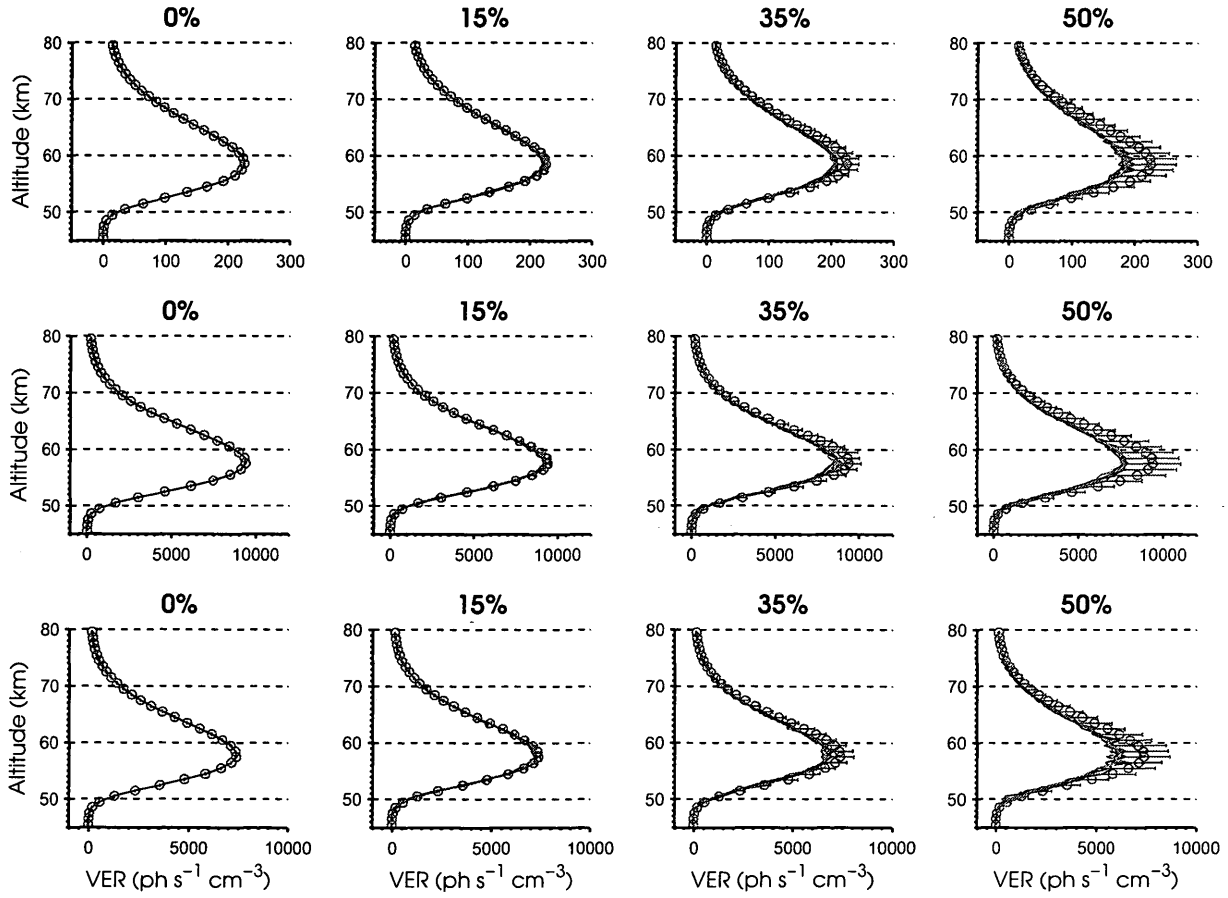

Figure 5.24: Case 6: Recovered volume emission rate profiles from the 10 simulated limb observed spectra for noise levels of 0%, 15%, 35% and 50% for $v' = 8$ recovered from spectral region A in the top row and for $v' = 1$ and $v' = 2$ recovered from spectral region B in the middle and bottom rows respectively. The red circles are the true temperatures and the red error bars indicate the root mean square error of the 10 volume emission rates recovered for the given height.

peak of the OH Meinel airglow layer. At the 50% noise level the negative offset increases beyond a 15% error limit. The cause of this offset is similar to the VER retrieval using the Onion Peeling approach (Case 2) discussed in 5.3.2 and is not likely to occur in real observations as, depending on the detector, the noise will not be directly proportional to the signal. Possible sources of noise are discussed in Chapter 6.

As shown in Fig. 5.25 the retrieval RMS percent errors pixel plot for the (8-6) band from region A and the (1-0) band from region B are almost identical, with similar RMS percent error at the bottom of the airglow emission layer and the same gradual increase of percent RMS error throughout the profile which exceeds the accuracy limit at the 50% noise level. Although the emissions of the two bands differ significantly in intensity, the noise applied to the spectrum is proportional to the emission and thus the accuracy of retrieval is very similar. The errors in the VER profiles recovered from the (2-1) band are slightly greater. The greater the number of emission lines used for the retrieval the greater the constraint on the recovered parameters. Accordingly with a smaller number of emissions the parameters to be recovered are less constrained and thus more prone to errors. As there are half as many transitions from the (2-0) band as there are from the (1-0) in region B, the VER retrievals of $v' = 2$ are more prone to error, exemplified by the slightly enhanced RMS error in the percent RMS error pixel plot shown in Fig. 5.25.

The full listing of height ranges of VER retrievals with percent RMS error less than 15% for the (8-6), (1-0) and (2-1) bands are summarized in Table 5.9 along with the RMS error of the the VER retrievals within the ranges. The height ranges

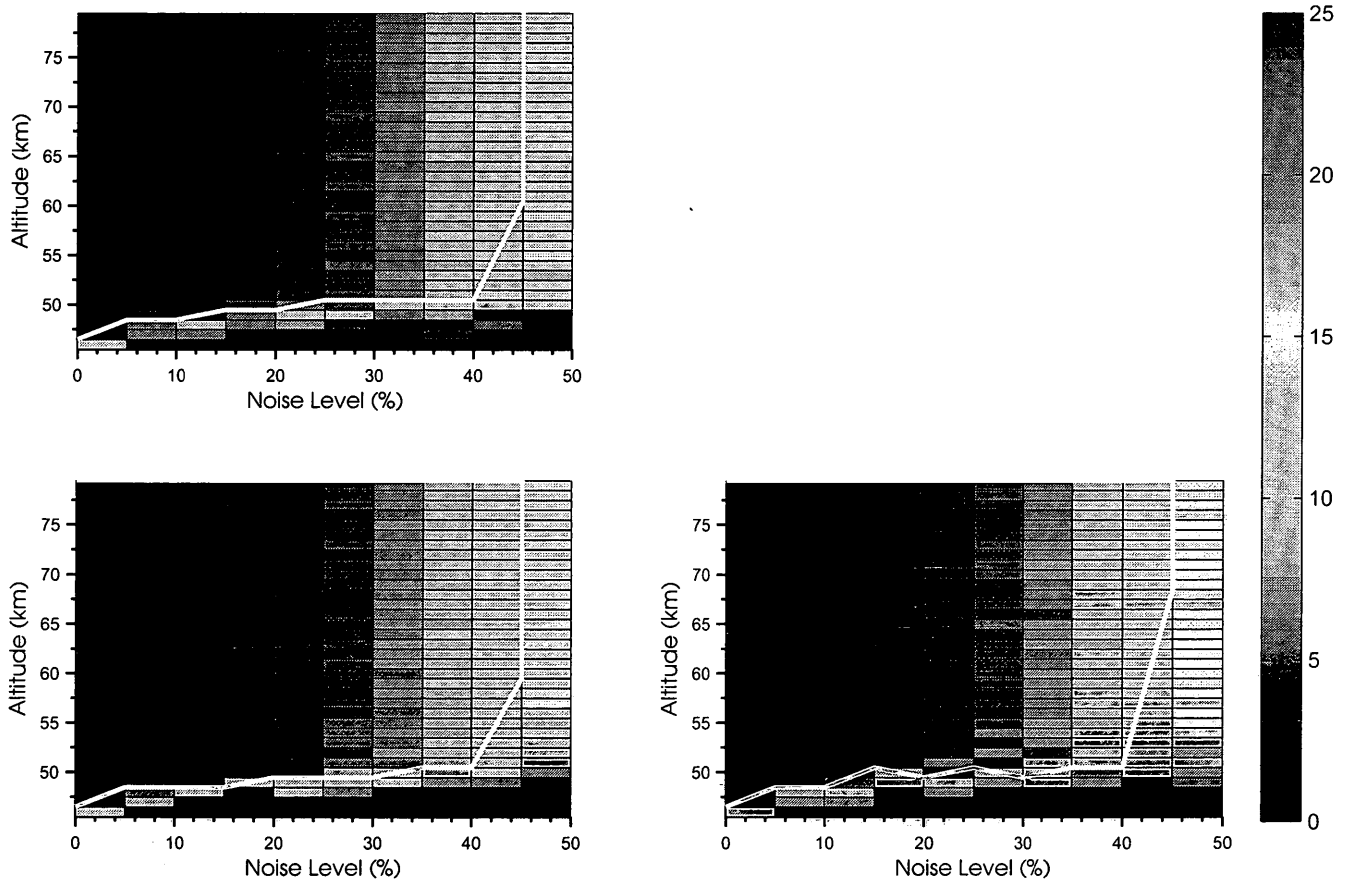

Figure 5.25: Case 6: Pixel plot of the percent RMS error of the volume emission rates recovered from the 10 simulated limb observations with noise levels ranging from 0 - 50%. The percent RMS errors of the $v' = 8$ volume emission rates retrieved from spectral region A are shown on in top left panel and the percent RMS errors of the $v' = 1$ and $v' = 2$ volume emission rates recovered from spectral region B are shown on the bottom left and bottom right panels, respectively. The white line delineates the height ranges where the percent RMS error is less than 15%. The units of the colour scale are in percent.

of accurate retrievals for the (8-6) and (1-0) bands are nearly identical. The height ranges for the (2-1) band are slightly more limited. The limitation may not be a direct consequence of fitting both bands simultaneously yet it is unavoidable as it is unlikely that a spectral region which meets the requirements for retrieval would also contain a large number of lines of all the bands contained within. The additional VER profile, however more sensitive to noise, is an advantage and has no effect on the retrieval of the primary band. Thus there are no drawbacks to the retrieval of two bands simultaneously although the profiles of the band with fewer emission lines within the spectral window may be less reliable.

	Region A		Region B			
	$v = 8$		$v = 1$		$v = 2$	
Noise Level	Height Range (km)	RMS (%)	Height Range (km)	RMS (%)	Height Range (km)	RMS (%)
0 %	46.5 - 79.5	0.02	46.5 - 79.5	0.61	46.5 - 79.5	0.80
5 %	47.5 - 79.5	1.38	48.5 - 79.5	1.24	48.5 - 79.5	1.64
10%	47.5 - 79.5	2.42	48.5 - 79.5	2.18	48.5 - 79.5	2.41
15%	48.5 - 79.5	2.29	48.5 - 79.5	5.07	50.5 - 79.5	2.31
20%	48.5 - 79.5	3.73	49.5 - 79.5	3.43	49.5 - 79.5	3.60
25%	50.5 - 79.5	4.45	49.5 - 79.5	4.98	50.5 - 79.5	4.72
30%	50.5 - 79.5	6.47	49.5 - 79.5	6.75	49.5 - 79.5	6.88
35%	50.5 - 79.5	8.84	50.5 - 79.5	8.80	50.5 - 79.5	8.68
40%	50.5 - 79.5	11.41	50.5 - 79.5	11.27	50.5 - 79.5	11.51
45%	60.5 - 79.5	14.20	59.5 - 79.5	14.11	68.5 - 79.5	14.56

Table 5.9: Case 6: Height ranges of volume emission rate retrievals with less than 15% RMS error and total percent RMS error for recovered VER within the height ranges.

In comparison to the VER retrievals using the Onion Peeling method described in section 5.3.2, the Global Optimization method is far less sensitive to the presence of noise, with retrievals with less than 15% error from spectra with up to 45% noise

in contrast to 20% for the Onion Peeling method.

5.5.3 Global Optimization Case 7: Simultaneous Temperature and Volume Emission Rate Recovery with the Global Optimization Approach

Finally the results of the simultaneous temperatures and volume emission rates retrievals with the Global Optimization approach from the previously mentioned synthetic limb observations with noise levels ranging between 0% and 50% are discussed in this section.

The recovered volume emission rate profiles for the simultaneous retrieval and the root mean square error at each height, shown in Fig. 5.26, do not differ significantly to those recovered in Case 6, just as the VER recovered in Case 3 did not differ from those recovered in Case 2. The same negative offset in recovered VER and slight increase in variability in recovered VER are apparent. The pixel plots (Figs. 5.25 and 5.27) are also very similar with the error at the 50% noise level exceeding a 15% recovery limit, and the gradual increase in error at the bottom of the OH Meinel Band airglow emission layer. The main difference is a slight increase in percent RMS error between 50 - 65 km at the 20% noise, continuing between 50 - 60 km in the recovered profiles of realizations with higher noise levels. This increase in error is associated with a slight increase in recovered temperature error that is discussed below.

There is, however, a difference in the recovered VER profiles from region A and region B in the magnitude of error of the least constrained heights. For the profiles recovered from region A the RMS error at the bottom of the profile slowly

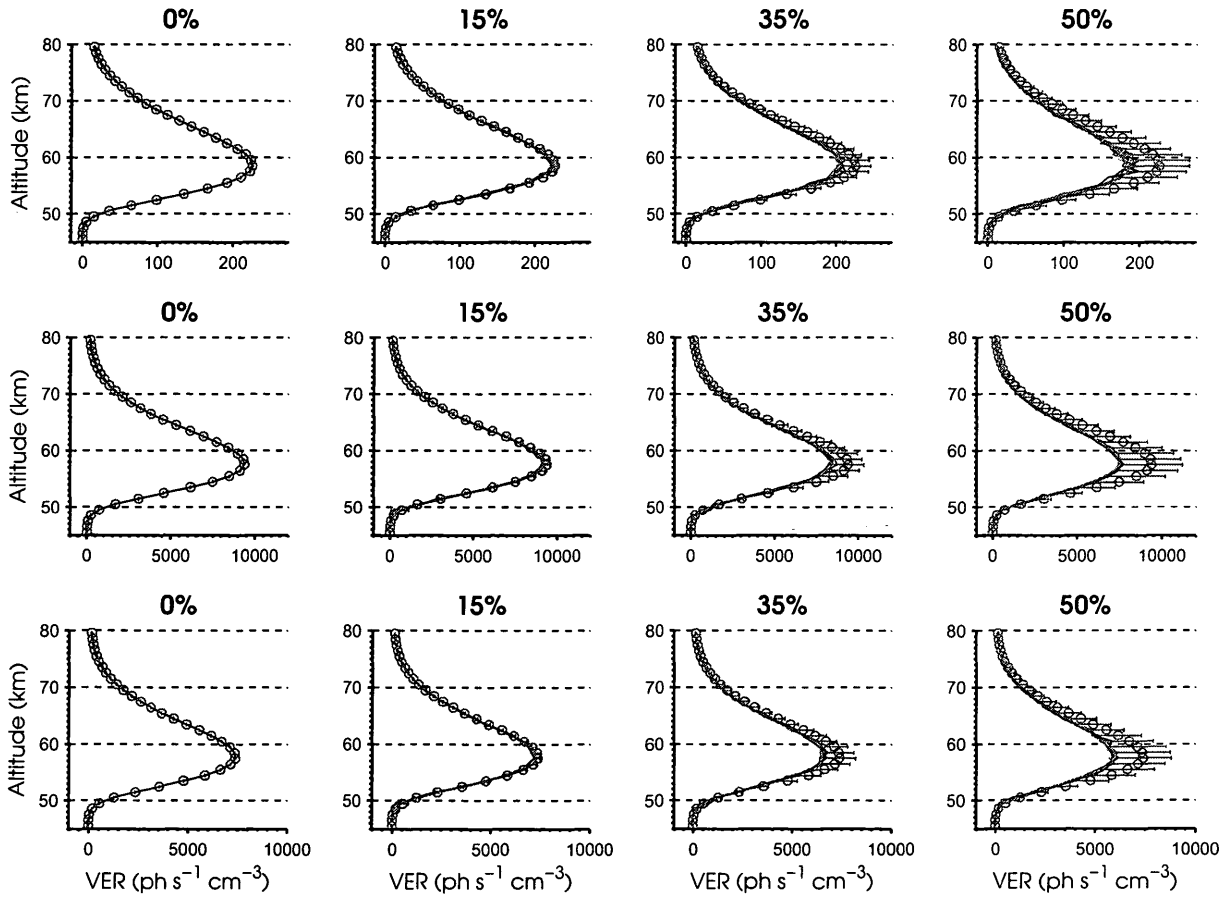

Figure 5.26: Case 7: Volume emission rate profiles recovered while simultaneously recovering temperatures from the 10 simulated convolved WBR spectra for noise levels for 0%, 15%, 35% and 50% for $v' = 8$ recovered from spectral region A in the top row and for $v' = 1$ and $v' = 2$ recovered from spectral region B in the middle and bottom rows respectively. The red circles are the true temperatures at each height and red error bars indicate the root mean square error of the 10 volume emission rates recovered for the given height.

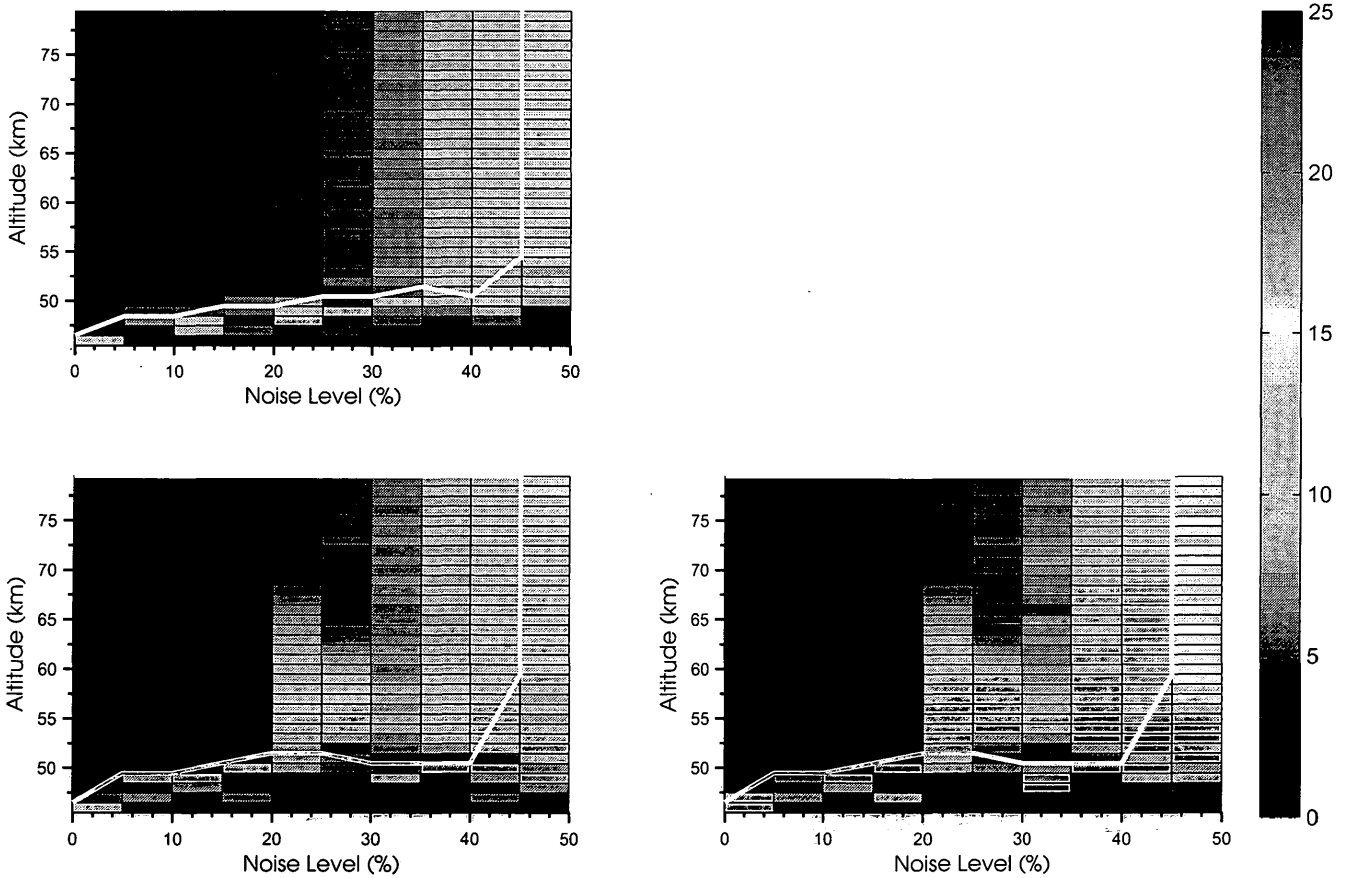

Figure 5.27: Case 7: Pixel plot of the percent RMS error of the volume emission rates recovered simultaneously with temperatures from the 10 simulated limb observations with noise levels ranging from 0 - 50%. The percent RMS error of the $v' = 8$ volume emission rates retrieved from spectral region A are shown in the top left panel and the percent RMS error of the $v' = 1$ and $v' = 2$ volume emission rates recovered from spectral region B are shown on the bottom left and bottom right panels, respectively. The white line delineates the height ranges where the percent RMS error is less than 15%. The units of the colour scale are in percent.

increases to 30% at the lowest layer. For both the $v' = 1$ and $v' = 2$ VER profiles recovered from region B there are large oscillations in the recovered profiles with RMS errors approaching 100%. These oscillations do not occur in the independent VER recovery of Case 6. There is also a decrease in the height range of retrievals with less than 15% percent RMS error in the profile recovered from during the region B realizations with 40% noise in comparison to the realizations of Case 6, noted in Table 5.10. The table also includes the total RMS error for all recovered VER within the given height ranges. This decrease in height range is caused by a minor increase in percent RMS error to between 16 - 17% for recovered VER for heights between 51.5 - 58.5 km, only slightly exceeding the accuracy requirement and is still within the stable region of the retrieval.

These differences suggest that when retrieving multiple volume emission rates, marginally improved results occur when recovering the VER independently of temperature for high noise levels. For low noise levels the difference is not significant.

Temperature retrievals improve when both temperatures and volume emission rates are recovered simultaneously. The recovered temperatures profiles for the 10 synthetic limb scan data sets at noise levels from 0% to 50%, shown in Fig. 5.28, differ from the independent temperature recovered profiles of Case 5 (Fig. 5.22). The scattered errors at mid altitudes at 40% and 50% for region A and at 50% for region B noted in Case 5 are not present. In addition the errors in the bottom of the OH Meinel airglow layer increase gradually to 30% at the lowest height level (at 30% error the fitting method fails to improve upon the *a priori* temperature profile) without the marked negative error near 50 km of Case 5.

The improvements are even more apparent in the pixel plot of RMS error,

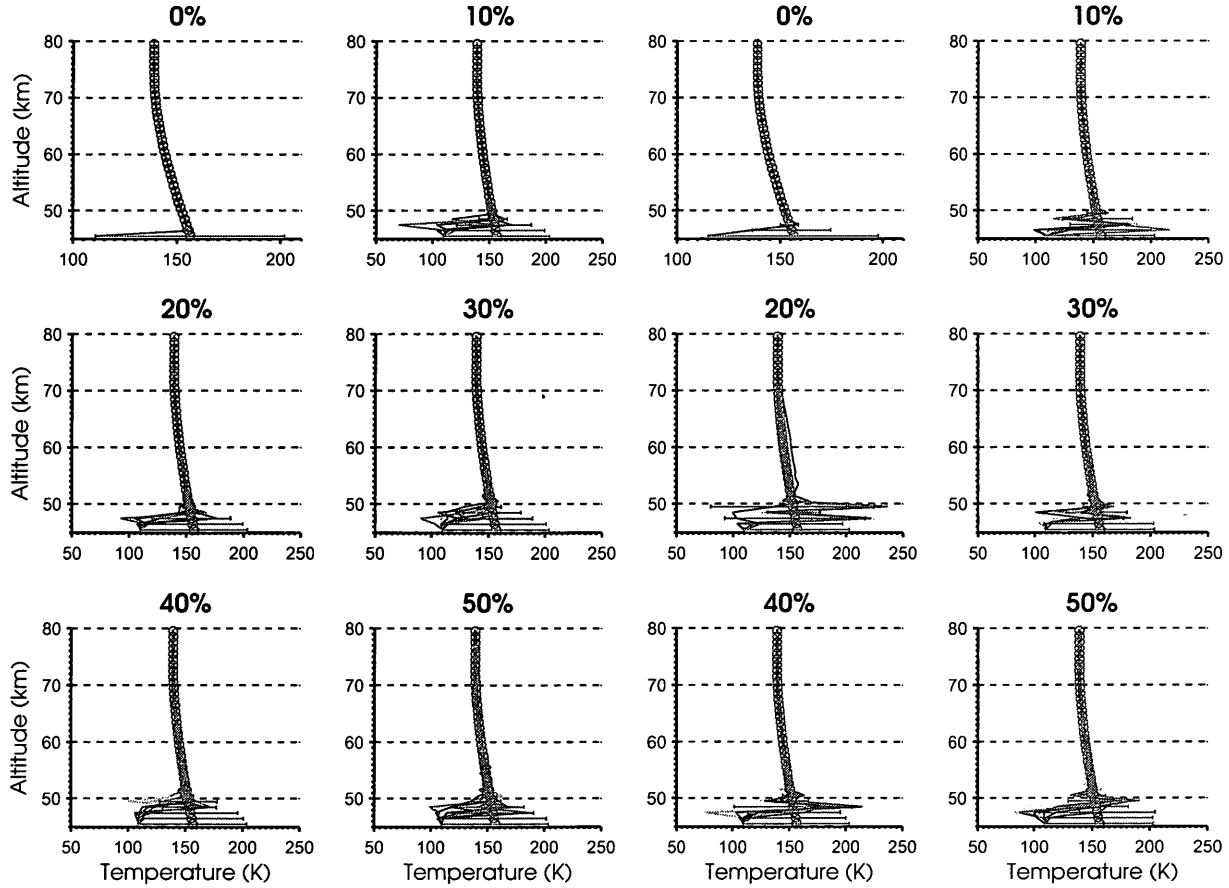

Figure 5.28: Case 7: Temperature profiles recovered while simultaneously retrieving volume emission rates from the 10 simulated limb observed spectra for noise levels ranging from 0 - 50%. The temperatures recovered from spectral region A are shown in leftmost two columns and from spectral region B in the rightmost two columns. The red circles indicate the true temperatures and the red error bars indicate the root mean square error of the 10 temperatures recovered at that height.

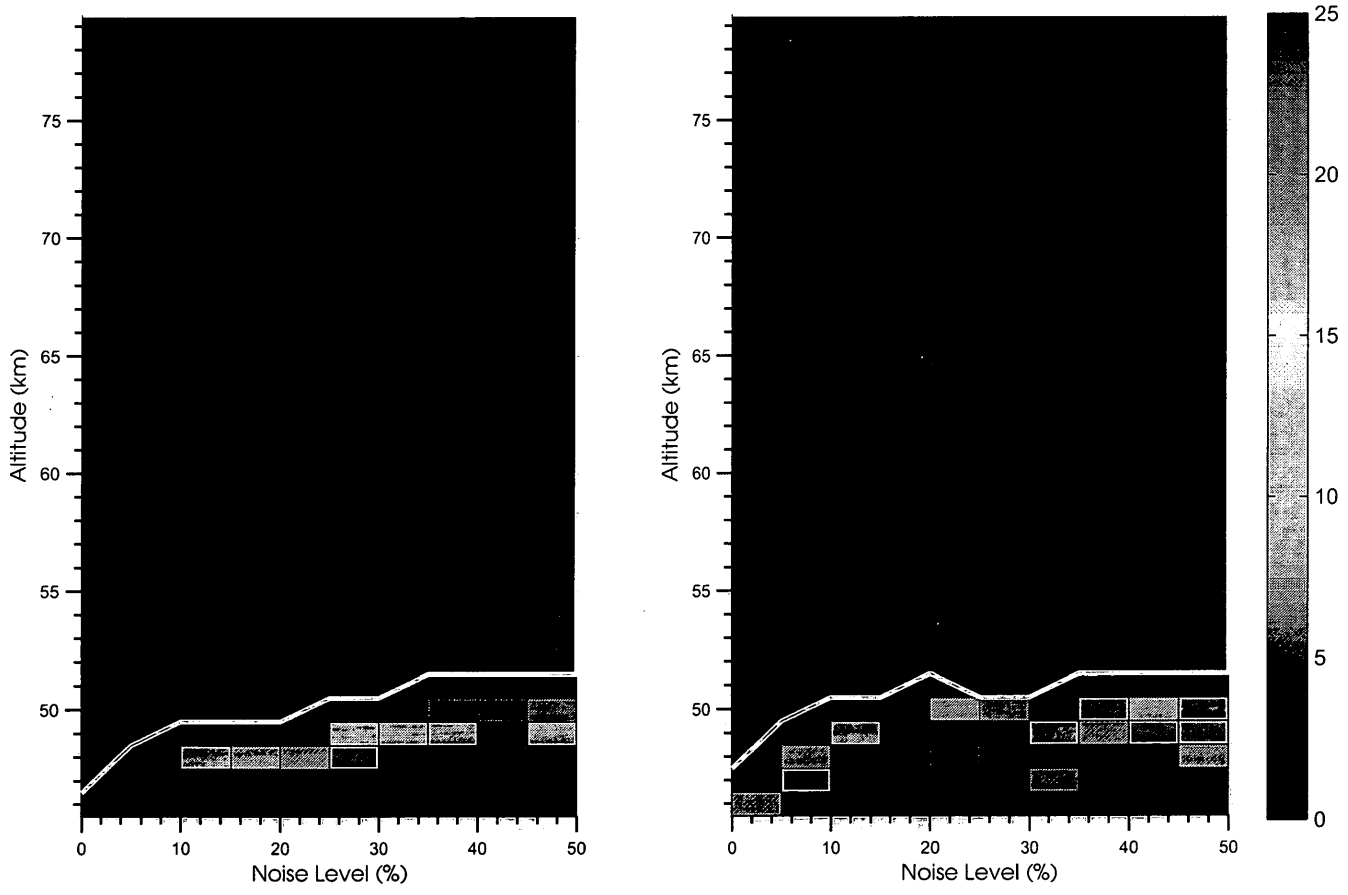

Figure 5.29: Case 7: pixel plot of the RMS error of the temperatures recovered along simultaneously with volume emission rates from the 10 simulated limb observations with noise levels ranging from 0-50%. RMS errors of profiles recovered from spectral region A are shown in the left panel and from spectral region B are shown in the right panel. The white line delineates the height ranges where the RMS error is less than 5 K. The units of the colour scale are in Kelvin.

Fig. 5.29. The increase in RMS error at the 50% noise level of Case 5 does not appear and the errors in the lowest height levels are confined to below 51.5 km. A slight increase in error occurs between 50 km and 70 km at the 20% noise level and a marginal increase in error occurs between 50 km and 60 km in the retrievals for higher noise levels. These regions of increased error correspond to regions of increased error in the VER retrieval error in both bands. This indicates an inter-relation of the retrieval of all three parameters. However, no clear cause could be identified.

The height range of recovered temperatures with retrieval error of less than 5 K can be found in Table 5.11, along with the root mean square error for all recovered temperatures within the range.

These results suggest that, overall, the simultaneous retrieval of temperatures and vibrational level volume emission rates using the Global Optimization retrieval method is preferable due to the significant improvement in temperature retrievals and only slightly less successful VER retrievals compared to the the independent retrieval of these parameters. However, the requirement for simultaneous retrieval of temperatures and VER that the lines of the negative set (P1(1), P1(2), Q1(1), Q1(2) and R1(1)) be in balance with the transition lines of the positive set (P1(3) - P1(14), P2(1) - P2(14), Q1(3) - Q1(14), Q2(1) - Q2(14), R1(2) - R1(14) and R2(1) - R2(14)) restricts the number of viable spectral regions.

Finally, when comparing the accuracy of the temperature and volume emission rate profile recovered using the Onion Peeling method, the approach using derived absolute WBR spectra and the Global Optimization method, this last method is clearly superior. The Global Optimization method is far less sensitive to noise and

	Region A		Region B			
	$v = 8$		$v = 1$		$v = 2$	
Noise Level	Height Range (km)	RMS (%)	Height Range (km)	RMS (%)	Height Range (km)	RMS (%)
0 %	46.5 - 79.5	0.02	46.5 - 79.5	0.65	46.5 - 79.5	0.82
5 %	48.5 - 79.5	1.64	49.5 - 79.5	1.59	49.5 - 79.5	1.16
10%	48.5 - 79.5	2.58	49.5 - 79.5	2.01	49.5 - 79.5	2.47
15%	49.5 - 79.5	2.38	50.5 - 79.5	2.79	50.5 - 79.5	2.60
20%	49.5 - 79.5	3.91	51.5 - 79.5	6.73	51.5 - 79.5	6.72
25%	50.5 - 79.5	4.48	51.5 - 79.5	6.32	51.5 - 79.5	6.28
30%	50.5 - 79.5	6.59	50.5 - 79.5	6.50	50.5 - 79.5	6.57
35%	51.5 - 79.5	8.61	50.5 - 79.5	8.97	50.5 - 79.5	9.00
40%	50.5 - 79.5	11.47	50.5 - 79.5	11.39	50.5 - 79.5	11.55
45%	54.5 - 79.5*	14.24	59.5 - 79.5	14.21	59.5 - 79.5*	14.43
*Some retrieved VERs in this range lie between 15% and 15.5%						

Table 5.10: Case 7: Height ranges of volume emission rate retrievals with less than 15% RMS error and total RMS percent error for recovered VER within the ranges.

	Region A		Region B	
Noise Level	Height Range (km)	RMS (K)	Height Range (km)	RMS (K)
0 %	46.5 - 79.5	0.3914	47.5 - 79.5	0.2413
5 %	48.5 - 79.5	0.6376	49.5 - 79.5	0.6913
10%	49.5 - 79.5	0.5283	50.5 - 79.5	0.3349
15%	49.5 - 79.5	0.8044	50.5 - 79.5	0.5829
20%	49.5 - 79.5	1.1087	51.5 - 79.5	1.5829
25%	50.5 - 79.5	0.9023	50.5 - 79.5	1.6328
30%	50.5 - 79.5	1.2136	50.5 - 79.5	1.0592
35%	51.5 - 79.5	1.018	51.5 - 79.5	1.1442
40%	51.5 - 79.5	1.35963	51.5 - 79.5	1.1835
45%	51.5 - 79.5	1.4998	51.5 - 79.5	1.1417
50%	51.5 - 79.5	1.6391	51.5 - 79.5	1.459

Table 5.11: Case 7: Height ranges of recovered temperatures with less than 5 K error and total RMS error of retrieved temperatures within the height ranges.

as such the accuracy of the recovered parameters in the presence of observational noise far surpasses the accuracy of the retrievals using either of the other two methods. The sole drawback of the Global Optimization method is that the simultaneous retrieval of all parameters from every height level is computationally expensive, but the recent advancements in computer technology mitigate this concern.

6 Instrument requirements

In this chapter the instrument requirements for the detection of the OH Meinel Band airglow in the Martian atmosphere will be discussed and the capacity for the retrieval of temperatures and volume emission rates from such observations will be assessed. No specifics regarding the instrument design will be discussed for two reasons: 1) an instrument designed to observe the infrared spectrum of the Martian atmosphere would likely have multiple research goals not solely the observation of the OH Meinel Bands and thus the design would have to allow for considerations beyond the scope of this work, and 2) any suggestions made here regarding possible technologies will likely become obsolete before the development of any such instrument. Instead the rough order of magnitude estimate of the optical requirements necessary for the observation of OH Meinel band airglow will be determined. Furthermore, the sensitivity of the retrieval to the vertical resolution and such optical properties as the spectral resolution and the sampling interval will be characterized.

6.1 Spectral Region

The first step in specifying instrument requirements is to identify a target spectral window. As discussed in the Introduction, observations of wavelength bin radiances (WBR) of transitions from $v' = 1$ or $v' = 2$ are required to discriminate between the three proposed deactivation models: Collisional Cascade, Sudden Death and the alternate model suggested by *Krasnopolsky* (2010). The vibrational distribution of the Sudden Death model is used as the limiting case as the emissions associated with this model are the weakest and thus the most difficult to detect. Emissions from low N' levels of the $v' = 1$ and the $v' = 2$ vibrational levels are more likely to be thermalized with the surrounding atmosphere. When thermalized, the rotational temperature of OH(v') corresponds to the temperature of the background atmosphere (*i.e.*, $T_{ROT} = T_{atm}$). Emission lines of low N' levels of intermediate v' levels could also be used as long as the expected errors due to NTLE rotation, shown in Fig. 2.7, are taken into account. In this work we restrict candidate spectral windows to those containing transitions from low N' levels of the $v' = 1$ and the $v' = 2$ vibrational levels.

Most low N' emissions of the (2-1) band overlap with emissions of the (1-0) band thus a retrieval algorithm incorporating emission from both bands is necessary. This adds an additional constraint since for the simultaneous retrieval of volume emission rates and temperatures there must be a balance between emissions which increase with increasing temperature (positive set) at Martian atmospheric temperatures and emissions which decrease with increasing temperature (negative set) as discussed in Chapter 5. These requirements greatly reduce the number of

possible target spectral regions. Furthermore the target spectral window must avoid any other possible strong nighttime emissions, such as the O_2 IR atmospheric band and CO_2 atmospheric emissions, which could contaminate the OH Meinel emission in the predominantly CO_2 atmosphere of Mars.

The most suitable spectral region is found to lie between $2.79\mu m$ and $2.95\mu m$, shown for all three deactivation models in Fig. 6.1. This is the spectral region we used to simulate retrievals from a region containing two bands in Chapter 5 and is described in greater detail therein. This spectral window avoids the strong emissions of the O_2 IR atmospheric band at 1.27 μm and the CO_2 4.3 μm atmospheric emission. The (1-0) and (2-1) bands which lie within this window have been unambiguously identified in the nighttime Venus atmosphere by the VIRTIS (*Piccioni et al.*, 2008) which suggests that these bands may also be detected on Mars. It is important to note that although this region contains emissions from high N' rotational levels of the (1-0) band, as listed in Table 5.2, these emissions are very weak in comparison to the emissions from low N' levels of the (1-0) and (2-1) bands. Their inclusion should not introduce significant error as discussed in Chapter 2.

Another possible approach is to select a set of micro windows that meet the requirements and fit them simultaneously. Although this approach is not explored in this work, it has the potential to add flexibility to the spectral window selection process.

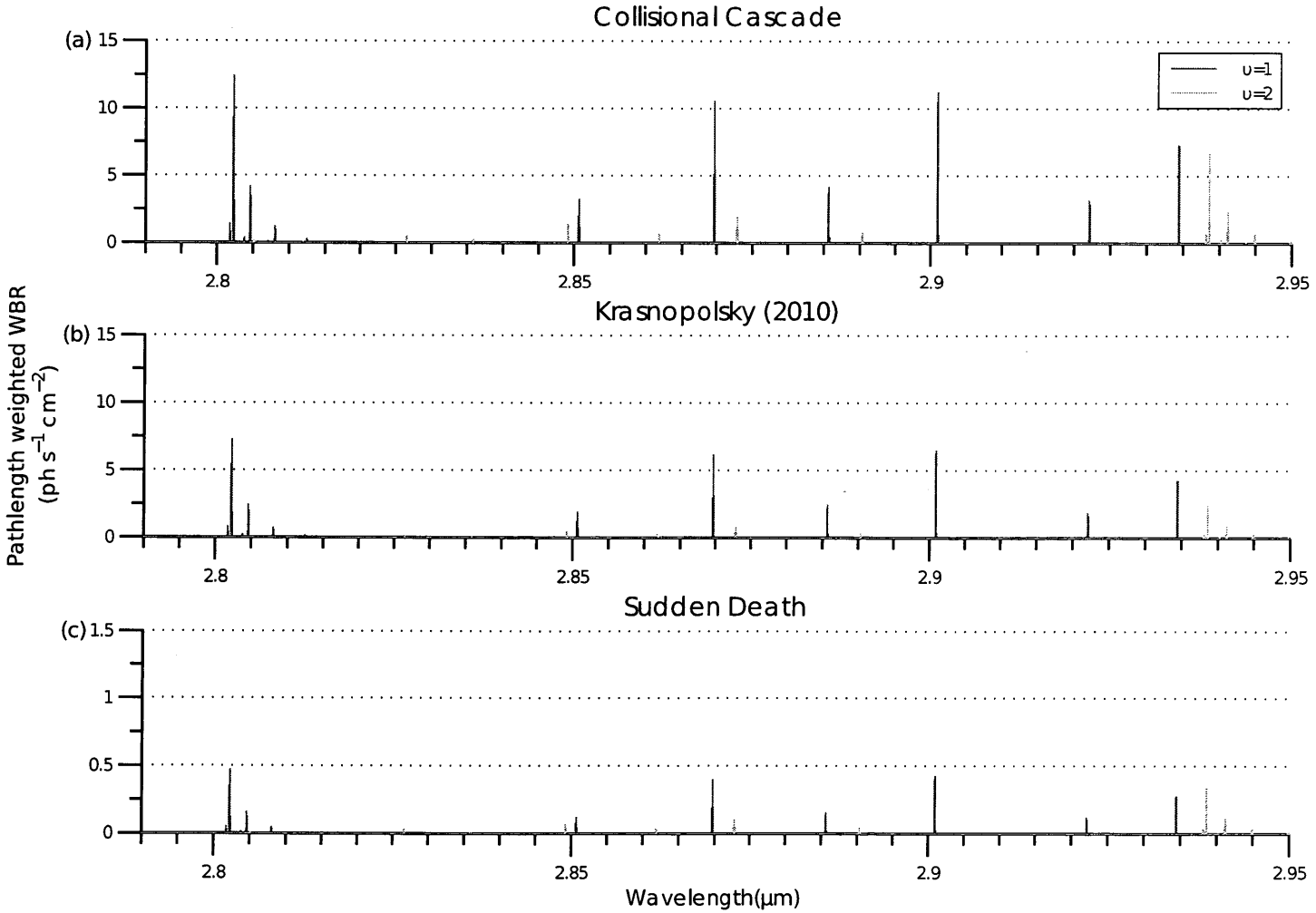

Figure 6.1: Synthetic pathlength weighted wavelength bin radiance spectrum of target spectral region (2.79 μm - 2.95 μm) a tangent height of 79.5 km for the three deactivation models: (a) the Collision Cascade deactivation model (b) the model suggested by *Krasnopolsky* (2010) and (c) the Sudden Death model.

0.6 is used.

Shot noise arises due to the random arrival rate of photons on the detector. This random arrival rate takes the form of a Poisson distribution. The standard deviation in the measurement of N photoelectrons is $\sqrt{N}$ (*Shepherd*, 2002). For $q_e\mathbf{R}^{\mathbf{full}}t_sA\Omega$ phototelectrons, the shot noise will be $\sqrt{q_e\mathbf{R}^{\mathbf{full}}t_sA\Omega}$ and is added in quadrature to the other sources of noise. η_D is the dark noise produced by thermally generated carriers. It is common practice to cool remote sensing instruments, to reduce the dark current noise to a negligible level. η_R is the read out noise. Modern detectors are designed to have low readout noise levels and employ techniques such as multiple correlated sampling and electron multiplication by the detectors internal gain to lower the readout noise (*Magnan*, 2011). In addition various post-processing methods are also used to further reduce the effects of readout noise on observations (*Snyder et al.*, 1995). Although neither dark current noise nor readout noise can be completely suppressed, in this work it is assumed that these types of noise are negligible and that observations are shot noise limited. Thus the SNR is calculated as follows,

$$SNR = \frac{q_e\mathbf{R}^{\mathbf{full}}t_sA\Omega}{\sqrt{q_e\mathbf{R}^{\mathbf{full}}t_sA\Omega}} \tag{6.2}$$

Therefore, in a sense, the results presented here represent the upper limit in terms of signal to noise ratio for the given $t_sA\Omega$ magnitude.

6.3 Detection

For unambiguous detection of OH Meinel Band nightglow in the Martian atmosphere it is necessary that the observed emission exceed the noise by a reasonable amount. In this work we will assume the limit of detection as recommended in *Montmessin et al.* (2011) for the positive detection of the ozone Hartley band in the atmosphere of Venus: For definite identification the observed signal must exceed the noise level by a factor of five, or in other words the signal-to-noise ratio must exceed 5. However, it is not necessary that all emissions in the spectral region meet this requirement, nor is it necessary that the signal-to-noise ratio be met throughout the limb scan. The peak SNR of the entire simulated limb scan, meaning the highest SNR value for all observations for all tangent heights, using the modeled volume emission rates of the Sudden Death deactivation model from *García Muñoz et al.* (2005) with a resolution of $1\mathring{A}$ and sampling interval of $1\mathring{A}$ are compared to determine a rough order of magnitude estimate of the $t_s A\Omega$ necessary for detection. As shown in Fig 6.2 (a) at a $t_s A\Omega$ of 10^{-5} s cm^2 sr, the peak SNR is greater than 5. The peak SNR is 7.55 at 29 387 $\mathring{A}$ for the tangent height of 59.5 km and is the P1(1) emission of the OH(2-1) band. At this value of $t_s A\Omega$, the SNR for the P1(2) emission of the OH(1-0) band for tangent heights between 53.5 and 70.5 km, the Q1(1) emission of the same band for tangent heights 48.5 - 72.5 km and the Q1(1) emission of the (2-1) band for tangent heights between 45.5 and 71.5 km are all above the detection limit. Detection of these three emission lines would confirm the presence of OH Meinel Band airglow in the Martian atmosphere.

At $t_s A\Omega = 10^{-5}$ s cm^2 sr the peak signal-to-noise ratio for the Collisional Cas-

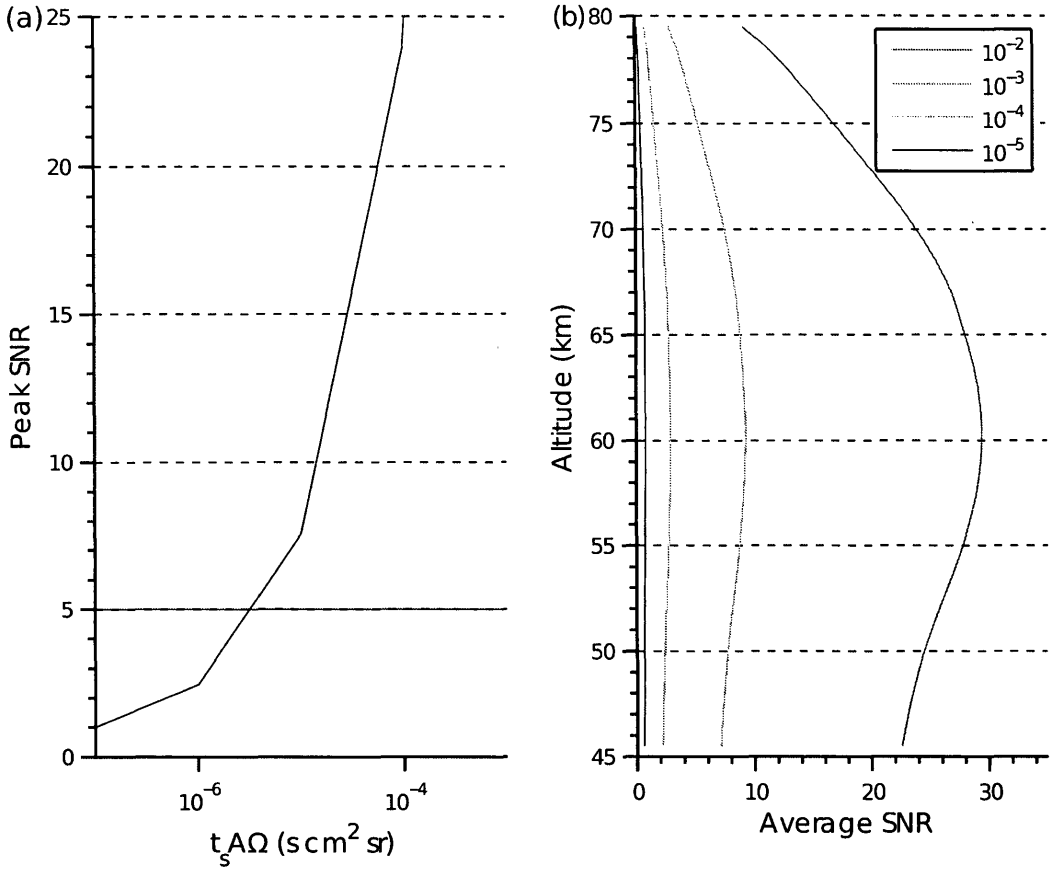

Figure 6.2: Effects of varying the $t_s A\Omega$ value on the signal to noise ratio for the Sudden Death deactivation model for observations with Poisson noise. In (a) the SNR of the observation with the highest SNR for all sampled wavelengths in the 2.79 μm - 2.95 μm region and for all tangent heights are plotted against $t_s A\Omega$. The red solid line indicates the detection limit. In (b) the average of the non-zero SNRs for a given tangent height is plotted for $t_s A\Omega$ values from 10^{-5} to 10^{-2} s cm^2 sr.

cade model is 154.7 and for the model suggested in *Krasnopolsky* (2010) the peak SNR is 113.3, both well above the detection limit.

However, temperature and volume emission rate retrieval at this throughout would not be possible under the Sudden Death deactivation model. The requirements for retrieval will be discussed in detail in the following section.

6.4 Temperature and volume emission rate retrieval

For accurate simultaneous retrieval of temperatures and volume emission rates it is important that the majority of the emission lines within the target spectral region exceed the detection limit as the balance between the emission lines that decrease with temperature and those that increase must be maintained. In addition it is critical that this balance is conserved for a range of tangent heights for a profile to be recovered. Therefore the average signal-to-noise ratios for each tangent height, *i.e.*, the average of all non-zero SNR values in the target spectral region for the given tangent height, at each test $t_s A\Omega$ value will be compared to determine the $t_s A\Omega$ necessary for retrieval of temperatures and VERs. As the Global Optimization method was determined to be the most robust of the retrieval methods discussed in Chapter 5, it is used in these temperatures and volume emission rates retrievals. Poisson noise is used to simulate the shot noise. A vertical resolution of 1 km, a Gaussian instrument function with a spectral resolution of $1\mathring{A}$ and a sampling interval of $1\mathring{A}$ are used for these simulations. The effects of varying the resolution, sampling interval and vertical resolution will be discussed in the following section.

The average SNR for a $t_s A\Omega$ of 10^{-5} s cm^2 sr, shown in Fig. 6.2 (b), is near 0 at all

heights and thus retrieval of temperatures and VERs for the Sudden Death Model would not be possible. As shown in Fig 6.3, the temperature and volume emission rate profiles recovered from simulated observations under the Sudden Death model with a $t_s A\Omega$ of 10^{-5} s cm^2 sr oscillate wildly, never approaching the true profiles and in most cases are more erroneous than the *a priori* profile.

However, for the Collision Cascade model and *Krasnopolsky* (2010) model retrieval of temperatures and volume emission rates are possible. The temperature and VER profiles recovered during the 10 Collisional Cascade realizations, shown in Fig. 6.4 all follow a similar form. The profile can be divided into four altitude regions: from the top of the airglow layer downward the VER are increasing in altitude region 1, then peak in region 2, start decreasing in region 3 and are very weak in region 4 (see Fig 1.2 and Fig 1.4).

In the first altitude region, composed of the uppermost heights of the OH Meinel Band airglow layer, all recovered profiles for the three sought after parameters are prone to error at the topmost height levels; 5 K, 3% and 9% RMS error for temperature, $v' = 1$ VER and $v' = 2$ VER, respectively. This inaccuracy is due to the relatively weak emission at the highest point of the emission layer, as shown in Fig 1.2 and Fig. 1.4 and consequently lower signal-to-noise ratios. As the altitude decreases, the volume emission rates increase and the amount of error decreases which causes the SNR to increase, reaching a region of relatively constant error.

This second altitude region comprises heights in the middle of the OH Meinel airglow layer, which coincides with height of the peak emission of the OH Meinel nightglow. The RMS value of this near constant error value is 1 K, 0.5% and 1% for the three aforementioned parameters.

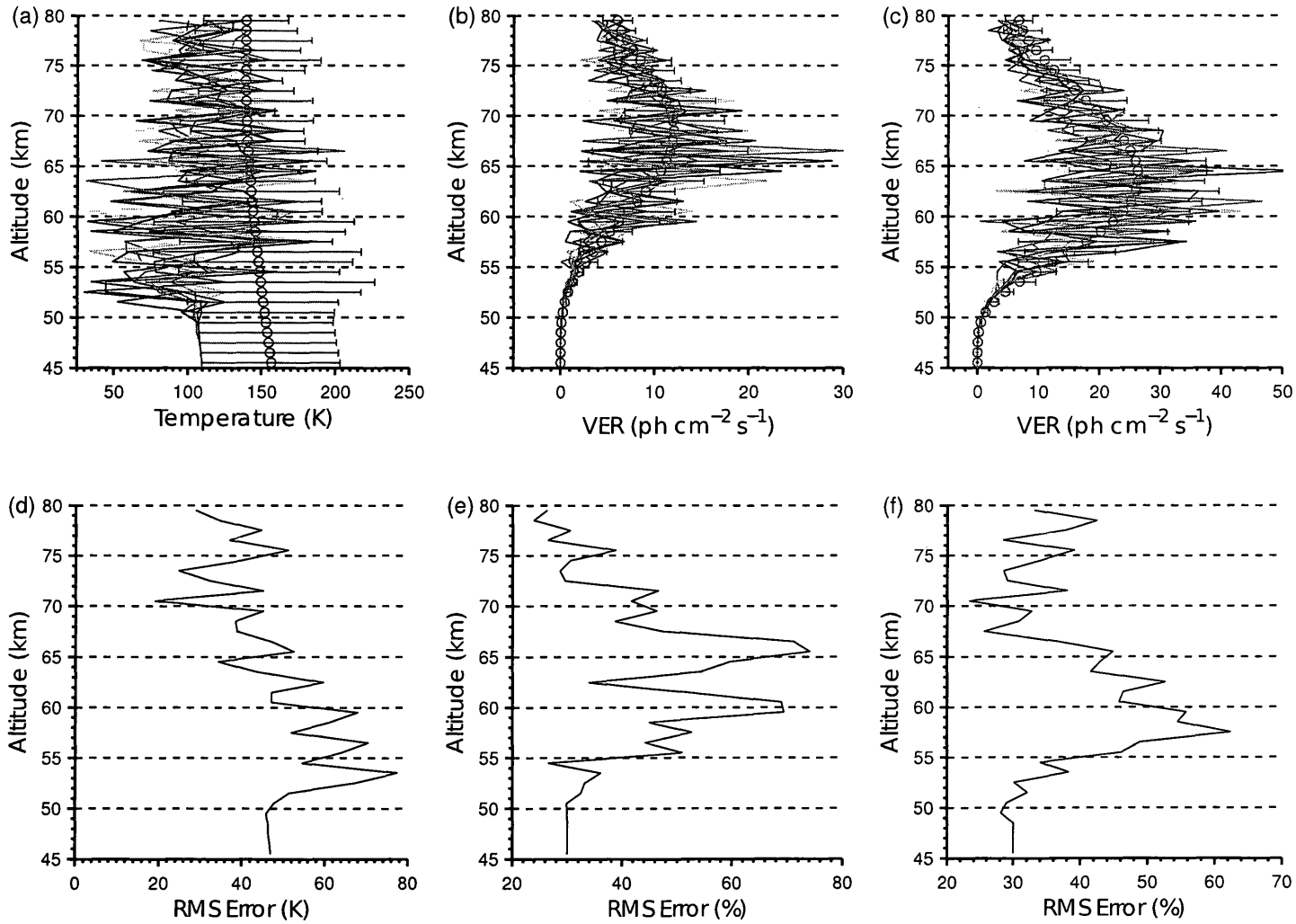

Figure 6.3: The recovered temperature and volume emission rate profiles for the $v' = 1$ and $v' = 2$ vibrational levels are plotted for 10 sets of synthetic limb observations of the 2.79 μm - 2.95 μm region in (a), (b) and (c), respectively. The observations were simulated for the Sudden Death model with a $t_s A\Omega$ of 10^{-5} s cm^2 sr at a 1 $\mathring{A}$ resolution and sampling interval of 1 $\mathring{A}$ and with Poisson noise. The red circles indicate the true profiles and the red error bars indicate the RMS errors. The temperature RMS errors are plotted in (d) and VER RMS errors for the $v' = 1$ and $v' = 2$ are plotted in (e) and (f).

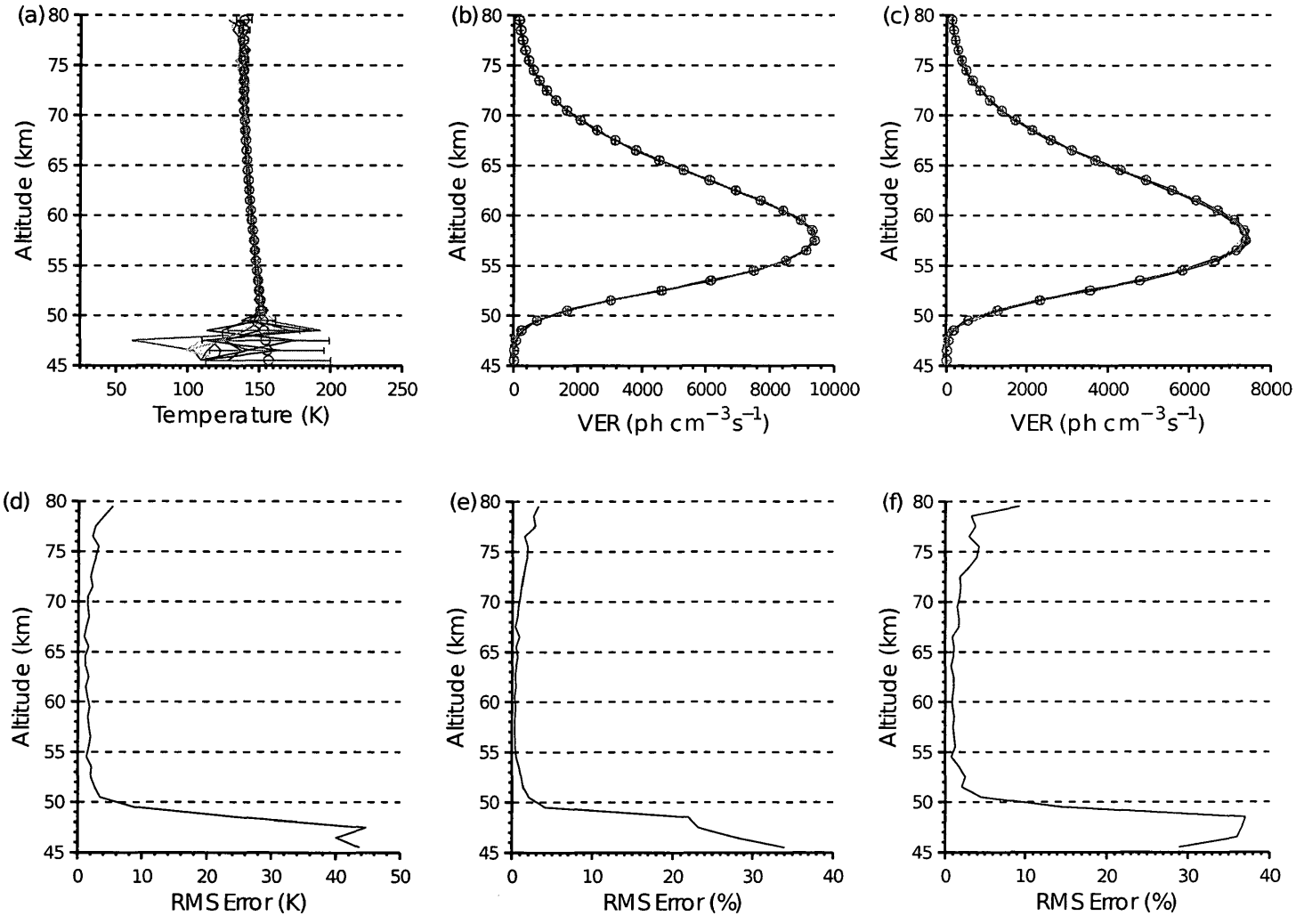

Figure 6.4: The recovered temperature and volume emission rate profiles for the $v' = 1$ and $v' = 2$ vibrational levels are plotted for 10 sets of synthetic limb observations of the 2.79 μm - 2.95 μm region in (a), (b) and (c), respectively. The observations were simulated for the Collisional Cascade model with a $t_s A\Omega$ of 10^{-5} s cm^2 sr at a 1 $\AA$ resolution and sampling interval of 1 $\AA$ and with Poisson noise. The red circles indicate the true profiles and the red error bars indicate the RMS errors. The temperature RMS errors are plotted in (d) and VER RMS errors for the $v' = 1$ and $v' = 2$ are plotted in (e) and (f).

The third and fourth altitude regions cover approximately the 45.5 - 54.5 km height levels. In these regions the recovered parameters shift towards their *a priori* values and consequently the errors begin to increase as the height decreases. The increase in error is gradual in region 3, which comprises only a few heights and then the error increases more sharply in region 4, which comprises the remaining height levels. The reason for this shift is likely the optimization methods inability to properly distinguish the emission from the shot noise. The observed signal at these tangent heights is quite strong, as the instrument's line of sight crosses through the majority of the airglow layer, and consequently the shot noise of $\sqrt{N}$ noise is notable but not comparable to the observed emission. However, the contribution to the observed emission that is emitted from the tangent height layer is relatively small and is commensurate to the shot noise of the total signal. In addition these parameters are less constrained as the emission from their corresponding tangent heights contribute to fewer observations and are thus more prone to error.

The same general form, *i.e.*, minor error at the topmost layers decreasing to a minimum near the peak height of the OH Meinel emission and then increasing to maximum error at the bottommost heights, is apparent in recovered profiles for the model suggested by *Krasnopolsky* (2010), however there are other minor differences. The same form is also noted, with a reduction in the degree of the errors, in the recovered profiles for a hypothetical instruments with increased $t_s A\Omega$ discussed later in this section.

In the profiles recovered from the simulated observations for the model suggested by *Krasnopolsky* (2010), shown in Fig. 6.5, there are two distinctions from the form discussed above. First, the errors in the $v' = 2$ VER profile are larger: the peak

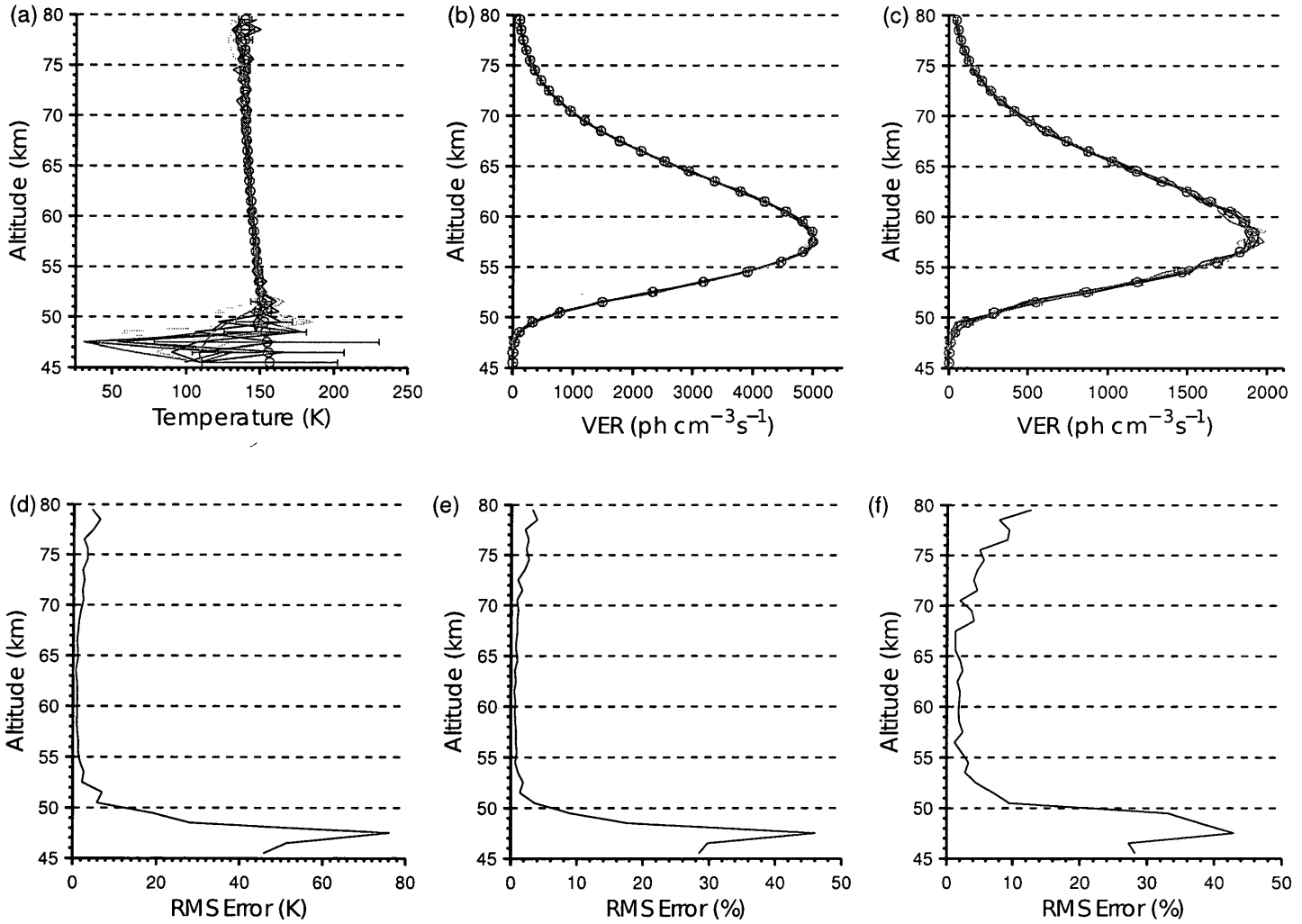

Figure 6.5: The recovered temperature and volume emission rate profiles for the $v' = 1$ and $v' = 2$ vibrational levels are plotted for 10 sets of synthetic limb observations of the 2.79 μm - 2.95 μm region in (a), (b) and (c), respectively. The observations were simulated for the *Krasnopolsky* (2010) model with a $t_s A\Omega$ of 10^{-5} s cm^2 sr at a 1 $\mathring{A}$ resolution and sampling interval of 1 $\mathring{A}$ and with Poisson noise. The red circles indicate the true profiles and the red error bars indicate the RMS errors. The temperature RMS errors are plotted in (d) and VER RMS errors for the $v' = 1$ and $v' = 2$ are plotted in (e) and (f).

at the top of the layer reaches 17% RMS error and consistent error value in the mid altitudes is 2%. This is likely caused by the relative weakness of the $v' = 2$ emission in comparison to the $v' = 1$ emission in this model (see Fig 1.4). The RMS error values for temperature and $v' = 1$ volume emission rates are similar to the Collisional Cascade model retrieval errors. The second distinction is that in all recovered profiles the retrieved parameters decrease to a deep minimum near 46.5 km - 48.5 km then increase again approaching the *a priori* value at the bottommost layers. This minimum corresponds to the peak in RMS error near the bottom of the emission layer shown in Fig. 6.5.

Measurements from a limb scanning instrument with a $t_s A\Omega$ of 10^{-5} s cm^2 sr would make it possible to (a) establish the presence of OH Meinel Band airglow in the Martian atmosphere, (b) substantiate one of the three deactivation models or provide evidence to support a new model and, should either the Collisional Cascade or the *Krasnopolsky* (2010) model prove to be valid, (c) recover temperatures and volume emission rates of the $v' = 1$ and $v' = 2$ levels.

At a $t_s A\Omega$ value of 10^{-4} s cm^2 sr the average signal-to-noise ratio for the Sudden Death model exceeds 1 for all but the 79.5 km height level and exceeds 2, or 50% noise, for all tangent heights below 71.5 km as shown in Fig. 6.2 (b). This amount of noise proves to be excessive for the Global Optimization method. The recovered profiles from the 10 realizations bear no resemblance to the true profiles as shown in Fig 6.6.

For both the Collisional Cascade and the *Krasnopolsky* (2010) models the recovered profiles using a hypothetical instrument with a $t_s A\Omega$ on the order of 10^{-4} s cm^2 sr follow the aforementioned general form, however there is a notable improvement

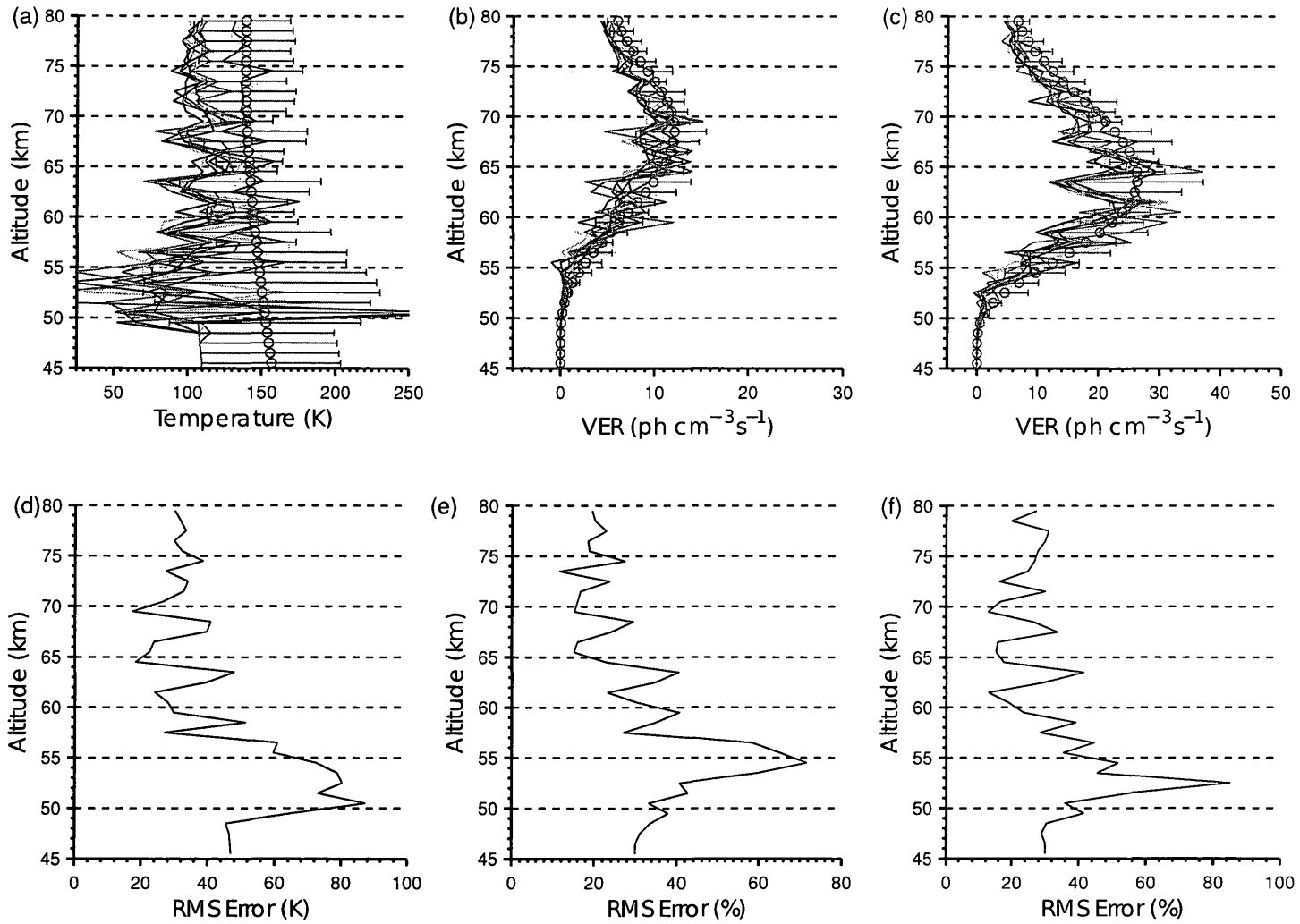

Figure 6.6: The recovered temperature and volume emission rate profiles for the $v' = 1$ and $v' = 2$ vibrational levels are plotted for 10 sets of synthetic limb observations of the 2.79 μm - 2.95 μm region in (a), (b) and (c), respectively. The observations were simulated for the Sudden Death model with a $t_s A\Omega$ of 10^{-4} s cm^2 sr at a 1 $\mathring{A}$ resolution and sampling interval of 1 $\mathring{A}$ and with Poisson noise. The red circles indicate the true profiles and the red error bars indicate the RMS errors. The temperature RMS errors are plotted in (d) and VER RMS errors for the $v' = 1$ and $v' = 2$ are plotted in (e) and (f).

$t_s A\Omega$ s cm^2 sr		Collision Cascade model 10^{-3}	10^{-4}	10^{-5}	*Krasnopolsky* (2010) model 10^{-3}	10^{-4}	10^{-5}
Altitude Region	Temperature	0.26K	1.06K	5.29K	0.36K	1.39K	6.87K
1 peak	$v' = 1$ VER	0.3%	0.9%	3.2%	0.3%	0.9%	4.5%
RMS error	$v' = 2$ VER	0.4%	1.4%	9.2%	0.8%	2.8%	14.3%
Altitude Region	Temperature	0.07K	0.31K	0.6K	0.1K	0.34K	1.05K
2 average	$v' = 1$ VER	0.05%	0.2%	0.4%	0.07%	0.2%	0.8%
RMS error	$v' = 2$ VER	0.1%	0.2%	1%	0.2%	0.6%	1.9%

Table 6.1: Comparison of retrieval accuracy from synthetic observations under the Collisional Cascade and *Krasnopolsky* (2010) deactivation models with $t_s A\Omega$ values of 10^{-3}, 10^{-4} and 10^{-5} s cm^2 sr.

in accuracy in comparison to the hypothetical instrument with a $t_s A\Omega$ value of 10^{-5} s cm^2 sr. The recovered profiles using the total volume emission rates derived under these models are shown in Fig. 6.7 and Fig. 6.8, respectively. The errors in altitude region 1 are diminished and the near constant errors at mid-altitudes of altitude region 2 are also reduced. The errors in the third and fourth regions are relatively unchanged. These improvements are summarized in Table 6.1.

Finally for a hypothetical instrument with a $t_s A\Omega$ value of 10^{-3} s cm^2 sr the Sudden Death model average signal-to-noise ratio for the target spectral region has a minimum of 3 and exceeds 5, our detection limit, for heights between 45.5 km and 75.5 km as shown in Fig. 6.2 (b). The RMS error for the 10 realizations, shown in Fig. 6.9, remains fairly constant above 60.5 km for all three recovered profiles with an average RMS error of 2.3 K for temperatures and 1.7% and 2.4% for the volume emission rates of the $v' = 1$ and $v' = 2$ vibrational levels. Below 60.5 km the magnitude of retrieval error gradually increases in all three recovered profiles. Below 56.5 km for the recovered $v' = 1$ VER profiles and below 54.5 km

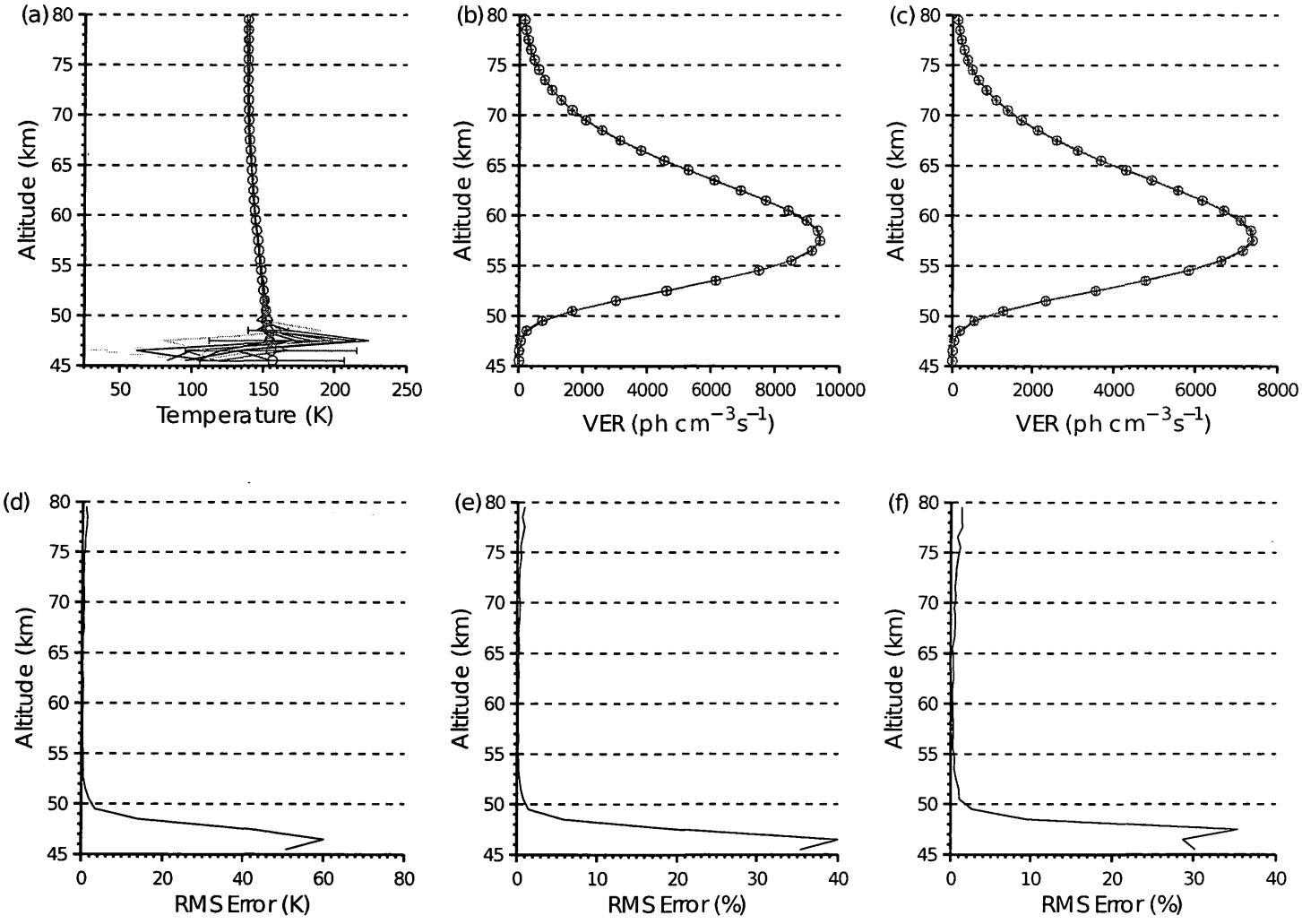

Figure 6.7: The recovered temperature and volume emission rate profiles for the $v' = 1$ and $v' = 2$ vibrational levels are plotted for 10 sets of synthetic limb observations of the 2.79 μm - 2.95 μm region in (a), (b) and (c), respectively. The observations were simulated for the Collisional Cascade model with a $t_s A\Omega$ of 10^{-4} s cm^2 sr at a 1 $\mathring{A}$ resolution and sampling interval of 1 $\mathring{A}$ and with Poisson noise. The red circles indicate the true profiles and the red error bars indicate the RMS errors. The temperature RMS errors are plotted in (d) and VER RMS errors for the $v' = 1$ and $v' = 2$ are plotted in (e) and (f).

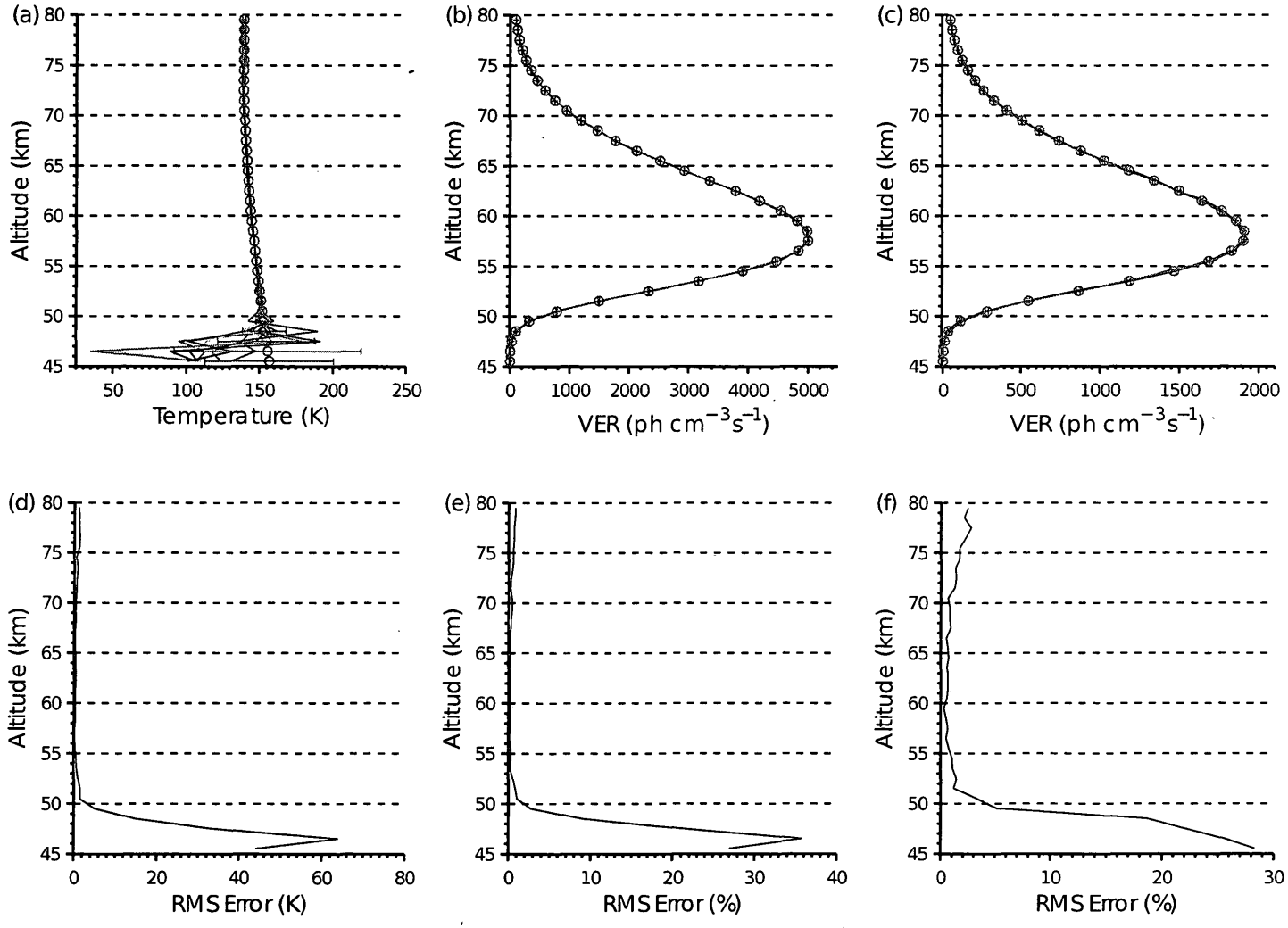

Figure 6.8: The recovered temperature and volume emission rate profiles for the $v' = 1$ and $v' = 2$ vibrational levels are plotted for 10 sets of synthetic limb observations of the 2.79 μm - 2.95 μm region in (a), (b) and (c), respectively. The observations were simulated for the *Krasnopolsky* (2010) model with a $t_s A\Omega$ of 10^{-4} s cm^2 sr at a 1 $\mathring{A}$ resolution and sampling interval of 1 $\mathring{A}$ and with Poisson noise. The red circles indicate the true profiles and the red error bars indicate the RMS errors. The temperature RMS errors are plotted in (d) and VER RMS errors for the $v' = 1$ and $v' = 2$ are plotted in (e) and (f).

for the temperature and the $v' = 2$ VER profiles the recovered parameters increase sharply, then oscillate while gradually shifting towards and finally converging on their *a priori* values for the three bottommost heights. The error trends in the recovered profiles bear some resemblance to the form noted in the retrievals for the other two deactivation models. Accurate retrievals are possible at a $t_s A\Omega$ on the order of 10^{-3} s cm^2 sr for the Sudden Death deactivation model but are limited to the heights above 60.5km.

Again the accuracy of the recovered profiles under the Collisional Cascade, shown in Fig. 6.10, and the model suggested in *Krasnopolsky* (2010), shown in Fig. 6.11, increases with the increase in $t_s A\Omega$. The slightly larger error at the top of the OH Meinel airglow layer noted in the retrievals for the previous two $t_s A\Omega$ values is almost nonexistent. The root mean square errors are compared to the retrieval errors of with lower $t_s A\Omega$ values in Table 6.1.

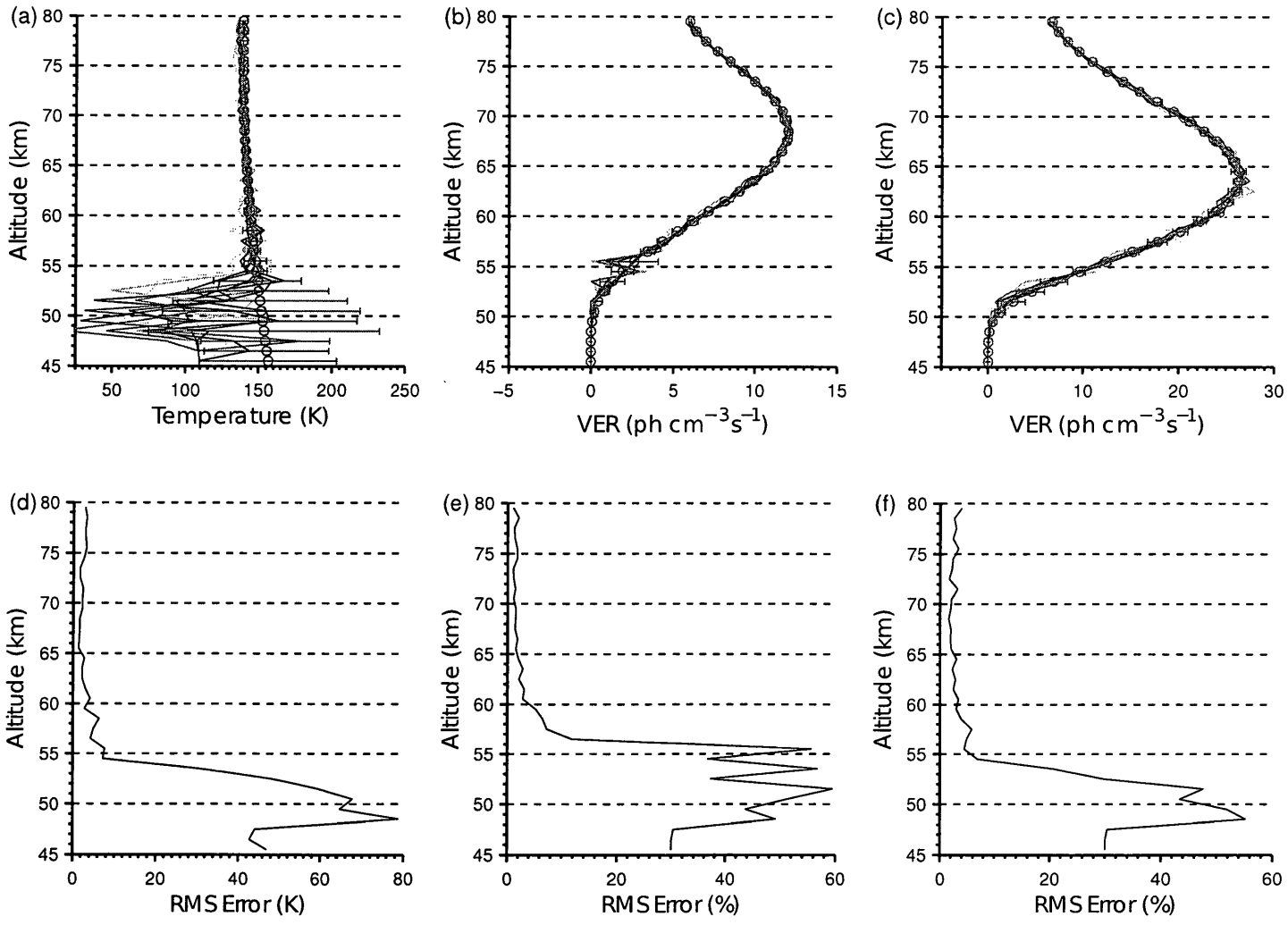

Figure 6.9: The recovered temperature and volume emission rate profiles for the $v' = 1$ and $v' = 2$ vibrational levels are plotted for 10 sets of synthetic limb observations of the 2.79 μm - 2.95 μm region in (a), (b) and (c), respectively. The observations were simulated for the Sudden Death model with a $t_s A\Omega$ of 10^{-3} s cm^2 sr at a 1 $\mathring{A}$ resolution and sampling interval of 1 $\mathring{A}$ and with Poisson noise. The red circles indicate the true profiles and the red error bars indicate the RMS errors. The temperature RMS errors are plotted in (d) and VER RMS errors for the $v' = 1$ and $v' = 2$ are plotted in (e) and (f).

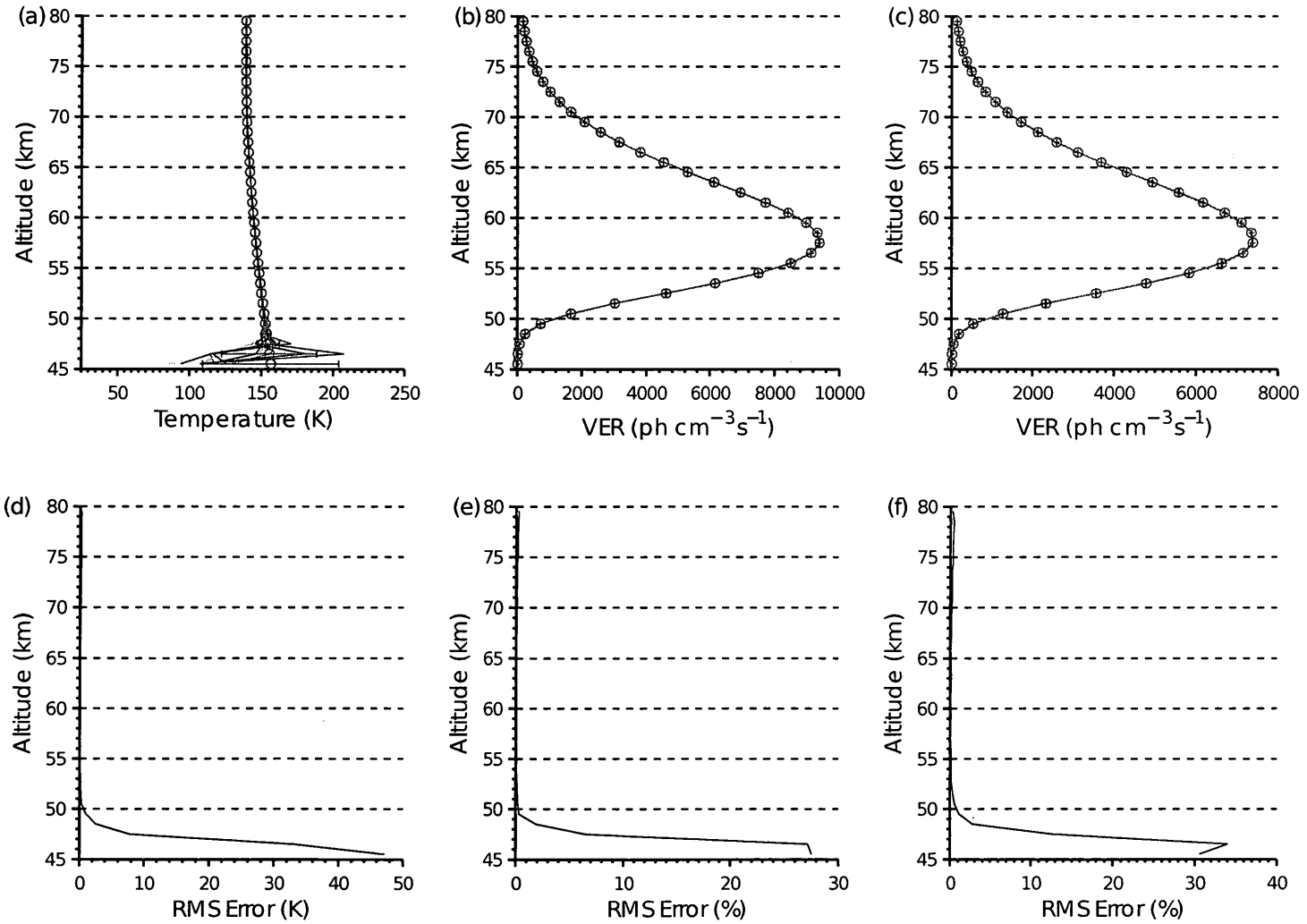

Figure 6.10: The recovered temperature and volume emission rate profiles for the $v' = 1$ and $v' = 2$ vibrational levels are plotted for 10 sets of synthetic limb observations of the 2.79 μm - 2.95 μm region in (a), (b) and (c), respectively. The observations were simulated for the Collisional Cascade model with a $t_s A\Omega$ of 10^{-3} s cm^2 sr at a 1 $\mathring{A}$ resolution and sampling interval of 1 $\mathring{A}$ and with Poisson noise. The red circles indicate the true profiles and the red error bars indicate the RMS errors. The temperature RMS errors are plotted in (d) and VER RMS errors for the $v' = 1$ and $v' = 2$ are plotted in (e) and (f).

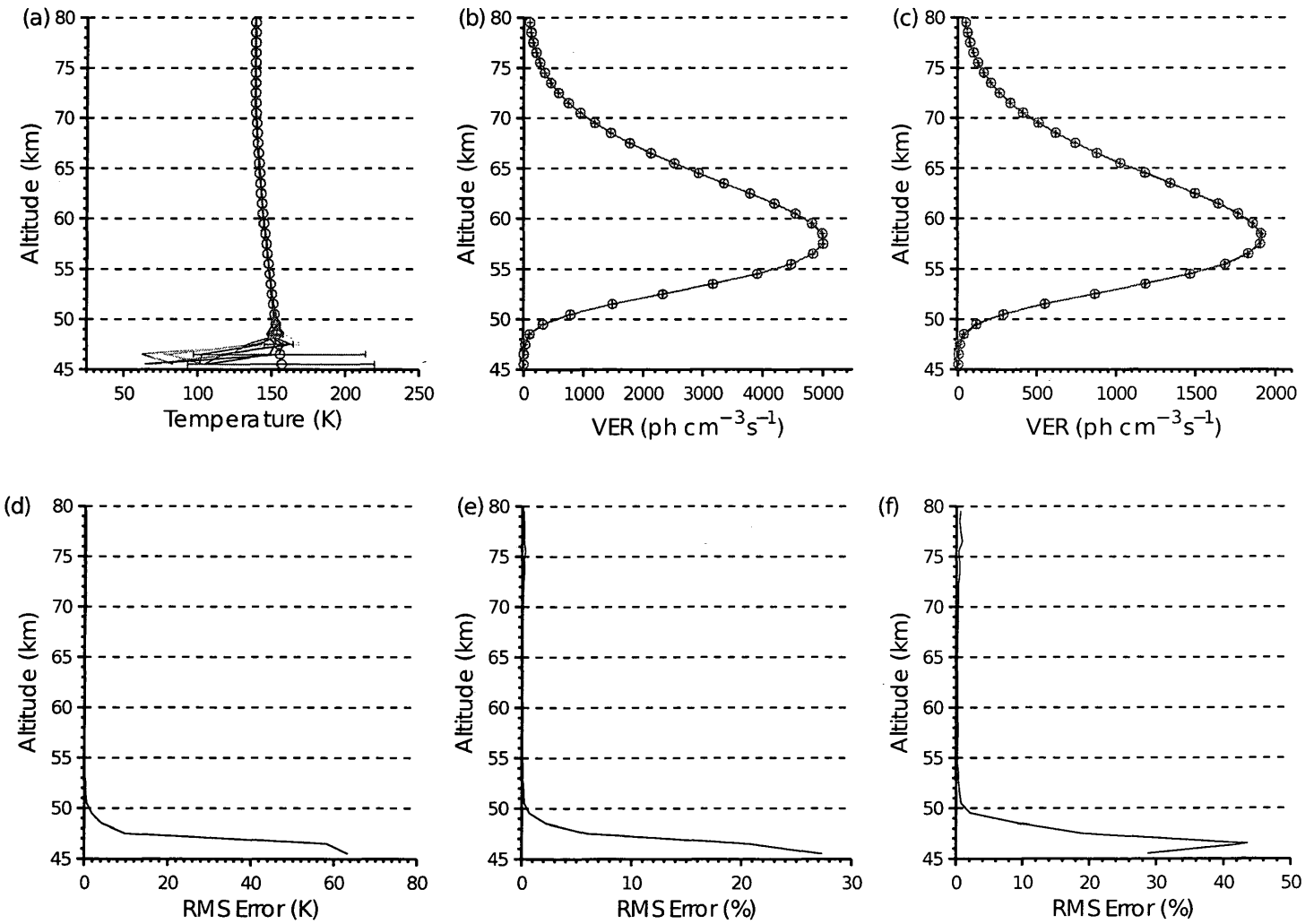

Figure 6.11: The recovered temperature and volume emission rate profiles for the $v' = 1$ and $v' = 2$ vibrational levels are plotted for 10 sets of synthetic limb observations of the 2.79 μm - 2.95 μm region in (a), (b) and (c), respectively. The observations were simulated for the *Krasnopolsky* (2010) model with a $t_s A\Omega$ of 10^{-3} s cm^2 sr at a 1 $\mathring{A}$ resolution and sampling interval of 1 $\mathring{A}$ and with Poisson noise. The red circles indicate the true profiles and the red error bars indicate the RMS errors. The temperature RMS errors are plotted in (d) and VER RMS errors for the $v' = 1$ and $v' = 2$ are plotted in (e) and (f).

6.5 Sensitivity studies: Effect of varying sampling interval, spectral resolution and vertical resolution on retrieval

In the previous simulations the synthetic observations have been generated for an instrument with a fairly high resolution ($1\mathring{A}$), sampling interval of $1\mathring{A}$ (1 observations per $1\mathring{A}$) and vertical resolution (1 km), however observations of this quality may not be possible. In this section the effects of varying these optical and viewing properties on the observations and on possible retrievals are assessed.

First, to evaluate the sensitivity of the observations, the peak and average signal-to-noise ratios for varying spectral resolutions, sampling intervals and vertical resolutions are compared in Fig. 6.12.

A decrease in resolution, *i.e.*, an increase in width of the instrument function, effectively broadens the observed emission lines and correspondingly decreases the peak intensity of the instrument function, thus decreasing the peak signal to noise ratio in a given wavelength bin while simultaneously increasing the wings. The peak SNR decreases exponentially with decreasing resolution, as shown in Fig. 6.12 (a) and the signal away from the line centres will be somewhat increased. However, since Possion noise is proportional to the square root of the signal, a small increase of a weak signal will have very little effect on the SNR. The result of which is to maintain the SNR necessary for retrieval any decrease in resolution would require an increase in signal which can be achieved by increasing $t_s A\Omega$. We have not taken into account the resolution requirements for atmospheric background removal. In addition it is desirable to distinguish the P, Q and R branches of the transitions which requires a relatively fine resolution.

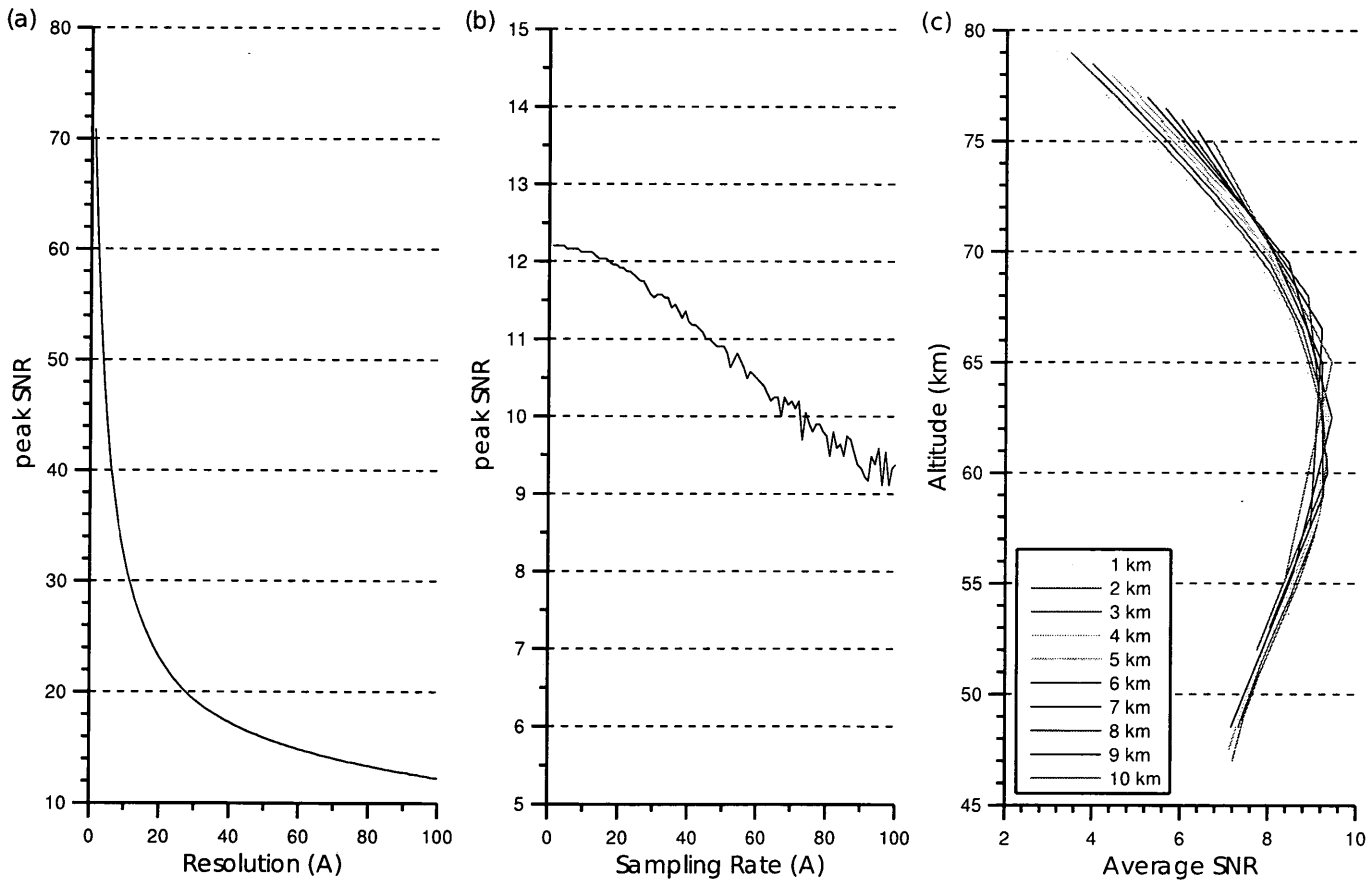

Figure 6.12: Sensitivity of SNR to spectral resolution, sampling interval and vertical resolution for observations with Poisson noise. The peak SNR for varying spectral resolutions and peak SNR for varying sampling intervals are compared in (a) and (b), respectively. The average SNR at different tangent heights for varying vertical resolutions are compared in (c).

The sampling interval does not directly affect the intensity of the signal, just the measurement wavelengths, thus the peak signal-to-noise ratio varies little with differing sampling intervals, shown in Fig. 6.12 (b). Accordingly, the recovered temperature and volume emission rate profiles and their associated RMS error for simulated observations with 20$\mathring{A}$ resolution and a $t_s A\Omega$ value of 10^{-2} s cm^2 sr, shown in Fig. 6.13, vary only slightly with sampling interval. However, the sampling interval is directly related to the number of observations made by the instrument within the spectral region; *i.e.*, an increase in sampling interval by a factor of 2 decreases the number of observations by half. As discussed in Chapter 5 the accuracy of the retrieval is related to the degree of constraint on the recovered parameters which in turn is a consequence of the number of observations. Therefore the accuracy of the retrieval is contingent upon the sampling interval to a certain degree. There is also a minimum sampling interval. The use of the Levenberg-Marquardt optimization method requires that the system of non linear equations be well constrained. Thus the retrieval of a temperature and the $v' = 1$ and $v' = 2$ volume emission rates require at least three observations at each tangent height. However, the sampling interval is unlikely to ever approach this limit because the sampling interval should never exceed the spectral resolution, and at this minimum sampling interval the resolution would be so low that no useful information could be discerned from such a spectrum. In general, the decrease in retrieval accuracy due to a increase in the sampling interval is secondary to the effects of reducing the spectral resolution and thus the retrieval of state parameters is relatively insensitive to sampling interval.

The vertical resolution is a very important property of any scanning instrument

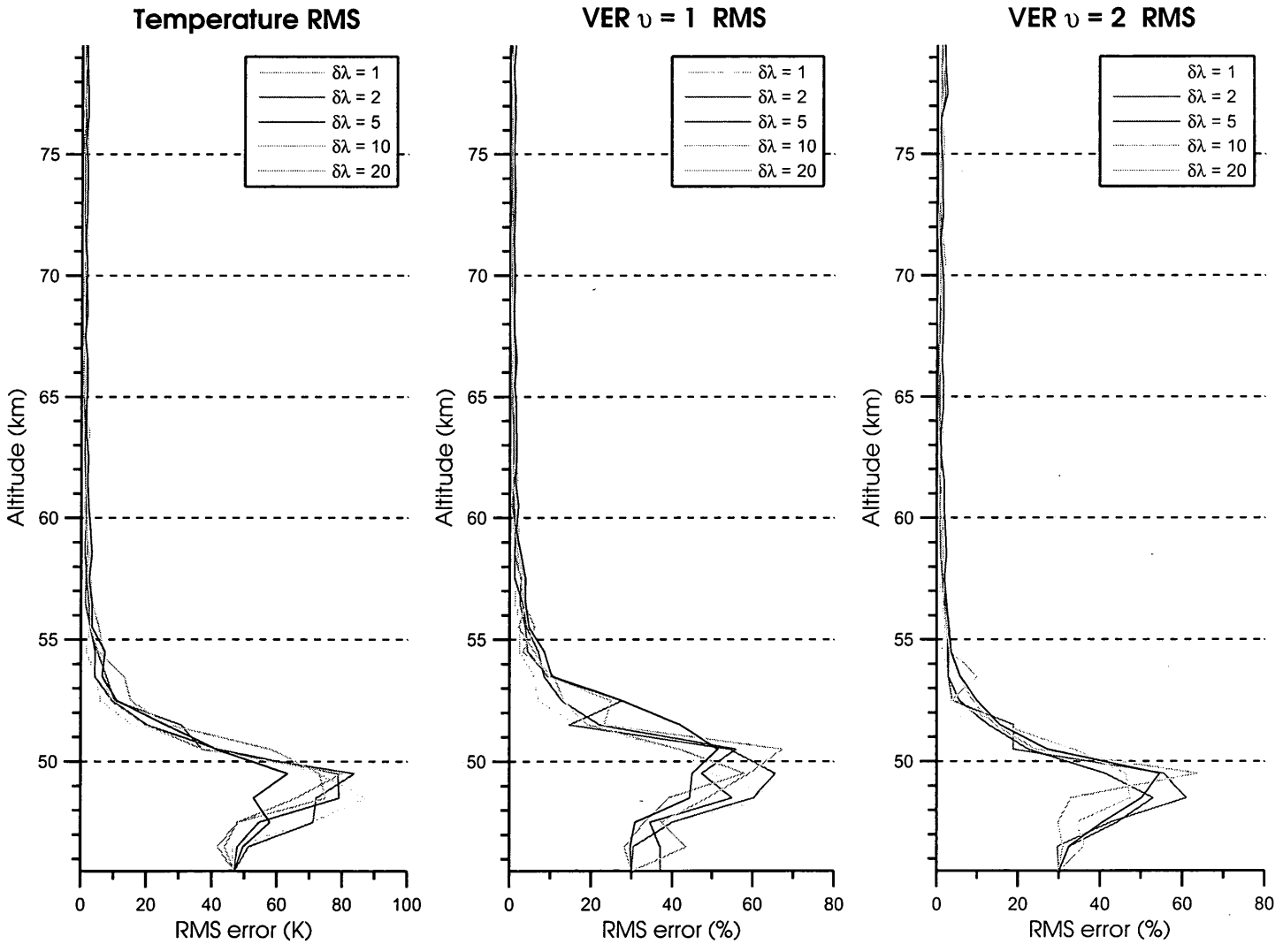

Figure 6.13: The recovered temperature RMS errors and volume emission rate percent RMS errors for $v' = 1$ and $v' = 2$ for sampling intervals of 1 $\mathring{A}$, 2 $\mathring{A}$, 5 $\mathring{A}$, 10 $\mathring{A}$ and 20$\mathring{A}$ are plotted in (a) (b), and (c), respectively. The synthetic observations were generated with a $t_s A\Omega$ value of 10^{-2} s cm^2 sr, spectral resolution of 20 $\mathring{A}$ and vertical resolution of 1 km under the Sudden Death deactivation model with Poisson noise.

as it relates to the sensitivity of the recovered profile to variations with height. High vertical resolutions require very high pointing accuracies, thus it is advantageous to lower the vertical resolution when possible to allow more flexibility in the instrument design. The RMS errors of ten Sudden Death deactivation model realizations using the COSPAR temperature profile (*Seiff*, 1982) as the true profile for vertical resolutions ranging from 1 km to 10 km are shown in Fig. 6.14, the corresponding recovered profiles are shown in Fig 6.15. The true temperature and volume emission rate profiles values are averaged to simulate observations of an instrument with a given vertical resolution and a set of simulated observations is generated using appropriate pathlengths. The temperature and VER profiles are then retrieved from these observations. The recovered temperature profiles are then linearly interpolated back onto the 1 km grid for comparison with the true temperature profile.

The temperature retrieval clearly benefits from the decrease in vertical resolution, a more consistent temperature profile is recovered with less fluctuations as the vertical resolution is decreased from 1 to 3 km. The profiles tend to shift negatively towards the *a priori* as previously noted at the bottom of the profile. The height of this shift depends the vertical resolution. As the COSPAR temperature profile is quite linear there is no discernible penalty for decreasing the vertical resolution, save for the decline in vertical range particularly at the top of the OH Meinel airglow layer as the temperatures recovered at the lowest heights tend to be inaccurate and thus excluding them is not disadvantageous. However, this temperature profile is an averaged profile and does not correspond to the true temperature profile at a given time. A temperature profile reflecting the immediate state of the atmosphere

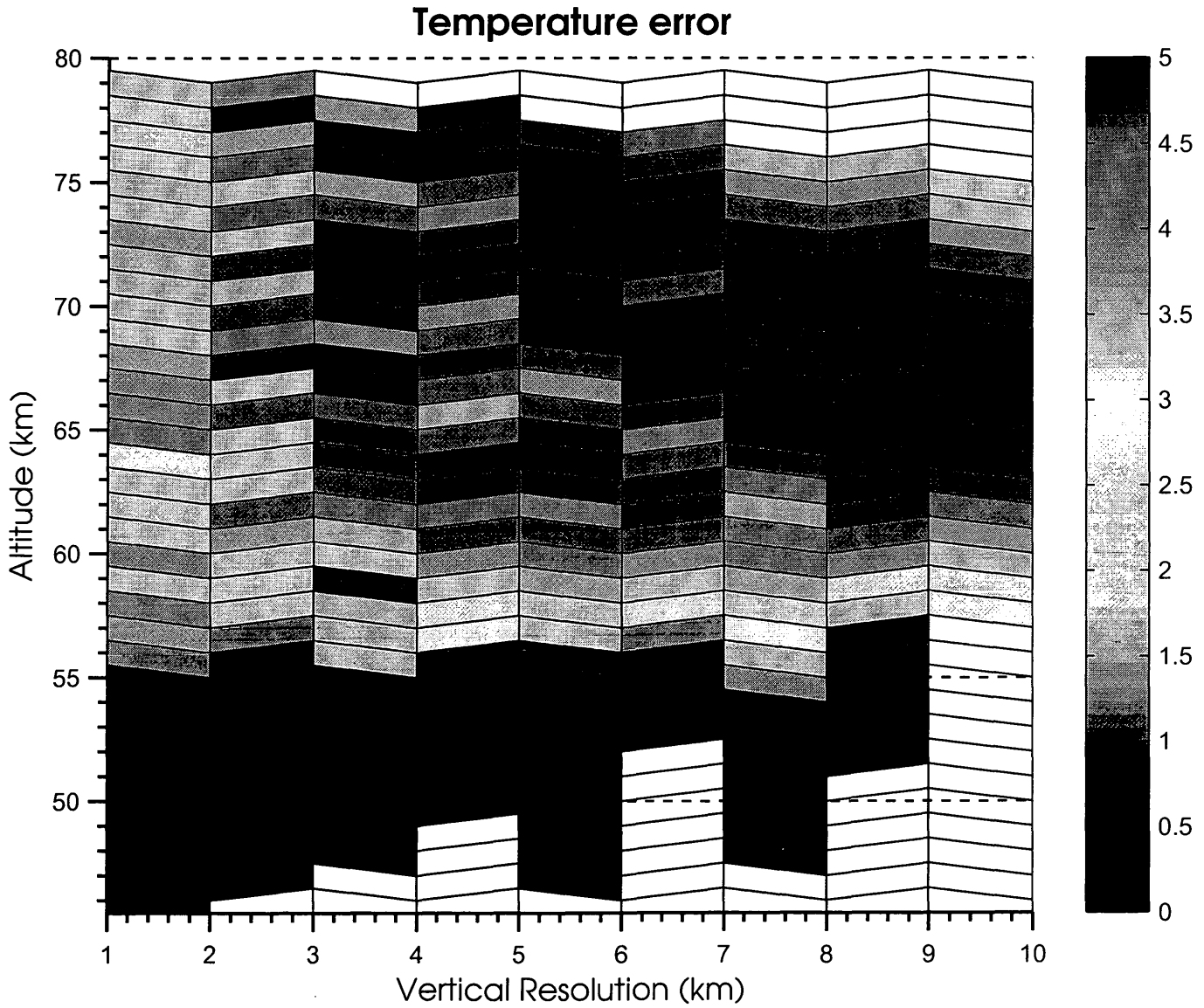

Figure 6.14: Root mean square error of 10 recovered temperature profiles for vertical resolutions varying from 1 to 10 km using COSPAR temperature profile. The simulated data sets were generated for an instrument with a $t_s A\Omega$ value of 10^{-3} s cm^2 sr, a 1 $\mathring{A}$ spectral resolution and a sampling interval of 1 $\mathring{A}$ for the Sudden Death deactivation model with Poisson noise. The units of the colour scale are in degrees Kelvin. Note the element shapes are slightly skewed due to slightly different height interpolation intervals.

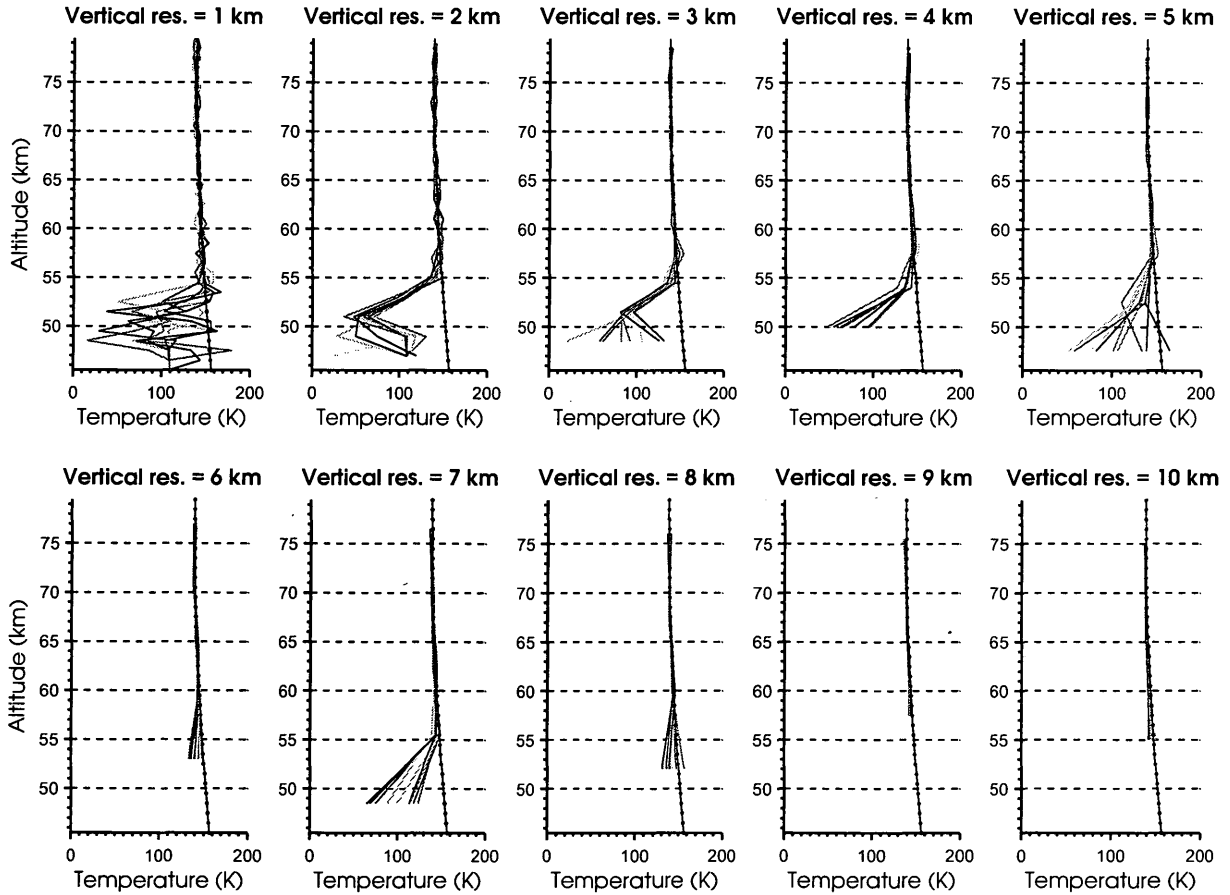

Figure 6.15: Recovered temperature profiles for vertical resolutions varying from 1 to 10 km using COSPAR temperature profile. Ten simulated data sets were generated for an instrument with a $t_s A\Omega$ value of 10^{-3} s cm^2 sr, a 1 $\mathring{A}$ spectral resolution and a sampling interval of 1 $\mathring{A}$ for the Sudden Death deactivation model with Poisson noise.

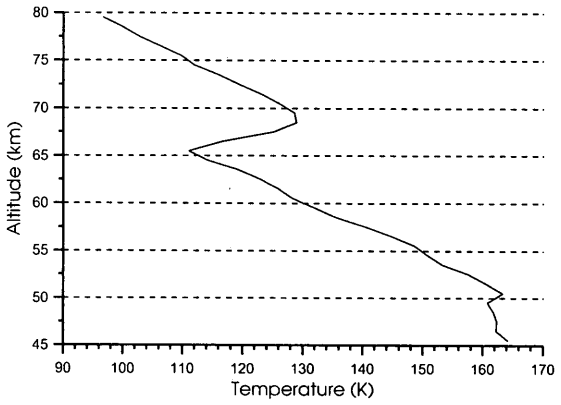

Figure 6.16: Temperature profile derived from the density profile measured during the entry, descent and landing phase of the Mars Pathfinder mission (*Schofield et al.*, 1997).

would instead contain structure caused by planetary waves such as thermal tides and gravity waves, and it is precisely this structure which may be lost with the decrease in vertical resolution.

Instead the Mars Pathfinder atmospheric temperature profile (*Schofield et al.*, 1997), shown in Fig. 6.16, derived from the density profile measured during the entry, descent and landing phase of the mission is used to assess the effect of increasing the vertical resolution. The Mars Pathfinder measured a deep temperature minimum at 80 km which coincides with the top of the OH Meinel airglow layer, followed by a local maximum just below 70 km and local minimum just above 65 km. These fluctuations are thought to be caused by the superposition of waves on the nighttime cooling (*Schofield et al.*, 1997). The root mean square of the simulated retrievals using the Mars Pathfinder temperature profile for a hypothetical instrument with a $t_s A\Omega$ value of 10^{-3} s cm^2 sr for the Sudden Death deactivation model are shown in Fig. 6.17. The associated recovered profiles are shown in Fig. 6.18.

Similar to the COSPAR temperature profile retrievals, an increase in accuracy

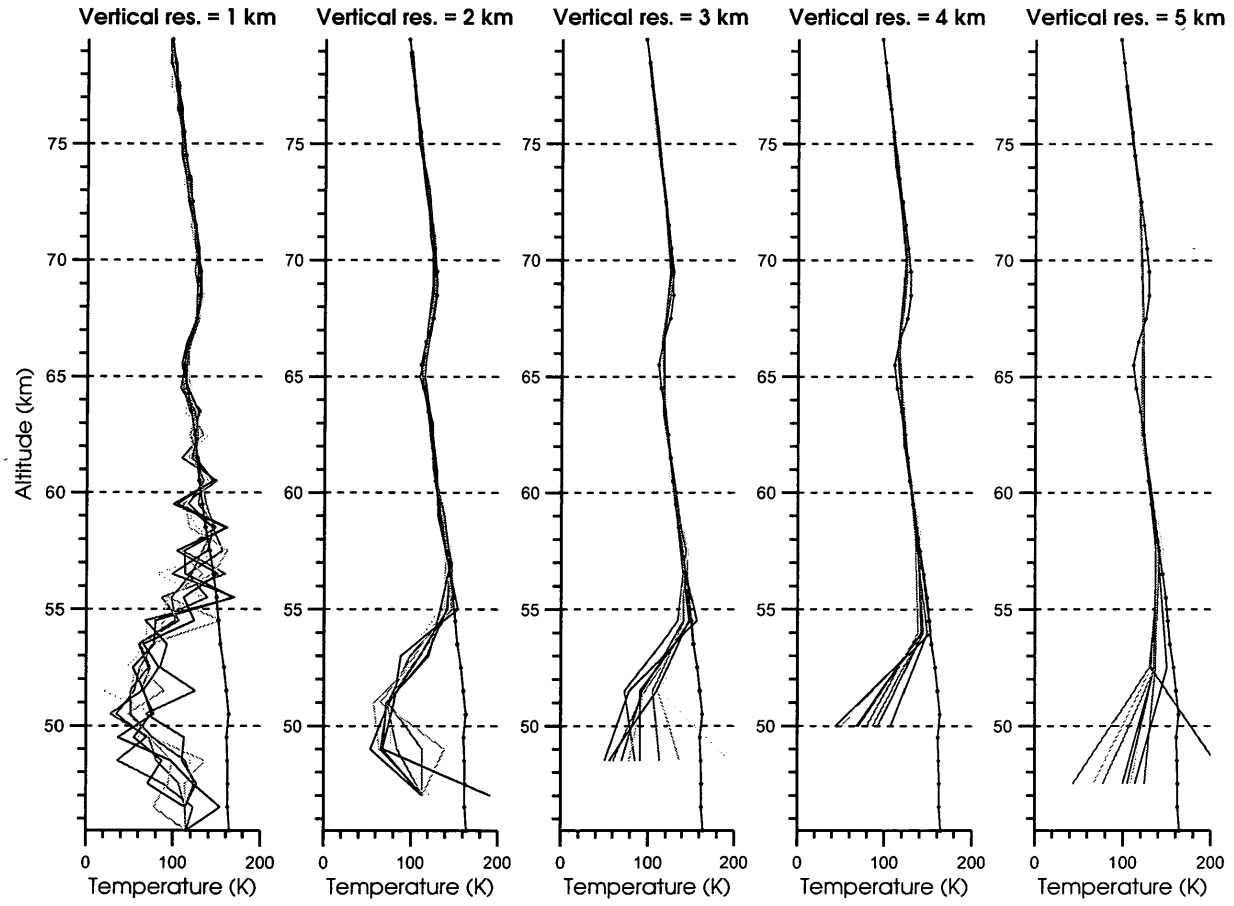

Figure 6.18: Recovered temperature profiles for vertical resolutions varying from 1 to 5 km using Mars Pathfinder temperature profile. Ten simulated data sets were generated for an instrument with a $t_s A\Omega$ value of 10^{-3} s cm^2 sr, a 1 $\mathring{A}$ spectral resolution and a sampling interval of 1 $\mathring{A}$ for the Sudden Death deactivation model with Poisson noise.

is observed as the vertical resolution decreases from 1 km to 2 km. There is also an increase in RMS error below 56.5 km unrelated to the vertical resolution. The key difference lies between just below 70 km and near 65.5 km, the altitudes of the local maximum and local minimum. As the vertical resolution decreases to 3 km and beyond the difference between the recovered profile and the true profiles at the local maximum and minimum increase. At a vertical resolution of 5 km these features are lost completely and an average temperature is recovered. The most accurate temperature profiles are recovered at a vertical resolution of 2 km.

Finally the sensitivity of the volume emission rate retrieval to the vertical resolution is discussed. Linear interpolation is not used for the volume emission rates as the shape of the profile is non linear. Instead the recovered emission rates are fit to a Chapman function of the following form (*Gao et al.*, 2010):

$$V(z) = V_{max} exp(\frac{1}{2}(1 - \frac{z - h_{max}}{a(z - h_{max} + b)} - exp(-\frac{z - h_{max}}{a(z - h_{max} + b)}))) \qquad (6.3)$$

where $V(z)$ is the OH Meinel airglow emission rate for a given vibrational level at altitude z. V_{max} is the peak emission rate, h_{max} is the corresponding height and a and b are parameters relevant to the half width of the layer. These four values are simultaneously optimized to the observed VER profiles by the Levenberg-Marquard non-linear fitting algorithm. The recovered Chapman fits are shown in Fig 6.19 and Fig 6.20. Although the shapes of the $v' = 1$ and $v' = 2$ volume emission rate profiles differ, similar discrepancies between the Chapman fit profiles and the true VER profile are noted. The VERs below 52.5 km are overestimated slightly by the Chapman function, this disparity increases with decreasing vertical resolution.

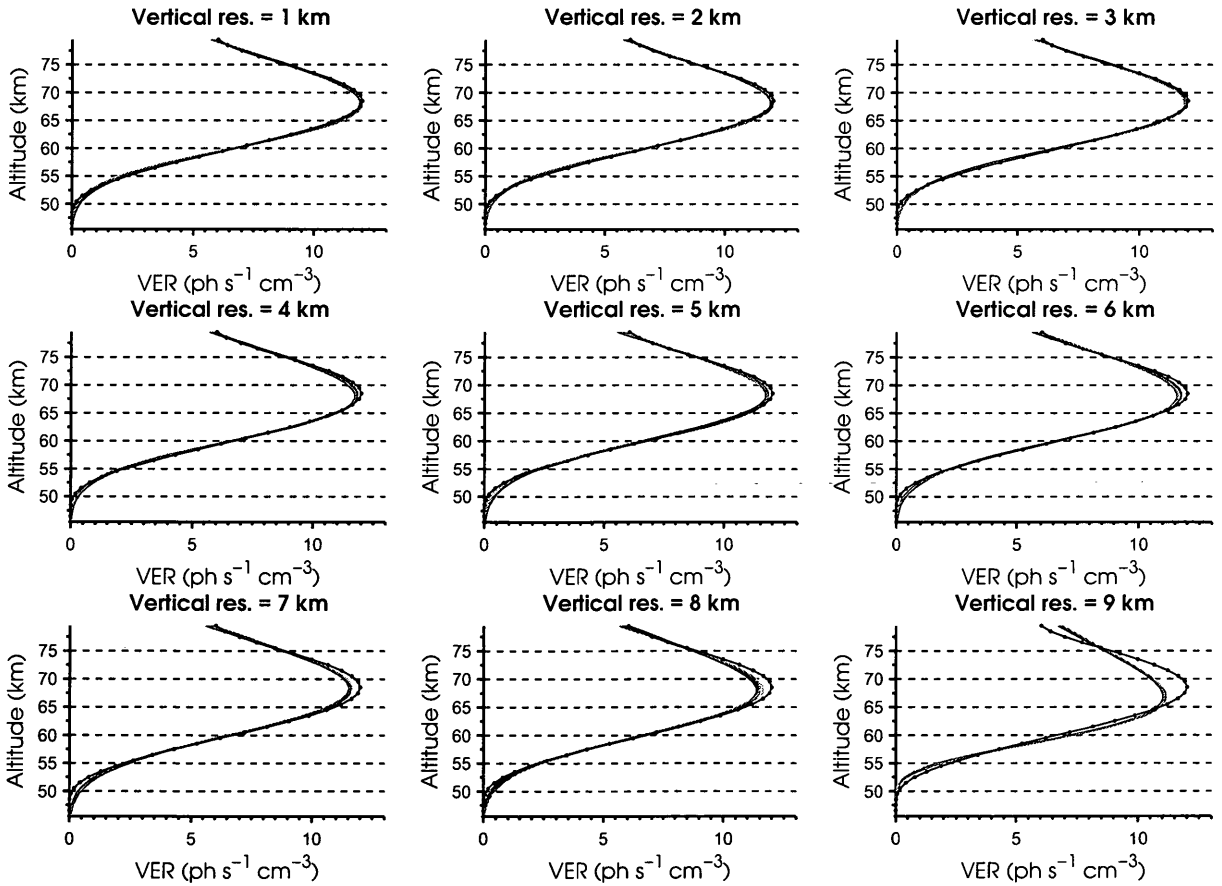

Figure 6.19: Chapman fit of recovered volume emission rate profiles for the $v' = 1$ vibrational level with vertical resolutions varying from 1 km to 10 km. The synthetic observations were generated for a hypothetical instrument with with a $t_s A\Omega$ of 10^{-3} s cm^2 sr, a 1 $\mathring{A}$ spectral resolution and sampling interval of 1 $\mathring{A}$ under the Sudden Death deactivation model with Poisson noise.

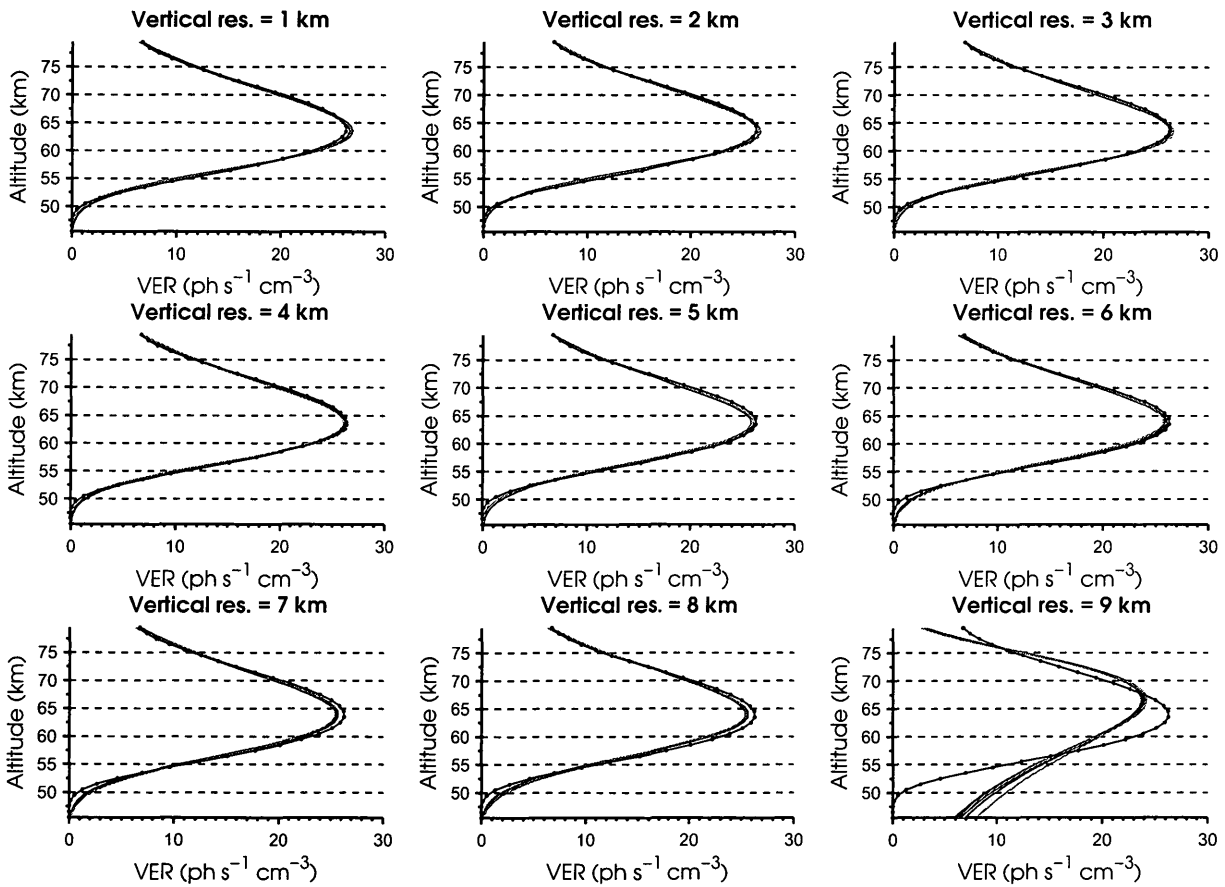

Figure 6.20: Chapman fit of recovered volume emission rate profiles for the $v' = 2$ vibrational level with vertical resolutions varying from 1 km to 10 km. The synthetic observations were generated for a instrument with with a $t_s A\Omega$ of 10^{-3} s cm^2 sr, a 1 $\mathring{A}$ spectral resolution and sampling interval of 1 $\mathring{A}$ under the Sudden Death deactivation model with Poisson noise.

The overestimation in the fit VERs is greater in the $v' = 1$ profiles in this altitude region. An underestimation of the peak emissions appears at a vertical resolution of 4 km for $v' = 1$ and 5 km for $v' = 2$ which also subsequently increases as the vertical resolution decreases further. Finally, at a vertical resolution of 9 km the recovered Chapman functions differ more substantially from the true volume emission rate profiles. Thus for accurate retrieval of the VER profiles a vertical resolution of less than 9 km is required although the accuracy increases for higher vertical resolutions in general.

For best results for both temperature and volume emission rate retrieval an observational vertical resolution of 2 km should be selected since the recovered temperature profiles at the vertical resolution are more accurate throughout the OH Meinel airglow layer and the VER profiles are well captured by the Chapman function.

7 Conclusions and Future Work

7.1 Summary

Remote sensing using observations of nighttime OH Meinel airglow is a technique which has been extensively used to study the Earth's atmosphere and more recently it has begun to be employed to gain a better understanding of the Venusian atmosphere. This technique has yet to be successfully employed in Mars exploration. Observations of the rotational-vibrational OH spectrum can be used to recover OH rotational temperatures and the volume emission rates of the excited OH molecules which produce the airglow. Conservative estimates suggest that for the excited OH molecules with low vibrational and rotational states, the rotational levels are thermalized with the surrounding atmosphere and thus the temperatures recovered from transitions of these molecules are equivalent to the atmospheric temperature. In addition, the rotational temperatures can be used to study the atmospheric wave dynamics. The volume emission rates, in conjunction with other observations, can be used to gain a better understanding of both the odd hydrogen and odd oxygen cycles in the Martian atmosphere. Thus observations of nighttime OH Meinel airglow would allow us to gain valuable insight into the mechanisms which dominate the middle Martian atmosphere.

The relaxation process of the excited OH Meinel molecules which are deactivated through collisions instead of emission is not well understood. Three possible deactivation processes have been suggested: Sudden Death, Collisional Cascade and a third method put forth by *Krasnopolsky* (2010). For these three models, the volume emission rates for the $v' = 1$ and $v' = 2$ vibrational levels differ in intensity according to model estimates. Thus observations of emissions from the Martian OH Meinel nightglow could potentially corroborate one of these models and resolve the uncertainty in the deactivation process.

To recover temperatures and volume emission rates the Levenberg-Marquardt iterative optimization method coupled with Optimal Estimation technique is used to fit the OH Meinel Band wavelength bin radiance (WBR) spectrum. For a complete vertical profile limb observations are necessary. This necessitates a methodology for decomposing these observations to isolate the emissions from the different height levels. Three different approaches were compared: the Onion Peeling method, a method tailored to the OH Meinel nightglow observations involving derived absolute wavelength bin radiance spectra and the Global Optimization method. Of the three, the Global Optimization proved to be the most robust in the presence of simulated noise. There is, however, potential for improvement in the method involving derived absolute WBR spectra which will be discussed below. These methods were also tested in three possible modes: temperature retrieval, volume emission rate retrieval and simultaneous recovery of both temperatures and volume emission rates. The simultaneous retrieval of temperatures and volume emission rates is the most versatile of modes and the recovered profiles are only slightly less accurate than the profiles recovered in the other modes. Furthermore, both the temperature

retrieval mode and VER retrieval mode require knowledge of the parameter not being recovered (*i.e.*, knowledge of the VERs for temperature retrieval and *vice-versa*). Possible sources for temperature and VER information are complimentary instruments and photochemical models. The profiles obtained from these sources would likely contain some inherent error which would likely increase the retrieval error and thus reduce the discrepancy in accuracy between the simultaneous and independent retrievals. Since the simultaneous retrieval method is not restricted to use on the Martian atmosphere, the method can be used to recover temperatures and excited OH VER in any atmosphere where OH Meinel airglow is emitted such the atmospheres of Earth and Venus.

Although more comprehensive, the simultaneous retrieval of temperatures and volume emission rates imposes additional requirements on the potential spectral region used for fitting in addition to the conditions required for atmospheric temperature retrieval and for the investigation of the collisional deactivation process of excited OH molecule. The number of potential spectral regions which meet all these conditions is limited. However, one potential region has been identified. It lies between 2.79 μm and 2.95 μm and is composed of emissions of the (1-0) and (2-1) bands of the OH Meinel airglow. Through simulations the rough order of magnitude estimate of the instrument $t_s A\Omega$ value necessary for the detection of OH Meinel nightglow within this spectral region, regardless of the deactivation process, was determined to be 10^{-5} s cm^2 sr. At this $t_s A\Omega$ value simulated recovered temperature and VER profiles are fairly accurate for both the Collisional Cascade model and the deactivation model suggested in *Krasnopolsky* (2010). However, the profiles recovered using the modelled volume emission rates for the Sudden Death

model at this $t_s A\Omega$ value were essentially meaningless. A $t_s A\Omega$ value of 10^{-3} s cm^2 sr is necessary for relatively accurate retrieval of temperatures and VERs for the Sudden Death model. The sensitivity of the retrievals to the spectral resolution, sampling rate and vertical resolution were also assessed.

7.2 Future work

There are two avenues for advancement in this work: further improvement in the retrieval methods and validation.

In particular the retrieval method involving derived absolute wavelength bin radiance spectra has potential for improvement. The method involves two phases of optimization: initially, the observed radiances are fitted to determine the absolute WBR spectra for each height layer, after some manipulation these derived WBRs are then fitted to recover temperatures. In this work the fitting method used in the first phase does not take account of instrumental errors associated with the observations. Clearly, a fitting method that considers the observational errors and has some methodology, such as optimal estimation, for determining the fitting errors which could then be used in the second optimization would substantially improve the accuracy of the retrieval. However, the problem of the two phase fitting would remain. An approach where both these fittings would be done simultaneously may prove to be more beneficial.

The retrieval method presented here must be validated by comparison with limb measurements with established temperature or volume emission rates. Since the simultaneous optimization approach is independent of photochemical model

or complementary instruments, the method can be applied to observations of OH Meinel nighttime airglow in the Earth's and Venus' atmospheres.

Two potential sources for validation data are the SCIAMACHY (SCanning Imaging Absorption spectroMeter for Atmospheric CartograpHY) instrument on board ENVISAT and the VIRTIS (Visible and Infra-Red Thermal Imaging Spectrometer) instrument on board the Venus Express. SCIAMACHY is a passive spectrometer which observes backscattered, reflected, transmitted or emitted radiation between 240 and 2380 nm of the Earth's atmosphere and surface. The spectral region covered by the instrument includes many OH Meinel emission bands, specifically the Δv = 2, 3, 4 bands. Temperatures are recovered from the (3-1) band of OH Meinel airglow using the approach described in *von Savigny et al.* (2004) which could be used for validation. VIRTIS-M-IR, the mapping subsystem of the VIRTIS instrument, is an imaging spectrometer covering the 1 - 5μm wavelength range in both the nadir and the limb. Observations of the (1-0), (2-1) and (2-0) bands of OH Meinel nightglow by VIRTIS-M-IR have been reported in *Soret et al.* (2010) and the distribution and characteristics of the airglow layer were described. SPICAV/SOIR (Ultraviolet and Infrared Atmospheric Spectrometer) also on board Venus Express recovers CO_2 rotational temperatures which can be used for comparison. Good agreement with these derived temperature profiles would validate the approach for temperature and excited OH volume emission rate retrieval from limb measurements of OH Meinel nightglow.

Appendix A Summary of Successful Mars Exploration Missions

Mission[7]	Launch Date	Description
Mariner 4	11/28/1964	Fly by mission. First close up pictures of planet confirming presence of craters and thin CO_2 atmosphere. A small intrinsic magnetic field was also detected.
Mariner 6 and 7	02/24/1969 & 03/27/1969	Fly by missions. Together they took measurements of surface and atmospheric temperatures, molecular composition of surface, and atmospheric pressure. Over 200 pictures were acquired.
Mars 2	05/19/1971	Lander crashed-landed due to braking block failure. Orbiter returned measurements until 1972.

[7] *National Aeronautics and Space Administration* (Accessed 29 October 2011)

Mars 3	05/28/1971	Lander was first successful landing on Mars but failed after relaying 20 seconds of video. Orbiter returned orbiter returned measurements of surface temperature and atmospheric composition until August, 1972.
Mariner 9	05/30/1971	First US spacecraft to enter an orbit around a planet other than Earth. First high resolution images of the moons Phobos and Deimos. River and channel-like features observed.
Mars 4	07/21/1973	Failed to enter orbit but returned some images and data during fly by.
Mars 5	07/25/1973	Acquired images in preparation for Mars 6 and 7 missions.
Mars 6	08/05/1973	Lander returned atmospheric descent data but failed before landing.
Viking 1 & 2	08/20/1975 & 09/09/1975	Landers provided detailed color panoramic views of the Martian terrain and monitored the Martian weather. Orbiters mapped planet's surface, acquiring over 52,000 images.
Mars Global Surveyor	11/07/1996	Mapped the surface of Mars from 1998 to 2006.
Mars Pathfinder	12/04/1996	Stationary lander and rover. Rover explored the area surrounding the lander.

2001 Mars Odyssey	04/07/2001	On-going mission. Studies geology, climate, and mineralogy of Mars and serves as communication relay for future missions.
Mars Express	06/02/2003	On-going mission. Studies the geology, atmosphere, surface environment, history of water and potential for life on Mars. Communication failure with lander, Beagle 2.
Mars Exploration Rover Mission	06/10/2003 & 07/07/2003	On-going mission. Two rovers, Spirit and Opportunity, search for and characterize a variety of rocks and soils that hold clues to past water activity.
Mars Reconnaissance Orbiter	08/12/2005	On-going mission. Provides highly detailed information regarding the surface, subsurface and atmosphere of Mars.
Phoenix Mars Lander	08/04/2007	Studied the history of water and habitability potential in the Martian arctic's ice-rich soil.

References

Anderson, D. E., Jr. (1974), Mariner 6, 7, and 9 Ultraviolet Spectrometer Experiment: Analysis of Hydrogen Lyman Alpha Data, *J. Geophys. Res.*, *79*.

Angelats i Coll, M., F. Forget, M. A. López-Valverde, P. L. Read, and S. R. Lewis (2004), Upper atmosphere of Mars up to 120 km: Mars Global Surveyor accelerometer data analysis with the LMD general circulation model, *J. Geophys. Res.*, *109*, E01,011.

Baker, D. J., and A. T. Stair Jr (1988), Rocket measurements of the altitude distributions of the hydroxyl airglow, *Phys. Scripta*, *37*, 611–622.

Bates, D. R., and M. Nicolet (1950), Atmospheric Hydrogen, *Planet. Space Sci.*, *62*, 106–110.

Bernath, P. (2005), *Spectra of Atoms and Molecules*, Topics in Physical Chemistry Series, Oxford University Press.

Bertaux, J., F. Leblanc, S. Perrier, E. Quemerais, O. Korablev, E. Dimarellis, A. Reberac, F. Forget, P. Simon, S. Stern, and B. Sandel (2005), Nightglow in the upper atmosphere of Mars and implications for atmospheric transport., *Science*, *307*, 566–569.

Bertaux, J. L., B. Gondet, J. P. Bibring, F. Montmessin, and F. Lefèvre (2011), First detection of O2 recombination nightglow emission at 1.27μm in the atmosphere of Mars With OMEGA/MEX and comparison with model, in *Mars Atmosphere: Modelling and observation*, edited by F. Forget & E. Millour, pp. 334–336.

Brain, D. A., and B. M. Jakosky (1998), Atmospheric loss since the onset of the Martian geologic record: Combined role of impact erosion and sputtering, *J. Geophys. Res.*, *1032*, 22,689–22,694.

Burtt, K. D., and R. D. Sharma (2008), Near-resonant energy transfer from highly vibrationally excited OH to N_2, *J. Chem. Phys.*, *128*, 124,311.

Carlotti, M. (1988), Global-fit approach to the analysis of limb-scanning atmospheric measurements, *Appl. Optics*, *27*, 3250–3254.

Carlotti, M., B. M. Dinelli, P. Raspollini, and M. Ridolfi (2001), Geo-fit approach to the analysis of limb-scanning satellite measurements, *Appl. Optics*, *40*, 1872–1885.

Chamberlain, J. W. (1961), *Physics of the aurora and airglow*, 100-123 pp.

Charters, P. E., R. G. MacDonald, and J. C. Polanyi (1971), Formation of vibrationally excited OH by the reaction H + O3, *Appl. Optics*, *10*, 1747–1754.

Clancy, R. T., M. J. Wolff, B. A. Whitney, B. A. Cantor, M. D. Smith, and T. H. McConnochie (2010), Extension of atmospheric dust loading to high altitudes during the 2001 Mars dust storm: MGS TES limb observations, *Icarus*, *207*, 98–109.

Coxon, J. A. (1980), Optimum molecular constants and term values for the X 2Π $v \leq 5$ and A $2\Sigma^+$ $v \leq 3$ states of OH, *Can. J. Phys.*, *58*, 933–949.

Coxon, J. A., and S. C. Foster (1982), Rotational analysis of hydroxyl vibration - rotation emission bands: Molecular constants for OH $X^2\Pi$, $6 \leq v \leq 10$, *Can. J. Phys.*, *60*, 41–48.

Dasch, C. J. (1992), One-dimensional tomography - A comparison of Abel, onion-peeling, and filtered backprojection methods, *Appl. Optics*, *31*, 1146–1152.

Degenstein, D. A., E. J. Llewellyn, and N. D. Lloyd (2003), Volume emission rate tomography from a satellite platform, *Appl. Optics*, *42*, 1441–1450.

Degenstein, D. A., E. J. Llewellyn, and N. D. Lloyd (2004), Tomographic retrieval of the oxygen infrared atmospheric band with the OSIRIS infrared imager, *Can. J. Phys.*, *82*, 501–515.

Déjardin, G., and Bernard, R. (1938), Les bands de la molécule OH dans le spectre du ciel nocturne, in *Comptes rendus hebdomadaires des séances de l'Académie des sciences*, pp. 1747–1749.

Ehresmann, B., S. Burmeister, R. F. Wimmer-Schweingruber, and G. Reitz (2011), Influence of higher atmospheric pressure on the Martian radiation environment: Implications for possible habitability in the Noachian epoch, *J. Geophys. Res.*, *116*, A10,106.

Forbes, J. M., A. F. C. Bridger, S. W. Bougher, M. E. Hagan, J. L. Hollingsworth, G. M. Keating, and J. Murphy (2002), Nonmigrating tides in the thermosphere of Mars, *J. Geophys. Res.*, *107*, 1690–1695.

Forget, F., F. Hourdin, F. Fournier, C. Hourdin, O. Talagrand, M. Collins, S. R. Lewis, P. L. Read, and J.-P. Huot (1999), Improved general circulation models of the Martian atmosphere from the surface to above 80 km, *104*, 24,155–24,175.

Forget, F., F. Montmessin, J.-L. Bertaux, F. González-Galindo, S. Lebonnois, E. Quémerais, A. Reberac, E. Dimarellis, and M. A. López-Valverde (2009), Density and temperatures of the upper Martian atmosphere measured by stellar occultations with Mars Express SPICAM, *J. Geophys. Res.*, *114*, E01,004.

Gao, H., J. Xu, and Q. Wu (2010), Seasonal and QBO variations in the OH nightglow emission observed by TIMED/SABER, *J. Geophys. Res.*, *115*, A06,313.

García Muñoz, A., J. C. McConnell, I. C. McDade, and S. M. L. Melo (2005), Airglow on Mars: Some model expectations for the OH Meinel bands and the O_2 IR atmospheric band, *Icarus*, *176*, 75–95.

García-Muñoz, A. (2006), I. Airglow on Mars: Model predictions for the oxygen IR atmospheric band at 1.27 micrometers, the hydroxyl radical Meinel bands and the hydroxyl radical A-X band system. II. Physical and chemical aeronomy of HD 209458b, Ph.D. thesis, York University.

Harrison, A. W., and D. J. W. Kendall (1973), Airglow hydroxyl doublet ratio temperatures., *J. Geophys. Res.*, *78*, 4697–4701.

Harrison, A. W., E. J. Llewellyn, and D. C. Nicholls (1970), Night airglow hydroxyl rotational temperatures., *Canadian Journal of Physics*, *48*, 1766–1768.

Heaps, H. S., and G. Herzberg (1952), Intensity distribution in the rotation-vibration spectrum of the OH molecule, *Z. Phys. A-Hadron Nucl*, *133*, 48–64.

Heppner, J. P., and L. H. Meredith (1958), Nightglow emission altitudes from rocket measurements, *J. Geophys. Res.*, *63*, 51–65.

Herzberg, G. (1950), *Spectra of Diatomic Molecules*, Molecular Spectra and Molecular Structure, Van Nostrand.

Herzberg, G. (1951), The Atmospheres of the Planets (with Plates III and IV), *J. Roy. Astron. Soc. Can.*, *45*.

Herzberg, G. (1971), *The spectra and structures of simple free radicals; an introduction to molecular spectroscopy*, Cornell University Press, Ithaca.

Hill, E., and J. H. van Vleck (1928), On the quantum mechanics of the rotational distortion of multiplets in molecular spectra, *Phys. Rev.*, *32*, 250–272.

Hunten, D. M., and M. B. McElroy (1966), Quenching of Metastable States of Atomic and Molecular Oxygen and Nitrogen, *Rev. Geophys.*, *4*, 303–328.

Innis, J. L., F. A. Phillips, G. B. Burns, P. A. Greet, W. J. R. French, and P. L. Dyson (2001), Mesospheric temperatures from observations of the hydroxyl (6-2) emission above Davis, Antarctica: a comparison of rotational and Doppler measurements, *Ann. Geophys.*, *19*, 359–365.

Isaksen, I. S. A., and S. B. Dalsøren (2011), Getting a Better Estimate of an Atmospheric Radical, *Science*, *331*, 38–39.

Jakosky, B. M., R. O. Pepin, R. E. Johnson, and J. L. Fox (1994), Mars atmospheric loss and isotopic fractionation by solar-wind-induced sputtering and photochemical escape, *Icarus*, *111*, 271–288.

Jenniskens, P., and C. O. Laux (2004), Search for the OH ($X^2\Pi$) Meinel Band Emission in Meteors as a Tracer of Mineral Water in Comets: Detection of N_2^+ (A-X), *Astrobiology*, *4*, 109–121.

Khomich, V. Y., A. I. Semenov, and N. N. Shefov (2008), *Airglow as an Indicator of Upper Atmospheric Structure and Dynamics*, Springer, New York.

Kistiakowsky, G. B., and F. D. Tabbutt (1959), Gaseous Detonations. XII. Rotational temperatures of the hydroxyl free radicals, *J. Chem. Phys.*, *30*, 577–581.

Kleinböhl, A., J. T. Schofield, D. M. Kass, W. A. Abdou, C. R. Backus, B. Sen, J. H. Shirley, W. G. Lawson, M. I. Richardson, F. W. Taylor, N. A. Teanby, and D. J. McCleese (2009), Mars Climate Sounder limb profile retrieval of atmospheric temperature, pressure, and dust and water ice opacity, *J. Geophys. Res.*, *114*, E10,006.

Krasnopolsky, V. A. (2010), Venus night airglow: Ground-based detection of OH, observations of O_2 emissions, and photochemical model, *Icarus*, *207*, 17–27.

Krasnopolsky, V. A. (2011), Atmospheric chemistry on Venus, Earth, and Mars: Main features and comparison, *Planet. Space Sci.*, *59*, 952–964.

Krasnopolsky, V. A., and A. A. Krysko (1976), On the night airglow of the Martian atmosphere, in *Space Research XVI*, edited by M. J. Rycroft, pp. 1005–1008.

Lide, D. (Internet version 2012), *CRC handbook of chemistry and physics: a ready-reference book of chemical and physical data*, CRC Handbook of Chemistry and Physics, 92th Ed, CRC Press.

Livesey, N. J., and W. G. Read (2000), Direct retrieval of line-of-sight atmospheric structure from limb sounding observations, *Geophys. Res. Lett.*, *27*, 891–894.

Magalhães, J. A., J. T. Schofield, and A. Seiff (1999), Results of the Mars Pathfinder atmospheric structure investigation, *J. Geophys. Res.*, *104*, 8943–8955.

Magnan, P. (2011), Single-photon imaging for astronomy and aerospace applications, in *Single-Photon Imaging, Springer Series in Optical Sciences*, vol. 160, edited by P. Seitz and A. J. Theuwissen, pp. 301–327, Springer Berlin / Heidelberg.

Marquardt, D. W. (1963), An algorithm for least-squares estimation of nonlinear parameters, *SCIAM Journal*, *11*, 431–441.

Marsh, D. R., A. K. Smith, M. G. Mlynczak, and J. M. Russell (2006), SABER observations of the OH Meinel airglow variability near the mesopause, *J. Geophys. Res.*, *111*, S05.

McConnochie, T. H., J. F. Bell, D. Savransky, M. J. Wolff, A. D. Toigo, H. Wang, M. I. Richardson, and P. R. Christensen (2010), THEMIS-VIS observations of clouds in the martian mesosphere: Altitudes, wind speeds, and decameter-scale morphology, *Icarus*, *210*, 545–565.

McDade, I. C., and E. J. Llewellyn (1987), Kinetic parameters related to sources and sinks of vibrationally excited OH in the nightglow, *J. Geophys. Res.*, *92*, 7643–7650.

McDade, I. C., and E. J. Llewellyn (1988), Mesospheric oxygen atom densities inferred from night-time OH Meinel band emission rates, *Planet. Space Sci.*, *36*, 897–905.

McDade, I. C., and E. J. Llewellyn (1993), Satellite airglow limb tomography. Methods for recovering structured emission rates in the mesospheric airglow layer, *Can. J. Phys.*, *71*, 552–563.

Meinel, A. B., II (1950), OH Emission Bands in the Spectrum of the Night Sky. II., *Astrophys. J.*, *112*, 120–130.

Melosh, H. J., and A. M. Vickery (1989), Impact erosion of the primordial atmosphere of Mars, *Nature*, *338*, 487–489.

Meriwether Jr., J. W. (1989), A review of the photochemistry of selected nightglow emissions from the mesopause, *J. Geophys. Res.*, *94*, 14,62914,646.

Mies, F. H. (1974), Calculated vibrational transition probabilities of OH($X^2\Pi$), *J. Mol. Spectrosc.*, *53*, 150–188.

Migliorini, A., G. Piccioni, A. Cardesn Moinelo, and P. Drossart (2011), Hydroxyl airglow on Venus in comparison with Earth, *Planet. Space Sci.*, *59*, 974–980.

Modest, M. (2003), *Radiative Heat Transfer*, Academic Press.

Montmessin, F., J. L. Bertaux, F. Lefvre, E. Marcq, D. Belyaev, J.-C. Grard, K. O., A. Fedorova, V. Sarago, and A. C. Vandaele (2011), A layer of ozone detected in the nightside upper atmosphere of Venus, *Icarus*, *216*, 82–85.

National Aeronautics and Space Administration (Accessed 29 October 2011), A Chronology of Mars Exploration, `http://history.nasa.gov/marschro.htm`.

Nicolet, M. (1948), Deductions regarding the state of the high atmosphere, in *The Emission Spectra of the Night Sky and Aurorae*, p. 36, Reports of the Gassiot Committee.

Pendleton, W., Jr., P. Espy, D. Baker, A. Steed, and M. Fetrow (1989), Observation of OH Meinel (7, 4) P(N-double-prime = 13) transitions in the night airglow, *J. Geophys. Res.*, *94*, 505–510.

Pendleton, W. R., Jr., P. J. Espy, and M. R. Hammond (1993), Evidence for non-local-thermodynamic-equilibrium rotation in the OH nightglow, *J. Geophys. Res.*, *981*, 11,567–11,579.

Perminov, V. I. (2009), Seasonal temperature variations near the mesopause according to the hydroxyl emission measurements in Zvenigorod, *Geomagn. Aeron+*, *49*, 797–804.

Perry, R. S., and W. K. Hartmann (2006), Mars primordial crust: Unique sites for investigating proto-biologic properties, *Origins Life Evol. B.*, *36*, 533–540.

Piccioni, G., P. Drossart, E. Suetta, M. Cosi, E. Ammannito, A. Barbis, R. Berlin, A. Boccaccini, G. Bonello, M. Bouy, F. Capaccioni, G. Cherubini, M. Dami, O. Dupuis, A. Fave, G. Filacchione, Y. Hello, F. Henry, S. Hofer, G. Huntzinger,

R. Melchiorri, J. Parisot, C. Pasqui, G. Peter, C. Pompei, J. M. Ress, A. Semery, A. Soufflot, and the VIRTIS Co-I team (2007), VIRTIS: The Visible and Infrared Thermal Imaging Spectrometer, *ESA Special Publication, SP 1295*, 1–27.

Piccioni, G., P. Drossart, L. Zasova, A. Migliorini, J.-C. Gérard, F. P. Mills, A. Shakun, A. García Muñoz, N. Ignatiev, D. Grassi, V. Cottini, F. W. Taylor, S. Erard, and The Virtis-Venus Express Technical Team (2008), First detection of hydroxyl in the atmosphere of Venus, *Astron. Astrophys.*, *483*, L29–L33.

Ranganathan, A. (2004), The Levenberg-Marquardt Algorithm.

Rodgers, C. D. (1976), Retrieval of atmospheric temperature and composition from remote measurements of thermal radiation, *Rev. Geophys.*, *14*, 609–624.

Schofield, J. T., J. R. Barnes, D. Crisp, R. M. Haberle, S. Larsen, J. A. Magalhes, J. R. Murphy, A. Seiff, and G. Wilson (1997), The Mars Pathfinder Atmospheric Structure Investigation/Meteorology (ASI/MET) Experiment, *Science*, *278*, 1752–1758.

Seiff, A. (1982), Post-Viking models for the structure of the summer atmosphere of Mars, *Adv. Space Res.*, *2*, 3–17.

Sentman, D. D., E. M. Wescott, R. H. Picard, J. R. Winick, H. C. Stenbaek-Nielsen, E. M. Dewan, D. R. Moudry, F. T. Sa˜O Sabbas, M. J. Heavner, and J. Morrill (2003), Simultaneous observations of mesospheric gravity waves and sprites generated by a midwestern thunderstorm, *J. Atmos. Sol.-Terr. Phys.*, *65*, 537–550.

Shepherd, G. G. (2002), *Spectral Imaging of the Atmosphere*, *International geophysics series*, vol. 82, Academic Press, Boston.

Shklovsky, I. S. (1950a), Identification of the infrared luminescence of the nigh sky with the rotation-vibration bands of the OH hydroxyl molecules., *Dokl USSR Acad Sci*, *75*, 371–374.

Shklovsky, I. S. (1950b), Quantitative analysis of the hydroxyl emission intensity of the night sky, *Dokl USSR Acad Sci*, *75*, 789–792.

Shklovsky, I. S. (1951), On the nature of the infrared radiation of the night sky, *Izv. Crimea Astrophys. Observ.*, *7*, 34–58.

Snyder, D. L., C. W. Helstrom, A. D. Lanterman, M. Faisal, and R. L. White (1995), Compensation for readout noise in CCD images, *J. Opt. Soc. Am. A*, pp. 272–283.

Soret, L., J.-C. Gérard, G. Piccioni, and P. Drossart (2010), Venus OH nightglow distribution based on VIRTIS limb observations from Venus Express, *Geophys. Res. Lett.*, *370*, L06,805.

Steck, T., M. Höpfner, T. von Clarmann, and U. Grabowski (2005), Tomographic retrieval of atmospheric parameters from infrared limb emission observations, *Appl. Optics*, *44*, 3291–3301.

Takahashi, H., and P. Batista (1981), Simultaneous Measurements of OH(9,4), (8,3), (7,2), (6,2) and (5,1) Bands in the Airglow, *J. Geophys. Res*, *86*, 5632–5642.

Takahashi, H., P. P. Batista, R. A. Buriti, D. Gobbi, T. Nakamura, T. Tsuda, and S. Fukao (1999), Response of the airglow OH emission, temperature and mesopause wind to the atmospheric wave propagation over Shigaraki, Japan, *Earth Planets Space*, *51*, 863–875.

Taylor, M. J., P.-D. Pautet, A. F. Medeiros, R. Buriti, J. Fechine, D. C. Fritts, S. L. Vadas, H. Takahashi, and F. T. São Sabbas (2009), Characteristics of mesospheric gravity waves near the magnetic equator, Brazil, during the SpreadFEx campaign, *Ann. Geophys.*, *27*, 461–472.

Turnbull, D. N., and R. P. Lowe (1989), New hydroxyl transition probabilities and their importance in airglow studies, *Planet. Space Sci.*, *37*, 723–738.

Viereck, R. A., and C. S. Deehr (1989), On the interaction between gravity waves and the OH Meinel (6-2) and the O2 atmospheric (0-1) bands in the polar night airglow, *J. Geophys. Res.*, *94*, 5397–5404.

von Savigny, C., K.-U. Eichmann, E. J. Llewellyn, H. Bovensmann, J. P. Burrows, M. Bittner, K. Höppner, D. Offermann, M. J. Taylor, Y. Zhao, W. Steinbrecht, and P. Winkler (2004), First near-global retrievals of OH rotational temperatures from satellite-based Meinel band emission measurements, *Geophys. Res. Lett.*, *311*, L15,111.

Witasse, O. (2000), Modelisation des ionosphere planetaires et de leur rayonnement: la Terre et Mars, Ph.D. thesis, Universite Joseph Fourier.